Correlation of FluidFM® Technology and Fluorescence Microscopy for the Visualization of Cellular Detachment Steps

Korrelation der FluidFM® Technologie und Fluoreszenzmikroskopie zur Visualisierung von zellulären Ablöseschritten

Doctoral thesis for a doctoral degree
at the Graduate School of Life Sciences,
Julius-Maximilians-Universität Würzburg,
Section: Biomedicine

Submitted by

Franziska Weigl

from

Reichenberg

Würzburg, **2022**

Correlation of FluidFM® Technology and Fluorescence Microscopy for the Visualization of Cellular Detachment Steps

Korrelation der FluidFM® Technologie und Fluoreszenzmikroskopie zur Visualisierung von zellulären Ablöseschritten

Doctoral thesis for a doctoral degree
at the Graduate School of Life Sciences,
Julius-Maximilians-Universität Würzburg,
Section: Biomedicine

Submitted by

Franziska Weigl

from

Reichenberg

Würzburg, **2022**

Submitted on: ……..

Members of the Thesis Committee

Chairperson: Prof. Dr. Christian Wegener

Primary Supervisor: Prof. Dr. Jürgen Groll

Supervisor (Second): Prof. Dr. Markus Sauer

Supervisor (Third): Prof. Dr. Franz Jakob

Date of Public Defence: ……..

Date of Receipt of Certificate: ……..

This thesis was performed from April 2018 until March 2022 at the Department for Functional Materials in Medicine and Dentistry (FMZ) at the Institute of Functional Materials and Biofabrication at the University of Würzburg (Würzburg, Germany) under the supervision of Prof. Dr. rer. nat. Jürgen Groll.

"It always seems impossible until it's done."

- Nelson Mandela

List of Publications and Conference Contributions

Publications:

First author:

- **F. Weigl**, C. Blum, A. Sancho, J. Groll, Correlative Analysis of Intra- Versus Extracellular Cell Detachment Events Via the Alignment of Optical Imaging and Detachment Force Quantification, *Advanced Materials Technologies*, **2022**, 2200195.

Co-author:

- S. Müller, **F. Weigl**, C. Bezold, C. Bächer, K. Albrecht, S. Gekle, A Hyperelastic Model for Simulating Cells in Flow, *Biomechanics and Modeling in Mechanobiology*, **2021**, 20, 509.
- D. Nahm, **F. Weigl**, N. Schäfer, A. Sancho, A. Frank, J. Groll, C. Villmann, H.-W. Schmidt, P. D. Dalton, R. Luxenhofer, A Versatile Biomaterial Ink Platform for the Melt Electrowriting of Chemically-Crosslinked Hydrogels, *Materials Horizons*, **2020**, 7, 928.

Conference contributions:

Oral presentation:

- **F. Weigl**, Correlation of FluidFM® Technology and Fluorescence Microscopy for the Visualization of Cellular Detachment Steps, *International Conference on Biofabrication (ISBF)*, **2021**, Virtual Conference.

Poster presentation:

- **F. Weigl**, Correlation of FluidFM® Technology and Fluorescence Microscopy for the Visualization of Cellular Detachment Steps, *Joint Meeting of Dreiländertagung and Multinational Congress on Microscopy*, **2021**, Virtual Conference.
- **F. Weigl**, A new Strategy to Measure Intercellular Adhesion Forces in Mature Cell-Cell Contacts, *Gordon Research Conference – Cell Contact and Adhesion*, **2019**, Switzerland.

Awards:

- Best Poster Award – Instrumentation and Methods, *Joint Meeting of Dreiländertagung and Multinational Congress on Microscopy*, **2021**, Virtual Conference.

Table of content

Abbreviation and symbol index

Abbreviation	**Meaning**
AFM	Atomic force microscopy
AJ	Adherens junction
B	Blocking filter
BBB	Blood-brain-barrier
bFGF	Basic fibroblast growth factor
BSA	Bovine serum albumin
CAM	Cell adhesion molecule
cAMP	Cyclic adenosine monophosphate
CCD	Charge-coupled device
CD144	Cluster of differentiation 144
CD31	Cluster of differentiation 31
CdSe	Cadmium selenide
CLEM	Correlative light electron microscopy
CMOS	Complementary metal-oxide semiconductor
CO_2	Carbon dioxide
D	Dimension
ddH_2O	Double distilled water
Dm	Dichroic mirror
DM	Dense midline
DMEM	Dulbecco's modified eagle medium
DMT	Derjaguin-Muller-Toporov
DNA	Deoxyribonucleic acid
DP	Desmoplakin
Dsc	Desmocollins
Dsg	Desmoglein
*d*STORM	Direct stochastic optical reconstruction microscopy
EC	Ectodomain
E-cadherin	Epithelial-cadherin
ECGS	Endothelial cell growth supplement
ECM	Extracellular matrix

e.g.	Exempli gratia (’for example‘)
EGF	Epidermal growth factor
Em	Emission filter
EM	Electron microscopy
E-selectin	Endothelial-selectin
et al.	Et alii
Ex	Excitation filter
FA	Focal adhesion
F_{adh}	Adhesion force
FAK	Focal adhesion kinase
FCS	Fetal calf serum
FD-curve	Force-distance curve
F_i	Indentation force
FIB	Focused ion beam
FL	Fluorescence microscopy
FL-FluidFM®	Correlated fluorescence and fluidic force microscopy
FluidFM®	Fluidic force microscopy
FP	Fluorescent protein
GFP	Green fluorescent protein
GJ	Gap junction
HBMVEC	Human brain microvascular endothelial cell
H_2O	Water
HeLa	Human epithelial cell
HEPES	(4-(2-hydroxyethyl)-1-piperazineethanesulfonic acid)
HUAEC	Human umbilical artery endothelial cell
HUVEC	Human umbilical vein endothelial cell
ICAM	Intercellular cell adhesion molecule
ICS	Intercellular space
IDP	Inner dense plaque
i.e.	Id est (‘that is’, ‘namely’, or ‘in other words’)
Ig	Immunoglobulin
IP_3	Inositol trisphosphate
ISC	Intersystem crossing
JAM-A	Junctional adhesion molecule
JKR	Johnson-Kendall-Roberts

LED	Light emitting diode
L-selectin	Leukocyte-selectin
MDF	Maximum detachment force
MEW	Melt electrowriting
N-cadherin	Neuronal-cadherin
ODP	Outer dense plaque
PALM	Photoactivated localization microscopy
PBS	Phosphate-buffered saline
P-cadherin	Placental-cadherin
PCL	Poly(ε-caprolactone)
PECAM	Platelet endothelial cell adhesion molecule
PEtOzi	Poly(2-ethyl-2-oxazine)
Pg	Plakoglobin
PID	Proportional-integral-derivative
PIFOC	Piezo-driven objective positioner
Pkp	Plakophilins
PLL-*g*-PEG	Poly(L-lysine)-*grafted*-poly(ethylene glycol)
PMT	Photomultiplier
PSD	Position-sensitive photodetector
P-selectin	Platelet-selectin
PZT	Piezoelectric actuator
QD	Quantum dot
R-cadherin	Retinal-cadherin
REF52	Rat embryonic fibroblast
ROI	Region-of-interest
RT	Room temperature
SCFS	Single-cell force spectroscopy
SDS	Sodium dodecyl sulfate
SEM	Scanning electron microscopy
Si	Silicon
Si_3N_4	Silicon nitride
SNR	Signal-to-noise-ratio
SR	Super-resolution
STED	Stimulated emission depletion
TEER	Transepithelial/transendothelial electrical resistance

TIRFM	Total internal reflection fluorescence microscopy
TJ	Tight junction
UV	Ultraviolet
VACV	Vaccinia virus
VASP	Vasodilator-stimulated phosphoprotein
VCAM	Vascular cell adhesion molecule
VE-cadherin	Vein endothelial-cadherin
VEGF	Vascular endothelial cell growth factor
v2	Speed of 2 µm s^{-1}
v5	Speed of 5 µm s^{-1}
YFP	Yellow fluorescent protein
ZO	Zonula occludens

Formular symbol	**Meaning**
α	Half-opening angle
c	Speed of light
d	Cantilever deflection signal
d_m	Minimum resolvable distance
E	Photon energy
E_γ	Young's modulus
F	Force
h	Plank's constant
n	Refractive index
NA	Numerical aperture
k	Cantilever spring constant
k_{calib}	Calibrated cantilever spring constant
R	Radius
w	Mooney-Rivlin ratio
x	Cantilever deflection
δ	Cantilever deflection sensitivity
δ_{calib}	Calibrated cantilever deflection sensitivity
δ_{ind}	Indentation
λ	Wavelength
ν	Poisson's ratio

Mathematical unit	Meaning
cm	Centimeter
d	Day
fL	Femtoliter
h	Hour
J	Joul
kDa	Kilo Dalton
kHz	Kilo Hertz
m	Meter
mg	Milligram
min	Minute
mL	Milliliter
MPa	Mega Pascal
ms	Millisecond
N	Newton
nm	Nanometer
nN	Nanonewton
ns	Nanosecond
Pa	Pascal
pL	Picoliter
pN	Piconewton
s	second
V	Volt
µg	Microgram
µL	Microliter
µm	Micrometer
µN	Micronewton
°	Degree
°C	Degree celsius
%	Percentage

List of figures

List of figures

CHAPTER 1

Introduction and aims of the thesis

The phenomenon of cell adhesion is responsible for the complex multicellularity of the human body.[1,2] However, cells do not only "stick" together, but rather form an extraordinary network of cell contacts that serve as mechanical linker[3,4], communication hubs for signal and force transduction[5-7], or as selective barrier[8,9]. Thus, cell adhesion plays a crucial role in many functional processes such as tissue morphogenesis and regeneration[10-12] or in the origin and cure of common diseases such as arthritis[13,14], cancer[15-18], or cardiovascular disorders[19,20]. Moreover, the attraction or aversion of cells to a substrate can be decisive for the success or failure of an implanted biomaterial and thus for the quality of a patient's life.[21-23]

This has created tremendous interest on establishing a variety of techniques that provide more insights into the complexity of cell adhesion. Depending on the specific interest, they were focused on cellular attachment or detachment, or the analysis of a cellular population versus single-cell experiments.[10] An overview of the most important cell adhesion studies and their applications in biotechnological research is illustrated in **Figure 1**.

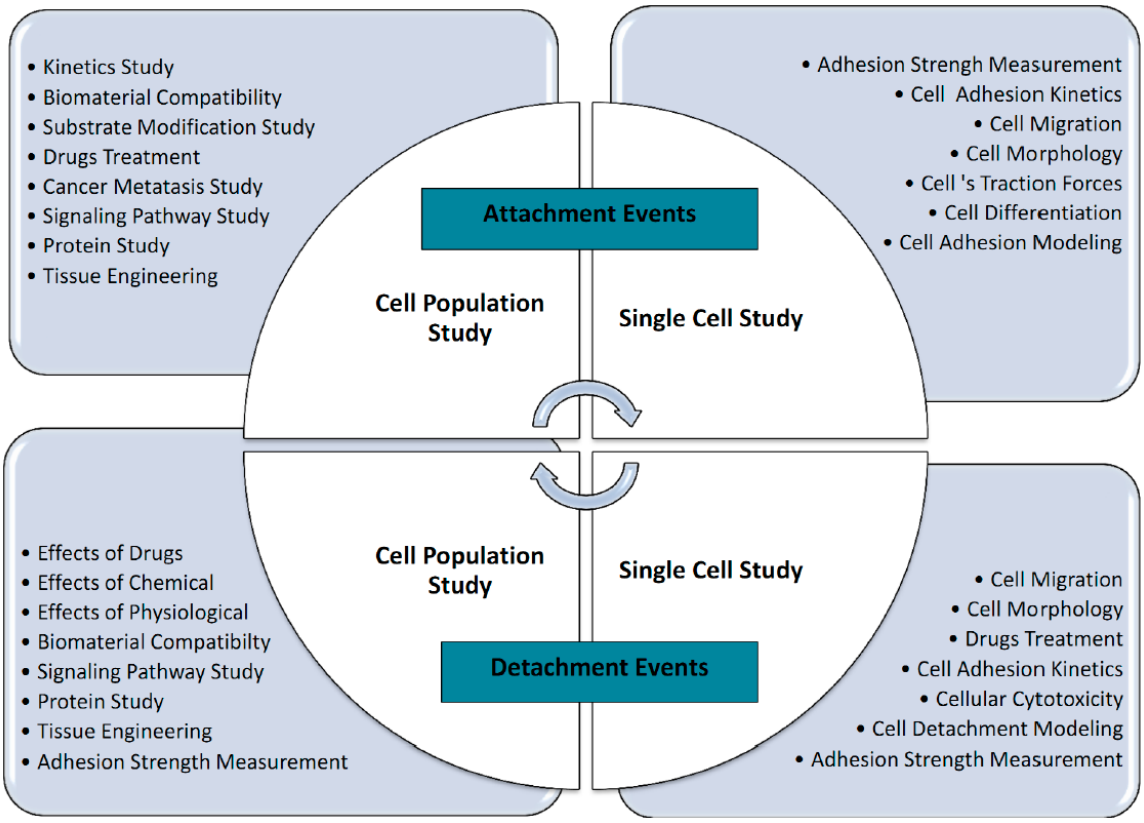

Figure 1: Overview of the most important cell adhesion studies and their applications in biotechnological research. The studies are classified by cellular attachment and detachment events and further grouped into cell population and single-cell studies. Reprinted from reference[10] as open-access article distributed under the terms of the Creative Commons CC BY license, which permits the free re-use in any medium.

One of the most prominent methods for studying single-cell adhesion is the Atomic Force Microscopy (AFM). By combining AFM with the highly sensitive Single-Cell Force Spectroscopy

(SCFS), the quantification of unbinding forces of single molecular bonds or of an entire cell is possible.[24,25] For this purpose, a cell is chemically attached to a functionalized cantilever, approached towards a substrate or another cell and subsequently separated after a given contact time, ranging from several seconds to minutes. During this whole cycle, cantilever deflection is measured, representing the corresponding adhesion force.[25,26]

Besides the quantification of adhesion forces, Fluorescence Microscopy (FL) became one of the key pillars for the analysis of cell adhesion.[27] Especially the advanced methods of super-resolution (SR) microscopy like direct Stochastic Optical Reconstruction Microscopy (*d*STORM) or Stimulated Emission Depletion (STED) revolutionized the characterization of adhesive contacts by visualizing single proteins within a nanometer range.[28-32] However, none of these innovative techniques alone can address and completely unravel the complexity of cell adhesion. Thus, the development of complementary and correlative AFM techniques became increasingly important in the last decades.[33-36] Up to date, the performance of such methods is often hampered by interference effects between cantilever and fluorescence excitation light, usually resulting in a sequential data acquisition and superimposition afterwards.[27,34,37,38] Nevertheless, a truly simultaneous operation of AFM and confocal FL was recently presented, taking the approach of hybrid characterization tools to next level.[27]

Apart from the advancement and progress in studying cellular biomechanics via multifunctional devices, there is still a noteworthy shortcoming of AFM that cannot be remedied by the integration of FL. One of the main limitations is its restriction to the study of early-stage adhesion.[24,25,39,40] To overcome this limitation, the Fluidic Force Microscopy (FluidFM®) was established by the group of Zambelli in 2009.[41] It combines the precise force-control of AFM with the benefits of microfluidics and thus allows a pressure-modulated and reversible cellular immobilization at the cantilever tip.[41,42] This further enables the detachment of mature cell contacts, whose adhesion forces, ranging from piconewton to even micronewton, would normally exceed the chemical attachment between a cell and a functionalized AFM cantilever.[25,40,43,44] Since then, FluidFM® became the gold-standard method for quantifying the adhesive characteristics of spread cells.[40,44] However, the question of real-time optical tracking of the biomechanical processes occurring during cellular detachment of mature cell contacts is still unanswered.

The **overall aim of this thesis** was the establishment of a novel multifunctional device correlating FL and FluidFM® technology (FL-FluidFM®) which enables the visualization of cellular detachment and, at the same time, the quantification of corresponding detachment forces. This provides a novel characterization method and, thus, new insights into the complex biomechanics of cell adhesion. For this purpose, both the focus stability and optical resolution of the microscope were

optimized by hardware and software adaptation. The functionality of this system was verified by proof-of-principle experiments which optically tracked fluorescently labeled cells while truly simultaneously recording the corresponding detachment forces. The establishment of a protocol for correlated data analysis further aimed the unambiguous matching between quantified force-jumps and the visualized steps of cellular unbinding.

Chapter 2 provides an overview of the theoretical background concerning this thesis. First, the FluidFM® technology and its setup and functionality are presented. This is followed by an overview on its different applications with a special emphasize on the FluidFM®-based force spectroscopy. Afterwards, the FL is introduced by explaining the fundamentals of fluorescence light, possible fluorophores, and hardware requirements. Subsequently, an overview of the development of correlated microscopy is given. Finally, the phenomenon of cell adhesion is explained by focusing on cell adhesion molecules (CAMs), the different types of adhesion, and the characteristics of cell bonding and rupture.

The results of this thesis and their discussion are given in **Chapter 3**. Initially, the focus was on the evaluation of a conventional FluidFM® system and its application in indentation and cell-substrate adhesion. This is followed by the presentation of the design and fabrication of a novel correlated FL-FluidFM® system. Its functionality was verified by a comparison with the conventional method in terms of optimized optical features and force spectroscopy. Afterwards, proof-of-principle experiments demonstrated for the first time the simultaneous feasibility of force-curve quantification and fluorescence visualization of a detached cell. This also includes the discussion of challenges regarding interference effects. Subsequently, a newly established analysis workflow was explained in detail, revealing unambiguous matches between intracellular unbinding and cellular detachment steps. Here, unbinding theories presented so far in literature were experimentally confirmed. Based on the successful establishment of a correlative FL-FluidFM® workflow, a comparison of cell-cell and cell-substrate adhesion was presented, focusing on two different cell types. This was followed by the analysis of the detachment behavior of single and interconnected endothelial cells. Finally, the formation of intercellular junctions was investigated via fluorescent visualization and discussed in terms of primary and immortalized cell types as well as their dependence on the prior cultivation time.

An integral discussion of all presented results as well as further perspectives for future studies are given in **Chapter 4**.

Chapter 5 provides a summary of this thesis in English and German.

Chapter 1

An overview of the experimental materials and methods used in this thesis is presented in **Chapter 6**. Here, a detailed description of the cell culture is given, followed by the methods of fluorescent labeling and the performance of FL. Afterwards, the application of conventional FluidFM®-based SCFS is explained, providing detailed information for cantilever preparation and indentation as well as adhesion experiments. The correlated FL-FluidFM® performance is subsequently described, focusing on the data acquisition and the corresponding analysis. The investigation of cell-cell adhesion is given at the end of this chapter.

The **Appendix A** provides a standard operating procedure for correlated FL-FluidFM®. First, the hardware components and associated software as well as their commissioning are explained in detail. Subsequently, the individual steps of the experimental workflow are provided, starting with the cantilever installation and preparation. Thereafter, a description of the implemented software workflow and the following data acquisition of indentation as well as cell adhesion experiments is presented. The latter are distinguished between conventional and correlated performances. Finally, an overview of troubleshooting and suitable hints is given as well as important contacts for technical support.

CHAPTER 2

State of knowledge

2.1 Fluidic Force Microscopy (FluidFM®)

Fluidic Force Microscopy, named FluidFM®, was invented by Zambelli's group at ETH Zürich in 2009[41] and is, therefore, a quite novel technology in the field of biophysics. It is characterized by the fact that it combines the high-resolution technique of Atomic Force Microscopy (AFM) with microfluidics. In this way, FluidFM® offers a variety of applications including precise and gentle cell sorting[45], highly controlled delivery of bioactive reagents[41] or intracellular injection[46]. Moreover, the use of microchanneled cantilevers instead of functionalized ones, enables FluidFM® to quantify mature cell adhesion with forces in the range of piconewton to several micronewton.[40,43] FluidFM® overcomes various limitations of conventional AFM and, thus, emerged to be one of the most powerful tools in addressing biological questions in the last decade.[47]

Due to the fact that FluidFM® is an extension and innovation of AFM, there are several analogies and correspondences in hardware composition and performance. Therefore, unless otherwise stated, the reader can assume that AFM-based illustrations and concepts presented in this thesis, are equally valid for FluidFM®.

2.1.1 Setup and functionality

The hardware composition of a FluidFM® setup is based on a conventional AFM and illustrated in **Figure 2**. Here, a cantilever, called AFM probe, is mounted on a piezoelectric actuator (PZT) which regulates its vertical positioning.[48-50] During a measurement, the sample-cantilever interaction is accurately captured via a force-induced cantilever deflection measured with a laser beam which is reflected from the backside of the cantilever onto a position-sensitive photodetector (PSD).[49-51] In this way, any change in cantilever bending can be detected via a shift in the position of the laser spot upon the PSD and transferred to the PZT via feedback loop.[41,49] This whole composition is mounted on top of an optical microscope enabling the visualization of sample and cantilever.[25] However, there is one remarkable difference in the composition of AFM and FluidFM® referring to the AFM probe. Instead of merely solid and chemically functionalized cantilever normally used in AFM, FluidFM® performance is based on a hollow cantilever with a microchannel connected to an external pressure controller via tubing.[43,47,52] This channel can be filled with an arbitrary solution, allowing the FluidFM® to fully operate in a liquid surrounding. Moreover, a local dispensing of a chosen solution through the cantilever aperture or the aspiration and release of a target cell is feasible, depending on the applied pressure.[25,50]

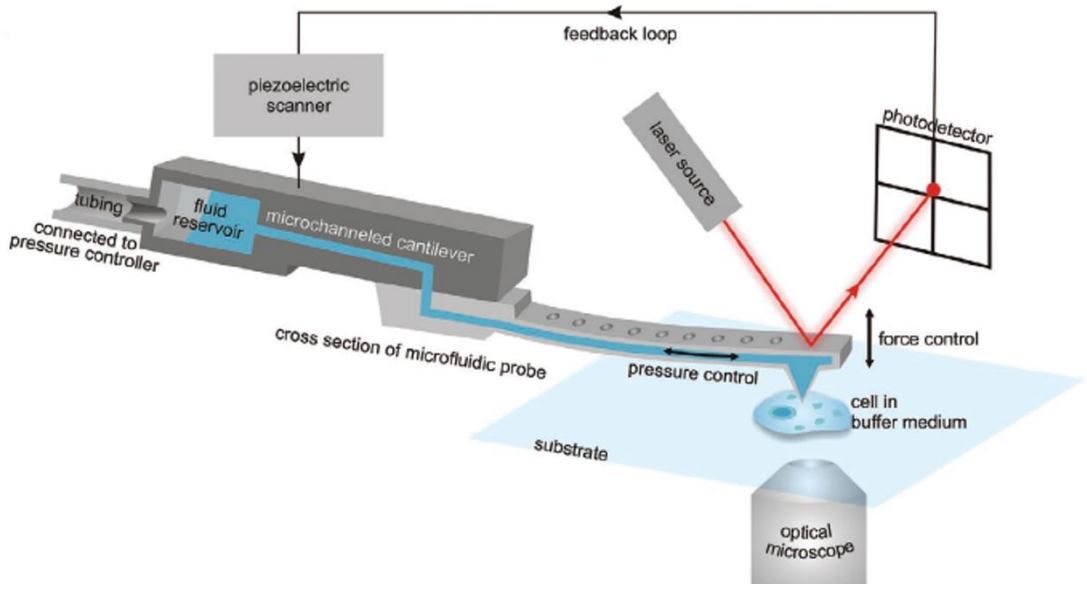

Figure 2: Schematic illustration of a FluidFM® setup. The main component is a microchanneled cantilever that is connected to a pressure controller at its free end. Its vertical movement is regulated via a piezoelectric scanner (PZT). The cantilever deflection is measured by a laser that is reflected at the cantilever tip and directed to a photodetector (PSD). In this way, any change in cantilever bending is detected via a shift in the position of the laser spot upon the PSD and transferred to the PZT via feedback loop. Reproduced and adapted from reference[43] as open-access article distributed under the terms of the Creative Commons Attribution CC BY license.

Analogous to AFM, the FluidFM® probe is usually made of silicon nitride (Si_3N_4) and coated with a gold layer on its backside to increase its reflectivity.[25,38,49,53] In the commercially available probes, the embedded microchannel with several supporting pillars is generated by either etching or thermical bonding of two silicon (Si) wafers forming a channel height of 0.2 to 1 µm.[25,41,43,50] Subsequently, an aperture can be formed by using either focused ion beam (FIB) or photolithography resulting in openings between 300 nm to 8 µm.[25,43,50] As illustrated in **Figure 3**, the cantilever is generally formed in a rectangular shape (~150 µm long and 25 µm wide) and, depending on the experimental purpose, either tipless or equipped with a pyramidal tip at its apex.[50] Thereby, the latter one is distinguished by its different aperture positions. Cellular injection, for instance, is usually performed with a syringe-like probe carrying the aperture beside the apex of the pyramidal tip while an aperture directly at the end of the tip is preferred for fluid delivery.[41,46] By contrast, tipless cantilevers are used to accomplish cellular detachment or single-cell displacement by aspirating and releasing a target cell.[43,45] Furthermore, this type of cantilever offers the possibility to perform the well-known AFM indentation technique by suctioning a colloidal bead to the cantilever's aperture and, thus, evaluating elastic properties of a cell.[50,54,55]

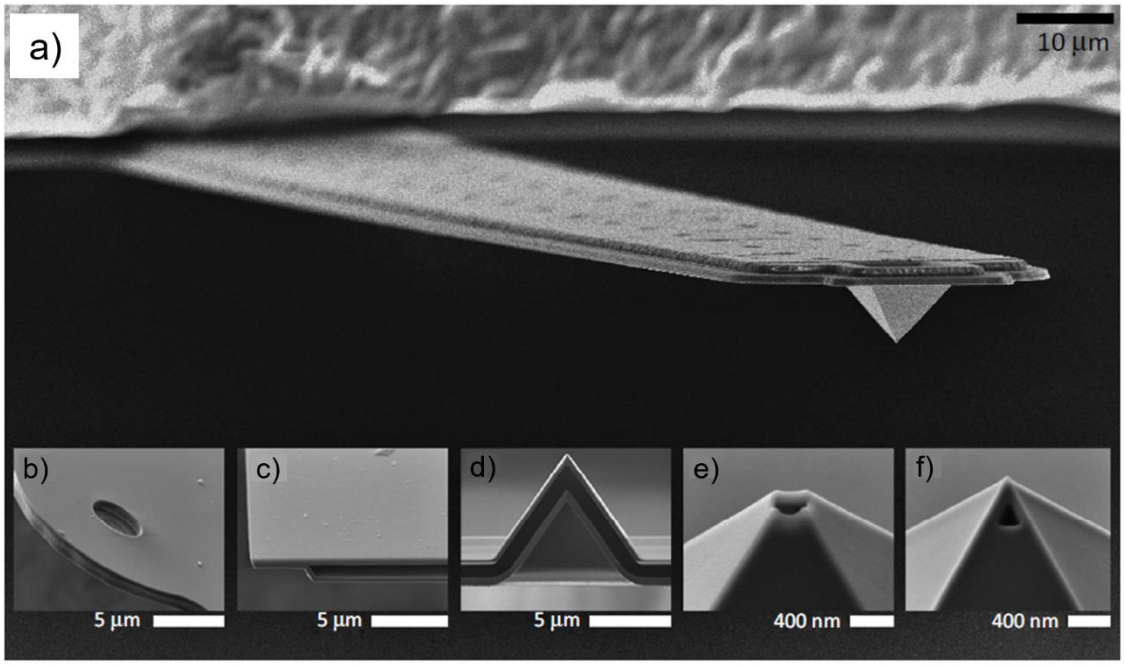

Figure 3: Scanning electron microscopy (SEM) images of exemplary cantilevers for FluidFM® experiments. (a) Large view of a hollow AFM probe with a pyramidal tip at its end. The inner space is supported by several rows of pillars visible as darker spots on the backside of the cantilever. (b) Tipless cantilever with an aperture at its apex. (c) and (d) Zoomed images of, respectively, a microchannel and a pyramidal tip after cutting a microchanneled probe with focused ion beam (FIB). (e) Zoomed image of a pyramidal tip with its opening directly at the end. (f) Zoomed image of syringe-like tip with the opening at the side of the apex. Reprinted and adapted from reference[25], Copyright (2014) with permission from Elsevier.

2.1.2 Applications

The advancement of implementing a pressure controlled microfluidic probe into the AFM-based FluidFM® system provides access for novel single-cell analysis. There are five main functionalities of FluidFM®: fluid delivery, cell sorting, cellular injection/extraction, cell adhesion, and indentation.[25,50] All of them benefit from the high accuracy in force control and the precisely regulated pressure control but differ in their experimental purpose. While the first three are focused on the manipulation of single cells, cell adhesion and indentation, in contrast, evaluate binding strength and mechanical properties of individual cells via force spectroscopy.[43,50] In the following chapters, the different FluidFM® functionalities are described more in detail, especially highlighting the Single-Cell Force Spectroscopy (SCFS)-based cellular detachment as main application in this thesis.

2.1.2.1 Fluid delivery

The primary purpose of FluidFM® was to introduce a universal liquid delivery system for local liquid dispensing and stimulation of single cells.[41] Therefore, the microchanneled cantilever is

filled with a solution containing bioactive reagents, positioned onto a target cell via highly sensitive feedback control and followed by a pressure induced liquid release with volumes smaller than a femtoliter.[41,56] In this context, Meister *et al*. (2009) presented the fluorescent labeling of living neuroblastoma cells by gently touching the cell membrane with a pyramidal cantilever filled with CellTracker green.[41] This fluorescent dye is known for its membrane permeability and its fluorescent performance depending on the enzymatic activity of a cell. After several minutes of maintaining the contact, the cell revealed a fluorescent signal while adjacent cells did not, proofing an accurate and local diffusing into the target cell. Moreover, it demonstrated that the cell was not damaged and still has a working metabolism.[25,41]

Besides the delivery of soluble molecules, this FluidFM® functionality was also performed for a controlled virus infection onto individual human epithelial (HeLa) cells.[56] Here, a tipless cantilever was filled with a buffer solution containing fluorescently labeled vaccinia virus (VACV) and dispensed through the cantilever aperture onto a selected, single cell. By using Fluorescence Microscopy (FL), the viral infection of the cell could be monitored revealing an increased infection with higher number of viruses as well as a cooperative link between VACVs during the early stage of infection.[50,56]

This concept of local dispensing can be extended to any soluble particle small enough to flow through the cantilever channel and, therefore, offers a strategy for a drug delivery system analyzing single-cell reaction towards external stimuli under physiological conditions.[25,50]

2.1.2.2 Cell sorting

Besides the established concept of fluid delivery, FluidFM® offers the possibility of pick-and-place experiments. Thereby, a cell is firmly attached onto the cantilever tip by applying a slight negative pressure, transferred to another, predefined position, and released by a gentle overpressure. The use of tipless cantilevers with different opening sizes enables the spatial manipulation or isolation of eucaryotic and procaryotic cells under physiological conditions.[25,44] This experimental approach was first demonstrated by Dörig *et al*. (2010), successfully accomplishing pick-and-place experiments with bacterial, yeast, and mammalian cells ranging from 1.5 to 20 µm in diameter.[44] Moreover, the transfer of yeast cells from one glass slide to an agar coated plate was feasible maintaining the cell attached to the AFM probe even in air.[44]

A more advanced approach combining the functionality of fluid delivery and cell sorting was presented by Guillaume-Gentil *et al*. (2013).[45] Until then, the spatial manipulation of cells was mostly focused on non-adherent cells, but as demonstrated in their study the cellular isolation of adherent cells using FluidFM® is also feasible. Here, single HeLa cells were directly transferred from their culture dish onto another substrate or microwell.[45] Therefore, the microchannel was

loaded with a solution containing trypsin and a fluorescent marker which was then locally dispensed on a cell of interest by applying a slight overpressure. Using the pressure controller, the dispensed volume of trypsin solution could be varied and regulated to the release of several tens of picoliter activating the selective detachment of single HeLa cells within a confluent monolayer.[45] Afterwards, the detached cell could be easily aspirated and attached onto the cantilever tip, followed by the controlled displacement and isolation of the chosen cell. A successful cellular release without cell damage was achieved by applying a non-fouling cantilever coating based on poly(L-lysine)-*grafted*-poly(ethylene glycol) (PLL-*g*-PEG).[45,50]

With this FluidFM®-based approach of cell sorting, it is not only possible to transfer selective cells to a target area and observe their behavior but also to remove unwanted cells and, therefore, form a cell pattern of interest which is important, for instance, for engineering neural circuits.[50,57]

2.1.2.3 Cellular injection/extraction

The force-controlled fluidic injection and extraction is another strategy in single-cell manipulation. Its principle is based on the approach of fluid delivery but with a syringe-like probe to penetrate the cellular membrane with the sharp apex of the pyramidal tip. Instead of only gently touching a cell, the cantilever tip is inserted inside a cell by applying a higher forward force on the cell surface which can be recognized as force relaxation peaks during the detection of an approach force-curve.[43,46,50] Once the pyramidal tip has perforated the membrane, bioactive reagents can be dispensed providing access to direct intracellular perturbation. In a first study, the successful intracellular injection was demonstrated by releasing a membrane impermeable fluorescent dye into the cytoplasm of neuroblastoma cells.[41] Later on, this approach was extended to an intranuclear injection by inserting a fluorescent marker that is impermeable for the outer membrane but permeable for the nuclear membrane. After nuclear injection of a HeLa cell, the dye diffused into the cytoplasm but remained inside the cell guaranteeing a complete recovery of the plasma membrane after cantilever retraction. Additionally, another intranuclear injection was performed with a fluorescent marker that is impermeable for the nuclear membrane. Here, the dye stayed enclosed in the nucleus without any diffusion into the cytosol demonstrating a successful resealing of the nuclear membrane after injection.[46] Moreover, this study was confirmed by a controlled delivery of plasmid DNAs encoding green fluorescent protein (GFP) into the nucleus of HeLa cells successfully revealing a maximum of fluorescent signal after only 17 h and, therefore, demonstrating a high injection efficiency without affecting cell viability.[46,50]

Instead of dispensing a liquid into a cell, this approach of single-cell manipulation also offers the possibility to perform intracellular extraction. Thereby, a negative pressure is applied after injection to extract intracellular structures into the microchannel followed by cantilever retraction

and fluid release onto analytical substrates.[50] In a first study, Guillaume-Gentil *et al.* (2016) presented the extraction of tunable volumes of intracellular content by injecting GFP expressing HeLa cells.[58] The extraction of fluorescent intracellular structures, like ribonucleic acid, peptides, and proteins, and its distribution in the cantilever microchannel could be optically monitored via FL. A comprehensive study of cell viability after extraction identified the nuclear extraction to be more critical for cell viability than the cytoplasmic one. In the latter case, 82% of HeLa cells remained viable even after extracting a significant proportion of their cytoplasm.[43,50,58] The extracted intracellular content can then be studied by various biochemical analysis including enzymatic activity assays, gene expression or mass spectroscopy of metabolites.[50,58,59]

2.1.2.4 FluidFM®-based force spectroscopy

In contrast to the aforementioned applications focusing on the manipulation of single-cells, FluidFM® can also be used to perform force spectroscopy. Here, the AFM probe is moved exclusively in the vertical direction and, thus, acting as force sensor. By approaching a surface and subsequently retracting the cantilever at a preset tip velocity, the tip-sample interaction forces can be measured as function of the corresponding tip-sample distance, resulting in a so-called force-distance curve (FD-curve) (**Figure 4**).[25] By separating this FD-curve into its two segments of forward (approach) and backward (retraction) curve, the quantification of characteristics like sample height, surface deformations, or elasticity as well as the energy and adhesion forces of biological surfaces or even single molecules can be quantified.[25,60,61] In the following chapters, the recording and interpretation of FD-curves is described in detail.

2.1.2.4.1 Force-distance curve (FD-curve)

To generate a FD-curve, the originally measured cantilever deflection has to be converted into the corresponding force. Therefore, Hooke's law (**Equation 1**)

$$F = k \cdot x = k \cdot d \cdot \delta \tag{1}$$

is applied by considering the cantilever as a spring. Thus, the force F [N] between cantilever tip and surface is correlated to the cantilever spring constant k [N m^{-1}], meaning its stiffness, and the cantilever deflection x [m] which is composed of the deflection signal d [V] and the deflection sensitivity δ [m V^{-1}].[40,62] The experimental acquisition of a whole FD-curve is separated into several steps which is exemplary illustrated in **Figure 4**. First, the AFM probe vertically approaches the sample from a certain distance (blue curve, step 1) until the so-called contact point is reached, describing the moment of first contact between cantilever and sample surface.[60,63] Here, the deflection is still zero. With proceeding approach, the cantilever bends until a setpoint of

maximum indentation force (F_i) is reached (step 2). This is followed by the second section of the FD-curve, the cantilever retraction (step 3).[60,63,64] During this process, the cantilever bending starts to decrease again until the turning point of no deflection is reached. By further retracting the AFM probe and in case of adhesive bonds, the cantilever deflection begins to increase again, but now with a downward bending towards the sample, resulting in a rising negative force, called adhesion force (F_{adh}).[60,63] After crossing the highest point of force, called maximum detachment force (MDF) (step 4), the cantilever deflection diminishes once again until either the initial position is reached again, or until further detachment steps, e.g. of single molecules, are overcome (step 5).[49,60,63] As already implicated by the different force designations, the two curve sections of approach and retraction entail different information about the properties of a biological sample. While the approach-curve is commonly used for the analysis of deformations and elastic properties, the retraction part describes the adhesive behavior of a sample including cellular membrane properties, ligand-receptor cooperativity, or binding strength.[24,64]

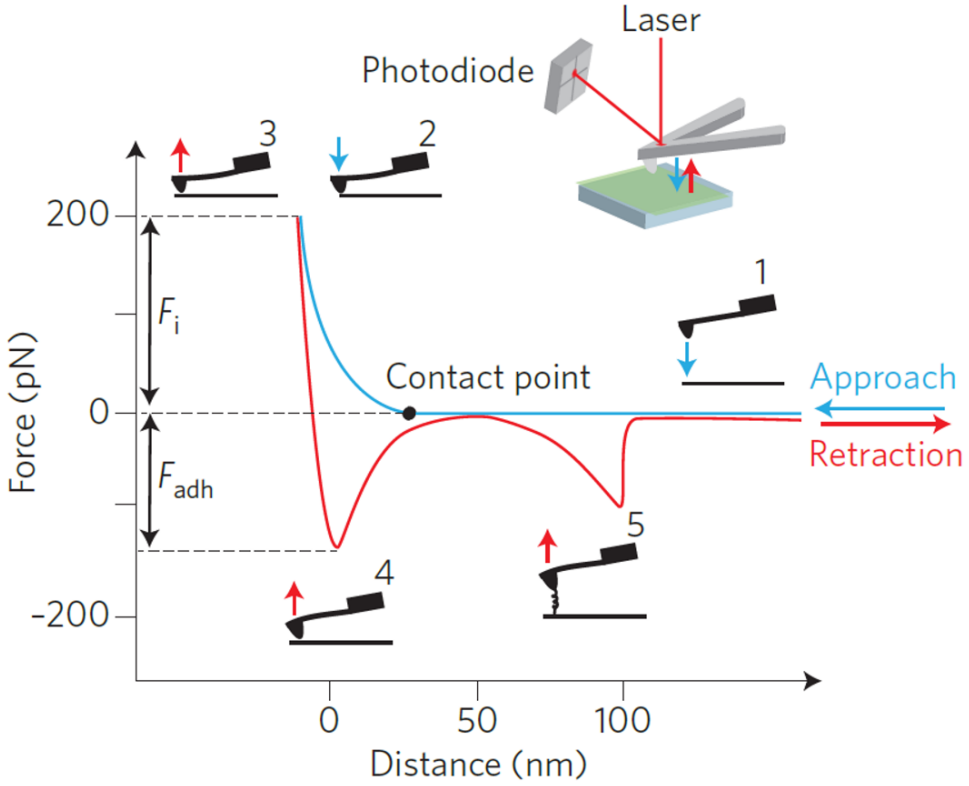

Figure 4: Composition of a force-distance curve (FD-curve). The curve is separated into two main sections, the cantilever approach (blue) and its retraction (red). Initially, the cantilever is positioned at a certain distance above the sample (step 1). After passing the contact point, the cantilever reveals an upwards deflection (step 2) corresponding to an indentation force (F_i). The cantilever retraction entails a decrease and downward shift in deflection representing the adhesion force (F_{adh}, step 3, 4). In case of, for instance, single molecule adhesion, the cantilever shows multiple steps of increased forces until the initial position is reached again. Adapted by permission from Springer Nature: Nature Nanotechnology[60], Copyright (2017).

2.1.2.4.2 Cell adhesion

The invention of SCFS brought the quantitative study of cell adhesion under near-physiological conditions onto the next level. Historically, cell adhesion was initially evaluated by washing assays, for instance, the spinning-disc or flow chamber assay, estimating adhesion forces via a controlled flow of media.[24,65,66] Here, the cells are seeded onto a substrate and rinsed with physiological buffer resulting in a comparison of lost, non-adherent and remaining cells.[67] Since these bulk methods are based on a force estimation over the totality of studied cells, the more advanced approach of single-cell analysis was established. AFM-based SCFS, for instance, represents a well-known method for the adhesion force quantification of individual cells. Here, a cell is chemically attached onto a functionalized cantilever and brought into contact with a target surface or another cell, assessing the corresponding unbinding forces of whole cell adhesion or even of single receptor/ligand bonds in a range of ~10 pN to ~100 nN.[24-26,39,67] With the invention of FluidFM®, this strategy could be advanced towards the examination of forces up to several micronewton, generally occurring after the complete maturation of focal contacts.[40] By immobilizing a cell onto the cantilever aperture via negative pressure, Potthoff *et al.* (2012) presented a serial quantification of adhesion forces of mature yeast and mammalian cells for the first time.[39] Since then, FluidFM®-based SCFS was used to study the complexity of cellular detachment including cell-substrate[39,68] and cell-cell adhesion[40,42,69] of microbial[39,70] and mammalian cells[40,42] as well as the dependence on parameters like surface topography[71,72] or the phase of adhesion (early or mature)[68].

The basic workflow of FluidFM®-based SCFS is schematically illustrated in **Figure 5a**. Here, a tipless cantilever is approached towards a spread cell (green particle) firmly adhering on a substrate. After reaching a predefined force setpoint and gently contacting the cell surface, a negative pressure is applied inducing an adequate cellular immobilization on the cantilever aperture while force feedback ensures a constant positioning. This pressure is kept constant while subsequently retracting the cantilever again and, thus, detaching the cell. After the complete de-adhesion, a slight overpressure ensures the cellular release enabling a serial quantification with the same cantilever.[39,40,43] Instead of cantilever-guided cellular de-adhesion, it is also possible to use the sample stage as moving component which is often beneficial when longer pulling ranges are required to completely detach a cell.[73] However, in both cases, the cantilever deflection and, therefore, the adhesion force is detected as described in **Chapter 2.1.1**. An exemplary FD-curve is illustrated in **Figure 5b**. As already mentioned in **Chapter 2.1.2.4.1**, a FD-curve provides different information about cellular characteristics. Thus, the evaluation of adhesive characteristics of living cells is concentrated on the retraction-curve and can be separated into three unbinding phases.[24]

Initially, after a firm immobilization of the cell, the cantilever starts to retract inducing a pulling force on the cell (**Figure 5b (I)**). With increasing force and in dependence on the strength and amount of adhesive bonds, the cell starts to detach.[24,38] After passing the MDF, the detachment process is entering the second phase revealing a complex force pattern. Here, the cellular de-adhesion is dominated by two types of unbinding steps: (i) the so-called jumps/rupture events ('j' events) (**Figure 5b (II)**) and (ii) the tether events ('t' events) (**Figure 5b (III)**). Whereas 'j' events are characterized by a ramp-like increase in force, force-plateaus prior a step are visible, when pulling a tether.[38,74] The former one is linked to the rupture of a single or cluster of adhesive bonds that remain connected to the cytoskeleton. The stretching of these membrane-cortex linkers induces the non-linear force increase right before a rupture.[67,75] In contrast, the appearance of a 't' event is predominantly described by an extrusion of a membrane tether out of the cellular cortex which mostly occurs at the third and, therefore, final phase of a detachment process. Here, solely the cell membrane is still in contact with a substrate (or another cell), exclusively mediating the last steps of de-adhesion until the cell is fully detached.[24,38,74]

While analyzing and interpreting the information behind a FD-curve, it is important to consider that the biological processes behind the de-adhesion are far more complex and have been subject of intensive experimental and theoretical research for decades.[76-80] Besides the depicted unbinding steps of jumps and tether, the whole cellular detachment process is also influenced by parameters like cell elasticity, mechanical properties of the membrane, binding dynamics or cell size to name just a few.[24,38,78,81] Moreover, experimental parameters like cantilever retraction speed, contact force, substrate roughness, or contact time have an influence on how a cell detaches.[74] Especially, the latter one is a limiting factor for the performance of AFM-based SCFS. This is related to the fact that the formation of stronger adhesive bonds increases with longer contact times resulting in forces which exceed the binding forces between a cell and a functionalized cantilever.[25,74] Therefore, AFM-based SCFS is limited to the investigation of early-stage adhesion with contact times ranging from milliseconds to several minutes.[24,74] Furthermore, the cantilever functionalization itself which is usually based on an adhesive coating with, for instance, lectins[73,82], streptavidin[83], or proteins like collagen[84] or fibronectin[84,85] has the potential to perturb the structural and functional state of a cell and, therefore, the slope of a subsequent recorded FD-curve.[25] These limitations are avoided by the integration of microchanneled cantilevers and the reversible cellular immobilization using FluidFM®.

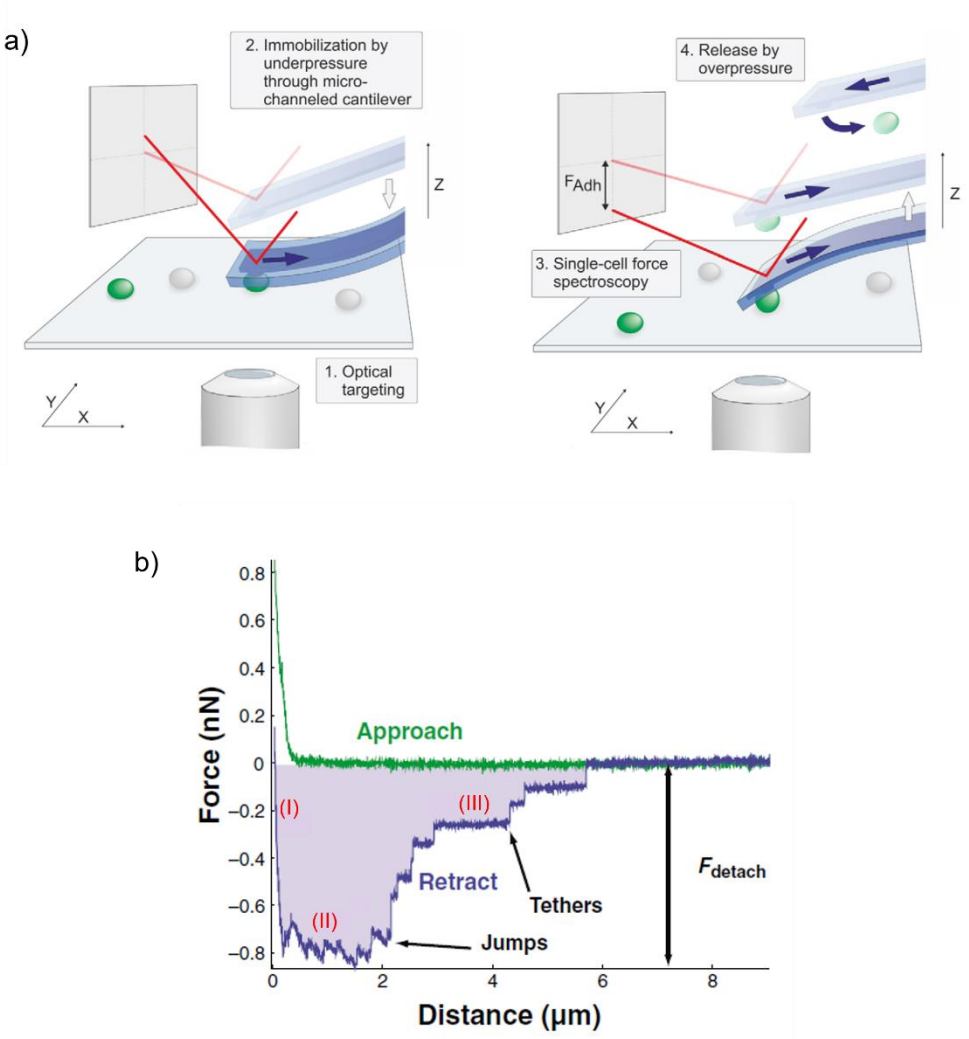

Figure 5: Exemplary procedure of FluidFM®-based single-cell force spectroscopy (SCFS). (a) Schematic view of the experimental principle. After the cantilever approach, a cell is immobilized at the aperture via negative pressure. By the followed cantilever retraction, a cell is detached from its surface and subsequently released by the application of an overpressure. During the process, the cantilever deflection is detected via a reflected laser. (b) Exemplary FD-curve composing of an approach (green) and retraction (purple) section. The retraction-curve represents the unbinding process of a cell starting with an increase in force that is related to the pulling force on a cell (I). After passing the MDF, the cell starts to detach showing mainly to characteristic types of unbinding steps: jumps (II) and tether (III). (a) Reprinted from reference [39] as open-access article distributed under the terms of the Creative Commons Attribution License, which permits unrestricted use, distribution, and reproduction in any medium. (b) Reproduced with permission of the Journal of Cell Science, reference[24].

2.1.2.4.3 Colloidal nanoindentation

Since its first presentation more than 30 years ago, the strategy of AFM-based nanoindentation has not fundamentally changed.[86] It is based on an AFM probe that is firmly connected to a spherical colloid by 'gluing' or sintering it at the cantilever aperture and, thus, acting as nanoindentor.[87,88] By slightly compressing a sample surface followed by a cantilever retraction, mechanical properties of, e.g., polymer films or soft matter like cells can be investigated.[89-92]

Nevertheless, this approach is faced with some limitations. One of the main disadvantages is the irreversible immobilization of the colloid hindering fast switching between spherical probes which is of special interest when analyzing specific biomolecular interactions requiring functionalized probes.[50,93] Nowadays, FluidFM® offers an alternative and optimized version of the well-established AFM nanoindentation technique.[54,55] Unlike the conventional AFM-based approach, here, a single colloid can easily be aspirated to the cantilever aperture and released via overpressure. In this way, Dörig *et al*. (2013) demonstrated a serial use of chemically coated colloids as well as the quantification of elastic properties of human embryonic kidney cells via indentation.[93] In a more recent study, Lüchtefeld *et al*. (2020) proposed an advanced method for the determination of actin cortex mechanics exclusively by calculating the cellular stiffness as function of the indentation depth named 'Elasticity spectra'.[94]

In principle, the experimental workflow of AFM- and FluidFM®-based nanoindentation is equal. In the latter case, aspiration of a spherical colloid to the aperture is performed first, followed by the recording of a FD-curve. Afterwards, the approach section of the FD-curve is transformed into a force-indentation curve by subtracting the cantilever deflection from the vertical displacement. This results in a so-called separation, which in turn corresponds to the indentation starting from the contact point.[40,64] Subsequent, the so-called Young's modulus as indicator for elasticity is extracted by fitting the curve accordingly to a theoretical model. Depending on the used type of indenter and on the inclusion or neglect of adhesion forces, different models are applied, for instance, Johnson-Kendall-Roberts (JKR)[95-97], Derjaguin-Muller-Toporov (DMT)[97], or Hertz-Sneddon model[93,94]. Especially, the latter one is preferred in case of spherical or conical tips while JKR and DMT are chosen for considering adhesion forces inside and outside the contact area.[64,81,98,99] Furthermore, the Hertzian theory presumes an infinitely hard sphere indenting a flat and soft substrate and, thus, resulting in a small deformation.[89,100] This is described by the following **Equation 2**:

$$F = \frac{4 \cdot E_\gamma \cdot R^{1/2}}{3 \cdot (1 - \nu^2)} \cdot \delta_{ind}^{3/2} \qquad (2)$$

where F [N] is the measured force, E_γ the Young's modulus [Pa], ν the Poisson's ratio, δ_{ind} the indentation [m], and R [m] the radius composing of the indenter and cell/sample radii, respectively.[40,89]

2.2 Fluorescence Microscopy (FL)

Since Ernst Abbe's contribution to the theory of microscopy in 1873[101], conventional light microscopy became one of the key pillars in visualizing biological samples. Together with the phenomenon of fluorescence, which was excessively investigated in the 19th and early

20th century, the foundation for nowadays FL was laid.[102] Since then, the development and optimization of instrument design and fluorescent markers has steadily progressed to more advanced setups like Total Internal Reflection Fluorescence Microscopy (TIRFM)[103] or super-resolution (SR) systems such as direct Stochastic Optical Reconstruction Microscopy (*d*STORM)[104,105] or Photoactivated Localization Microscopy (PALM)[106,107], visualizing cells down to single molecules with a resolution of a few nanometers.[28,108] Because of its non-invasive imaging of even living organisms, FL became an indispensable technique in the field of biological and medical research.[109]

2.2.1 Fundamentals of fluorescence light

The effect of fluorescence light is based on an interaction of matter and electromagnetic radiation. Here, a fluorescent molecule absorbs a photon of a certain energy and subsequently emits light of lower energy within nanoseconds, called fluorescence light.[110,111] This loss in energy is based on different photophysical effects occurring during the absorption-emission process, as illustrated in the Jablonski diagram (**Figure 6**). Depending on the total energy of an absorbed photon, an electron in its ground singlet state S0 is excited in a higher energetic singlet state S1 or higher, each of these electronic states being composed of several vibronic states. Via non-radiative vibronic relaxation and internal conversion, a higher excited electron is transferred into the lowest energetic vibronic singlet state S1.[112] During the following return to the electronic ground state S0, fluorescent light of lower energy and therefore longer wavelength is emitted. This is associated with the reciprocal relationship of photon energy and wavelength ($E = hc/\lambda$, where E [J] is the photon energy, h [Js] is Plank's constant, and c [m s^{-1}] and λ [m] are the speed and wavelength of light in vacuum, respectively).[113] This energetic transition between absorption and emission is known as 'Stokes shift'.[110,111,113] Besides the straight return to the ground state via fluorescence, there is also the very unlikely option of intersystem crossing (ISC).Here, with regard to quantum theory, an electron switches from an excited singlet S to a long-lasting excited triplet T state via spin-flip.[112] More precisely, the opposite orientation of paired electrons, as usually found in the singlet state, is replaced by a pair of nonbonding electrons which reveal a quantum theoretically 'forbidden' parallel spin orientation. In this case, the transition to the ground state S0 is represented by the emission of phosphorescence light.[112-114]

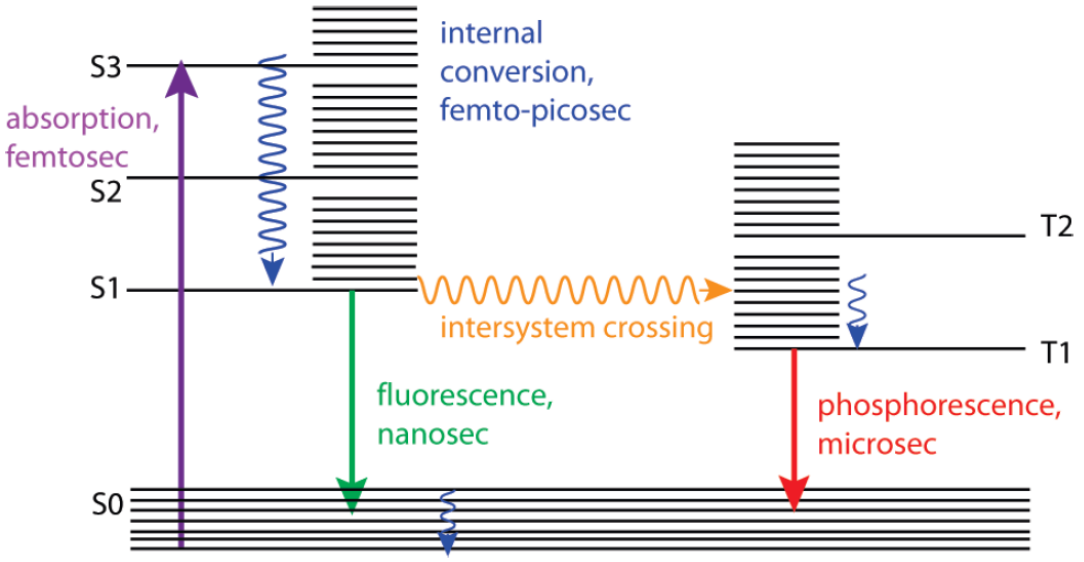

Figure 6: Jablonski-diagram. The interaction of matter and electromagnetic radiation causes the emergence of light of lower energy. An electron in the vibronic ground state S0 is excited in a higher energetic vibronic state of S1 or higher via the absorption of light (purple arrow). Through non-radiative relaxation or internal conversion (blue, sinusoidal arrow), a higher excited electron is transferred to the lowest energetic singlet state S1. Directly turning back to the ground state S0 causes the appearance of fluorescence light. Another option, albeit with very low probability, is the intersystem crossing, where an electron is shifted from an excited singlet to a long-lasting triplet state T. From here the return to the ground state S0 is represented by the effect of phosphorescence. Reprinted with permission from[112]. Copyright (2010) American Chemical Society.

2.2.2 Fluorophores

Today there is a huge toolbox of fluorescent probes that can be used for fluorescent labeling spanning the whole visible section of the electromagnetic spectrum. Depending on the experimental purpose one can choose, for instance, between organic fluorophores[115,116], fluorescent proteins[117,118] or semiconductor based materials like quantum dots (QDs)[119,120]. At the same time, there was developed a wide range of labeling techniques allowing the visualization of whole cells and single biomolecules, leading to a better understanding of biological features such as cellular dynamics or signal transduction.[121,122]

2.2.2.1 Types of fluorophores and fluorescent labeling

Fluorescent proteins (FP)

The most prominent representative of FPs is the GFP as it was found as chemiluminescent molecule in the jellyfish *Aequorea Victoria*.[123] Since its first cloning in 1992 by Prasher *et al*. (1992), GFP has been extensively advanced to several variants providing improved photostability, enhanced brightness and most important a wider range of available wavelengths such as yellow

FP (YFP) or red FP.[115,121,124] In this way, GFP as well as its mutants can be genetically co-expressed to a target protein in a variety of organisms like bacteria or yeast cells, but also in plants or mammalian cells. This allows a highly specific fluorescent labeling of cellular compartments without background signal.[102,112,118] Moreover, by the expression in living cells using transient transfection, dynamic processes of proteins can be visualized and optically tracked in real time.[125,126] Nevertheless, the application of FP-based fluorescent labeling also has some limitations. For instance, since FPs are quite large with a molecular weight of ~25 kDa, the natural biological behavior or functionality of proteins may be affected by steric effects. Another drawback is the limited spectral range compared to other fluorescent dyes, such as organic or synthetic fluorophores, even though modern FPs already offer improved optical parameters.[109,117,127]

Organic fluorophores

Compared to FPs, organic fluorophores are much smaller (< 1 kDa) and have superior optical features such as a wide spectral range, great photostability and, in many cases, a higher brightness.[115,118] In addition, they are commercially available in various designs.[128] However, they also have a major drawback, namely their lack in specificity. To circumvent this limitation, there are different labeling techniques such as the immunofluorescence staining and the peptide-based labeling. The former one generates fluorescent labeling via specific antibodies while the latter one is based on the conjugation of an organic fluorophore to a small peptide which exclusively binds to a cellular structure.[109,118] In the case of immunostaining, a permeabilization of the plasma membrane is required, guaranteeing the easy access of antibodies to reach a biomolecule of interest. However, this strategy involves the fixation of a cell and, therefore, is inappropriate for live-cell imaging.[115,125,126] In contrast, the peptide-based technology has the potential to label cellular structures in living cells *in vitro* as well as *in vivo*.[129,130] Even though these techniques provide a higher specificity, there remains a risk of unwanted background signal since the fluorescent labeling unlikely reaches a rate of 100% of linkage. This results in free dyes and a non-specific signal which therefore requires purification steps.[118] Moreover, the broad emission of organic fluorophores can cause a spectral overlap, complicating the analysis of fluorescent signal, especially in the case of multiple color imaging.[102,118]

Quantum dots (QDs)

Besides the use of FPs or organic fluorophores, there is another class of fluorescent markers: inorganic nanocrystals or QDs, usually containing a cadmium selenide (CdSe) or cadmium telluride core and a zinc sulfide shell.[115,119] Due to their semiconductor properties, QDs are characterized by a broad excitation profile and, at the same time, a narrow emission peak at a discrete

wavelength preventing a spectral overlap.[118,131] The range of absorption and emission only depends on the synthesis-controlled size and shape of a nanocrystal, enabling the design of any arbitrary excitation or fluorescence wavelength.[112,122] In contrast to FPs or organic dyes, QDs are especially suitable for the application in repetitive imaging or long-term studies due to their high photostability and a fluorescence lifetime of about 10 to 100 ns.[102,115] Their outstanding brightness is helpful for single-particle tracking and further allows the use of very low laser intensities which is particularly important for live-cell imaging.[132] However, even though semiconductor nanocrystals provide many advantages, there is the concern about cytotoxicity due to heavy metal ions such as cadmium and selenium. As discussed in detail by Kargozar *et al*. (2020), there are several mechanisms that could explain QD cytotoxicity, such as core degradation and thus the release of toxic metals or the interaction of QDs with intracellular components.[119] Hence, the research and establishment of a biocompatible surface modification shielding the inner toxic core from its environment plays a crucial role for a successful application in live-cell experiments.[119,120] There are various studies demonstrating no obvious toxicity with regard to cell proliferation or viability when using CdSe-based QDs, if an appropriate surface coating is applied.[122,132-134]

2.2.2.2 Optical parameters

Apart from the use of a suitable hardware setup and the choice of an appropriate fluorophore fitting the experimental purpose, there are additional optical parameters that should be considered to achieve high-quality fluorescence imaging. These include the fluorescence spectrum and possible interferences, the fluorescence lifetime, the photostability, or the brightness of a fluorophore.[118]

Even though scientific literature usually refers to only one single absorption or emission wavelength associated with the maximum peak values indicated in the marker specifications, fluorophores in fact exhibit a broad spectrum of excitation and emission wavelengths.[111] Moreover, the absorption and emission spectra of different fluorophores tend to overlap which can induce an unwanted crosstalk when applying multi-color imaging.[111] To prevent this phenomenon, the use of fluorescent markers with a large stokes shift or with clearly differing fluorescence spectrum is mandatory.[111,113] In some cases, however, this crosstalk is essential, for example in the study of intermolecular interactions using Förster Resonance Energy Transfer. Here, the absorption spectrum of a fluorophore overlaps with the emission spectrum of an excited and very close (< 10 nm) fluorophore, resulting in the emission of a photon that is shifted to a larger wavelength via non-radiative energy transfer.[135,136]

The presence of such a fluorescence quencher can in turn have an impact on the fluorescence lifetime of a fluorophore, even though this parameter is a more intrinsic property of a fluorescence

marker and ,thus, independent of experimental parameters such as the excitation wavelength or the duration of light exposure.[112] More precisely, fluorescence lifetime is described as the average time that an excited fluorophore remains in its energetically unstable state before it returns to its ground state and therefore depends, for example, on the structure and type of a fluorophore.[112,113,118]

Besides its lifetime, the photostability of a fluorescent marker is another important optical aspect in fluorescence imaging. In principle, a dye can infinitely run the cycle of excitation and emission but in reality, the actual amount depends on the type of fluorophore and on the experimental conditions.[113,137,138] For good fluorophores the number of cycles can reach 10 000 to 40 000.[113] However, irreversible photobleaching remains one of the most restricting factors during FL.[113] One option to prolong the photostability of a fluorophore is to reduce the light intensity as well as the duration of sample illumination to the minimum that is needed for generating an image. At the same time, the collection of fluorescence light should be enhanced by optimizing the microscopic hardware including filters, objectives, and the detector.[111,137-139] The continuous progress in the development of fluorophores provides an increasing photostability which also benefits the brightness of a dye as another important optical parameter.

The brightness or intensity of a dye is primarily determined by the extinction coefficient and the quantum yield.[140] The former describes how efficiently light is absorbed by a fluorophore while the quantum yield specifies the ratio of emitted photons per absorbed photon.[115,127,138] Consequently, a fluorophore with a low rate in non-radiative deactivation compared to its rate of fluorescence means a high quantum yield. Together with a high extinction coefficient this reveals a fluorophore with the highest brightness.[118,137] In addition, a high quantum yield also entails a lower probability of ISC which is in turn associated with photobleaching.[113,118] Considering all these optical parameters, it is obvious that the suitable choice of fluorophore plays a crucial role in a successful performance of FL.

2.2.3 The principle of fluorescence microscopy

The key principle of a fluorescence microscope is based on the concept of epi-illumination where both excitation and emission light passage through the same objective.[113,137,139] To achieve, however, a fluorescence image of high quality, the separation of excitation and emission light is mandatory (**Figure 7**). Therefore, a special beam splitter, called dichroic mirror (Dm), is required. This mirror operates in a way that the shorter wavelengths of excitation light are reflected while the longer wavelengths of the emission signal are transmitted towards a detector or camera.[111,113,137] Although these mirrors are designed in a way that their transition between

reflection and transmission zone lays between the excitation and emission peak of a fluorophore, they generally encompass a range of wavelengths and therefore are rarely specific. This issue can be minimized either by using fluorophores with large stokes shifts or by integrating two additional filters: an excitation filter (Ex) and a blocking (B)/emission filter (Em).[111,113,137] The former one functions as a selective pre-filter, allowing only a narrow band of excitation light to reach the Dm, while the blocking filter ensures that only longer wavelengths of the emission signal pass through. With the combination of these three filters, a precise separation between excitation and emission light is reached, ideally providing a fluorescence image without any background signal of other wavelengths.[113,137] By using a light emitting diode (LED)-based light source which provides only a single wavelength for excitation instead of a mercury or xenon bulb, the quality of fluorescence imaging of a specimen can be further optimized.[111]

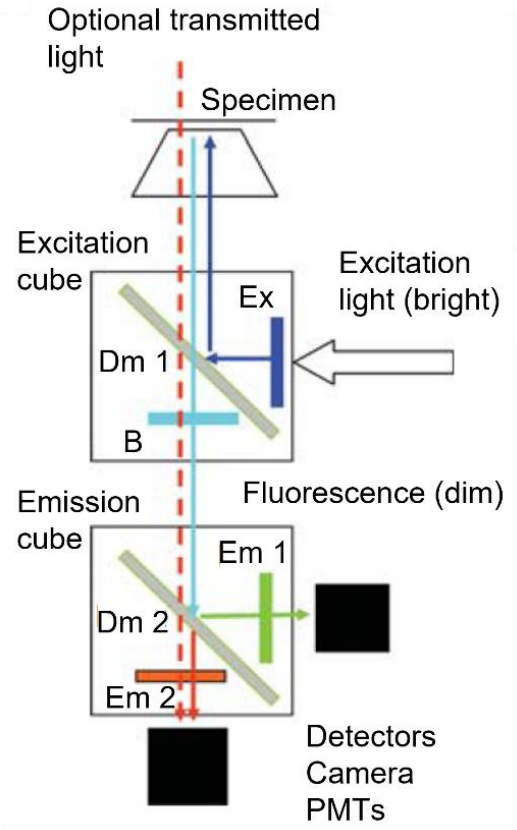

Figure 7: Schematic view of an epi-fluorescence microscope. The excitation light (dark blue) is integrated into the microscope via an excitation filter (Ex) and reflected by a dichroic mirror (Dm 1) towards the specimen passing the objective. The emission signal (light blue) of the sample is then directed through the objective again and transmitted through the Dm 1. A blocking filter (B) ensures that only longer wavelengths will reach the emission cube, consisting of another dichromic mirror (Dm 2) and two emission filters (Em 1 and 2) that additionally block unwanted light. Here, the fluorescence signal is separated into two beams (green and orange) and further directed to detectors such as a camera or photomultiplier (PMT). The brightfield illumination of a sample is possible by using transmitted light (dashed orange line) that passes both the excitation and emission cube to reach a detector. Reproduced and adapted from reference[111], Copyright (2014), Cold Spring Harbor Laboratory Press.

Besides the precise signal separation, the spatial resolution of a microscope is also critical for the quality of a fluorescence image. Here, the theorem of Ernst Abbe named 'diffraction limit' plays a decisive role, approximating the resolution of a microscope as (**Equation 3**)

$$d_m = \frac{\lambda}{2NA} = \frac{\lambda}{2n \cdot sin\alpha} \quad (3)$$

where d_m [m] is the minimum resolvable distance between two structures, λ [m] the wavelength of the used light, and NA the numerical aperture of the objective which is defined by the refractive index n of the immersion medium between sample and objective lens, and the half-opening angle α [°] of the objective's aperture.[101,108,113] Both the wave nature of light and the optical features of an objective are limiting factors. However, in order to achieve high optical resolution, and because the nature of light cannot be changed, modern microscopic systems are often equipped with so-called immersion objectives. These are characterized in particular by the fact that they come up with a large half-angle and an immersion medium based on oil (n = 1.518) or water (n = 1.33) instead of air (n = 1.0), resulting in a high numerical aperture of about NA = 1.4.[141,142] In this way, the number of collected photons can be increased, while the refraction and reflection of light at the interface between the cover glass and the immersion medium is decreased (**Figure 8**).[113]

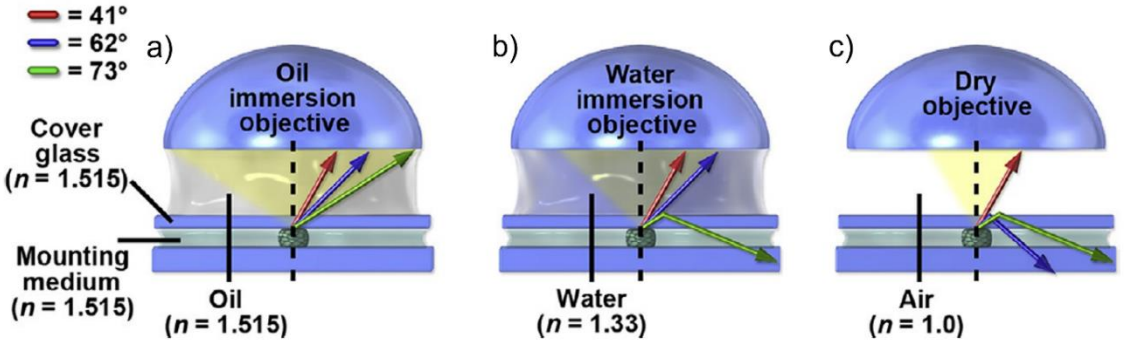

Figure 8: Exemplary light paths for oil, water, and dry objectives. The angles of refraction light illustrated as red, blue, and green arrows refer to the normal shown as black dashed line. (a) An oil immersion objective with the same refractive index for the oil and the mounting medium of the sample enables the collection of emission light coming from angles of up to 73°. (b) Water as immersion medium reveals an increased reflection of light of higher angles due to a smaller half-angle opening. (c) Dry objectives exhibit the highest discrepancy between immersion and mounting medium and provide the lowest yield of light. Reprinted from publication[143], Copyright (2014), with permission from Elsevier.

Combined with a wavelength in the range of visible light, for example λ = 555 nm, a resolution of ~200 to 300 nm in lateral and ~500 to 800 nm in axial direction can be reached.[108,111] Together with the simplicity in operation and handling, this makes conventional FL the standard method for the investigation of biological samples. Nevertheless, cellular compartments such as single proteins or organelles cannot be captured in detail via traditional FL. Therefore, more sophisticated technologies such as Structured Illumination Microscopy and even techniques with

sub-diffraction resolution like *d*STORM or Stimulated Emission Depletion (STED) Microscopy were established in the last decades.[110,144] The combination of different microscopic techniques plays an increasingly important role in today's biological and medical research.

2.3 Correlated microscopy

In the last decades, correlative microscopy, combining the strength and qualities of two or more microscopic techniques, emerged to be a very important tool in the field of biophysics. By addressing one sample or the same region-of-interest (ROI) in a multifunctional way, complementary and often unique structural, morphological, mechanical, and biochemical information can be obtained, significantly exceeding the capabilities of a single-applied method.[145-147]

FL provides a compatibility with living cells in a large field-of-view, an exceptional specificity via fluorescent labeling and an ease in handling, at least compared to many more complex techniques.[148] Nevertheless, even advanced SR fluorescence techniques such as *d*STORM or PALM are inferior to the sub-nanometer resolution of electron microscopy (EM). However, EM suffers in turn from a limited viewing window as much as it does from incompatibility with wet or living specimens.[148,149] The correlative light electron microscopy (CLEM) has been one of the most widely used methodical combinations for decades, involving a successful approach of overcoming the aforementioned limitations. Moreover, it enables the monitoring of live-cell dynamics and the structural visualization of cells within the resolution of nano- to even picometers.[147,148,150] Since its establishment in the 1980s, this multifunctional approach was continuously improved referring to the microscopic hardware including also SEM and transmission EM, sample preparation or fluorescent labeling.[151,152] Especially in the neuroscience, CLEM enabled the addressing of long-standing neurobiological questions such as the signal transmission via synaptic vesicles measuring over only a few nanometers.[153-156] Furthermore, Fermie *et al*. (2018) presented a more advanced study of single organelle dynamics connected to their 3D ultrastructure by correlating live-cell imaging with 3D EM.[157]

Besides CLEM, also AFM as prominent high-resolution surface imaging technique was combined with several types of light microscopy.[158] This method differs from EM as it can provide 3D images of cells via cantilever scanning. This makes fixation or labeling redundant and, therefore, allows the investigation of living samples.[148,159] Moreover, it has the huge advantage that not only the topographic profile of a cell, but also its mechanical properties can be directly probed, exceeding the capabilities of similar imaging methods.[148,160] Nevertheless, analogue to other high-resolution techniques, AFM suffers from a small field-of-view. This can be circumvented by incorporating FL

which in turn provides the imaging of specific and fluorescently labeled cellular components.[159] El-Kirat-Chatel and Dufrêne (2012) correlated AFM with FL to fluorescently visualize the infection process of macrophages with *Candida albicans* as well-known fungal pathogen and, on the other hand, to profile the macrophage surface with nanoscale resolution.[161] In addition, the integration of SR imaging techniques into AFM has become increasingly important in the evolution of multifunctional devices. The combination of two techniques with the same order of resolution has the potential of correlating topography and fluorescence imaging on a single-molecule level.[160] Consequently, AFM was correlated with a variety of SR techniques over the years, as illustrated in **Figure 9**. For instance, Odermatt *et al*. (2015) presented a high-resolution correlative system combining AFM with *d*STORM and PALM, respectively.[35] In this way, they quantified the density of actin filaments in a 3D topography and additionally examined time-resolved imaging of the reaction of a living cell to nanomechanical stimuli.[35] In another study, Mathur *et al*. (2000) combined AFM with TIRFM to investigate the force transmission in endothelial cells.[162] By applying AFM-based indentation on the apical cell surface, they visualized a reorganization of focal contacts on the basal membrane indicating a global force transmission from the apical to the basal cell surface.[162]

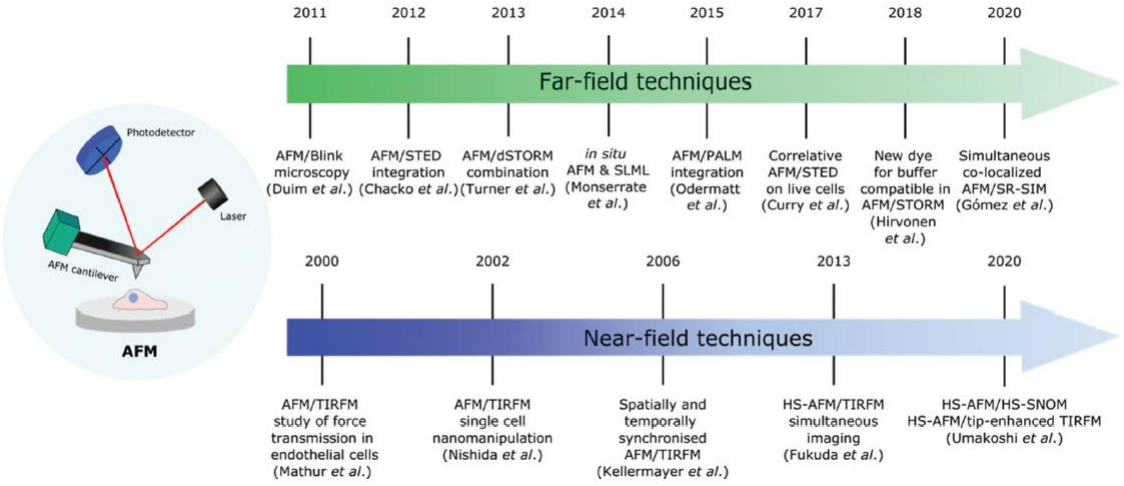

Figure 9: Exemplary timeline of major advancements in combining AFM with fluorescence techniques. Over the years there was established a variety of hybrid systems, combining AFM with both far-field and near-field microscopy. These impressive advances have helped to bridge the gap between the achievable resolution of AFM and optical microscopy. Reproduced from reference[158] with permission from the Royal Society of Chemistry.

Despite all this progress in multifunctional devices, there is only little literature on correlative approaches specifically related to the more advanced AFM-based FluidFM® technology. Nevertheless, there are research groups that combined FluidFM® with FL to further support and complement their results. For instance, the group of J. Vorholt (2016) demonstrated cellular

extraction by optically tracking the withdrawal of fluorescently labeled intracellular content. In this way, they visualized the cellular extraction through the semitransparent cantilever and simultaneously observed a significant decrease in fluorescent signal within the cell.[58] In another study, Roder and Hiller (2018) combined FluidFM® and FL for the highly localized delivery of a fluorescent dye inducing physiological reactions on living complex tissues.[163] This pressure-controlled delivery system was also used in a further study for a targeted isolation of single mammalian cells out of an adherent monolayer. Here, the delivery of fluorescently labeled trypsin was monitored yielding to a controlled detachment of a cell followed by its displacement via pick-and-place experiments. Moreover, by fluorescently labeling a single cell or a bunch of cells with different dyes, a targeted cell sorting was demonstrated using combined FL and FluidFM®.[45] However, comparing these examples of correlative microscopy, it is noticeable that they are all focused on the performance of single-cell manipulation which was described in **Chapter 2.1.2**. The application of FluidFM®-based force spectroscopy together with FL is even more rare. Nevertheless, Potthoff *et al*. (2015) quantified the bacterial adhesion forces using FluidFM®-based SCFS.[70] Prior to the detachment process, they selected a target cell via FL.[70] In another study, they compared the adhesion forces of wild-type and mutant yeast cells, distinguished and optically selected via fluorescent labeling.[39] Consequently, for both single-cell manipulation and SCFS, FL serves more as a pre-selection tool than truly contributing to a scientific question. Moreover, most of these studies are actually based on a sequential performance of experiments with subsequent data correlation to avoid typical complications of simultaneous application.[35,164-168] This includes, for example, an appropriate sample preparation that meets both microscopic requirements at the same time, such as fixation, fluorescent labeling or the surrounding medium of a sample. Furthermore, an exact ROI alignment and a precise and automated data acquisition should be guaranteed.[145,146] But especially in the case of force spectroscopy, a simultaneous correlation between FluidFM® and FL is challenging due to a possible cross-talk between cantilever and the fluorescent excitation light as already claimed by Friedrichs *et al*. (2013).[38]

There are two main phenomena well-known in the context of correlative AFM: first, an excitation light-induced spurious cantilever deflection falsifying a correct force spectroscopy and second, an induced cantilever luminescence possibly distorting the fluorescence imaging. Cazaux *et al*. (2015) demonstrated that the shape and extent of cantilever bending strongly depend on the power of excitation light as well as on a present or absent gold-coating at the cantilever backside.[37] Moreover, the way of deflection (downward or upward) is influenced by the used wavelength. In the case of a gold layer, an illumination with ultraviolet (UV) light generated a strong upward bending while light in the visible range caused the cantilever to deflect downward. By contrast,

cantilever without a gold-coating revealed a noticeably lower deflection when irradiated with visible light, but in general an overall significantly higher baseline fluctuation.[37] Additionally, Fernandes *et al.* (2020) stated that cantilever parameters such as geometry or stiffness should be further taken into account when circumventing these phenomena.[27] Regarding the cantilever luminescence, the most widely used cantilever materials Si_3N_4 and Si may generate an autoluminescence of the AFM probe probably overlapping with the fluorescence emission signal.[27,164] This in turn hinders an appropriate blocking without losing useful parts of the emission spectrum. Furthermore, Kassies *et al.* (2005) stated that the application of crystalline instead of amorphous Si, which is normally used for cantilever manufacturing, would provide a much lower luminescence due to its indirect band gab making crystalline Si to a very inefficient light source.[164] Nevertheless, the continuous advancement in instrumentation and sample preparation allows more and more research groups to realize the truly simultaneous application of hardware-site correlated techniques. For instance, Selhuber-Unkel *et al.* (2010) simultaneously used conventional AFM and FL to demonstrate that the lateral spacing of adhesion receptors such as integrin as well as the loading rate during the detachment strongly determines the strength of cell adhesion.[85] Another study used correlative AFM and confocal laser scanning microscopy for simultaneous real-time imaging of cells while monitoring the surface ultrastructure, sample morphology, adhesion, and mechanical properties as well as optically tracking fluorescently labeled molecules.[169] However, the simultaneous application of FluidFM® and FL has not been reported in literature so far.

2.4 Cell adhesion

The characteristic of cells to stick to an extracellular matrix (ECM) or to adjacent cells is crucial for the multicellularity of mammalian tissues. It plays a fundamental role in diverse physiological mechanisms and functions including tissue morphogenesis, cell communication, migration, or differentiation.[10,170] Moreover, mutations of cell adhesion receptors contribute to developmental disorders and diseases, such as arthritis[13,171], cardiovascular disease[19], or cancer[172,173]. Consequently, for the therapeutic treatment and cure of such diseases, it is essential to understand the complexity of cell adhesion.

2.4.1 Cell adhesion molecules (CAMs)

The concept of cell adhesion is based on a variety of molecules mediating the adhesion of cells to an ECM or to another cell. Over the last years, a huge number of specific molecules have been identified and classified due to their structural and functional similarities. The most prominent

surface receptor families are integrins, selectins, cadherins, and members of the immunoglobulin (Ig) superfamily (**Figure 10**).[174-176] Most of them are integral membrane proteins composed of intracellular, transmembrane, and extracellular domains with the latter binding to appropriate ligands.[177,178] Depending on their counter-receptors, the cell adhesion molecules (CAMs) are traditionally grouped in cell-cell or cell-matrix adhesion molecules. A typical representative of the latter ones is the integrin family, which anchors a cell to the ECM by directly binding to extracellular ligands such as fibronectin, collagen, or laminin.[10,177] The exact binding specificity, however, is defined by the combination of its subunits, α and β, resulting in 24 heterodimeric family members.[179,180] At the intracellular side, integrins are connected to the actin cytoskeleton via so-called focal adhesion (FA) complexes, which are highly organized by a cluster of divers proteins and further described in **Chapter 2.4.2**. This bi-directional connection enables the direct crosstalk between intracellular and extracellular compartments for mechanotransduction and cell signaling leading to cell migration, differentiation, or proliferation.[10,170,181,182]

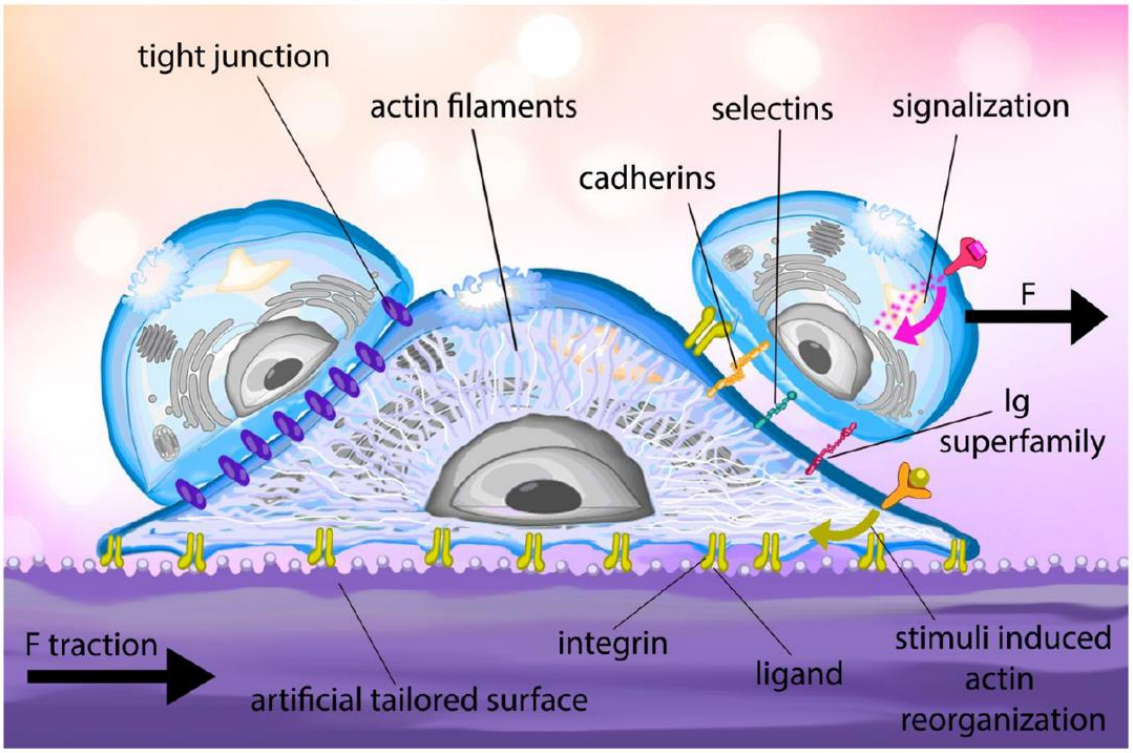

Figure 10: Schematic illustration of the cell adhesion process. An extracellular surface ligand binds to the integrin receptor which is located at the cell membrane. Throughout the cell adhesion process, the actin cytoskeleton is rearranged and a traction force in the substrate is generated. The rearrangement of actin filaments can be further induced via external stimuli. After cell-substrate adhesion, a cell can further interact with neighboring cells through other cell adhesion proteins such as cadherins, selectins or members of the immunoglobulin (Ig) superfamily. This interaction can lead to a variety of multiprotein complexes, such as tight junctions, which stimulate the intercellular communication and mechanical stability in tissues. Reprinted from publication[176], Copyright (2019), with permission from Elsevier.

The cohesion of adjacent cells, on the other hand, is attributed to the CAM families of cadherins, selectins, and members of the Ig superfamily. Besides their structural differences, they are further classified by their type of ligands. Cadherins preferably form homophilic bonds while members of the Ig superfamily form both homophilic and heterophilic bonds.[174,183] Selectins, by contrast, are associated with calcium-dependent binding to carbohydrates. They are the most recently described protein family of CAMs with three sub-classes, E-, P-, and L-selectins originally named by the cell type of their first discovery: *e*ndothelial cells, *p*latelets, and *l*eukocytes.[183] They play a fundamental role in the initial stage of the 'rolling cell adhesion cascade' where circulating leukocytes are recruited to sites of infection or injury. Here, selectins are responsible for the leukocyte rolling on vascular surfaces where chemokines then trigger leukocyte integrins to enable the spreading and crawling and, finally, the para- and transcellular migration.[184-186] This immune reaction is further supported by members of the Ig superfamily such as intercellular CAM1 (ICAM1) and vascular CAM1 (VCAM1) serving as heterotypic ligands for integrins during leukocyte arrest.[184] Apart from this, a high number of Ig members contributes to divers steps of brain development including synapse formation and neuronal migration, and to the function and preservation of neuronal networks in the adult.[187] Other members were classified as markers for cancer progression. For instance, the melanoma CAM is suspected to be involved in the progression of melanoma, prostate and breast cancer.[188] In accordance with the contribution to a huge variety of physiological processes, the Ig superfamily with its more than 765 members represents the largest group of surface receptors. All members are composed of at least one N-terminal Ig or Ig-like domain, which is located at the extracellular site of the cell membrane and conveys cell-cell adhesion in a calcium-independent manner.[183,188] In contrast, cadherin-mediated cohesion requires the presence of calcium ions to maintain the structural integrity of the protein.[174,189] This large family of more than 350 adhesion molecules is divided into "classical" cadherins, i.e., neuronal (N)-, placental (P)-, retinal (R)-, and epithelial (E)-cadherins referring to the tissue in which they were originally found, desmosomal cadherins, and protocadherins.[174,190-193] The basic structure of classic cadherins is defined by a highly conserved cytoplasmic tail that is directly linked to the actin cytoskeleton and further connected via a single transmembrane domain to an extracellular N-terminal ectodomain (EC) of five tandem repeats. These external motifs are responsible for the strong adhesion of adjacent cells and, consequently the formation of intercellular adherens junctions (AJ). These junctions are typically characterized by a dense arrangement of E-cadherins, i.e., between intestinal epithelial cells.[174,190,194-196] The protocadherins are predominant in the nervous system, where they play an important role in the formation, maintenance, and dynamic modification of synapses.[191,193] Unlike classical cadherins,

the extracellular structure of protocadherins is not restricted to the number of EC domains which typically results in six or seven repeats.[191,193,197] The desmosomal cadherins are based on the same extracellular structure as the classical ones. However, there are three isoforms of desmocollins (Dsc) that exhibit a different splicing in their cytoplasmic domain, which might affect the strength of cytoskeletal linkage.[192,197,198] Nevertheless, desmosomal cadherins play the key role in another prominent anchoring junction named desmosome. Here, intermediate filaments of neighboring cells are strongly connected to provide mechanical stability within tissues that are regularly subjected to physical forces such as the cardiac muscle or epidermis.[199-201]

Apart from the presented main groups of CAMs, there are further proteins that play an important role in the intercellular adhesion and communication. These include occludin, claudins, and the zonula occludens (ZO) proteins ZO-1, ZO-2, and ZO-3 as well as connexins and innexins. The two latter ones are representatives of gap junctions (GJ), while occludin, claudins, and ZO are part of the so-called tight junctions (TJ), both representing important cell-cell junctions that are described in **Chapter 2.4.3** more in detail.[195,202,203]

2.4.2 Cell-substrate adhesion

For many years, cell-substrate adhesion and its functionality and structure have played a central role in the study of physiological processes such as cell migration, morphogenesis, wound healing, or immunity.[183,204-206] In simple terms, the procedure of cell-matrix adhesion is composed of two phases: an initial cell attachment via integrin-ligand binding and a rapid reinforcement. The latter occurs in three steps: first, cell spreading for an increase of the cell-substrate contact area, second, protein clustering via receptor recruitment, and third, FA assembly including an enhanced intracellular force distribution and membrane stiffening.[170,207] Due to their contribution to cell signaling, force transmission, and cytoskeletal regulation, the multiprotein complexes of FAs are highly essential in the development of cell-matrix adhesion.[181,208] They are composed of integrins as surface receptors and a cytoplasmic protein array that serves as direct linkage to the actin cytoskeleton. Especially the latter one and its molecular organization was unraveled at the nanometer scale in the last years due to the steady and revolutionary progress in light microscopy. Kanchanawong *et al*. (2010) presented a nanoscale architecture of integrin-based mature FAs (**Figure 11**) using three-dimensional (3D) SR-FL.[209] They revealed that integrin cytoplasmic tails and the actin cytoskeletal layer are vertically bridged by a ~40 nm thin central region consisting of specific but partially overlapping multiprotein strata. Here, the interior domain of integrins is coupled to the 'integrin signaling layer', which is composed of focal adhesion kinase (FAK) and paxillin considered to control the adhesion dynamics via signaling cascades. This is followed by a

'force transduction layer' represented by talin and vinculin. The final 'actin regulatory layer' is directly linked to the actin stress fibers and contains zyxin, vasodilator-stimulated phosphoprotein (VASP) and α-actinin.[209,210] In particular, zyxin is responsible for the force-dependent actin polymerization and stress fiber remodeling and exclusively found in mature focal contacts.[175,208,211] However, talin represents one of the main actors in the overall organization and function of focal contacts. Its highly polarized structure not only allows spatial interaction with the integrin-proximal region of FAK and paxillin, but also acts as a structural scaffold for FAs by spanning its stratified core and reaching the 'actin regulatory layer'.[175,209,210,212] Moreover, talin is critical for the first step of cell-matrix adhesion, since it highly increases the affinity to the ECM by triggering a conformational reorganization of the integrin.[180,208,213,214] For the subsequent formation and stabilization of FA complexes, talin recruits vinculin as binding partner, which promotes the clustering of stimulated integrins and further generates a reinforcement of the integrin-actin-linkage via the vinculin tail.[208,214] The overall formation of mature focal contacts has been demonstrated to be even more complex with about 160 molecules contributing to the integrin-mediated adhesion.[208] The entire network consists of almost 700 interconnections mainly representing binding or modification interactions such as the mutual inhibition or activation of components.[208] This complexity can be explained by the multi-domain nature of many plaque molecules. For example, paxillin, FAK, or vinculin have the ability to interact with more than ten different partners.[181]

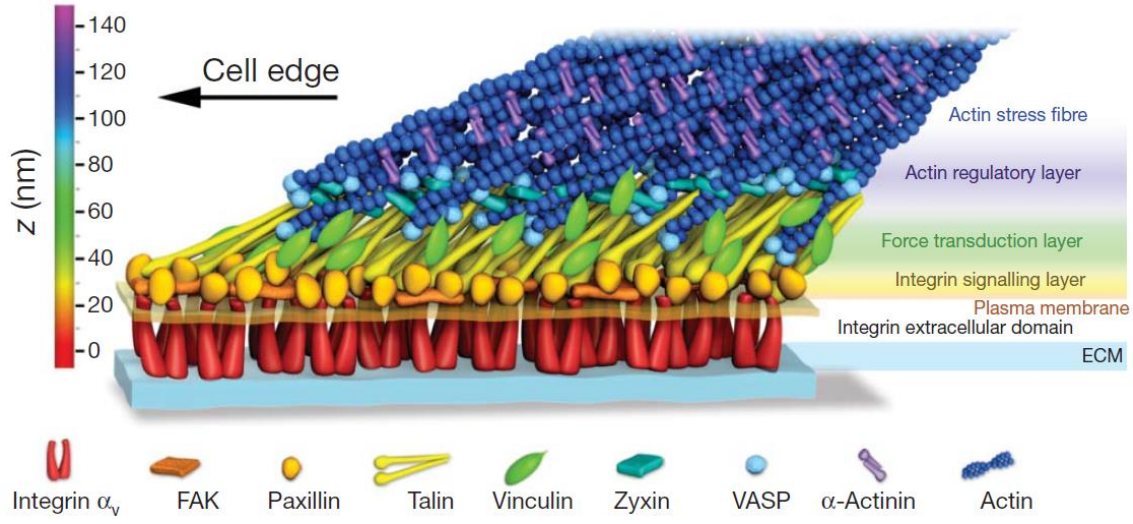

Figure 11: Schematic nanoscale architecture of focal adhesions. Integrins as transmembrane proteins attach the cell to an extracellular matrix (ECM) at its exterior domain. At its intracellular site, it is connected to the 'signaling layer' composed of focal adhesion kinase (FAK) and paxillin. This is followed by a linkage to talin and vinculin representing the 'force transduction layer'. The subsequent 'actin regulatory layer' consists of zyxin, vasodilator-stimulated phosphoprotein (VASP) and α-actinin directly linked to the actin stress fibers. Protein stoichiometry is not depicted. Reprinted by permission from Springer Nature Customer Service Center GmbH: Nature[209], Copyright (2010).

Besides the interactions inside the protein complex itself, the interplay between integrin spacing and surface properties like topography or chemical composition profoundly influences the generation of cell-matrix adhesion. Cavalcanti-Adam *et al*. (2007) demonstrated that the lateral spacing of ECM molecules containing arginine-glycine-aspartic acid controls the assembly of integrin receptors and, therefore, the dynamics of cell spreading, migration, or adhesion.[215] These findings were supported by other researchers, who investigated cell stiffness and adhesion strength and correlated the formation of FAs to a minimum lateral ligand spacing of less than 90 nm.[85,216] Apart from this, the topography of substrates is important, especially with respect to implants and their interactions with cells. When FAs on stainless steel and titanium surfaces were compared to collagen-coated glass coverslips, FAs showed a smaller size and lower mobility on the metal surfaces.[217] This was considered to induce a strengthening of the cell-ECM linkage but, at the same time, a weakening of the dynamic organization and remodeling of the ECM.[217] On flexible substrates, in contrast, the assembly of stress fibers and FAs was highly decreased. Here, FAs showed an irregular morphology with higher dynamic whereas those on rigid substrates revealed a normal shape and an increased stability.[218]

2.4.3 Cell-cell adhesion

Cell-cell adhesion plays a fundamental role in the development and maintenance of organs and tissues. The contacts between adjacent cells act as both, protective barriers from their surroundings and as diffusion channels to maintain homeostasis. This is particularly important in the epithelium as well as in the blood-brain-barrier (BBB), which needs a precisely regulated ion flux for correct functionality.[4,196,219]

The ability of neighboring cells to stick together is based on four intercellular junctions including TJs, AJs, desmosomes, and GJs, all consisting of a complex macromolecular structure.[4,195,220,221] Accordingly, their exact protein composition and respective function differs. As illustrated in **Figure 12**, TJs are mainly formed by transmembrane proteins such as claudins, occludins, and junctional adhesion molecules (JAM-A) as well as by three cytoplasmic proteins of the ZO family (ZO-1, ZO-2, ZO-3).[195,222] While integral proteins, and in particular claudin, act as backbone of the TJ, ZOs are responsible for the association with the actin cytoskeleton or AJs.[194,219] TJs are considered to have two main tasks: first, a barrier/gate function and second, a fence function.[194,223] The former one regulates the paracellular transfer of ions and solutes. A disturbance in the barrier function can trigger disorders like Crohn's disease, multiple sclerosis, edema, or blood-borne metastasis.[219,224,225] The second function maintains cell polarity, i.e., it avoids the intermixing of membrane proteins at so-called 'kissing points'. Thereby, TJs generate

an intercellular sealing by completely extinguishing the space between facing membranes.[222,224] By contrast, AJs and desmosomes preserve a narrow membrane separation of 15 to 20 nm at their contact points.[222]

AJs are mainly assembled by the transmembrane cadherins, in particular E-cadherins, which associate with the actin cytoskeleton via cytoplasmic catenins (**Figure 12**, Module 1).[4] Here, β-catenin (Module 2) links E-cadherin to α-catenin (Module 3) which, in turn, binds to actin filaments via an interface zone containing vinculin.[29,196,226] Similar to talin in integrin-mediated adhesion (**Chapter 2.4.2**), vinculin is crucial for the function of cadherin-based cohesion. After conformational activation, vinculin bridges the gap between the cadherin-catenin complex and the actin network. At the same time, it is responsible for the positioning of the actin regulators zyxin and VASP.[29] This entire complex contributes to a strong mechanical coupling of adjacent cells. Moreover, it stimulates a signaling cascade that promotes cell polarization, cytoskeletal organization, transcriptional regulation, and mechanotransduction.[4,29,227] Besides the classical cadherin-based cohesion, there are also AJs that contain a nectin-afadin complex. Analogously to cadherins, nectins provide a transmembrane domain and a cytoplasmic tail that is connected to an actin-binding protein, in this case, afadin.[195,228] However, there are two main distinctions between these two complexes: firstly, nectins can form both homophilic and heterophilic interactions with family-related members, and secondly, the nectin-afadin complex is unable to establish strong cohesion like cadherins.[195,229] Nevertheless, both complexes are fundamental for the development of AJs: While the attachment of neighboring membranes is initiated by nectins, the following formation of first adhesive contacts and subsequent strong AJs is promoted by cadherin recruitment.[195,223,228] In addition, Campbell *et al*. (2018) stated that the assembly of AJs is a requirement for the successive formation of TJs. [195] This is further supported by *in vitro* knockdown studies of afadin, α-catenin, and ZO-1 which resulted in a lack of TJ formation.[230,231]

Apart from TJs and AJs, desmosomes represent another important type of cell-cell junctions. They are specialized anchoring junctions, which preserve cell-cell adhesion even under substantial mechanical tension. This is of special importance for tissues that constantly endure physical stress, such as the myocardium.[4,199] Similar to AJs, the adhesive core of desmosomes is composed of transmembrane cadherins that form intercellular adhesion by mechanically connecting the cytoskeleton of adjacent cells. However, the desmosomal cohesion is based on the linkage of intermediate filaments instead of the actin cytoskeleton.[200,201] As illustrated in **Figure 12**, the desmosomal cadherin family consists of desmogleins (Dsg) and Dsc (Module 1). Their cytoplasmic domain is connected to plakoglobin (Pg) and plakophilins (Pkp) which are homologous to the β-catenin in AJs (Module 2). These, in turn, are linked to desmoplakin (DP) which, as cytoskeleton

adapter, associates with the stress-bearing intermediate filament network (Module 3).[192,220] Analogously to TJs, the development of desmosomes depends on a prior formation of AJs.[232] According to Lewis *et al*. (1997), Pg, which is the only common component of both, desmosomes and AJs, plays a crucial role in the desmosomal-AJ crosstalk.[232] Only the co-expression of E-cadherin and Pg stimulated the subsequent assembly of desmosomes.[232] In addition, for the full maturation of desmosomes, the presence of both Dsg and Dsc is essential.[233,234] The overall molecular composition and interaction of these complexes is also substantial for human health and disease. A dysfunction in cadherin-mediated cell-cell adhesion, including classical and desmosomal cadherins, has been associated with inherited disorders including life-threatening cardiac arrhythmias, skin and hair disorders, psychiatric diseases, or sensory defects such as blindness and deafness.[234,235]

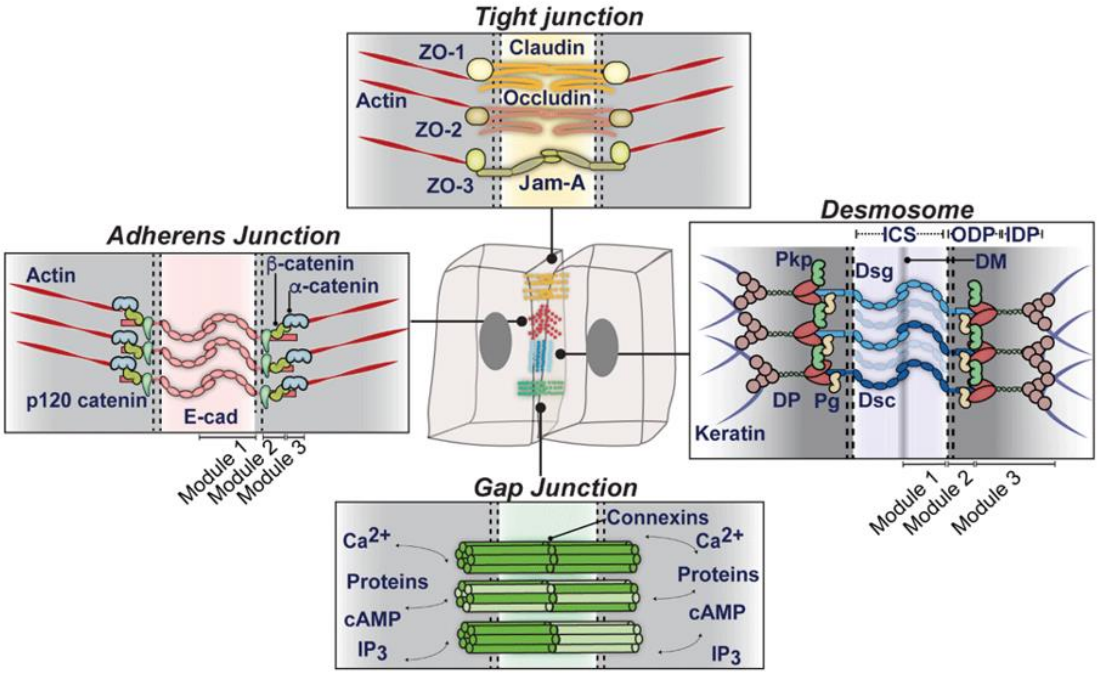

Figure 12: Schematic overview of major cell-cell junctions and their main components. Tight junctions are composed of the transmembrane proteins claudin and occluding which support the formation of the paracellular barrier. The assembly of these proteins is encouraged by the junctional adhesion molecule (JAM-A). On the intracellular site, this junction is strengthened via zonula occludens (ZO) proteins. Adherens junctions are responsible for the anchorage of the actin cytoskeleton of adjacent cells, mainly mediated by the classical cadherins (E-cad) (Module 1). These proteins are linked to actin filaments via the armadillo protein β-catenin (Module 2), the actin-binding protein α-catenin (Module 3), and the p120-catenin. Analogously, desmosomes are regulated by desmosomal cadherins which are classified as desmogleins (Dsg) and desmocollins (Dsc) (Module 1). These associate with armadillo proteins, plakoglobin (Pg) and plakophilins (Pkp) (Module 2), as well as with desmoplakin (DP) (Module 3) providing the linkage between keratin-containing intermediate filaments and the membrane. (Dense midline (DM), intercellular space (ICS), outer dense plaque (ODP), inner dense plaque (IDP)) GJs are composed of connexin proteins to build a connexin channel complex that enables the flow of small molecules, ions, and second messengers between the cells. (Cyclic adenosine monophosphate (cAMP), inositol trisphosphate (IP_3),). Reprinted from reference[220] as open-access article distributed under the terms of the Creative Commons Attribution License, which permits unrestricted use, distribution, and reproduction in any medium.

Besides the junctional complex of TJs, AJs, and desmosomes occurring in an apical-basal direction, there is the fourth type of intercellular connections, the GJs. They contribute to the electrical and chemical communication between cells via the formation of intercellular channels.[4,234] As illustrated in **Figure 12**, their molecular structure is quite simple compared to the other junctions. Here, the space between opposing membranes is bridged by so-called connexons, which are composed of six oligomerized connexins forming homotypic or heterotypic channel complexes.[236,237] These, in turn, assemble to microdomains which span the extracellular space and form the GJ. This enables the rapid exchange and transfer of ions, second messengers, e.g., cyclic adenosine monophosphate (cAMP) or inositol trisphosphate (IP_3), and small molecules of up to 1 to 2 kDa.[236,238] However, the specific permeability of GJs is defined by their exact channel composition as well as by the tissue where they are formed.[236] In the central nervous system, GJ-based neuronal communication is widely distributed. Due to their unobstructed diffusion of small molecules, GJs have the advantage of a delay-free signal transmission. This contrasts with the generally dominating synaptic communication, which is stimulated by chemical neurotransmitters and, therefore, suffers from a delay in the order of milliseconds.[239] Moreover, GJs, along with AJs and desmosomes, are part of a specialized region in the plasma membrane of cardiac muscle cells, called intercalated disc. This junctional complex correlates mechanical and electrical functions and, thus, regulates a synchronized contraction of cardiac myocytes and, thus, a proper working heartbeat.[220]

Finally, it is important to keep in mind that even though most studies are focused on cell-cell junctions as individual entities, none of these junctional complexes can be considered as a solo performer. It is rather an interlocking and interrelated network of many building blocks that are far from being completely understood. This perspective is also reflected by an increasing number of publications dealing with the crosstalk of the four major cell-cell junctions.[195,232,240-242]

2.4.4 Characteristics of molecular cell bonding and rupture

Apart from the molecular composition of adhesive cell contacts, the development and lifetime of cell adhesion strongly depends on the functionality and stability of its adhesive bonds. Especially under applied mechanical tension, it becomes apparent how resistant distinctive cell contacts are. Moreover, their behavior under stress provides information about the intermolecular dynamics of cell-adhesion and cell detachment.

Since the first theoretical description of adhesive bonding by George I. Bell in 1978, two binding models have been established and extensively studied over the last years, slip- and catch-bonds.[76,243] As illustrated in **Figure 13a**, the former ones are known to show an exponential

decrease of bond lifetime with increasing tensile force. Thereby, the external force is suggested to reduce the energy barrier between free states, inducing faster yielding of the molecules and, therefore, the shortening of bond lifetime.[78,244] Catch-bonds, by contrast, counter-intuitively reveal a prolonged lifetime with increasing tensile mechanical force (**Figure 13b**). Here, mechanical stress rearranges the molecules in a way that they are packed more tightly. Only after reaching a maximum of critical force load, the lifetime decreases until the bond fails.[244-247] The conventional slip-bonds have been experimentally proven in a variety of traditional receptor-ligand bonds such as streptavidin-biotin, or biotin-avidin.[247,248] The integrin family represents another prominent candidate for force-load analysis due to its high number of isoforms and its function as bi-directional mechanotransducer (**Chapter 2.4.1**).[182] For instance, both the αIIbβ3 integrin-fibrinogen as well as the $\alpha_v\beta_3$ integrin-fibronectin linkage represent a robust single molecule slip-bond.[249,250] Surprisingly, the $\alpha_5\beta_1$integrin isoform, as another fibronectin linker, shows a catch-bond behavior under force load.[251] This encouraged Novikova and Storm (2019) to analyze the interplay of both bonding types during adhesion cluster formation.[252] By means of a mathematical model, they demonstrated that a cluster of integrin-based slip- and catch-bonds shows a higher mechanical integrity under low force load. In parallel, a higher tensile force has the potential to reinforce and stabilize the entire FA complex.[252] However, the most prominent catch-bond formation is represented by the selectin family. Almost 20 years ago, Marshall *et al.* (2003) experimentally proofed the characteristic prolonged bond lifetime between P-selectins and its P-selectin glycoprotein ligand-1.[244] They further revealed that there is no pure catch-bonding, but rather a switch between catch- and slip-bonds. Above a critical force of ~10 pN, P-selectins showed the typical decrease in bond lifetime until complete failure. [244] A similar biphasic force response was also unveiled in L-selectins but, in this case, with a significantly higher critical force of about 50 pN.[253] Moreover, L-selectins require a minimum level of fluid shear stress to promote adhesive bonding.[254] This flow-adhesion behavior is important in the context of leukocyte-mediated inflammatory response. Here, L-selectins are mainly responsible for the leukocyte rolling. Below the shear threshold, most cells roll with high velocity and detach frequently (slip-bond). With rising shear stress, L-selectin induced tethering increases, which results in a more slowly and more regularly leukocyte rolling (catch-bond). With further increasing shear stress, the rolling velocity inclines again, and tether formation is constantly reduced (slip-bond).[185,186,254-256] This dynamic balance between bond formation and breakage is suggested to be essential for the prevention of inappropriate leukocyte aggregation under low blood flow which might occur for example during deep vein thrombosis.[185,254]

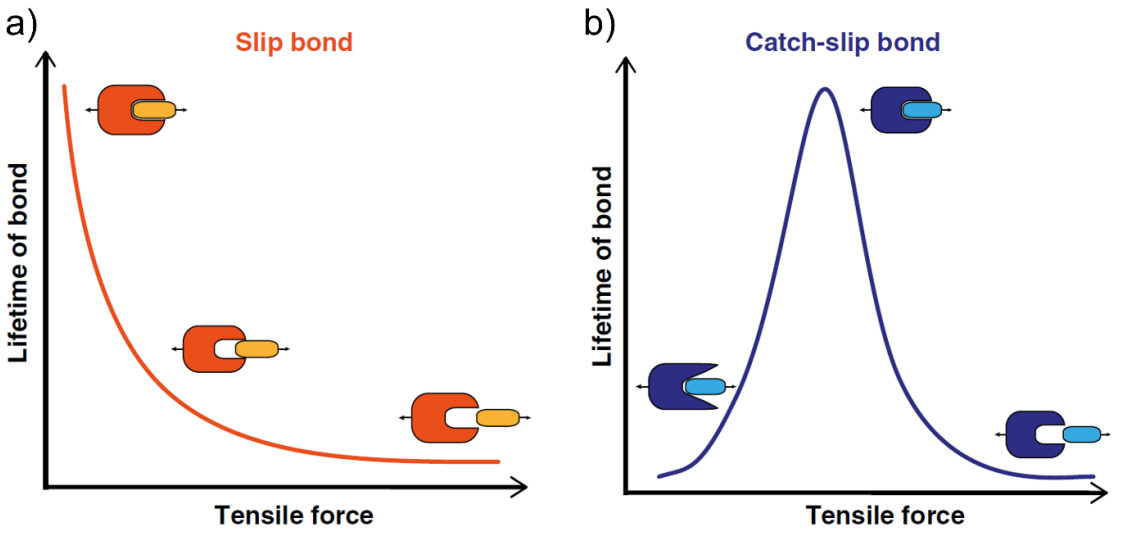

Figure 13: Schematic comparison of slip- versus catch-bonds. (a) The lifetime of slip bonds is characterized by an exponential decrease with increasing tensile forces. (b) Catch-bonds have the counter-intuitive property to reveal a prolonged lifetime with increasing tensile force. After exceeding a critical maximum force, the lifetime decreases exponential until the receptor-ligand bond breaks. Therefore, catch-bonds are composed of a catch-slip-bond transition instead of pure catch-bonding. Reproduced from reference[257], published under the Creative Commons CC-BY-NC-ND license, which permits non-commercial use of the work, without adaptation or alteration.

Besides the conventional catch- and slip-bonds, classical cadherins form another adhesive linkage, ideal-bonds, which were first experimentally demonstrated in E-cadherins by Rakshit *et al.* (2012).[243] In general, cadherins bind in two conformations, strand-swap and X-dimer. While the former one represents the classical slip-bond, the latter one shows the catch-bond indicating extended lifetime in the presence of tensile force.[243] Here, the extracellular domain of cadherins is supposed to bend under mechanical stress which results in the formation of long-living hydrogen bonds enclosing X-dimers into a tighter complex.[247] The ideal-bond of cadherins, however, is suggested to form when a X-dimer converts to strand-swap binding, making the adhesive bond insensitive to tensile forces and, thus, acts as a mechanical damper.[243,258] This dynamic rearrangement of adhesive bonding enables cadherins to tolerate high mechanical stress and to regulate the mechanical tension in adhesive cell-cell junctions.[243] For instance, Esfahani *et al.* (2021) demonstrated that cadherin-mediated cell-cell junctions can endure an externally applied strain of more than 200% before complete bond rupture.[259] This high resistant is considered to be based on an interplay of cell-cell adhesion strengthening and cytoskeletal adjustment. Especially the latter one serves as first response to mechanical tension. Due to its viscoelastic characteristics and the myosin contractility, the actomyosin cortex immediately induces a stress relaxation preventing a direct bond rupture.[259,260] This bridges the time of the more complex cell-cell adhesion enhancement. While the formation of catch-bonds only takes

seconds, the timescale of multiplication or assembly of adhesion complexes ranges from a few minutes to several hours after the first force load.[243,259] Consequently, an increase in tension that is faster than the stress relaxation is inevitably provoking a tension buildup and, finally, cell-cell junction failure.[259]

CHAPTER 3

Results and discussion

Parts of this chapter were published as original research articles:

Weigl, F.; Blum, C.; Sancho, A.; Groll, J.; Correlative Analysis of Intra- Versus Extracellular Cell Detachment Events Via the Alignment of Optical Imaging and Detachment Force Quantification, *Advanced Materials Technologies* **2022**, 2200195., reproduced from reference[261], licensed under a Creative Commons Attribution – Non Commercial 4.0 International License, which permits use, sharing, adaptation, distribution, and reproduction in any medium or format.
To increase readability, figures from the supplementary information have been included in the main text of this thesis.
The article is based on the work of the author of this thesis, Franziska Weigl, who performed the experiments and data analysis, wrote the manuscript and is the first author of the publication.

Müller, S. J.; **Weigl, F.**; Bezold, C.; Bächer, C.; Albrecht, K.; Gekle, S.; A Hyperelastic Model for Simulating Cells in Flow, *Biomechanics and Modeling in Mechanobiology* **2021**, 20, 509, reproduced from reference[262], licensed under a Creative Commons Attribution 4.0 International License, which permits use, sharing, adaptation, distribution, and reproduction in any medium or format.
The article includes work of the author of this thesis, Franziska Weigl, who performed parts of the experiments and wrote a section of the manuscript as second author of the publication.

Nahm, D.; **Weigl, F.**; Schaefer, N.; Sancho, A.; Frank, A.; Groll, J.; Villmann, C.; Schmidt, H.-W.; Dalton, P. D.; Luxenhofer, R.; A Versatile Biomaterial Ink Platform for the Melt Electrowriting of Chemically-Crosslinked Hydrogels, *Materials Horizons* **2020**, 7, 928, reproduced from reference[263], licensed under a Creative Commons Attribution - Non Commerical 3.0 Unported License, which allows redistribution and adaptation in any medium.
To increase readability, figures from the supplementary information have been included in the main text of this thesis.
The article includes work of the author of this thesis, Franziska Weigl, who performed parts of the experiments and its analysis, and wrote a section of the manuscript as second author of the publication.

3.1 Evaluation of the standard applications of conventional FluidFM®-based force spectroscopy

As illustrated in **Chapter 2.1**, the conventional FluidFM® technology offers a variety of different applications. To understand and learn the operation procedure and handling of FluidFM®-based force spectroscopy, the starting point of this thesis was set on the evaluation and application of indentation and classical cell adhesion measurements. Two different types of indentation experiments are presented in **Chapter 3.1.1**, including the examination of hydrogel fiber elasticity via colloidal indentation and the deformation of cells using tipless micropipette cantilevers. The investigation of cell adhesion forces is demonstrated in **Chapter 3.1.2**. All experiments of this section were performed with a conventional FluidFM® setup already described in detail by Sancho *et al*. (2017) and shortly depicted in the following chapter.[40]

3.1.1 Indentation

3.1.1.1 Colloidal indentation

Due to the well-known interplay between cells and their surrounding matrix directly influencing e.g., proliferation, adhesion, or differentiation, a reliable and efficient evaluation of mechanical or morphological characteristics of both cell and material represents an important aspect in the field of biophysics.[74,264-266] To date, FluidFM®-based nanoindentation as an improved version of the AFM-based technique (**Chapter 2.1.2.4.3**), is mainly applied to investigate the mechanical characteristics of cells exclusively.[93,94,267,268]

In the emerging field of tissue engineering, especially the mechanical characterization of potential future biomaterials plays a crucial role. Therefore, Nahm *et al*. (2020) established a novel biomaterial ink platform using poly(2-ethyl-2-oxazine) (PEtOzi)-based hydrogel fibers which were produced via melt electrowriting (MEW) and mechanically quantified through FluidFM®-based colloidal indentation.[263] The processing of these fibers was in particular special due to the fact that MEW is usually restricted to the use of hydrophobic and thermoplastic polymers such as poly(ε-caprolactone) (PCL).[269,270] Hydrogels, in contrast, correspond to the exact opposite due to their high water content and, therefore, represent a new material class in MEW.[263] Further details to the principle and processing of MEW as part of the evolving field of additive manufacturing is published in numerous articles and not part of this thesis.[269-272]

For the evaluation of fiber elasticity, a conventional FluidFM® system was used, mainly composed of a scan head (FlexAFM V5+ SLD, Nanosurf GmbH, Langen, Germany) combining AFM with FluidFM® technology (Cytosurge AG, Glattbrugg, Switzerland), an inverted microscope (AxioObserver Z1, Carl ZEISS AG, Oberkochen, Germany) carrying a piezoelectric sample stage of

100 µm retraction range (npoint LC400 controller, Nanosurf GmbH, Langen, Germany) with the scan head on top and a microfluidic system (Cytosurge AG, Glattbrugg, Switzerland) allowing the targeted application of negative or overpressure via a microchanneled cantilever.

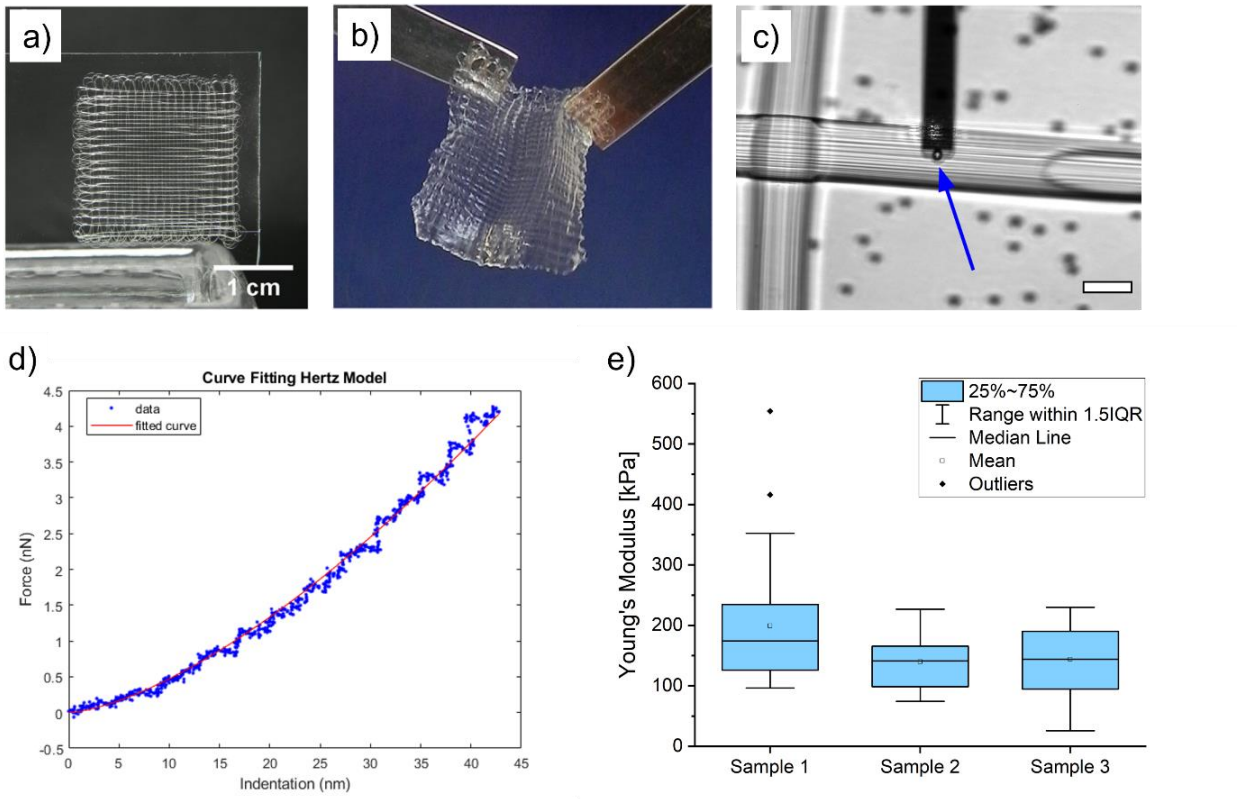

Figure 14: Examination of fiber stiffness of polymer fibers via colloidal indentation. (a) Layered structure of the MEW printed scaffold in a dry state. (b) After hydration and swelling, the scaffolds are mechanically robust and can be easily handled and transferred (scale bar not specified in the original image). (c) A cantilever with immobilized bead at its aperture (blue arrow) is brought into contact with a polymer fiber. Scale bar: 50 µm. (d) Exemplary force-indentation curve (blue) showing the increase in force after reaching the contact point and the corresponding fit (red line) in accordance with the Hertzian model. (e) Distribution of measured Young's moduli for three independent samples. (a, b, d, e) Reproduced and adapted from reference[263], distributed under a Creative Commons Attribution – Non Commercial 3.0 Unported License.

To examine the mechanical properties of the hydrogel fibers, a two-layered scaffold with a clearly defined fiber stacking was hydrated and inserted into the FluidFM® setup (**Figure 14a** and **b**). By aspirating a colloidal bead onto the cantilever aperture, as illustrated in **Figure 14c**, nanoindentation was performed. The fitting of the corresponding force-curves via Hertz model revealed Young's moduli between (0.140 ± 0.042) MPa and (0.20 ± 0.10) MPa (**Figure 14d** and **e**). This is consistent with other water content hydrogels but much softer when compared to PCL as gold-standard polymer for MEW.[269,271,273,274] While PCL represents a promising candidate for the application in stiff tissue environment such as cartilage or bone, the higher elasticity of hydrogels, which makes them also more flexible, is of special interest in the context of soft tissue

engineering.[263,269] For instance, the use of hydrogels exemplifies a powerful tool in ophthalmologic research serving, for example, as accommodating intraocular lens or soft contact lenses.[275,276] Moreover, due to their tissue-like features, hydrogels also play a crucial role in the field of cardiac tissue engineering. In this context, they are often utilized as supporting matrices mimicking the biomechanical and biochemical properties of native tissue and, thus, delivering viable cells into the heart for cardiac regeneration.[277,278]

Consequently, an appropriate examination of the mechanical characteristics is a crucial issue in the advancing field of biomaterial design. In this context, the FluidFM® technology represents a suitable method due to its fast and reversible colloidal exchange as well as its straightforward applicability in nanoindentation.

3.1.1.2 Cellular compression

Another important method in the field of additive manufacturing is 3D bioprinting. It aims the formation of 3D artificial multi-cellular tissue structures and, thus, the replacement of diseased or injured tissue.[279,280] During the printing process, a so-called bioink consisting of a biomaterial-based hydrogel, which encapsulates a suspension of cells, is pushed through a fine nozzle to subsequently form a tissue-like construct.[281] For this reason, not only the biomaterial has to fulfill specific requirements such as proper mechanical and chemical properties or a high biocompatibility, but also the cells have to withstand high mechanical stress to guarantee an accurate functionality of printed scaffolds.[280,282] Especially the latter aspect represents a major challenge in 3D bioprinting since hydrodynamic forces can cause large cellular deformations which, in turn, probably induce cell damage or even cell death.[262,282] How strong the cells react to the external stress, experienced during the printing process, is mainly influenced by the viscosity of the surrounding hydrogel, the nozzle size, and the elastic behavior of the cells.[262,282] Thus, a precise evaluation of the dependence between mechanical stress and cellular deformation is important for successfully creating cell-transporter medium and consequently tissue-like constructs. The most common approach of quantifying cellular elasticity is the Hertz model as described in **Chapter 2.1.2.4.3**. However, due to its limitation to small deformations, larger ones often cause major deviations from the approximations of the Hertzian theory.[100,283] Thus, the simulation of cell mechanics in 3D bioprinting requires a more advanced approach including complex elastic material properties.

Therefore, a novel numerical model was established and subsequently verified by comparing its predictions with the cellular compression of rat embryonic fibroblasts (REF52 cells) using FluidFM®-based indentation as presented by Müller *et al*. (2021).[262,284] The detailed mathematical derivation of this model is described in the corresponding publication and beyond the scope of

this thesis. In simple terms, however, it is especially characterized by a 3D simulation of cells in arbitrary flow where they are contemplated as elastic continuum in accordance with the hyperelastic Mooney-Rivlin model. Moreover, it provides the possibility of including cellular compartments such as the nucleus.[262] The experimental performance of cellular deformation was based on the same microscopic setup as presented in the previous chapter only differing in the fact that in this case, the micropipette was directly used as indenter without the application of a spherical bead.[262] This allowed the aspiration of a target and suspended cell onto the cantilever aperture as illustrated in **Figure 15a** and **b**. Afterwards the attached cell was compressed by approaching the surface until a large deformation of up to 80% was reached.[262] As illustrated in **Figure 15c**, the exemplary measured force-curves depicted with small squares initially reveal a slow increase until a deformation of about 40% is reached. This is directly followed by a rapid increase in force for large deformations. Moreover, although the difference in cell size is already considered within the calculations, it is clearly visible that the point of force growth changes between the individual cells indicating a definite variability of elastic behavior. Nevertheless, these experimental results reveal a very good agreement with the simulations, illustrated as colored solid lines (**Figure 15c**). Thereby, the Young's modulus defines the overall force progression while the Mooney-Rivlin ratio w determines the moment of force growth.[262] Moreover, the latter one revealed a stronger force upturn with decreasing shear moduli w as indicated in **Figure 15c** where the ratios of $w = 0.25$ show the earliest force growth. In contrast, the blue and red curve with ratios of $w = 0.5$ and $w = 1$, respectively, only start to increase at higher deformations. In case of Young's moduli, values of 110 Pa to 160 Pa were examined which is in the range of typical elastic moduli of cells.[285,286] Comparing the excellent matching results of experimental compression and simulation data with the Hertz theory illustrated as black line, the same progression is visible in case of very small deformations. However, with increasing deformations, a significant discrepancy is visible due to the linear behavior of the Hertzian model. This strengthens the need of the presented hyperelastic model, which allows a much more realistic prediction of cellular force-deformation behavior in strong hydrodynamic flows. Moreover, it provides a tool for biofabrication researchers to adjust the parameters of the 3D bioprinting process in a way that cell viability and consequently the functionality of tissue constructs can be preserved.

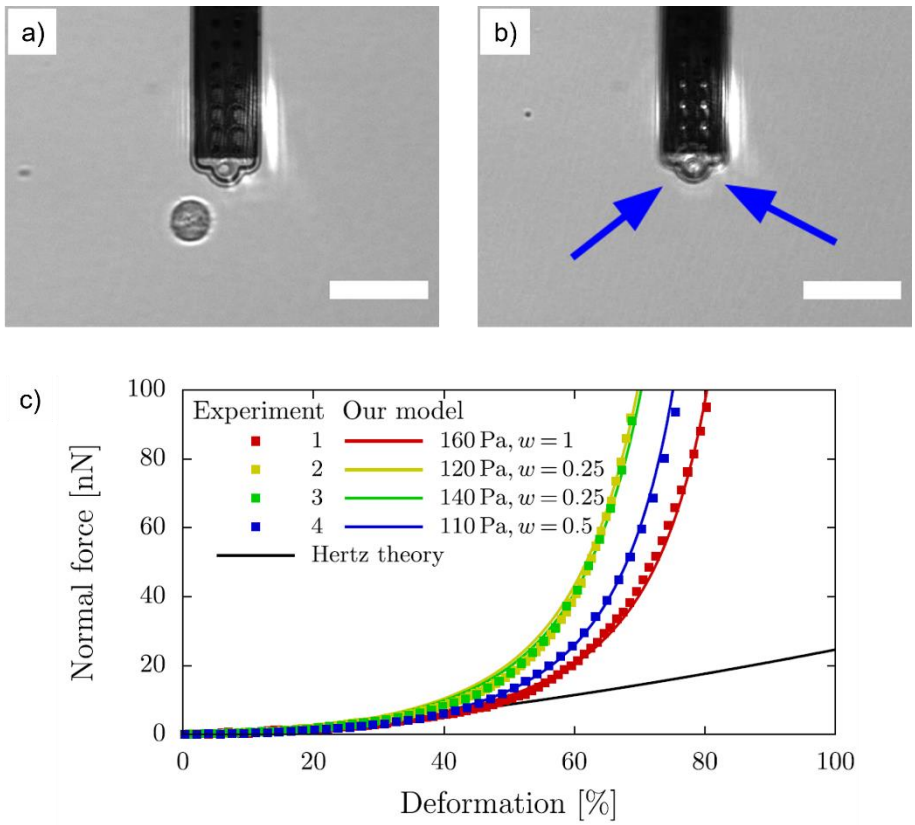

Figure 15: Evaluation of high cellular deformation via FluidFM®-based indentation. Exemplary image of a cantilever that is aligned towards a target and suspended REF52 cell (a), followed by its aspiration at the aperture (b) by applying a negative pressure. Scale bar: 50 µm. (c) Illustration of the dependence between normal force and deformation comparing the experimentally evaluated force data of compressed REF52 cells (squares) with the established hyperelastic model (colored lines) as well as with the conventional Hertzian model for spherical indenters (black line). (a and c) Reproduced from reference[262], distributed under a Creative Commons Attribution 4.0 International License, which permits use, sharing, adaptation, distribution, and reproduction in any medium or format.

3.1.2 Cell adhesion

Besides the investigation of material or cellular stiffness, also the study of cell adhesion is essential for the complex design and development of biomaterials. For instance, tissue-constructs that are inserted into blood vessels demand a non-adherent surface to prevent the occurrence of embolism or thrombosis. In contrast, biomaterials that serve as scaffolds for tissue regeneration require the adhesion of cells to promote proliferation and biosynthesis.[10,287] Thus, the successful implantation of a biomaterial strongly depends on the affinity or aversion of cells towards a substrate. In a more biological context, cell adhesion is essential for a variety of biological processes and functions such as cellular communication, migration, or differentiation.[10,267,288] However, it is also well-known that alterations in cell adhesion are responsible for diseases such as osteoporosis[289,290], atherosclerosis[291,292] , or cancer[172,293]. Especially the latter is characterized by reduced intercellular adhesiveness inducing the dissociation of malignant cells which, in turn,

adopt a more invasive phenotype and, finally, metastasize.[293] Therefore, a detailed evaluation of cell adhesion and its biomechanics plays a crucial role in the progression of therapeutic strategies as well as in the emerging field of biofabrication.

The FluidFM® technology with its integrated microfluidics (**Chapter 2.1.2.4.2**) represents a very suitable approach for quantifying the adhesion forces of mature cells. **Figure 16a** shows an exemplary force-curve of a spread and single REF52 cell (**Figure 16b**, marked with blue arrows) measured with a conventional FluidFM® system as described in **Chapter 3.1.1.1**. It is composed of the typical three sections of approach, immobilization, and retraction. As already described in detail in **Chapter 2.1.2.4.1** and **2.1.2.4.2**, the first phase represents the approach of cantilever and target cell until a contact is reached (approach, red section). This is followed by a constant suction pressure to immobilize the cell at the cantilever aperture (immobilization, green section). The last phase illustrates the retraction-curve, which shows the typical process of cellular detachment (retraction, blue section). Here, the force increases within a few seconds until the MDF is reached representing the highest point of cell-substrate binding.[74] This is followed by multiple detachment steps visible as abrupt force-jumps. After complete cell detachment, the force decreases to a minimum, which is often slightly shifted towards negative values. This is due to viscous drag and the additional weight of the attached cell, hindering the cantilever deflection to return to its initial state.[38] This progression in force is consistent with the ones of other studies using FluidFM® technology.[68,267] Moreover, the MDF of (-556 ± 149) nN especially highlights the capability of FluidFM® to measure high forces occurring at mature focal contacts. This was not possible if classical AFM was the only method for evaluating cell adhesion with high precision. As described in **Chapter 2.1.2.4.2**, AFM has the major drawback that it is limited to the evaluation of forces that do not exceed the adhesive forces between a cantilever and a chemically attached cell. Therefore, it is restricted to the measurement of early-stage adhesion which usually does not exhibit a distinct formation of focal or cell-cell contacts.[25,40]

The procedure of the cell detachment is further illustrated via a step-by-step composition of brightfield images recorded during the measurement (**Figure 16c**). Here, it is clearly visible that the optical tracking of the cell is hampered by both low resolution and a lack of focal stability, which increases with proceeding separation and reaches a maximum when the cell is fully detached. Consequently, a precise visualization of the cellular detachment and its individual unbinding steps at the cell-ECM interface is not feasible. However, this is not surprising considering that the establishment of FluidFM®-based SCFS was solely focused on the quantification and analysis of FD-curves and not on the high-resolution visualization of the corresponding separation process.[25,43,50] Nevertheless, the correlation of force data with the

cellular movement during detachment is of high interest when it comes to a deeper understanding of the complexity of cell mechanics. Moreover, the variety of detachment steps revealed in the force-curve are probably linked to different types of unbinding mechanisms such as tether formation, so-called jumps or the occurrence of slip or catch-bonds. Although these phenomena are already well described in literature, the focus has always been on the force-curve analysis or on a mathematical derivation.[38,74,78,244,294,295] However, an appropriate visualization of these unbinding steps and its specific correlation to the progression in force is still missing. In addition, the restriction of conventional FluidFM® to brightfield illumination hinders the monitoring of intracellular processes during cellular detachment. Consequently, the simultaneous application of fluorescence light and FluidFM®-based SCFS has the potential to reveal new insights into the biomechanics of cell adhesion.

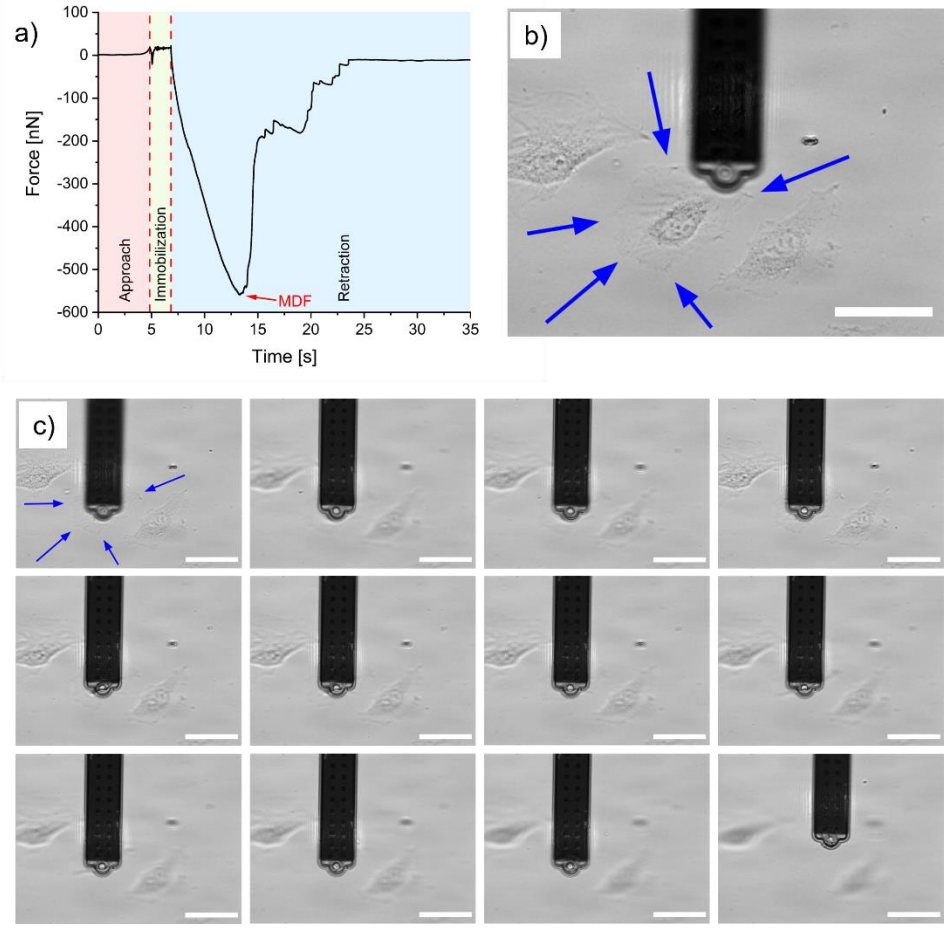

Figure 16: FluidFM®-based cell adhesion. (a) Exemplary force-curve of a whole cellular detachment process composing of three sections: approach (red), immobilization (green), and retraction (blue). The highest point of adhesion force is represented by the maximum detachment force (MDF). (b) Microscopic image of a single REF52 cell (blue arrows) that is aligned towards the cantilever. (c) Step-by-step composition of a detachment process recorded without focus control starting with a focused image during the approach (upper left image), an increasing loss in focus with proceeding measurement and ending with a blurry image after complete detachment (bottom right image). Scale bar: 50 µm.

3.2 Design and fabrication of the correlated FL-FluidFM® device

To achieve a correlated and simultaneous application of FL and FluidFM® technology, the establishment of a novel multifunctional hardware setup was necessary. Therefore, several hardware adjustments were performed including, for instance, the implementation of a new fluorescence light source, the optimization of focus stability and the integration of independent control units for each microscopic system.

First, an overview of the main components of the correlated FL and FluidFM® (FL-FluidFM®) setup is given (**Chapter 3.2.1**) followed by a schematic presentation of the device circuit and important interconnections as well as the working principle and the benefits of an integrated Piezo Flexure Objective Positioner (PIFOC) (**Chapter 3.2.2**).

3.2.1 Hardware setup

The establishment of multifunctional devices has emerged to be a hot topic in the understanding of biosciences due to its combined addressing of long-lasting biological questions. Already in 2012, *Nature* has highlighted the advantages of correlative microscopy by declaring two microscopes are better than one.[159] Especially AFM, as already described in **Chapter 2.3**, was combined with a variety of optical microscopy techniques like TIRFM[162,296,297] or *d*STORM[35,36] providing remarkable advances in biological research. However, the non-feasibility of simultaneous data acquisition as well as the restriction of AFM to early-stage adhesion represented a major drawback.[37,38] Thus, the FluidFM® technology was developed by Zambelli's group in 2009.[41] Besides its application for intracellular injection[46,58] and pick-and-place experiments[44,45], FluidFM® has become the gold-standard method for investigating mature cell adhesion[40,42,68]. Nevertheless, to the best of my knowledge, a multifunctional system that enables the quantification and visualization of mature cell adhesion at the same time is still lacking. To fill this gap, a novel in-house developed FL-FluidFM® device was established, paving the way towards real-time optical tracking of cellular detachment.

Figure 17 shows a schematic illustration of the main components (**Figure 17a** and **b**) as well as photographs of the multifunctional device in laboratory (**Figure 17c** and **d**). The base of this system was the conventional FluidFM® setup already described in **Chapter 3.1.1.1**. Hence, for the establishment of the novel device aiming the high-precision monitoring of cell detachments, the optimization of the optical components was crucial. Therefore, a high-numerical immersion oil objective (Plan-Apochromat 40x/1.4 Oil DICIII, Carl ZEISS AG, Oberkochen, Germany) as well as a piezo-driven PIFOC system (nanoFaktur GmbH, Villingen-Schwenningen, Germany) was implemented, providing high optical resolution and focus stability throughout an experiment

(**Figure 17b** and **d**). For a simultaneous visual control over the cantilever alignment and the FL, the output signal is directed to two independent cameras via a double-camera port including a reversible 50:50 beam splitter. The acquisition of fluorescence signal is accomplished using a monochromatic charge-coupled device (CCD) camera (AxioCam MRm, Carl ZEISS, Oberkochen, Germany) while laser spot alignment of the FluidFM® is performed with a complementary metal-oxide semiconductor (CMOS) camera (UI-3060CP-M-GL Rev.2, IDS Imaging Development Systems GmbH, Obersulm, Germany). A LED light source (Colibri 7, Carl ZEISS AG, Oberkochen, Germany) was implemented for the fluorescent illumination, providing up to seven fluorescence excitation lines and fast channel switching in the range of microseconds. By integrating a high efficiency filter set (90 HE LED Carl ZEISS AG, Oberkochen, Germany), four excitation wavelengths (385/475/555/630 nm) are available simultaneously. To shield any noise, the whole FL-FluidFM® system is placed on a vibration isolation base (Accurion Halcyonics-i4, Accurion GmbH, Göttingen, Germany) and covered by an acoustic protection box.

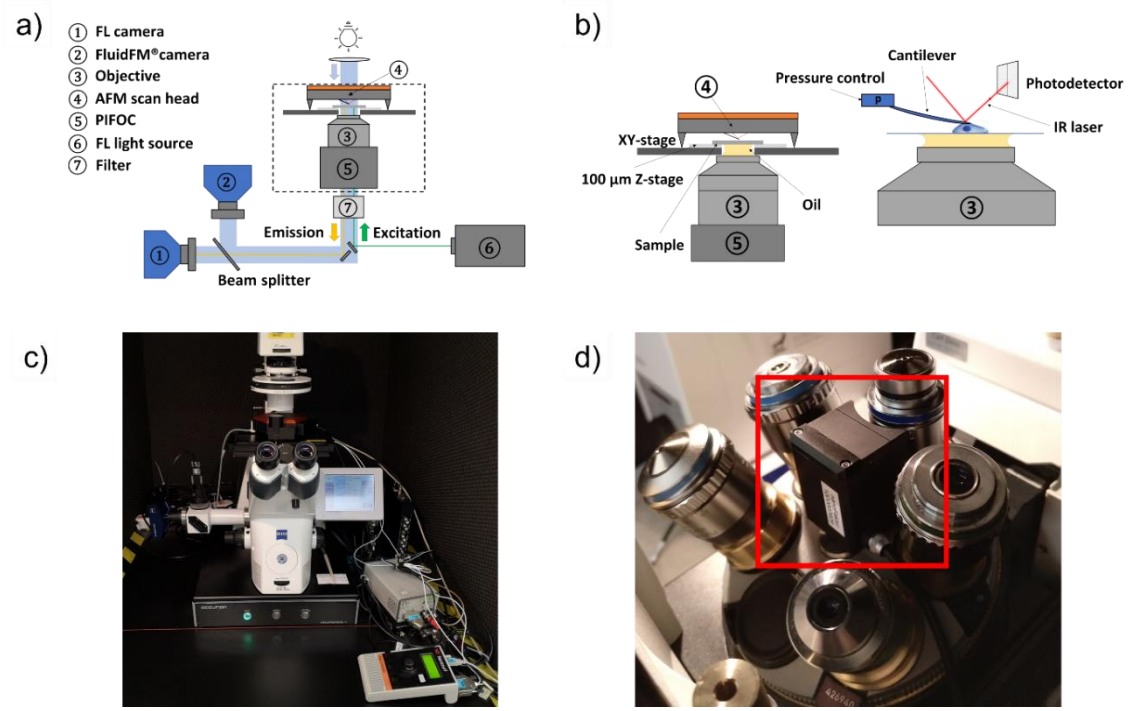

Figure 17: Composition of a customized FL-FluidFM® system. (a) Schematic setup of the whole multifunctional device based on a conventional FluidFM® system that is connected to a monochromatic light emitting diode (LED) light source for fluorescence illumination. The components marked with a black dashed square are illustrated more in detail in (b) showing the view of the interface between sample and high-numerical objective mounted on a Piezo Flexure Objective Positioner (PIFOC) module. (c) Photograph of the whole device in laboratory. (d) Photograph of the PIFOC carrying the high-resolution objective. Reproduced and adapted from reference[261], distributed as open-access article under the license of a Creative Commons Attribution (CC BY-NC 4.0).

3.2.2 Device circuit and working principle of a PIFOC

The achievement of a high optical resolution together with a high focus stability represented a crucial part for the realization of high-quality visualization of a cellular detachment. As schematically illustrated in **Figure 18a**, in a conventional FluidFM® setup, the focus level initially set onto the target cell stays at its position during the whole retraction process resulting in a total loss in focus and making an optical monitoring of cellular movement impossible. This can be referred to the fact that the invention of FluidFM® in 2009 was more focused on the establishment of a liquid delivery system via microfluidics than on a detailed sample visualization.[41] Moreover, for the conventional examination of mechanical properties or adhesion forces, a high precision in force spectroscopy is more important than a detailed and real-time optical monitoring.[39,70,93]

To circumvent this major drawback in a correlative FL-FluidFM® system, a piezo-driven PIFOC system was implemented allowing a precisely guided motion of the objective with a resolution in the nanometer range. This movement in turn was synchronized with the downward motion of the 100 µm z-stage, as illustrated in **Figure 18a** "FL-FluidFM®". In this way, a dynamic but stable focal plane was ensured, guaranteeing a continuous optical tracking of the cellular detachment without any loss in focus. This parallel movement of z-stage and objective driven by the PIFOC is achieved by controlling both components with the same input signal coming from the C3000 unit, as indicated in **Figure 18b** via green and yellow arrows. Moreover, a stable positioning is constantly regulated via a closed feedback loop. To further optimize the optical resolution, a high-numerical objective was implemented whose application is already well-established in the context of correlative SR-AFM microscopy.[34,35,167,298]

Besides the implementation of advanced hardware components, also the operation mode of the two technologies played a crucial role in the correlation of different microscopy techniques preventing mutual software blocking.[145,146] Therefore, FluidFM® and FL had to be operated independently meaning in detail that their respective controlling programs were performed on two separated computers. Moreover, a simultaneous addressing of the same hardware components with different commands from the two technologies had to be avoided, otherwise a system breakdown could occur. Since the FluidFM® software needs access to the microscope and its objectives for the focus control, the FL software was only connected to its fluorescence light source and its corresponding camera. Therefore, the change of objectives or filters had to be performed manually.

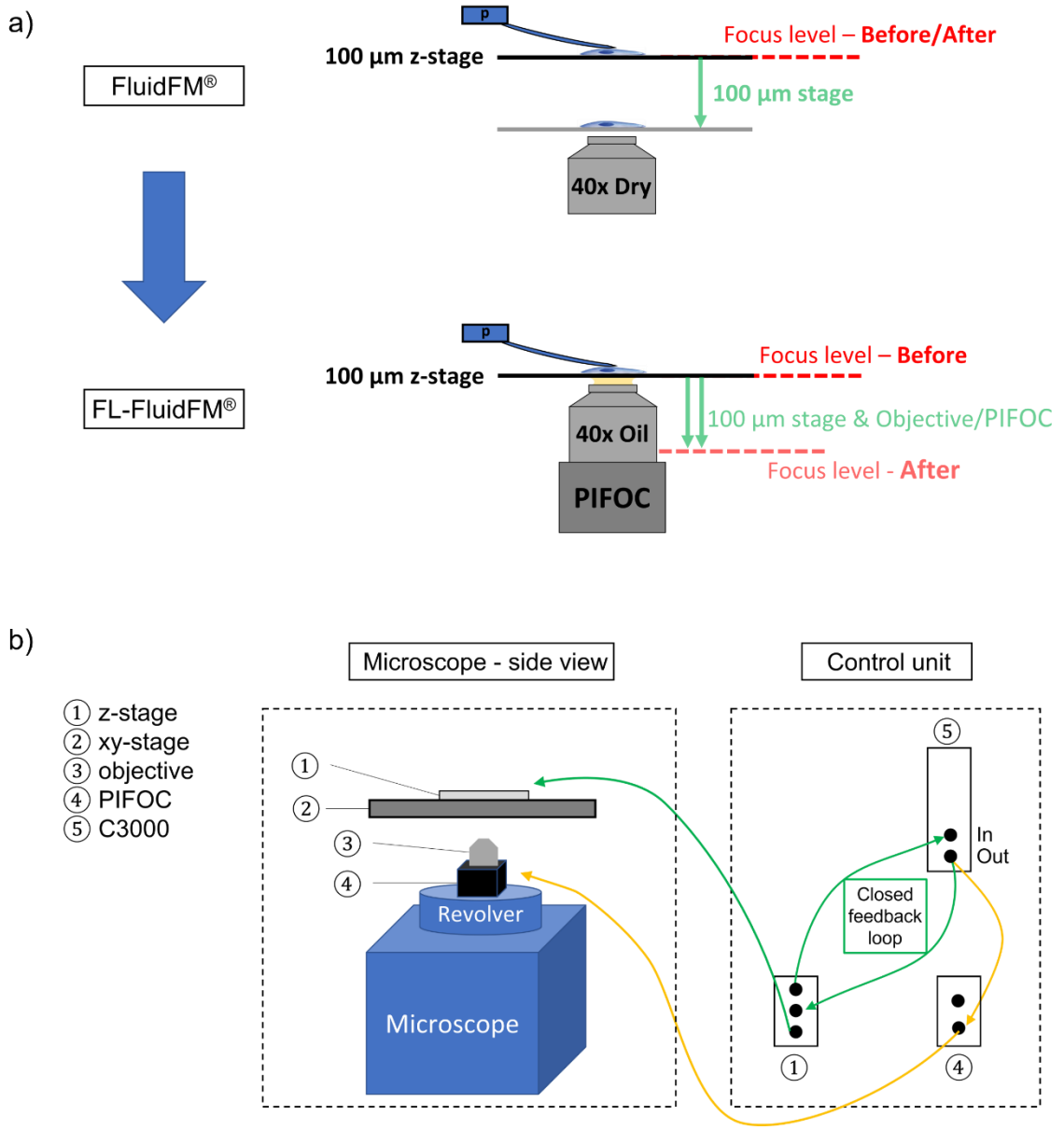

Figure 18: Schematic view of the working principle of a PIFOC. (a) A conventional FluidFM® is based on a dry objective and no focus control resulting in a low optical resolution and a loss in focus during cellular detachment which is guided via a downward movement of the sample stage. By contrast, the optical properties of a correlated FL-FluidFM® system are optimized by the implementation of a high-numerical oil objective and piezo-driven PIFOC ensuring a stable focus level throughout a whole experiment. Here, the preset focus stays on its level by using a synchronized movement of sample stage and objective. (b) The schematic side view illustrates the microscope as base carrying a revolver with the integrated PIFOC and objective. On top, there is the xy-stage holding the 100 µm z-stage. The synchronized movement of objective and z-stage is achieved by controlling both PIFOC (yellow arrows) and z-stage (dark green arrows) with the same input signal coming from the C3000 control unit. This is continuously regulated via a feedback loop running the z-stage in vertical direction (dark green arrows). Reproduced and adapted from reference[261], distributed as open-access article under the license of a Creative Commons Attribution (CC BY-NC 4.0).

3.3 Visualization of cellular detachments with optimized focus stability and high optical resolution

After successfully embedding a high-numerical immersion oil objective and a PIFOC system into the microscopic hardware, cellular detachment experiments of single REF52 cells were performed comparing the imaging qualities of the optimized FL-FluidFM® with the old, conventional FluidFM® setup (**Figure 19**). In both cases, three brightfield images are provided showing the start, a mid-step, and the end of a cellular detachment process. Considering that the standard FluidFM® has no focus control and only consists of a dry objective, it is not surprising that the performance of the conventional device shows a low optical resolution and no focus stability (**Figure 19a-c**). Thus, a detailed optical tracking of cellular movements during a detachment would be nearly impossible. By contrast, the implementation of an immersion oil objective entailed an optimized resolution which is beneficial for the more detailed analysis of intracellular movements during cellular de-adhesion. Especially in comparison with already well-established correlative AFM systems focused on the high-resolution visualization, it is noticeable that all of them are based on high-numerical objectives demonstrating its importance when designing a multifunctional device.[27,34,165,167,169,296]

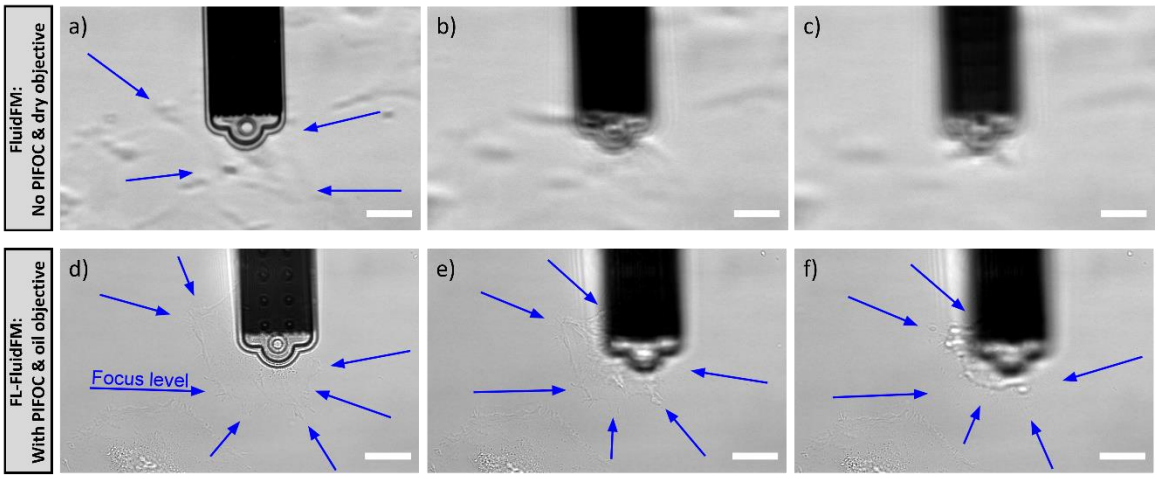

Figure 19: Comparison of the focus stability and optical resolution between a standard FluidFM® (a-c) and FL-FluidFM® setup (d-f). Both cases show a composition of three brightfield images taken at the beginning, in the middle and at the end of a cell detachment experiment. Blue arrows mark the respective cell which will be detached. (a-c) Images taken with a commonly used FluidFM® system show reduced optical resolution and a loss in focus. (d-f) Brightfield images illustrate the high optical resolution and high focus stability of a detachment process which was monitored using the correlated FL-FluidFM® device. Scale bar: 20 µm. Reproduced and adapted from reference[261], distributed as open-access article under the license of a Creative Commons Attribution (CC BY-NC 4.0).

Furthermore, the use of a PIFOC system results in high focus stability during the entire measurement as illustrated in **Figure 19d-f**. Here, the interface between cell and substrate stays

in the focal plane until the cell is fully detached (**Figure 19f**), enabling a real-time visualization of an entire unbinding process. This hardware configuration was also demonstrated in a study of Puech *et al*. (2006) where they used a piezo-driven objective for the monitoring of cell morphology while quantifying cell-cell adhesion forces using AFM.[73] Therefore, combining the integration of a PIFOC with the optimization of microscopic visualization qualities seems to pave the way for the first time to a real-time and correlated investigation of cellular insights and cell adhesion forces occurring during the detachment of mature cells.

3.4 Verification of FluidFM® functionality after successful adaptation of focus control and optical resolution

3.4.1 Comparison of force-distance curves

After successfully advancing the device by implementing the PIFOC and the oil immersion objective, the functionality of the setup was validated. Here, the focus was on the occurrence of noise caused by the additional component of mechanical motion when simultaneously positioning a PIFOC-controlled objective and the sample stage. This, in turn, can affect the highly sensitive force measurements. Furthermore, the oil film between objective and substrate could offer a direct transmission path of vibrations into the experimental medium surrounding the cantilever and thus also onto the cantilever itself. To ensure that vibrations did not negatively influence the high-sensitive measurement procedure of the FluidFM® technology, SCFS was performed by using the novel and focus-controlled as well as the conventional FluidFM® device.

Figure 20a illustrates the exemplary force-curve of a detached REF52 cell using either the standard FluidFM® (**Figure 20a (I)**) or the correlated FL-FluidFM® (**Figure 20a (II)**) setup without and with PIFOC and oil immersion objective, respectively. Both curves are composed of the typical three sections of approach, immobilization, and retraction and show a similar force progression with respect to the precision of the method. Especially the third section, which is the most important one for cell adhesion analysis, reveals a high number of multiple unbinding events in both cases. Comparing the shape of these exemplary force-curves with the ones of other studies, no remarkable difference was visible.[38,40,68,74] Also, the two MDFs are in the same order of magnitude when considering their standard deviations (FluidFM®: (-253 ± 75) nN and FL-FluidFM®: (-334 ± 91) nN)). At first sight, this indicates no apparent negative influence on the data acquisition using the advanced FL-FluidFM® that can be clearly attributed to the implementation of PIFOC or high-numerical objective. Nevertheless, the difference of almost one hundred of nanonewton between the two maximum forces cannot be disregarded. At first glance, this can be explained with the individuality of each cell regarding size and, therefore, contact area, stiffness, or the

number of focal contact points.[74,85] However, comparing the respective totality of cells recorded without or with improved optics (**Figure 20b (I)** and **(II)**), it is apparent that the cells investigated with the new hardware have with (-467 ± 106) nN an overall higher MDF on average than the ones investigated with the standard FluidFM® (MDF_{mean} = (-219 ± 78) nN), even though the overall course of detachment forces shows the typical progression in both cases.

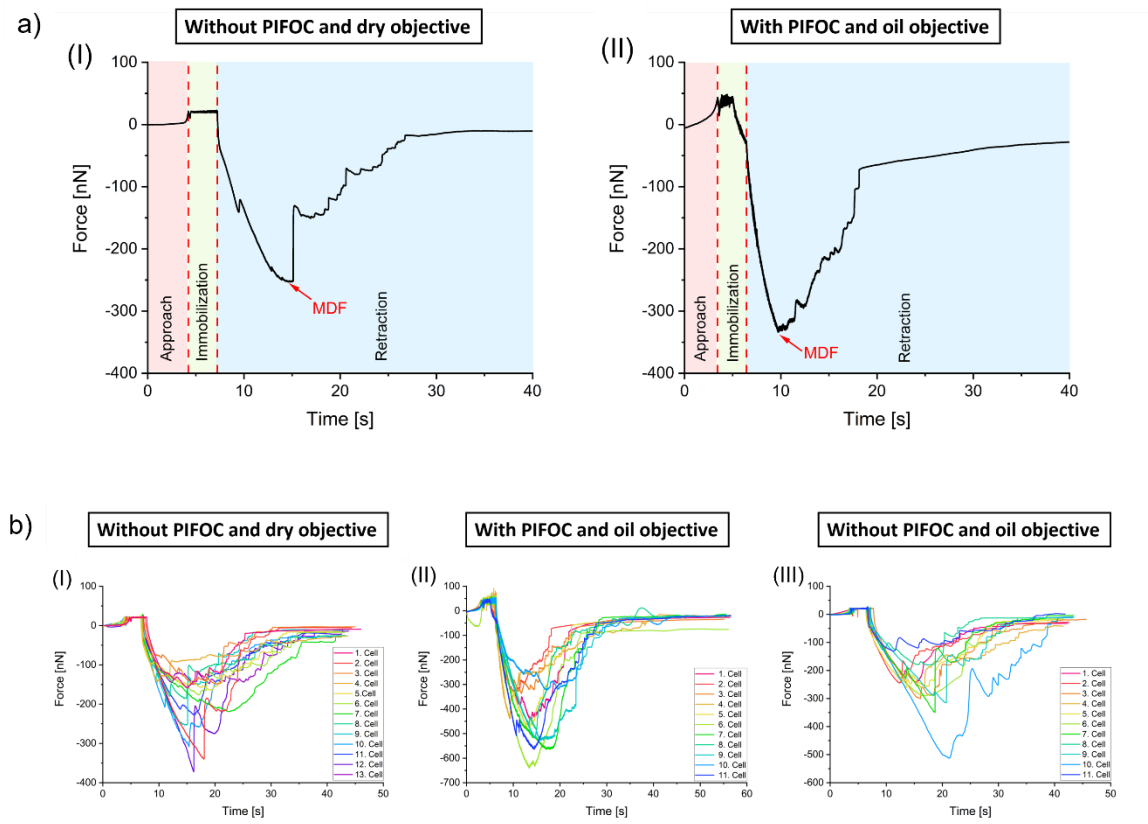

Figure 20: Exemplary FD-curves of detached REF52 cells using the conventional FluidFM® and the optimized FL-FluidFM® hardware. All experiments were recorded under brightfield illumination. (a) Both measurements show the typical force progression of approach, immobilization, and retraction as well as a maximum detachment force (MDF) at the highest point of force followed by several force-steps. (I) Exemplary force-curve of a detached REF52 cell, which was recorded with the standard FluidFM® device. (II) Force-curve of a cell that was detached from a substrate using the correlated FL-FluidFM® device. (b) Totality of detached REF52 cells using the conventional FluidFM® system (I), the correlated FL-FluidFM® device (II), and the correlated one but without the PIFOC, respectively (III). All curves reveal the typical way of cellular detachment, even though each cell shows an individual MDF, numbers of detachment steps and overall time of separation. (I) n = 13 REF52 cells were detached showing a MDF of (-219 ± 77) nN on average. (II) n = 11 REF52 cells were detached, revealing an overall higher MDF of (-467 ± 105) nN while the difference in the number of unbinding steps and needed time for detachment remains. (III) Force-curves of n = 11 REF52 cells presenting a mean MDF of (-281 ± 98) nN. Also in this case, the number of steps and the time of separation differs between the individual cells. Reproduced and adapted from reference[261], distributed as open-access article under the license of a Creative Commons Attribution (CC BY-NC 4.0).

To further analyze a possible effect of the setup adjustment, additional measurements were carried out only with an oil objective and without the PIFOC system (**Figure 20b (III)**). Here, the average MDF was with (-281 ± 98) nN in the same range of the one measured with the standard

FluidFM® device, clearly indicating that the high-numerical objective cannot be the reason for the deviation in MDFs. In addition, contemplating the already mentioned and well-established use of PIFOC and immersion oil objective in AFM and correlative microscopy, an impact on the quality of FluidFM® performance is very unlikely.[164,169,299-301] Nevertheless, there are other effects that should be taken into account as influencing factors such as the cantilever and its characteristic parameters as illustrated in the following chapter.

3.4.2 Cantilever properties as influencing factors

Due to the most likely exclusion of PIFOC and high-numerical objective as a possible source for the discrepancy in MDFs, the cantilever, and its properties as direct link to the measured forces have to be considered as interfering factors as well. The importance and influence of this parameters on the accuracy of force spectroscopy are already well-known in the research field of conventional AFM.[302,303] Nagy *et al*. (2019), however, recently discussed this issue in the context of FluidFM® by discussing the effect of micropipette cantilever spring constant and deflection sensitivity on the reliability of force spectroscopy data.[304] Here, they revealed that the standard error of already published SCFS data ranged from 11.8% to even 50%. These deviations are often explained via biological diversity but referring to Nagy *et al*. the cantilever calibration and even more the characteristics of aperture size, the underlaying substrate, and the position of the laser spot are crucial factors for the accuracy of calibration and, therefore, for force spectroscopy data.[304] Finally, they stated that especially the latter aspect is the most important one, significantly influencing the calibration accuracy of cantilever sensitivity and spring constant. Moreover, they reported that the most reliable spring constant values can be reached by positioning the laser spot on the first pair of cantilever pillars.[304] Nevertheless, the intrinsic fluctuation between different cantilevers cannot be prevented. Consequently, there are many parameters that can have an influence on the results of force spectroscopy.

In this context, a discrepancy between the measured MDFs which are illustrated in **Figure 21** is not surprising. Even though all experiments were performed with the same cantilever type and calibration method and almost equal laser spot positions, depending on the respective laser intensity, the use of two different cantilevers resulted in a significant parameter variation after calibration. Especially the calibrated spring constants k_{Calib} of the used cantilevers showed with 1.25 N m^{-1} and 2.55 N m^{-1} a remarkable difference, while the calibrated deflection sensitivities δ_{Calib} (without PIFOC: δ_{Calib} = 8.56 x 10^{-8} m V^{-1}, with PIFOC: δ_{Calib} = 8.31 x 10^{-8} m V^{-1}) were in the same order of magnitude. Considering the mathematical proportionality between the force and different cantilever parameters (**Equation 1**), it is very likely that the high difference in cantilever

stiffness is responsible for the discrepancy between the mean MDFs instead of the implementation of PIFOC or oil objective. This becomes especially clear, when comparing the respective MDF distributions with the corresponding spring constants as illustrated in **Figure 21**.

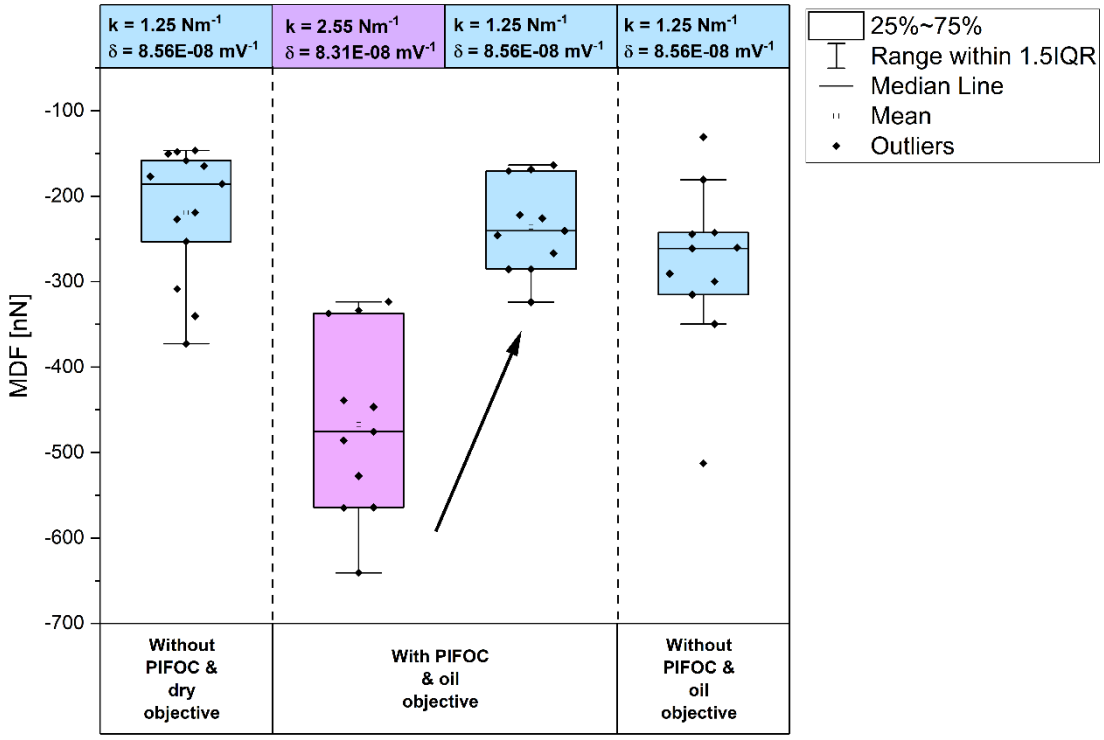

Figure 21: Comparison of the MDF depending on the different hardware configurations and cantilever parameters. The outer left and right box-plots show the force distribution of forces measured with the same cantilever (blue) and without PIFOC and dry objective (left) or oil objective (right). The two box-plots in the middle are based on the same raw data recorded with PIFOC and oil objective. Here, the purple box-plot indicates the force distribution recorded with the originally used cantilever, while the blue box-plot shows the force values calculated with the same cantilever parameters as used in the measurements without PIFOC. A comparison of these two box-plots reveals a noticeable shift towards lower forces demonstrating a strong dependence between detachment forces and cantilever parameters. Reproduced and adapted from reference[261], distributed as open-access article under the license of a Creative Commons Attribution (CC BY-NC 4.0).

Here, it is noticeable that low MDFs as in the case of "Without PIFOC and dry objective" and "Without PIFOC and oil objective" were both performed with the same cantilever of low spring constant. In contrast, the high MDFs which were quantified with the optimized FL-FluidFM® system (**Figure 21**: purple box-plot) were based on the cantilever whose calibrated spring constant was twice as high, yielding to overall much higher forces. Moreover, by comparing the original MDFs recorded with PIFOC (purple box-plot) with the ones calculated with the cantilever parameters used for the measurements without PIFOC, a clear shift towards lower forces is visible (**Figure 21**, "With PIFOC and oil objective", blue box-plot). Here, the average MDF of

(-236.15 ± 52.96) nN is in the same range as the ones without PIFOC. Therefore, it can be stated that neither the modification of the device nor the biological diversity of the cells is the decisive factor for the overall increase in MDF after setup optimization. Moreover, it can be concluded that the integration of PIFOC and oil objective allowed a real-time optical tracking of cellular detachment with extraordinary focus stability and high optical resolution for the first time.

3.5 Integration of fluorescence illumination for the visualization of cellular components during cell detachment

After the successful implementation of PIFOC and high-numerical objective, the next step in establishing a correlated FL-FluidFM® setup was the concurrent fluorescent visualization of cellular insights. For this purpose, fluorescence illumination was integrated into the experimental procedure. Furthermore, REF52 cells stably expressing paxillin-YFP as one of the well-known FA proteins[85,205,209], were additionally transiently transfected with LifeAct-mCherry to fluorescently label the F-actin cytoskeleton. This was followed by the performance of proof-of-principle experiments that, together with the high focus stability, demonstrated the successful feasibility of real-time optical tracking of an entire cell detachment process under fluorescence illumination (**Figure 22**).

Figure 22a shows an example of a dual-fluorescently labeled cell under brightfield illumination, well-aligned towards the cantilever. The fluorescently labeled paxillin (**Figure 22b**) and F-actin filaments (**Figure 22c**) are illustrated in green and orange signals, respectively. In addition, the overlay image (**Figure 22d**) demonstrates a spread cell morphology with paxillin allocated at the ends of elongated actin filaments. This is consistent with the study of Kanchanawong *et al*. (2010) who presented a 3D nanoscale architecture of FAs using SR-FL.[209] However, it has to be mentioned that although fluorescence images were recorded using dual-fluorescence illumination, the correlated acquisition of FL-FluidFM® data involved some challenges. As previously stated (**Chapter 2.3**), the coincidence of cantilever and fluorescence excitation light can cause disturbances in data acquisition, both in FL and force-curve acquisition. This was also the case in the present study which had to deal with both cantilever oscillation and cantilever luminescence. Referring to the latter one, especially the excitation light of paxillin (475 nm) provoked a pronounced cantilever autoluminescence overlapping the green paxillin signal and, therefore, hindering a removal by spectral filtering (**Figure 22b** and **d**). This is consistent with the study of Kassies *et al.* (2005) who determined high photoluminescence for cantilevers made of Si_3N_4.[164] The illumination with 555 nm, however, did not trigger any cantilever luminescence, enabling a detailed visualization of intracellular F-actin filaments (**Figure 22c**). This, in turn, contrasts with

the research of Lulevich *et al.* (2005).[305] They used a commercial Si_3N_4 AFM probe as a light source by illuminating it with either 488 nm or 532 nm wavelength, both causing photoluminescence. They further suggested that dangling bonds or photoluminescent Si nanocrystals within the Si_3N_4 could be the reason for the arising photoluminescence of Si_3N_4 cantilevers.[305] However, this is countered by Kistner etal. (2011), who identified the Si_3N_4 itself as responsible for the photoluminescence.[306]

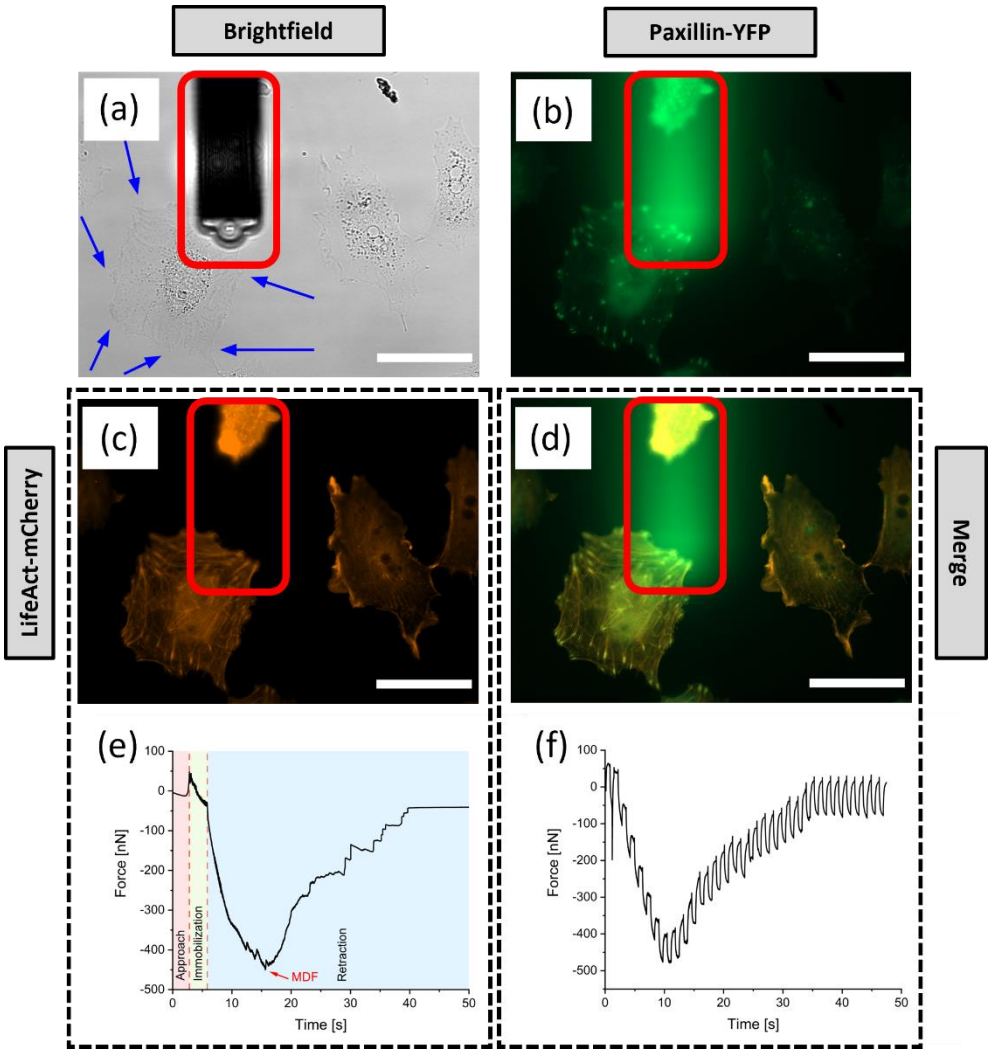

Figure 22: Integration of fluorescence illumination into the correlated data acquisition using FL-FluidFM®. (a) A REF52 cell stably expressing paxillin-YFP and transiently transfected with LifeAct-mCherry (F-actin) is visualized with brightfield illumination. The position of the cantilever is marked with a red square. The blue arrows point to the edge of the target cell. (b) The fluorescence image reveals green, fluorescent paxillin signal but also strong cantilever luminescence. (c) The fluorescence image of the cell shows no detectable cantilever autoluminescence but clearly visible F-actin filaments, illustrated with orange signal. (d) The dual-fluorescence image of the REF52 cell demonstrates the overlay signal of paxillin-YFP and LifeAct-mCherry. The green autoluminescence of the cantilever is clearly visible in this case. (e) The force-curve that was recorded simultaneously to the F-actin visualization is separated into the typical sections of approach, immobilization, and retraction and shows no obvious disturbance due to spurious cantilever bending. (f) The force-curve acquired under dual-fluorescence illumination exposes a strong sinusoidal signal overlaying the whole detachment process. Scale bar: 50 µm. Reproduced and adapted from reference[261], distributed as open-access article under the license of a Creative Commons Attribution (CC BY-NC 4.0).

To further investigate these effects, supplementary experiments were performed testing 385 nm and 630 nm as additional excitation wavelengths in the FL-FluidFM® setup. **Figure 23** views the effect of cantilever luminescence depending on the wavelength. While **Figure 23a** shows the cantilever under brightfield illumination, **Figure 23b** and **c** reveal the corresponding cantilever luminescence with an excitation light intensity of 50% and 100%, respectively. Analogous to the irradiation with 555 nm, a wavelength of 630 nm did not expose any photoluminescence for both intensities. The use of an excitation light in the range of UV light, however, revealed an even stronger effect compared to 475 nm wavelength, further increasing with 100% intensity. This behavior could induce the assumption that the effect of cantilever luminescence increases with decreasing wavelength. However, this contrasts with the already mentioned study of Kassies *et al.* (2005) who demonstrated their photoluminescence via an irradiation wavelength of 800 nm.[164] Summarized, this phenomenon is not yet fully understood and still needs some further research, which is beyond the scope of this thesis.

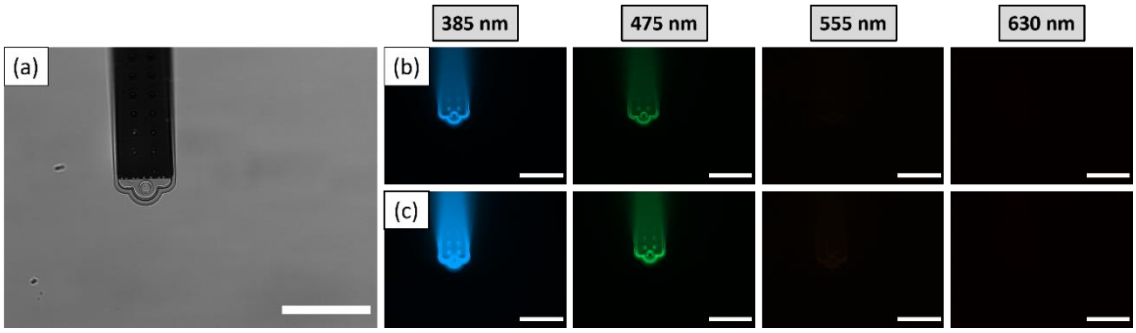

Figure 23: Cantilever luminescence depending on the wavelength of excitation light. (a) Brightfield image of a cantilever. (b) and (c) both show fluorescence images recorded with illumination light of 385 nm, 475 nm, 555 nm, and 630 nm wavelength with light intensities of 50% (b) or 100% (c) and an exposure time of 500 ms. In both cases the cantilever reveals clear photoluminescence for wavelengths of 385 nm and 475 nm, further increasing with higher light intensity. In contrast, no autoluminescence is visible, when using an excitation light of 555 nm or 630 nm wavelength. Scale bar: 50 µm. Reproduced from reference[261], distributed as open-access article under the license of a Creative Commons Attribution (CC BY-NC 4.0).

In the context of cantilever oscillation, the use of green excitation light (555 nm) represented also in this case the most suitable option. As illustrated in **Figure 22e**, the simultaneous fluorescence visualization and force quantification revealed no interference signal indicating a spurious cantilever bending. Moreover, analogous to the curves recorded with brightfield illumination (**Figure 20a**, **Chapter 3.4.1**), this graph exhibits the already described typical force progression of a cellular de-adhesion with a MDF in the same order of magnitude as described in **Chapter 3.4.1** ((-450 ± 136) nN). However, the dual-excitation light irradiation of a cell detachment experiment resulted in a sinusoidal signal overlapping the entire force-curve and, thus, making the analysis of cellular unbinding events impossible (**Figure 22f**). This is not surprising when referring to Friedrichs

et al. who already claimed in 2013 that the simultaneous collection of force-data and fluorescence images is impossible in most cases due to fluorescence light induced cantilever bending.[38] Furthermore, Cazaux *et al.* (2015) revealed a correlation between the material cantilever composition and the wavelength and intensity of the used excitation light, resulting in an AFM/fluorescence signal coupling.[37] They determined a stronger reaction for gold-coated than for uncoated cantilevers, with a wavelength of 470 nm in particular causing a striking cantilever deflection. In relation to the results of the present study, this could be an explanation for the pronounced cantilever oscillation that occurred under the dual-channel illumination (**Figure 22f**), where 475 nm and 555 nm were switched on and off alternately. However, in addition to the correlated FL-FluidFM® data recorded with 555 nm wavelength solely (**Figure 22e**), also the supplementary single-channel illumination using 475 nm revealed not even a hint of interference (**Figure 24**). Moreover, the force-curve shows the characteristic sections of cellular detachment with a MDF of (-305 ± 60) nN, which is in the same order of magnitude as the ones mentioned before (**Chapter 3.4.1**). Therefore, it can be suggested that the triggering factor causing cantilever oscillation is more the switching of the two channels than the beams themselves. Nevertheless, to precisely determine the cause of the sinusoidal signal, a systematic investigation of experimental parameters like excitation wavelength, exposure time, or intensity are necessary but beyond the scope of this thesis.

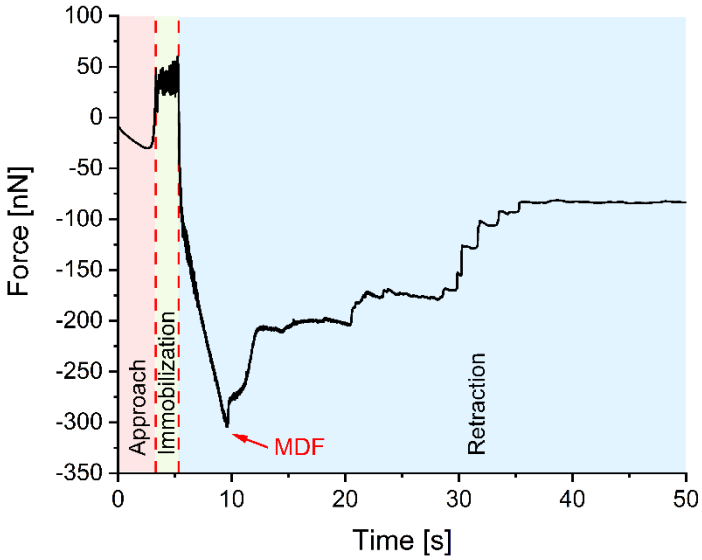

Figure 24: Force-curve of a REF52 cell using FL-FluidFM® with an excitation light of 475 nm wavelength. The force-curve consists of all typical force-patterns, including approach, cellular immobilization, and retraction with characteristic force-jumps, indicating the cellular unbinding. Throughout the entire measurement, there is no spurious signal visible which could be referred to an excitation light-induced cantilever oscillation or bending. Reproduced and adapted from reference[261], distributed as open-access article under the license of a Creative Commons Attribution (CC BY-NC 4.0).

Consequently, all correlated FL-FluidFM® experiments were performed using only the orange fluorescence signal ensuring a high-quality visualization and quantification of cell detachment processes at the same time. In this way, finally, the simultaneous fluorescence illumination was successfully integrated into the whole cellular detachment process without negatively affecting the data quality of force-curves.

3.6 Correlated analysis of FluidFM® data

To achieve a correlated and reliable data analysis, the highly synchronous performance of FL and FluidFM® represented an important role. Due to the complexity of time-dependent correspondence between two separated methods, many multifunctional devices, so far, perform their measurements in a sequential manner and superimpose their data afterwards.[35,165] While this has the advantage that a synchronized performance is not necessary, it also has the disadvantage that possible biological processes or cellular changes, occurring in the meantime, cannot be captured. By contrast, in the present study, a real concurrent performance of two technologies was achieved by manually starting both measurements at the same time and, therefore, providing complementary information about cell adhesion forces and their biomechanics at once. Similar to Selhuber-Unkel *et al.* (2010)[85], who combined AFM with FL to investigate the intermolecular spacing of integrin during cell detachment, this study allowed the analysis of the de-adhesion process by optically tracking the unbinding of F-actin filaments, which represent a direct link to focal contacts (**Chapter 2.4.2**).[209,307] The correlated analysis of this data was focused on the achievement of a precise matching between force-steps and visible unbinding events within a cell.

Figure 25a shows an exemplary force-curve of a detached REF52 cell. Here, each visible force-jump was marked by a linear fit, shown by purple lines. To consider a possible delay between the two independent software, the last detachment step was determined as a reference point. This step could be clearly identified in both force-curve and corresponding time-series, guaranteeing a consistent starting point for data correlation. Even though this evaluation method is a proof-of-principle study, a precise step-matching was feasible by comparing the time points of force-jumps with the moment of visible cellular unbinding. The number of force-steps, which could be attributed to certain unbinding events within an optically tracked cell, is displayed in **Figure 25b**. Here, all identified steps are highlighted with purple lines. The corresponding fluorescence image of the cell showing each identified spot of intracellular unbinding (arrow 1-20) is illustrated in **Figure 25c**. To further demonstrate the observed detachment process, a step-by-step image composition is shown in **Figure 25d**, highlighting the individual unbinding

spots of actin filaments with arrows. This time-resolved process shows the movement of the cytoskeleton during the detachment process that initially starts in the middle of the cell body (step 1-10). Then, the cytoskeletal unbinding spreads from the inside to the outside, until there is only a contact between cellular edge and surface (step 11-20). After complete separation of the cell, there is no further detectable fluorescence signal in the focus level.

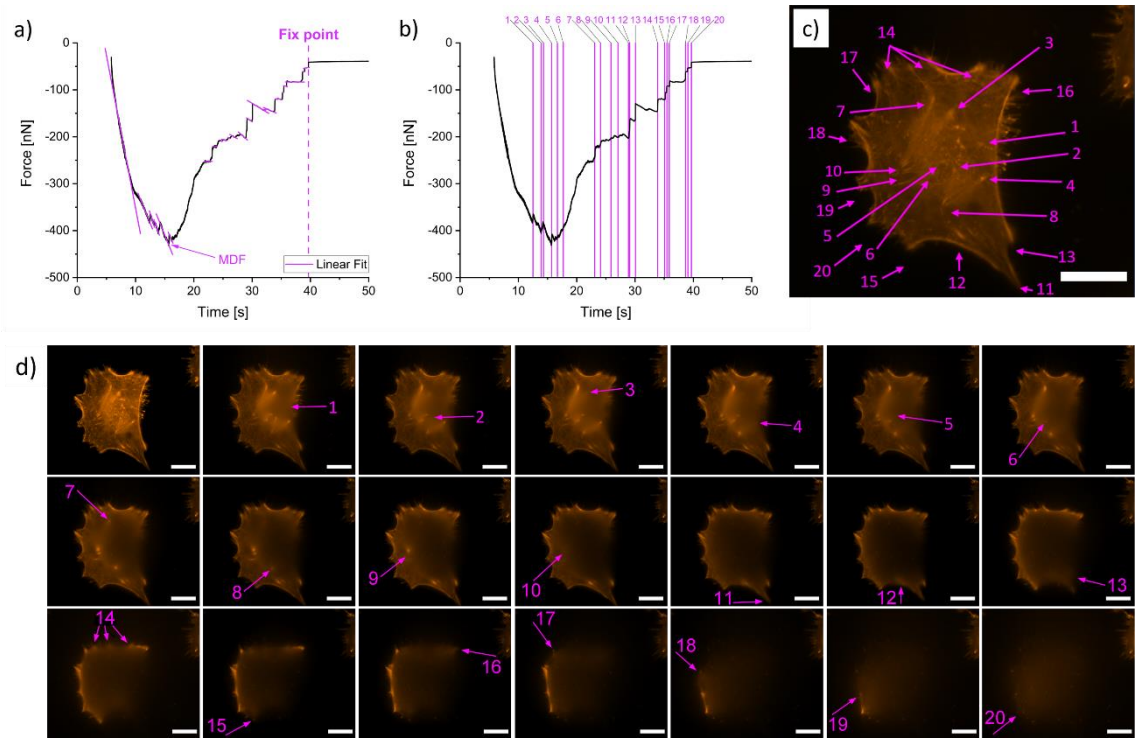

Figure 25: Correlated data analysis of an exemplary detachment experiment in which the unbinding process of a REF52 cell was performed using correlated FL-FluidFM® technology. (a) The exemplary force-curve shows linear fits of single force-jumps, which were marked with purple lines. The last force step serves as a fixed reference point (purple dashed line). (b) The purple lines sign each force-jump that could be attributed to a certain unbinding event visible in the corresponding fluorescence time-series (c and d) of the detachment process. (c) The corresponding spots of cellular unbinding are marked with purple arrows and the matching number. (d) A step-by-step image composition of the time-series recorded during the detachment process showing the position of the 20 identified unbinding events in (c). Scale bar: 20 µm. Reproduced from reference[261], distributed as open-access article under the license of a Creative Commons Attribution (CC BY-NC 4.0).

Comparing this described procedure of cellular de-adhesion with the fitted force-steps shown in **Figure 25a**, a correlation of the area of filamentous unbinding and force-jumps could be assumed. After starting the detachment process, the force rapidly increased until the MDF was reached within a few seconds. This could be referred to as a cellular stretching of the area around the nucleus, where the cell is immobilized and sucked onto the cantilever aperture. This is consistent with the study of Cohen *et al.* (2017)[42] which stated that the MDF generally appears at a short separation distance between cell and a substrate. Analogous to the investigation of Friedrichs *et al.* (2013)[38], this study demonstrated a time-dependent shrinkage of the cellular contact area

until only the cell edge is in contact with the surface (**Figure 25d**). Moreover, the exemplary force-curve, illustrated in **Figure 25a**, revealed a high number of discrete force-steps. A distinction can be made between two different types of steps: (a) the so-called jumps/rupture events ('j' events) and (b) the tether events ('t' events). Whereas 'j' events are characterized by a preceding ramp-like increase in force, force-plateaus prior a step are visible, when pulling a tether.[73,74] The latter predominantly appears in the final phase of a detachment process, when membrane-nanotubes (tether) are extracted out of the cellular cortex.[74] On the other hand, 'j' events mostly occur after exceeding the MDF. They represent the intracellular rupture of adhesive bonds that remain anchored to the cytoskeleton.[38,74] These two concepts of cellular unbinding could also be observed in the present study, showing 'j' events in the middle as well as force-plateaus at the end of a force-curve. Furthermore, this observation was also supported by an asymptotical change of slope distribution of linearly fitted detachment steps, as exemplary illustrated for analyzed force-curves in **Figure 26**.

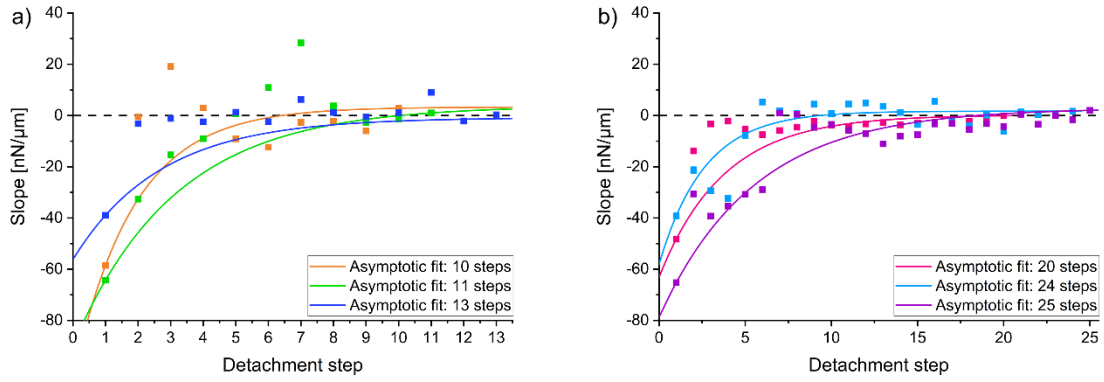

Figure 26: Dependence between slope distribution and detachment steps during a cellular de-adhesion using FL-FluidFM® technology. (a) and (b) illustrate the slope-detachment step dependence of three exemplary REF52 cells each showing 10, 11, and 13 (a) as well as 20, 24, and 25 detachment steps (b), respectively. Each slope distribution represents the totality of slopes of linearly fitted detachment steps within a force-curve. The respective course of the slope distributions was asymptotically approximated. Regardless the number of detachment steps, (a) and (b) show high negative slopes at the beginning of a detachment process, followed by a decline that settles around zero at the end. Reproduced and adapted from reference[261], distributed as open-access article under the license of a Creative Commons Attribution (CC BY-NC 4.0).

Regardless the number of detachment steps within a cellular de-adhesion, the highest degree of slope was visible at the beginning of a detachment process, indicating the appearance of rupture events. This was followed by a decline that settled around zero at the end, representing the force-plateaus of 't' events. Besides this force-curve analysis, the presented study also confirmed the linkage between the type of force-step and the region of cellular unbinding by visualizing the transition from a full body contact zone to a contact zone where the cell membrane is connected

to the surface exclusively (**Figure 25d**). Moreover, the specific optical tracking of fluorescently labeled F-actin filaments enabled the correlation of a high number of discrete force-steps with the corresponding spots of cellular unbinding, for the first time.

3.7 Cell-cell adhesion

3.7.1 Cell-cell versus cell-matrix adhesion

Due to its contribution in a variety of physiological processes such as embryogenesis and malignancy, intercellular cohesion represents an emerging field of research.[4,40,219] So far, there are several studies focusing on the quantitative analysis of adhesion forces or the visualization of cell-cell contacts and their proteins.[4,29,73,308,309] For instance, the process of endothelial-to-mesenchymal transition, which is engaged in cardiovascular development and disease, was characterized by a decrease of mature intercellular adhesion forces accompanied by a cellular flattening and stiffening.[40] Furthermore, Bertocchi *et al*. (2017) brought light to the macromolecular complexity of cell adhesion by presenting a multi-compartment nanoscale architecture of cadherin-based cell-cell contacts.[29]

To achieve a deeper understanding of specific cell-cell junctions and their molecular mechanism under stress, the correlated FL-FluidFM® technology offers an advanced approach. By using its optimized optical features, distinctions between endothelial cell-cell adhesion and cell-substrate adhesion mediated by REF52 cells could be analyzed. For this purpose, immortalized human umbilical vein endothelial cells (HUVECs) were cultured to form intercellular contacts and subsequently investigated via SCFS. **Figure 27a** shows an exemplary cell under brightfield illumination contacting two neighboring cells which is marked with two purple lines. The corresponding force-curve is illustrated in **Figure 27b**. Analogously to the exemplary force-curve recorded with a REF52 cell (**Chapter 3.6**, **Figure 25a**), this retraction-curve shows the typical way of cellular detachment. After surpassing the MDF, the force decreases and reveals a high number of detachment steps until full cellular separation. In total, 60 force jumps could be linearly fitted (**Figure 27b**, purple lines) and 31 of these successfully associated with visible unbinding events (**Figure 27c**, vertical purple lines). Nevertheless, the time-dependent data correlation of HUVECs was more challenging than the one of REF52 cells. This was mainly due to a very smooth force progression and closely spaced step transitions which is also indicated by the slope distribution shown in **Figure 27d**. Analogously to REF52 cells, the asymptotic fit reveals the typical shift from high to low slopes. However, while 't' events with a force plateau around zero are evidently visible within the last 20 steps, 'j' events with a preceded linear increase in force are less obvious. With exception of the first detachment step, most of the following 40 slopes are settled in a small range

between -20 and +20 nN µm^{-1} which results in a prompt and significant decline of the asymptotic fit. Compared to the high slopes of -80 to -20 nN µm^{-1}, which evidently imply the occurrence of 'j' events after surpassing the MDF of REF52 cells (**Chapter 3.6, Figure 26**), this slope distribution proposes less pronounced 'j' events. Moreover, it indicates that HUVECs provide only weak adhesive bonds that are connected to the cellular cortex. This could be attributed to the bonding behavior of slip-bonds, which are characterized by a rapid bond yielding under high force load.[78,244]

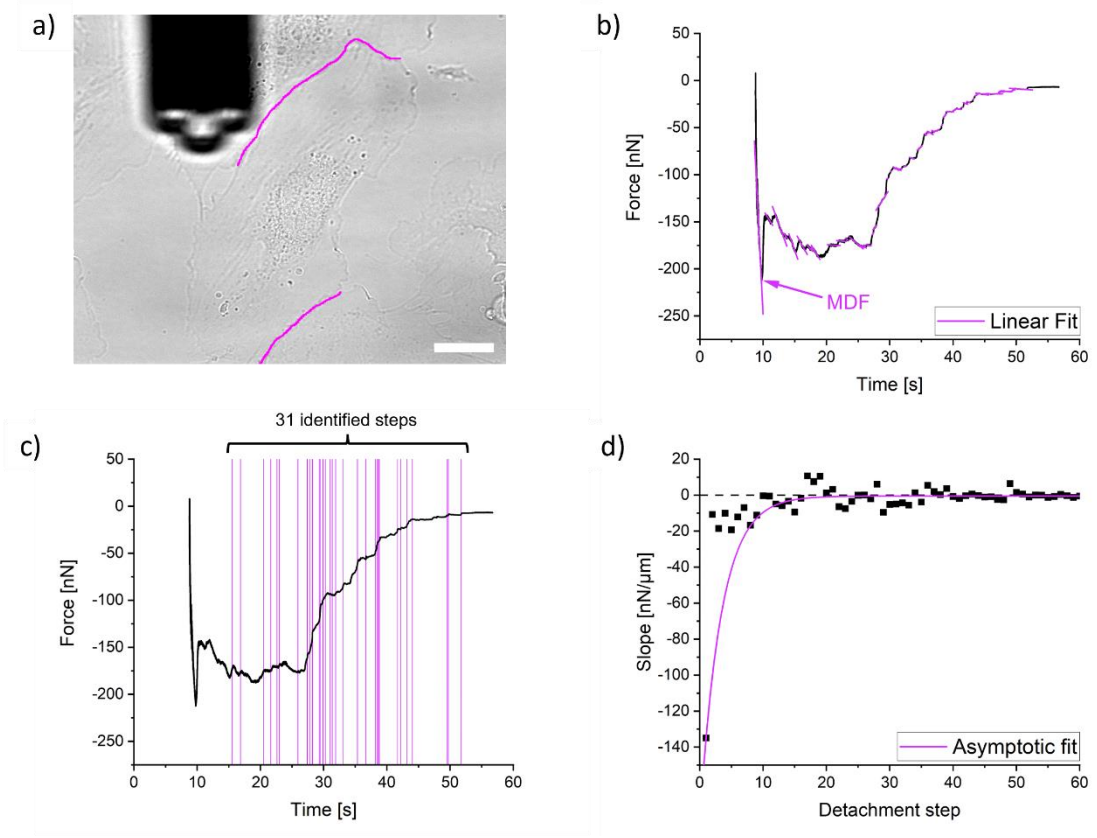

Figure 27: Exemplary FL-FluidFM®-based SCFS of a human umbilical vein endothelial cell (HUVEC) in cell-cell contact. (a) An exemplary HUVEC is visualized with brightfield illumination. The two purple lines indicate the interfaces with neighboring cells. (b) The corresponding force-curve shows the typical way of cellular detachment, including MDF and several detachment steps which are linearly fitted by purple lines. The vertical purple lines in (c) mark 31 identified force jumps which could be matched with a visualized unbinding step. (d) The dependence of slope and detachment steps is composed of 60 black squares, each representing the slope of one linear fit of a detachment step, and an asymptotical fit, showing the characteristic shift from high to low slopes. Scale bar: 20 µm.

However, this contrasts with the fact that endothelial cells are intended for the inner lining of blood vessels and, therefore, develop strong cohesive cellular sheets.[310-312] HUVECs, in particular, have been identified to form intercellular AJs that ensure a strong mechanical coupling between adjacent cells.[313] Here, the cadherin-catenin-actin complex usually forms a catch-bond under force load and ensures the maintenance of tissues.[246,314,315] In addition, Panorchan *et al.* (2006) demonstrated that the bonding of classical type II vein endothelial (VE)-cadherins in HUVECs is

less sensitive to rupture and entails a higher tensile strength than bonds, which are based on classical type I cadherins such as E-, or N-cadherins.[316] Consequently, the retraction-curve of a HUVEC cell was expected to show more pronounced force jumps, especially at the interface between adjacent cells.

However, this unexpected detachment behavior is not an isolated case of the exemplary cell, but rather a collective phenomenon of all studied HUVECs. As illustrated in **Figure 28**, the totality of HUVECs shows a separation process that is characterized by a stretchy and almost 'silky' unbinding with smooth force transitions. This is further accompanied by a long mean separation time of about 38 s, which is evidently longer than the 28 s of REF52 cells (**Chapter 3.4.1**, **Figure 20b (II)**). The respective mean MDFs are with (-418 ± 149) nN for HUVECs and (-467 ± 106) nN) for REF52 cells in the same order of magnitude. This is surprising, since according to Sancho *et al.* (2017), cohesion forces are composed of two forces, one from the cell-matrix interaction and one from the cell-cell contacts, usually resulting in an overall higher force compared to single cells.[40] Consequently, HUVECs with cell-cell contacts were expected to reveal a significantly higher MDF than individual REF52 cells, only expressing cell-substrate adhesion. Lastly, these findings indicate that the cell adhesion of the investigated HUVECs, including the formation of cell-cell contacts and FAs, was not working properly. This is further investigated in the **Chapters 3.7.2** and **3.7.3**.

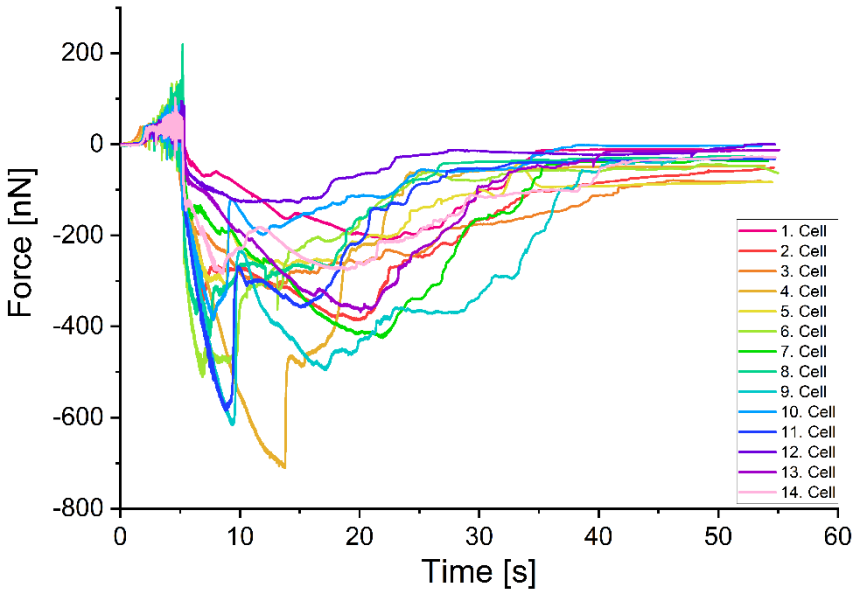

Figure 28: Totality of detached HUVECs. The force-curves of n = 14 HUVECs show the typical way of cellular detachment including, approach, immobilization pause, and retraction. The latter one is characterized by an overall very smooth force progression with closely spaced step transitions, a high number of detachment steps, and a long duration time until complete separation. However, the exact number of unbinding events, MDF, and detachment time differs between the individual cells.

3.7.2 HUVECs – single cells versus cell-cell contacts

To further investigate the detachment behavior of HUVECs, the adhesion forces of both single HUVECs and ones with cell-cell contacts were compared. Moreover, by applying two different retraction speeds, 2 µm s^{-1} (v2) and 5 µm s^{-1} (v5), the cellular unbinding at different force loads could be analyzed. As illustrated in **Figure 29a**, regardless of the retraction speed or type of cellular contact, all exemplary force-curves show the characteristic force progression of cellular separation. At the beginning, the force rapidly increases until the MDF is reached. This is followed by a force decrease, which contains several detachment steps linearly fitted with purple lines. However, the period of complete separation differed. While a retraction velocity of 2 µm s^{-1} needed 30 s to almost 50 s, the higher velocity of 5 µm s^{-1} reduced the time of cellular detachment to 15 s to 20 s. This phenomenon can be referred to the rising force load, which generally increases with higher retraction speed.[317] This force load, in turn, is responsible for the binding and dissociation rate of adhesive bonds.[74,78] More precisely, a force stressing an adhesive bond inclines with rising distance until the bond breaks.[78,317] This would be usually balanced by the intracellular recruitment of new bonds or by the redistribution of the applied force load to other bonds. However, if the externally applied force exceeds these intrinsic mechanisms, the cell will be detached at a higher rate.[74,315,317]

A speed-dependent difference was also observed in the slope distributions shown in **Figure 29b**. Although all asymptotic fits revealed the typical shift from high to low slopes, the lower tempo of retraction entailed a slope distribution that was predominantly located between -30 nN $µm^{-1}$ and +20 nN $µm^{-1}$, excluding the first detachment step. Analogously to the force-curve presented in **Chapter 3.7.1**, this indicates a smooth force progression and, thus, a 'slipping' de-adhesion process. A velocity of 5 µm s^{-1}, by contrast, showed slopes that even exceeded -100 nN $µm^{-1}$ which clearly implies the presence of pronounced 'j' events and, thus, a stronger adhesive bonding with the cortical cytoskeleton.[38,78,317] In addition, since the magnitude of 'j' events reflects the stochastic bond survival, this higher resistance towards increasing mechanical stress could be attributed to the formation of molecular catch-bonds.[38,74,243,245,318] However, this contrasts with the overall reduced lifetime of the cell adhesion which rather implies a bonding mechanism of slip-bonds.[74,245] Moreover, by comparing the respective totality of detached cells (**Figure 29c**), it is obvious that regardless of the retraction speed and after passing the MDF, their force progressions are predominantly characterized by smooth step transitions indicating a fast bond yielding. Nevertheless, considering that also catch-bonds could be overpowered by sufficient high force load, a retraction speed of 5 µm s^{-1} might exceed the critical force and consequently cause a rapid cellular detachment.[314,318] Hence, for a more detailed analysis of the molecular bonding behavior

of HUVECs, a systematic investigation under successive increasing tensile stress would be advisable.

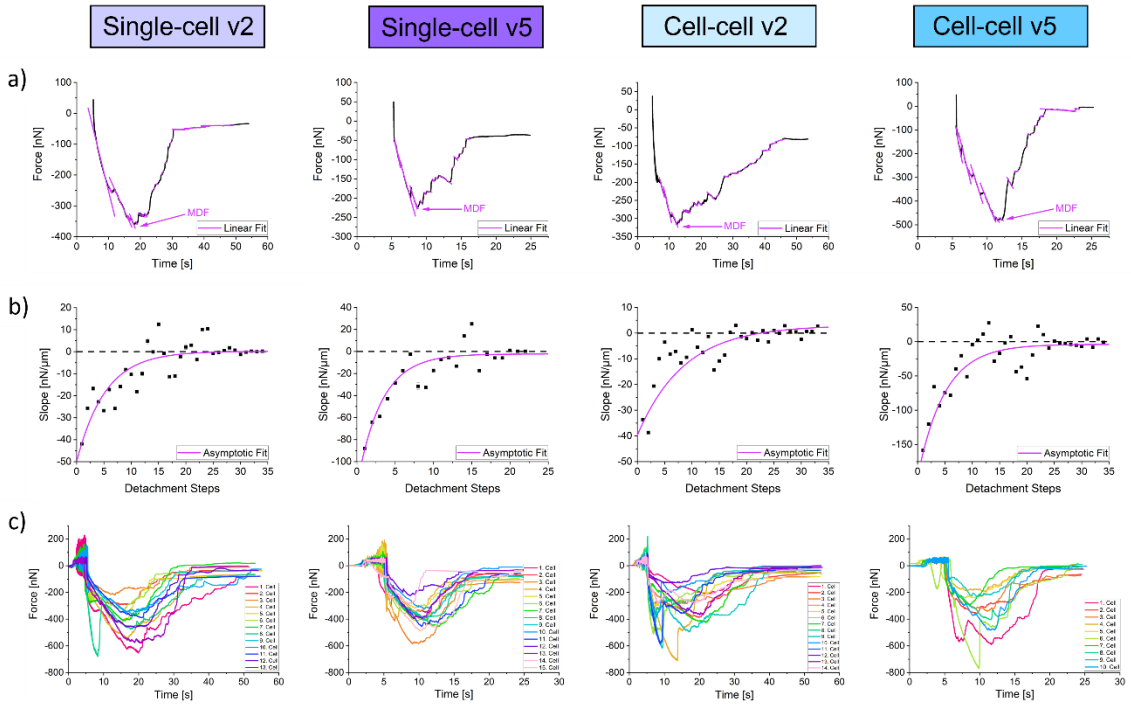

Figure 29: Comparison of speed-dependent adhesion forces measured with single HUVECs or under cell-cell contact. The purple and blue colored titles mark the experiments conducted with single or contacting cells, respectively. The lighter shade indicates in both cases a retraction speed of 2 µm s^{-1} (v2), while the darker one marks a velocity of 5 µm s^{-1} (v5). (a) Each experimental condition is represented by an exemplary force-curve that shows the MDF and several detachment steps which are linearly fitted with purple lines. (b) The corresponding slope distributions show the dependence between the slopes of linearly fitted force transitions in (a) and the associated detachment step. All progressions are asymptotically fitted and reveal a shift from high to low slopes that settle around zero. (c) The force-curves of the totality of cells for each experimental condition show a force progression that is dominated by smooth step transitions, especially after passing the MDF. The 'single cell v2' condition is based on n = 13 cells, while the higher speed is represented by n = 15 cells ('single cell v5'). In case of cell-cell contacts, the totality of cells is based on n = 14 and n = 10 cells, for a velocity of 2 µm s^{-1} and 5 µm s^{-1}, respectively.

Apart from the speed-dependent unbinding mechanisms, there is also a MDF related discrepancy between the detachment of single and adjacent HUVECs. As already mentioned in the previous **Chapter 3.7.1**, the adhesion force of cells expressing cell-cell junctions is expected to be higher than the one of cells, only expressing cell-substrate adhesion.[40] However, this expectation was already not fulfilled comparing HUVECs with REF52 cells, and becomes even more unlikely comparing single with interconnected HUVECs. As illustrated in **Figure 30**, the MDF distributions are for both bonding types in the same order of magnitude. More precisely, when comparing the mean MDFs of cells detached with 2 µm s^{-1}, it is noticeable that they are with (-439 ± 140) nN for single cells (light purple box-plot) and (-418 ± 149) nN for intercellular contacts (light blue box-plot) almost identical. The average detachment force of adjacent cells is even slightly smaller.

This can be also observed in the case of 5 µm s^{-1} retraction speed. Here, the mean MDF of individual HUVECs is with (-400 ± 91) nN (dark purple box-plot) a little bit higher than the one of interconnected cells ((-386 ± 171) nN) (dark blue box-plot). This highly contrasts with the study of Sancho *et al*. (2017) that investigated the adhesion forces of human endothelial cells from the umbilical artery (HUAECs).[40] When comparing individual with intercellularly connected HUAECs, they revealed an increase in the mean MDF of nearly 400 nN which clearly fulfills the expectation of rising cell-cell adhesion forces.[40] Moreover, the mean value of 1170 nN for interconnected HUAECs highly exceeds the one of HUVECs measured in this study.[40] However, this apparent discrepancy can be probably referred to the increased tightness of arterial-based intercellular junctions, which have to endure a higher shear stress level during blood flow than the ones of veins.[319,320] Apart from this controversy, the two types of HUVEC-mediated cell adhesion support the hypothesis of slip-bonding behavior once again. As depicted by two black arrows in **Figure 30**, the mean MDFs of cell-substrate and cell-cell adhesion decrease with respect to an increasing retraction velocity, which emphasizes the force-load dependent shortage of bond lifetime.[74]

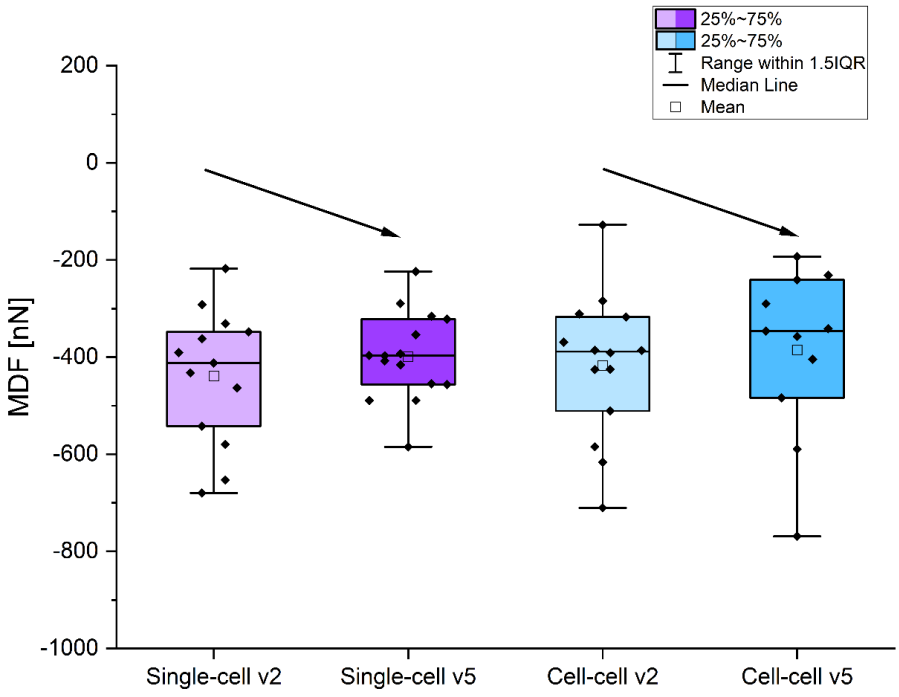

Figure 30: Overview of MDF distributions measured with single or interconnected HUVECs and two different retraction forces, respectively. The two purple box-plots show the MDFs of single HUVECs while the blue ones illustrate the MDF distribution of cell-cell adhesion. The lighter color indicates a retraction speed of 2 µm s^{-1} (v2), while the dark ones represent a speed of 5 µm s^{-1} (v5), respectively. All experimental conditions show a MDF distribution in the same range. However, the transition to a higher retraction velocity reveals a slight decrease in the respective mean MDFs for both adhesion types. This decline is indicated by the two black arrows.

3.7.3 Fluorescent visualization of cell-cell junctions

Apart from the quantitative analysis of adhesion forces, the FL technology has the potential to reveal and visualize insights of the molecular composition of a cell and, thus, provide further information about the unexpected detachment behavior of the investigated HUVECs.[137] Considering their endothelial characteristics, they were expected to show tight cell-cell junctions, especially containing VE-cadherin (cluster of differentiation 144, CD144) as mediator for AJ development.[321,322] To validate the existence of these proteins, confluent HUVECs were fluorescently labeled via immunofluorescence staining and subsequently visualized using conventional FL. Two exemplary fluorescence images of HUVECs, recorded after a cultivation time of three days (3d), are demonstrated in **Figure 31**. Here, the counterstained cellular nucleus and the CD144 protein are illustrated in blue and green signal, respectively. In addition, the platelet endothelial cell adhesion molecule (PECAM-1), also known as cluster of differentiation 31 (CD31), was fluorescently labeled as another intercellular contact marker.[323,324] As a member of the Ig superfamily, CD31 is highly expressed at cell-cell junctions and responsible for both the maintenance of endothelial cell junctional integrity and the fast rebuilding of the vascular barrier after inflammatory disease.[324-326] By comparing both fluorescence images, it is noticeable that the overall fluorescence signal is quite low. While the CD31 signal shows a tendency of junctional signal in the middle of the image, the CD144 marker is mostly located at the nuclear region. Here, only very low fluorescence signal can be observed at the edges of the cells. This highly contrasts with the junctional visualization of other studies, which reveal a defined localization of VE-cadherin at the cellular periphery.[327-329] Consequently, the results of this investigation probably indicate that either the formation of VE-cadherin-based intercellular junctions is barely developed or the CD144 antibody is not working correctly. To validate the functionality of the fluorescent markers, additional experiments were performed using two other endothelial cell types.

Analogously to the HUVECs, primary human brain microvascular endothelial cells (HBMVECs) were immunofluorescently labeled for CD144 and CD31 after three days of cultivation (**Figure 31**). Monolayers of this cell type are generally used for *in vitro* models of the BBB and, thus, represent an excellent example for strong TJ and AJ formation.[330-333] Compared to HUVECs, the fluorescence signal of HBMVECs is not remarkably different (**Figure 31**). Also in this case, the green signal of VE-cadherin mostly overlaps the blue signal of the cellular nucleus. Nevertheless, a slight signal increase is visible at the cellular edges. The staining of CD31, by contrast, shows a low but clear visualization of cellular junctions in the center of the exemplary image. To further confirm the used staining protocol, additional experiments with HBMVECs were accomplished after a prior cultivation time of seven days (7d) (**Figure 31**). Here, a strong signal increase was detectable for

both intercellular junction markers. The development of CD144-mediated cell-cell contacts is visible, even though the CD144 still shows a high signal overlap with the cellular nucleus. In case of the PECAM-1, the interfacing membranes between adjacent cells show a highly specific signal which is consistent with the results of other studies.[334,335]

In addition, an immortalized human vascular endothelial cell line (EA.hy926) was stained with anti-CD144 and anti-CD31 marker after seven days of cultivation (**Figure 31**). Similar to the fluorescence images recorded with HBMVECs, here, the fluorescence signal of both proteins can be evidently recognized, with a slightly higher intensity for PECAM-1. It is further noticeable that for EA.hy926 cells, the VE-cadherin signal is mostly located at the cellular periphery and not at the cellular nucleus. This generally confirms the functionality of the staining protocol. The remaining difference in signal quality between the exemplary cell types can be referred to a needed optimization of the specific staining parameters.

However, besides the optimization of the staining protocol, there are two further aspects which have to be considered: first, the different duration of cellular cultivation and second, the differences of primary and immortalized cells. Comparing the fluorescence signal derived after 3d and 7d, it is obvious that after a longer time of cellular growth, the formation of intercellular junctions is increased. This can be referred to the prolonged contact time of interfacing membranes, which promotes the maturation and tightening of cell-cell junctions.[74,315,336] As previously described (**Chapter 2.4.3**), the junctional assembly is a complex and time consuming process of several decisive steps. In short, after cell spreading and lamellipodia-derived first contacts, which are based on actin-rich membrane protrusions, the protein recruitment of CAMs starts.[195,337] Together with the activation of signaling mechanisms, the formation of nascent cell contacts is initiated and subsequently transformed into mature cell junctions via bond multiplication and actin-derived stabilization.[223,337,338] According to the study of Esfahani *et al.* (2021), this junctional maturation needs at least 16 h.[259] However, due to their focus on only single intercellular junctions within a confined contact zone, a longer duration can be assumed for the complete formation of intercellular junctions of a confluent monolayer. This probably provides an explanation for the lack of junctional formation in HUVECs and, thus, their unpredicted detachment behavior (**Chapter 3.7.1** and **3.7.2**). Furthermore, considering that cell adhesion forces were usually recorded after a cultivation time of only one to two days, this becomes even more evident.

Apart from this, also the discrepancy of immortalized cell lines and primary cells might influence the development of proper cell junctions. Cell lines, in general, entail several advantages such as an easy handling, a nearly unlimited material supply, and a consistent sample reproducibility

which makes them a powerful tool in biological research.[339] However, the choice of immortal cell lines instead of primary cells, also involves some drawbacks. Even though, cell lines should represent the characteristics of primary cells as close as possible, they often reveal deviations.[339] This can be referred to the process of immortalization, which usually includes a genetic manipulation and, thus, the alteration of the original phenotype.[339-341] These differences were already demonstrated in other studies, which compared the use of cell lines and primary cells in terms of immune response and gene expression. In both cases, the immortal cells revealed a significant lack of primary functional features.[342,343] This is consistent with the presented junctional formation of this examination which showed the best results for primary HBMVECs (**Figure 31**). However, considering that HUVECs are probably the best-characterized endothelial cells, their application as *in vitro* model for intercellular adhesion is still justified.[312] For future validations of proper cohesion, the transepithelial/transendothelial electrical resistance (TEER) technology represents a suitable add-on. Since the ohmic resistance across a cellular monolayer is directly related to the formation of robust cell junctions, the TEER represents a non-invasive determination of the junctional integrity of the endothelium and epithelium.[344,345]

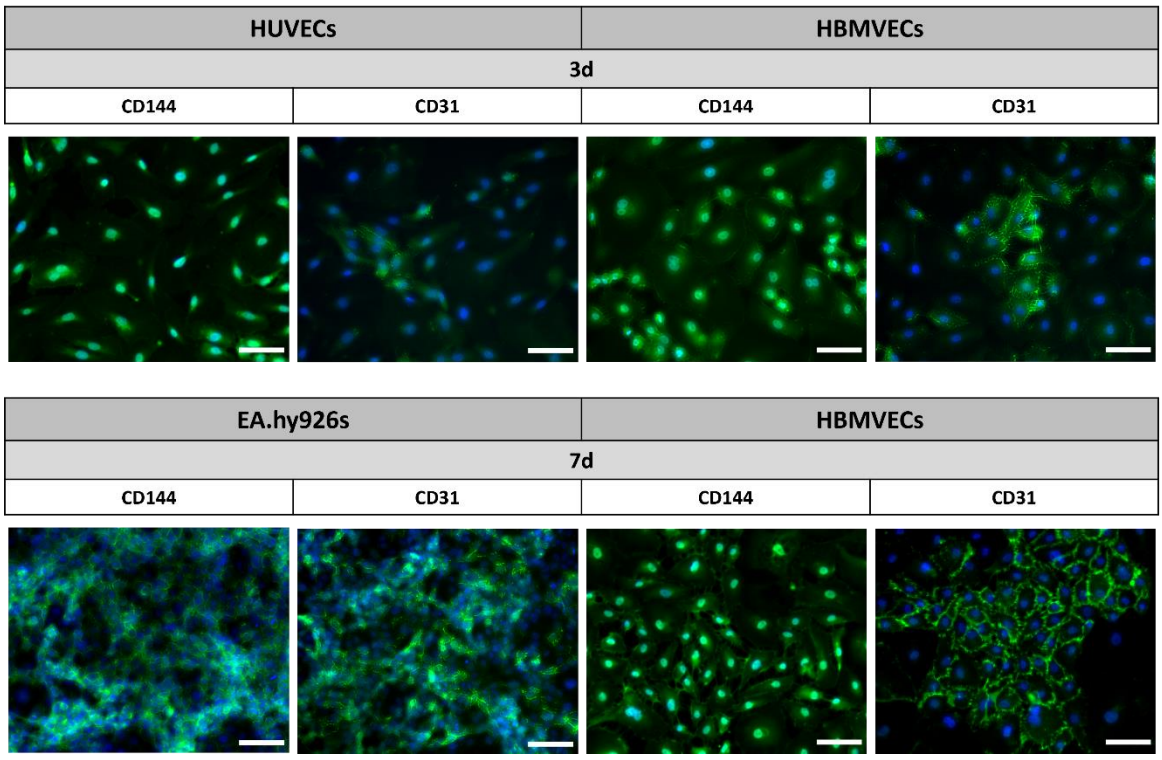

Figure 31: Exemplary immunofluorescence micrographs of HUVECs, HBMVECs, and EA.hy926 cells. Each cell type was fluorescently labeled for CD144, CD31, both illustrated in green signal, and the cellular nucleus which is shown in blue. The upper row demonstrates the detected fluorescence signal of HUVECs and HBMVECs after a prior cultivation time of three days (3d). The bottom row shows fluorescence images of HBMVECs and EA.hy926 cells which were recorded after an incubation time of seven days (7d). Scale bar: 100 µm.

CHAPTER 4

Integral discussion and further perspectives

So far, the study of cell adhesion has been mainly based on quantitative techniques such as AFM and FluidFM® and the visualizing method of FL.[29,68,75,82,209] Both technologies are powerful tools and absolutely essential for biological research. However, the information content of one technique alone is limited. Thus, the correlative microscopy represents an emerging field of current research.[145,169,296,346] The development of such methods, however, involves several challenges such as the combination of two hardware systems in one setup and the establishment of an appropriate workflow. This often entails new and unpredicted issues including interference effects or a complex sample preparation.[27,34] Consequently, an increasing number of research groups already work with a correlative microscope but perform their experiments in a sequential manner.[35,165,166] While this represents an advancement in the analysis of biological questions, the restriction to only one information at a time remains. Hence, a truly correlative hardware performance had to be developed.

The correlation of FluidFM® and FL, which was presented in this thesis, exemplifies a novel and powerful tool by addressing two biological questions at once. Its functionality was successfully proven via the simultaneous quantification of adhesion forces and the high-resolution visualization of cellular insights. More precisely, by optically tracking the cellular detachment process, an unambiguous match between single force steps and molecular unbinding events was achieved.

Optimizing the FL-FluidFM® workflow could include an automated starting of both measurements and would provide an easier handling. Up to now, force quantification and fluorescence visualization are activated manually with two hands and thus are inconvenient. With respect to data reproducibility and accuracy, a computer synchronization would minimize the currently occurring software delay and simplify the correlated data analysis. The latter one could be further optimized by using appropriate algorithms. This is already standard for step detection and FD-curve analysis of AFM-based SCFS, making the data analysis more efficient.[38,347,348] Regarding the FL-FluidFM® hardware, an additional beam splitter providing a ratio of, for instance, 90:10 would improve the correlated data performance. This would ensure a high detection efficiency of fluorescent signal while allowing at the same time a cantilever monitoring without removing this component from the beam path.

One of the hardest challenges during setup establishment was the compatibility of fluorescence excitation light and cantilever movement. Due to different interference effects, the correlated data acquisition of this study was limited to a wavelength of 555 nm. Therefore, additional experiments regarding dye applicability are advisable. Moreover, for the integration of dual-fluorescence visualization, the occurrence of the sinusoidal signal, overlapping the entire force-

curve, has to be further analyzed and reduced. A successful optical tracking of multiple labeled cells would take the correlative performance of FL-FluidFM® to next level.

Apart from the more hardware related optimization, there are further biological questions that can be addressed more in detail now. This refers on the one hand to a more advanced data analysis, but also to the investigation of cell-induced differences in cell adhesion. The latter one especially refers to the differences between cell-substrate and cell-cell adhesion. Here, additional experiments need to be done to clearly evaluate the characteristics of cohesion. Primary HUVECs or other primary cells such as the HBMVECs could be used and incubated for at least 7 days before the examination of cell adhesion forces. Afterwards, the correlative investigation with simultaneous fluorescence visualization can be applied. Therefore, live-cell staining has to be established which is often achieved via transient transfection.[125,126] However, nowadays there are innovative labeling techniques like the SNAP-/CLIP-tag technology, which covalently couples chemically synthesized fluorophores to proteins in living cells.[349,350] Compared to classical FPs, these self-labeling protein tags convince with a higher reaction rate and improved photostabiliy.[351,352] In the context of data analysis, the force-curve provides a variety of information about the characteristics of cell adhesion.[68,74] Besides the quantification of MDFs and force steps, the height and time-dependent length of a step might be especially useful for the interpretation of catch- and slip-bonds.[74] To further study the occurrence of these adhesive bonds, a systematic investigation of the force load-lifetime dependence should be done.[78,257] This can be performed via a successive increase of the retraction speed, which influences the bond survival and thus provides information about the unbinding behavior of cellular bonds.[74,78]

Regarding the emerging field of biofabrication, it may be interesting in the future to integrate artificial biomaterials or 3D scaffolds into the system. Depending on their specific application, they have to fulfill different adhesive aspects. For instance, the field of tissue regeneration requires an adhesive material surface that, in turn, promotes cellular attachment and subsequently proliferation and biosynthesis.[10,287] Also, the investigation of spheroids may represent an interesting topic in the future. Due to their increased intercellular interaction, they imitate the *in vivo* architecture of natural tissues and organs much more realistic than 2D cell cultures.[353,354] For a more comprehensive view of this 3D structure, the integration of the vertical light sheet imaging technique might be useful. Here, the implementation of an additional mirror system enables side-view imaging which offers a complete new perspective on a cell.[298] Especially for the study of cell mechanics, where a force is applied in the vertical direction, this technique represents a promising tool.

CHAPTER 5

Summary/Zusammenfassung

5.1 Summary

The **aim of this thesis** was the development of a correlated and multifunctional device which combines Fluidic Force Microscopy (FluidFM®) with Fluorescence Microscopy (FL) (FL-FluidFM®) and, thus, enables the truly simultaneous quantification of adhesion forces and fluorescent visualization of detached mature cells. Before hardware conversion, the focus was on the evaluation of standard applications of a conventional FluidFM® (**Chapter 3.1**). Here, colloidal indentation, cellular compression as well as conventional cellular detachment was performed. Subsequently, the system was modified for its correlative use including both hardware and software related adjustments (**Chapter 3.2**). For a simultaneous visualization, it was crucial to implement a high-resolution as well as a stable but dynamic focus level. This was achieved by the integration of a high-resolution oil immersion objective and a Piezo Flexure Objective Positioner (PIFOC). In addition, the correlative operation was separated into two independent computers preventing a mutual software blocking. The functionality of the hardware adaptation was evaluated by comparing the optical tracking of a cellular detachment with the conventional and optimized optical features (**Chapter 3.3**). A major improvement in visualization quality was identified. In the correlative system, the focus stayed on the cell throughout the entire measurement, while the conventional FluidFM® was accompanied by focus loss and a blurry visualization.

The performance of Single-Cell Force Spectroscopy (SCFS) after hardware modification was verified in **Chapter 3.4**. Two force-curves were compared, measured with the optimized and conventional hardware, respectively. Both were composed of the typical force progression including approach, immobilization, and retraction. Especially the third section revealed a high number of multiple detachment steps in each case. However, the maximum detachment forces (MDFs) revealed with (-253 ± 75) nN (FluidFM®) and (-334 ± 91) nN (FL-FluidFM®) a noteworthy difference which was also evident in the totality of investigated cells. This phenomenon could be clearly attributed to the spring constant of the used cantilevers which showed a significant discrepancy with 1.25 N m^{-1} and 2.55 N m^{-1} after calibration. Consequently, the hardware-related modification of the correlated system could be excluded as a source of error and, thus, its functionality successfully verified.

The next step in establishing a correlative device was the integration of fluorescence illumination (**Chapter 3.5**). Proof-of-principle experiments were performed by detaching single rat embryonic fibroblasts (REF52 cells) fluorescently labeled for paxillin and F-actin filaments. The visualization of paxillin and the dual-fluorescence illumination of both markers revealed pronounced cantilever autoluminescence. In addition, the latter showed a force overlapping sinusoidal signal which made

the analysis of cellular unbinding events impossible. However, fluorescence illumination of the cytoskeleton alone showed the same characteristic force profile as with brightfield illumination and no evidence of interference effects. Thus, together with the high focus stability and high resolution, a real-time optical tracking of a cellular detachment under fluorescence illumination was feasible for the first time.

After this successful performance of truly correlative FL-FluidFM®, a corresponding correlative data analysis was addressed in the following **Chapter 3.6**. Here, a three-step workflow was presented including manual force step fitting, the identification of visualized cellular unbinding, and a time-dependent correlation. This procedure revealed a link between the area of cytoskeletal unbinding and force-jumps. Moreover, the regional progression of cellular separation could be attributed to the distinct force steps of 'j' and 't' events which are related to intracellular rupture and the formation of membrane nanotubes (tether), respectively. This could be further confirmed by an investigation of the slope distribution of force steps which revealed a transition from high ('j' events) to low slopes around zero ('t' events).

With the completed establishment of the correlated device and a suitable data analysis, the adhesion of intercellular connected human umbilical vein endothelial cells (HUVECs) was investigated in **Chapter 3.7**. Their detachment characteristics were compared with the ones of individual REF52 cells, first. Due to their endothelial character and, thus, the formation of strong adherens junctions, HUVECs were expected to show more pronounced 'j' events. Moreover, since cohesion is composed of both cell-substrate and cell-cell adhesion, the MDFs of interconnected cells are usually significantly higher. However, *in vitro*, HUVECs showed an overall unbinding behavior that was dominated by 'slipping' step transitions and MDFs in the same order of magnitude as the ones of single REF52 cells. This detachment behavior was also recognized when quantifying unbinding forces of single and interconnected HUVECs. The use of two different retraction speeds showed differences in the unbinding mechanism, but a clear assignment to slip- or catch-bond-mediated unbinding was not possible. In addition, the speed-dependent MDFs of single and interconnected HUVECs were in the same order of magnitude, with cell-cell contacts being slightly lower. This contrasted with the expected strong cohesiveness of endothelial cells and further indicated a lack of cell-cell contact formation. With this knowledge as background, the formation of intercellular junctions was further investigated and compared between HUVECs, primary human brain microvascular endothelial cells (HBMVECs), and immortalized human vascular endothelial cells (EA.hy926) by fluorescent visualization of two marker proteins of intercellular junctions, vein endothelial (VE)-cadherin and platelet endothelial cell adhesion molecule (PECAM-1). This unveiled that both the previous cultivation duration and the cell type

have a major impact on the development of intercellular junctions. The highest and most specific emission signal was detected when using primary HBMVECs and a previous cultivation time of 7 d. HUVECs, which were cultured for a maximum of 3 d prior to their experimental investigation, showed only a low fluorescence signal for both markers. This most likely explains their unexpected unbinding behavior during cellular detachment.

In summary, the correlative FL-FluidFM® technology represents a powerful novel approach, which enables the truly contemporaneous performance of force-curve quantification and detachment step visualization and, thus, has the potential to reveal new insights into the mechanobiological properties of cell adhesion.

5.2 Zusammenfassung

Ziel dieser Arbeit war die Entwicklung eines korrelativen und multifunktionalen mikroskopischen Geräts, das Fluidkraftmikroskopie (FluidFM®) mit Fluoreszenzmikroskopie (FL) verbindet (FL-FluidFM®) und dadurch die gleichzeitige Quantifizierung von Zelladhäsionskräften und die fluoreszente Visualisierung des Ablösevorgangs ermöglicht. Vor dem Umbau der Hardware lag der Fokus zunächst auf der Evaluierung von Standardanwendungen eines konventionellen FluidFM®'s (**Kapitel 3.1**). Hierfür wurden die Methoden des kolloidalen Eindrückens, der zellulären Kompression sowie der konventionellen Zellablösung durchgeführt. Anschließend wurde das System für seine korrelative Anwendung modifiziert, wobei sowohl hard- als auch softwareseitige Anpassungen vorgenommen wurden (**Kapitel 3.2**). Für eine simultane Visualisierung des Ablösevorgangs war es entscheidend, eine hohe Auflösung sowie eine stabile, aber dynamisch flexible Fokusebene zu generieren. Dies wurde durch die Implementierung eines hoch-auflösenden Immersionsobjektivs und eines piezogesteuerten Objektiv-Positionierers (PIFOC) realisiert. Zusätzlich wurde die korrelative Steuerung des Systems auf zwei unabhängige Computer aufgeteilt, wodurch eine gegenseitige Software-Blockade der beiden mikroskopischen Einheiten verhindert werden konnte. Die Funktionalität der Hardware-Adaption wurde über die optische Verfolgung einer Zellablösung evaluiert. Ein Vergleich der konventionellen mit der optimierten optischen Hardware-Ausstattung zeigte eine wesentliche Verbesserung der mikroskopischen Visualisierungsqualität (**Kapitel 3.3**). Im korrelativen System blieb der Fokus während der gesamten Messung auf der Zelle, während das konventionelle FluidFM® mit einem Fokusverlust und einer unscharfen Visualisierung einherging.

Nach Anpassung der Hardware wurde die Durchführbarkeit von Einzel-Zell Kraftspektroskopie (SCFS) in **Kapitel 3.4** verifiziert. Hierbei wurden zwei Kraftkurven miteinander vergleichen, die jeweils mit der optimierten und der konventionellen Hardware gemessen wurden. Beide zeigten den typischen Kraftverlauf, der sich aus den Abschnitten der Annäherung, Immobilisierung und dem anschließenden Rückzug zusammensetzte. Insbesondere der dritte Bereich beinhaltete in beiden Fällen eine hohe Anzahl an multiplen Ablöseschritten. Die maximalen Ablösekräfte (MDFs) unterschieden sich allerdings mit (-253 ± 75) nN (FluidFM®) und (-334 ± 91) nN (FL-FluidFM®) deutlich, was sich auch in der Gesamtheit der Zellen widerspiegelte. Dieses Phänomen konnte auf die Federkonstante der verwendeten Kantilever zurückgeführt werden, die nach der Kalibrierung mit 1.25 N m^{-1} und 2.55 N m^{-1} eine auffällige Diskrepanz aufwiesen. Die Hardware-bedingte Modifikation des korrelativen Systems konnte folglich als Fehlerquelle ausgeschlossen und dessen Funktionalität erfolgreich nachgewiesen werden.

Der nächste Schritt in der Etablierung eines korrelativen Mikroskops war die Integration von Fluoreszenzlicht (**Kapitel 3.5**). In Experimenten zum Nachweis der prinzipiellen Durchführbarkeit wurden einzelne embryonale Ratten-Fibroblasten (REF52 Zellen) abgelöst, deren Paxillin und F-Aktin Filamente fluoreszent markiert waren. Sowohl die Visualisierung von Paxillin allein als auch die duale Fluoreszenzbeleuchtung beider Marker führten zu einer ausgeprägten Kantilever-Autolumineszenz. Darüber hinaus löste die duale Beleuchtung ein kraftüberlagerndes sinusförmiges Signal aus, was eine detaillierte Analyse von zellulären Ablöseschritten unmöglich machte. Die alleinige Fluoreszenzbeleuchtung des Zytoskeletts zeigte hingegen das gleiche charakteristische Kraftprofil wie unter Hellfeldbeleuchtung und keinen Hinweis auf Interferenzeffekte. Einhergehend mit der hohen Fokusstabilität und der hohen Auflösung wurde somit erstmals eine Zellablösung in Echtzeit und unter Fluoreszenzbeleuchtung optisch nachverfolgt.

Im Anschluss an die erfolgreiche Durchführung von simultaner FL-FluidFM® Mikroskopie wurde die entsprechende korrelative Datenanalyse im folgenden **Kapitel 3.6** behandelt. Hier wurde ein dreistufiger Arbeitsablauf vorgestellt, der eine manuelle Kraftkurvenanpassung, die Identifizierung von visualisierten zellulären Ablöseschritten und eine zeitabhängige Korrelation umfasste. Dabei konnte die von innen nach außen verlaufende zytoskeletale Ablösung den spezifischen Kraftschritten der sogenannten ‚j' und ‚t' Ereignisse zugeordnet werden. ‚j' Ereignisse stehen hierbei für eine intrazelluläre Ruptur, während sich ‚t' Ereignisse durch die Bildung von Membran-Nanoröhrchen auszeichnen. Dieser Zusammenhang konnte zusätzlich durch eine Untersuchung der Steigungsverteilung der Kraftsprünge bestätigt werden, die einen Übergang von hohen (‚j' Ereignissen) zu niedrigen Steigungen um den Nullpunkt (‚t' Ereignisse) ergab.

Nach der Etablierung des korrelierten Systems und einer geeigneten Datenanalyse wurde in **Kapitel 3.7** die Adhäsion von interzellulär verbundenen Endothelzellen aus humanen Nabelschnurvenen (HUVECs) untersucht. Zunächst wurden deren Ablöseeigenschaften mit jenen von einzelnen REF52 Zellen verglichen. Aufgrund ihres endothelialen Charakters und der damit verbundenen Bildung von starken adhärenten Knotenpunkten wurde bei den HUVECs eine deutliche Ausprägung von ‚j' Ereignissen erwartet. Darüber hinaus setzt sich die Kohäsion sowohl aus der Zell-Substrat als auch aus der Zell-Zell-Adhäsion zusammen, was für gewöhnlich darin resultiert, dass MDFs von miteinander verbundenen Zellen signifikant höher sind. *In vitro* zeigten die HUVECs jedoch insgesamt ein Ablöseverhalten, das von „gleitenden" Schrittübergängen mit geringer Steigung dominiert wurde. Die MDFs von HUVECs und einzelnen REF52 Zellen lagen darüber hinaus in der gleichen Größenordnung. Dieses Ablöseverhalten wurde sowohl für einzelne als auch für Zellen im Verbund beobachtet. Die Anwendung zweier verschiedener

Rückzugsgeschwindigkeiten führte zwar zu Unterschieden im Ablösemechanismus, eine eindeutige Zuordnung zu ‚Gleit'- oder ‚Fangbindung' vermittelter Ablösung war allerdings nicht möglich. Darüber hinaus lagen die geschwindigkeitsabhängigen MDFs von einzelnen und miteinander verbundenen HUVECs in der gleichen Größenordnung, wobei die Zell-Zell Kontakte etwas geringer ausfielen. Entgegen der Erwartung von hoher Kohäsion deutete dieses Verhalten auf einen Mangel an Zell-Zell Kontaktbildung hin. Vor dem Hintergrund dieser Erkenntnisse wurde die Bildung von interzellulären Verbindungen zwischen HUVECs, primären mikrovaskulären Endothelzellen aus dem menschlichen Gehirn (HBMVECs) und immortalisierten menschlichen vaskulären Endothelzellen (EA.hy926) verglichen. Hierfür wurden jeweils zwei Markerproteine für interzelluläre Kontakte, Venenendothel-(VE)-Cadherine und Thrombozyten-Endothelzell-Adhäsionsmoleküle (PECAM-1), fluoreszent visualisiert. Dabei zeigte sich, dass sowohl die vorangegangene Kultivierungsdauer als auch der Zelltyp einen starken Einfluss auf die Ausbildung von interzellulären Kontakten haben. Das höchste und spezifischste Emissionssignal wurde bei der Verwendung von primären HBMVECs und einer vorangegangenen Inkubationszeit von 7 d detektiert. HUVECs, die vor ihrer experimentellen Untersuchung maximal 3 d kultiviert wurden, zeigten hingegen nur ein sehr geringes Fluoreszenzsignal für beide Marker. Diese Beobachtung stützte folglich die Vermutung einer geringen Ausprägung von interzellulären Kontakten und lieferte gleichzeitig eine mögliche Erklärung für das unerwartete Ablöseverhalten der HUVECs.

Abschließend lässt sich sagen, dass die korrelative FL-FluidFM® Technik einen sehr vielversprechenden neuen Ansatz darstellt, der die gleichzeitige Durchführung von Kraftkurven-Quantifizierung und fluoreszenter Visualisierung von Ablöseschritten ermöglicht und damit großes Potential hat zukünftig neue Einblicke in die Mechanobiologie der Zelladhäsion zu eröffnen.

CHAPTER 6

Experimental section

Parts of this chapter were published as original research articles:

Weigl, F.; Blum, C.; Sancho, A.; Groll, J.; Correlative Analysis of Intra- Versus Extracellular Cell Detachment Events Via the Alignment of Optical Imaging and Detachment Force Quantification, *Advanced Materials Technologies* **2022**, 2200195., reproduced from reference[261], licensed under a Creative Commons Attribution – Non Commercial 4.0 International License, which permits use, sharing, adaptation, distribution, and reproduction in any medium or format.
To increase readability, figures from the supplementary information have been included in the main text of this thesis.
The article is based on the work of the author of this thesis, Franziska Weigl, who performed the experiments and data analysis, wrote the manuscript and is the first author of the publication.

Müller, S. J.; **Weigl, F.**; Bezold, C.; Bächer, C.; Albrecht, K.; Gekle, S.; A Hyperelastic Model for Simulating Cells in Flow, *Biomechanics and Modeling in Mechanobiology* **2021**, 20, 509, reproduced from reference[262], licensed under a Creative Commons Attribution 4.0 International License, which permits use, sharing, adaptation, distribution, and reproduction in any medium or format.
The article includes work of the author of this thesis, Franziska Weigl, who performed parts of the experiments and wrote a section of the manuscript as second author of the publication.

Nahm, D.; **Weigl, F.**; Schaefer, N.; Sancho, A.; Frank, A.; Groll, J.; Villmann, C.; Schmidt, H.-W.; Dalton, P. D.; Luxenhofer, R.; A Versatile Biomaterial Ink Platform for the Melt Electrowriting of Chemically-Crosslinked Hydrogels, *Materials Horizons* **2020**, 7, 928, reproduced from reference[263], licensed under a Creative Commons Attribution - Non Commerical 3.0 Unported License, which allows redistribution and adaptation in any medium.
To increase readability, figures from the supplementary information have been included in the main text of this thesis.
The article includes work of the author of this thesis, Franziska Weigl, who performed parts of the experiments and its analysis, and wrote a section of the manuscript as second author of the publication.

6.1 Cell culture

6.1.1 Rat embryonic fibroblasts (REF52 cells)

Adherent REF52 cells stably expressing paxillin-YFP (kindly provided by the laboratory of Alexander Bershadsky at Weizmann Institute of Science, Israel) were cultivated in Dulbecco's Modified Eagle Medium (DMEM-GlutaMAX, Life Technologies, USA) supplemented with 10% fetal bovine serum (FBS, Sigma-Aldrich Inc., St. Louis, USA), 1% penicillin/streptomycin (10,000 U mL^{-1}, Life Technologies, USA) and 1% (4-(2-hydroxyethyl)-1-piperazineethanesulfonic acid (HEPES) buffer (1 M, Sigma-Aldrich, Inc., St. Louis, USA). The cells were sub-cultured twice a week and stored at 37 °C with a 5% CO_2 supply.

6.1.2 Human umbilical vein endothelial cells (HUVECs)

For the cultivation of adherent human umbilical vein endothelial cells (HUVECs) (HUV-EC-C [HUVEC], ATCC® CRL-1730TM, Virginia, USA), F-12K medium (Ham's F-12K (Kaighn's) Medium, Thermo Fisher Scientific Inc., Waltham, USA) was supplemented with 10% fetal calf serum (FCS), 1% penicillin/streptomycin and heparin (Heparin sodium salt from porcine intestinal mucosa Grade I-A, Merck KGaA/Sigma Aldrich, Darmstadt, Germany) with a final concentration of 0.1 mg mL^{-1}. Before sub-cultivation, endothelial cell growth supplement (ECGS) (Corning™ Endothelial Cell Growth Supplement, Thermo Fisher Scientific Inc., Waltham, USA) was added with a final concentration of 100 µg mL^{-1} to complete the growth medium. For this, a stock solution of 30 mg mL^{-1} ECGS was prepared and stored at -20 °C. For cell seeding, culture flasks were coated with 0.1% gelatin for at least 1 h at room temperature (RT). Also, in this case, sub-cultivation was performed twice a week depending on the cell density. The culture medium was replaced every two days.

6.1.3 Primary human brain microvascular endothelial cells (HBMVECs)

Primary human brain microvascular endothelial cells (HBMVECs) were cultivated in microvascular endothelial cell growth medium (enhanced) supplemented with a microvascular endothelial cell growth supplement kit (enhanced) (PELOBiotech GmbH, Planegg/Martinsried, Germany) consisting of basic fibroblast growth factor (bFGF), epidermal growth factor (EGF), vascular endothelial cell growth factor (VEGF), long R3 IGF-1, hydrocortisone, 5% FCS, and L-glutamine. Before sub-cultivation, culture flasks were coated for 5 min with ready-to-use speed coating solution (PELOBiotech GmbH, Planegg/Martinsried, Germany) at RT. Depending on the cell

density, the cells were sub-cultured twice a week with a seeding density of 2 x 10^4 cells cm^{-2} and stored at 37 °C with 5% CO_2 supply.

6.1.4 Human vascular endothelial cells (EA.hy926)

For the investigation of fluorescence labeling of the cell-cell contact protein marker CD31 and CD144, already seeded and for immunostaining prepared immortalized human vascular endothelial cells (EA.hy926) were kindly provided by the laboratory of Philipp Wörsdörfer from the Institute of Anatomy and Cell Biology at the University of Würzburg.

6.2 Fluorescent labeling

6.2.1 Transient transfection

REF52-paxillin-YFP cells were additionally transiently transfected with LifeAct-mCherry (kindly provided by the laboratory of Alexander Bershadsky at Weizmann Institute of Science, Israel), a fusion protein that specifically binds to F-actin filaments. Lipofectamine2000 (Thermo Fisher Scientific Inc., Waltham, USA) was used as transfection reagent. The preparation of the lipid-DNA-complex was performed with Opti-MEM (Thermo Fisher Scientific Inc., Waltham, USA) as reduced serum media. One day before transfection, the cells were seeded at a density of 2000 to 3000 cells cm^{-2} on 40 mm glass-bottom dishes (WillCo Wells B.V., Amsterdam, Netherlands) carrying a metal ring of 2.2 cm in diameter and mounted with 1 mL of serum-free culture media. On the day of transfection, a lipid-DNA-complex containing 0.5 to 1 µg DNA was added to the cells and incubated at 37 °C. After 5 to 6 h, the transfection media was replaced by the corresponding culture media and stored in the incubator at 37 °C. The next day, the transfected cells were ready to use. Right before the experimental investigation, the cells were carefully rinsed two to three times with 1x Dulbecco's phosphate-buffered saline (PBS) (Sigma-Aldrich Inc., St. Louis, USA) followed by a coverage with FluoroBrite solution (Thermo Fisher Scientific Inc., Waltham, USA) providing a reduction of background signal and higher signal-to-noise-ratio (SNR). Directly before the performance of correlated FL-FluidFM® experiments, the metal ring was removed. Each sample was used for a maximum of 1.5 to 2 h.

6.2.2 Immunofluorescence staining

For the immunostaining of CD31 and CD144 in HUVECs, HBMVECs, and EA.hy926 cells, 48 well plates (Nunclon Delta, Thermo Fisher Scientific Inc., Waltham, USA) were coated with 0.1% gelatin and speed coating solution for HUVECs and HBMVECs, respectively. To achieve a formation of mature cell-cell contacts, HUVECs and HBMVECs were seeded at a density of 33 000 cells cm^{-2} and

22 000 cells cm^{-2}, respectively, while the EA.hy926 cells were directly ready-to-use as mentioned in **Chapter 6.1.4**. After an incubation time of at least three days, the cells were rinsed with 1x PBS and fixed for 10 min with 4.5% formaldehyde (Roti-Histofix, Carl Roth GmbH & Co. KG, Karlsruhe, Germany). Then, all wells were washed three times with 1x PBS and permeabilized for 5 min with 0.2% Triton-X-100 (Carl Roth GmbH & Co. KG, Karlsruhe, Germany). After blocking for 30 min with 2% bovine serum albumin (BSA) (Sigma-Aldrich Inc., St. Louis, USA), primary antibodies for CD31 (1:50) (ab28364, abcam, Cambridge, UK) or CD144 (1:100) (V1514, Merck KGaA/Sigma Aldrich, Darmstadt, Germany) were added, both diluted in 1% BSA and 0.1% Triton-X 100 and incubated at 4 °C over night. The cells were rinsed three times with 1x PBS the next day and mounted with the secondary antibody solution for 1 h at RT. Therefore, AlexaFluor488 (Invitrogen by Thermo Fisher Scientific Inc., Waltham, USA) was diluted in PBS with a ratio of 1:400. At the end of incubation time, two to three drops of Hoechst 33258 (1:1000) (Merck KGaA/Sigma Aldrich, Darmstadt, Germany) were added per well and further incubated for about 8 min. Afterwards, all wells were rinsed once again with 1x PBS three times and subsequently mounted with FluoroBrite solution to achieve a high SNR during FL.

6.3 Fluorescence microscopy

6.3.1 Device setup

The visualization of fluorescently labeled cells either by transient transfection or by immunostaining was performed on a stand-alone fluorescence microscope. This system was based on an inverted microscope (AxioObserver, Carl ZEISS AG, Oberkochen, Germany) and a monochromatic camera (AxioCam 506 mono, Carl ZEISS AG, Oberkochen, Germany). For the fluorescent illumination, a light source with four LEDs (Colibri 7, Carl ZEISS AG, Oberkochen, Germany) was used providing red, green, blue, and UV light. Image acquisition was performed via the corresponding ZEN 2.6 software while image processing and analysis were done using ImageJ.

6.3.2 Fluorescence imaging

6.3.2.1 Transient transfection

For the fluorescent analysis of transient transfected REF52-paxillin-YFP cells, a 40x high-numerical objective (Plan-Apochromat 40x/1.4 oil DIC (UV) VIS-IR, Carl ZEISS AG, Oberkochen, Germany) was used to ensure a high-resolution imaging. To visualize actin filaments, the cells were illuminated with an excitation light of 555 nm at an intensity of 100% and an exposure time of 700 ms. On the other hand, paxillin was excited via a LED module providing light of 475 nm wavelength. A low intensity of 25% and an exposure time of 500 ms guaranteed almost no photobleaching.

6.3.2.2 Immunofluorescence

The fluorescent signal of immunostained HUVECs, HBMVECs, and EA.hy926 cells was captured with a 20x dry objective (LD Plan-Neofluar 20x/0.4 Korr Ph 2, Carl ZEISS AG, Oberkochen, Germany). For the visualization of the cellular nucleus, a wavelength of 385 nm was used. Depending on the emission signal strength, light intensity and exposure time were adjusted. In the case of HUVECs and HBMVECs the intensity was set to 100% together with an exposure time of 250 ms. For the investigation of EA.hy926 cells, the light intensity was reduced to 50% and the exposure time to 100 ms. The visualization of CD31 and CD144 was performed by using a LED module providing light of 475 nm wavelength. Also, in this case, the illumination parameters had to be modified in accordance with the emission signal. For all cell types, the intensity was set to 100% for both markers while the exposure time differed between the cell types. In the case of EA.hy926 cells, an exposure time of 700 ms was chosen, whereas HUVECs and HBMVECs were illuminated with a duration of 500 ms.

6.4 FluidFM®-based SCFS

All measurements of **Chapter 3.1** were performed on a conventional FluidFM® system whose setup was explained in detailed in **Chapter 3.1.1.1**. The following sections describe its applicability and the corresponding parameters for the examination of colloidal indentation, cellular compression, and conventional cell adhesion.

6.4.1 Cantilever preparations

FluidFM® technology was performed using Si-based microfluidic probes (FluidFM® micropipette cantilever, Cytosurge AG, Glattbrugg, Switzerland) which are equipped with a microchannel and an aperture at the free end. On the other side, the micropipette was connected to a pressure system (Cytosurge AG, Glattbrugg, Switzerland). Before an experiment, each cantilever was prepared by calibrating the spring constant as well as the deflection sensitivity via build-in procedures of the Cytosurge and Nanosurf software. For an application in a complete liquid surrounding, the fluid reservoir of the FluidFM® cantilever was loaded with HEPES-2 buffer (10 mM HEPES supplemented with 150 mM sodium chloride (NaCl) solution, pH = 7.4) and pushed into the microchannel by applying a slight overpressure. The alignment of the microfluidic probe was performed by using a near-infrared super-luminescence-diode (NIR SLD). The piezo-regulated movement of the cantilever was controlled via a closed feedback-loop within the scan head.

6.4.2 Colloidal indentation

To evaluate the elastic properties of polymer fibers, cantilevers of 4 µm aperture and a nominal spring constant of 0.3 N m^{-1} were used. Polyethylene glycol-coated polystyrene beads of 10 µm in diameter (Micromer® 01-54-104, Micromod Partikeltechnologie GmbH, Rostock, Germany) were immobilized at the cantilever tip via a suction pressure of -700 mbar and utilized as colloidal indenter. Before each experiment, the cantilever spring constant as well as its deflection sensitivity was calibrated with a software implemented tool, but in this case together with the aspirated bead. For the examination of the fiber stiffness, nanoindentation was performed on three independent two-layered scaffolds with 25 to 30 FD-curves per sample, addressing each time a different spot and omitting the fiber intersections. The cantilever approach was performed at 500 nm s^{-1} until a setpoint of 3 nN was reached. To achieve a high amount of data points, the data acquisition frequency of the approach section was set to 6 kHz. The Young's moduli E_γ were evaluated from the approach-curve of the spectroscopy cycle. Therefore, the first steps of data processing were performed using Excel. By applying Hook's Law (**Chapter 2.1.2.4.1**, **Equation (1)**), the primary data of approach and retraction given as data in the form of cantilever deflection and z-stage position versus time, were converted into the form of force versus indentation. This was followed by the application of a custom program written in Matlab 2017 (Mathworks, Natick, USA) which provided an automated finding of the contact point and a subsequent fitting in accordance with the Hertzian model for spherical indenters (**Chapter 2.1.2.4.3**, **Equation (2)**). Here, the Poisson's ratio ν was set to 0.5 while the radius R was represented by the radius of the bead (5 µm) and the radius of the fibers (12.5 µm).

6.4.3 Cellular deformation

For the evaluation of cellular deformation, all measurements were performed with tipless cantilevers of 8 µm aperture and a nominal spring constant of 2 N m^{-1}. Immediately before an experiment, the cells were detached by using accutase (Sigma-Aldrich Inc., St. Louis, USA) ensuring to address only single cells. Subsequently, a suspended cell was directly aspirated at the cantilever tip and immobilized by applying a negative pressure of -60 mbar. Afterwards, cellular deformation was examined by compressing the cell between the cantilever and the substrate surface. Therefore, the cantilever was approached with a speed of 3 µm s^{-1} until a setpoint of 100 nN was reached and subsequently retracted with 5 µm s^{-1}. During this procedure, the suction pressure was kept constant. Only after finishing the measurement, a positive pressure of several hundreds of mbar was applied releasing the cell from the cantilever aperture. Analogous to the colloidal indentation, also in this case, a high data acquisition frequency of 6 kHz was chosen. Moreover,

the data processing was based on the same principle, described in the previous **Chapter 6.4.2**. However, here, the contact point was determined manually and defined as the cantilever position where the force starts to increase. The Poisson's ratio ν was set to 0.48 while the radius R was only represented by the cells in these experiments. Therefore, the size of the target and uncompressed cell was determined by the mean of a horizontal and a vertical diameter, measured using the software ImageJ.

6.4.4 Cell adhesion

For the acquisition of FluidFM®-based cell adhesion forces, REF52-paxillin-YFP cells were seeded at a density of 3000 to 4000 cells cm^{-2} onto a 40 mm glass bottom dish (WillCo Wells B.V., Amsterdam, Netherlands). The sample preparation was performed one day in advance to ensure the formation of mature cell contacts. For force data acquisition, tipless cantilevers with a nominal spring constant of 2 N m^{-1} and an aperture of 8 µm were used. Right before the measurement, the working distance between cantilever and cell was automatically set via a build-in procedure of the Cytosurge-ARYA software (Cytosurge AG, Glattbrugg, Germany). By starting the cellular de-adhesion process, the cell is approached with a speed of 5 µm s^{-1}. After reaching a setpoint of about 30 nN, the cell is attached at the cantilever tip by applying a negative pressure between -500 and -600 mbar, depending on the cell size. To ensure a proper sealing, a pause of 2 to 3 s was accomplished, followed by the retraction of the sample stage with a speed of 2 µm s^{-1}. A constant suction pressure ensured cellular immobilization throughout the whole cellular detachment. During this process, data acquisition was performed under brightfield illumination and with a frequency of 512 Hz. The Cytosurge software automatically generated videos of the cellular de-adhesion. All measurements were accomplished at RT and with the corresponding culture medium as surrounding solution. Samples were used for a maximum of 1.5 h.

The recorded raw data of a cellular detachment was extracted on and processed in Excel, in accordance with the procedure of indentation analysis which was described in **Chapter 6.4.2**. However, in this case, the step of cellular immobilization had to be considered additionally. For the determination of the overall time progression, the given times of approach, pause, and retraction were added up. With this, a whole cell detachment process could be displayed as force-versus time-curve and graphical illustrated using OriginPro2020.

6.5 FL-FluidFM® performance

6.5.1 FL-FluidFM® data acquisition

FL-FluidFM® data acquisition was operated on separate computers for independent but simultaneous control of the correlated methods. FL was performed by using ZEN 2.6 as imaging software of ZEISS (Carl ZEISS AG, Oberkochen, Germany). The control unit of FluidFM® experiments was composed of two software: the Cytosurge-ARYA for cantilever alignment and a defined cell detachment workflow, and the Nanosurf C3000 FluidFM-T controller unit (Nanosurf GmbH, Langen, Germany) for monitoring of the cantilever deflection as well as the movement of the 100 µm z-stage and PIFOC. All measurements were based on a micropipette cantilever with a nominal spring constant of 2 N m^{-1} and an aperture of 8 µm. Cantilever preparations were accomplished in the same way as depicted in **Chapter 6.4.1**.

Prior to each experiment, the sample stage was set to the highest position of +50 µm, followed by a cantilever approach with 5 µm s^{-1} until a set point of 30 to 50 nN was reached. A defined working distance between the cantilever and a targeted cell was achieved by subsequently retracting the z-stage by 20 µm. With starting the FL-FluidFM® measurement, the z-stage moved upwards until the cantilever and cell were in contact and a setpoint between 30 and 50 nN was reached, followed by the immobilization of the cell by applying a negative pressure of -400 to -500 mbar. A stable sealing between micropipette and cell was achieved by a pause of 2 to 3 s in which the sample stage position and force were kept constant. Afterwards, while maintaining a constant suction pressure, the 100 µm z-stage was retracted with a speed of 2 µm s^{-1} until the lowest stage position of -50 µm was reached. During this backward movement, the detachment process of an immobilized cell was recorded with a frequency of 1024 Hz, while at the same time, the fluorescence microscope acquired a time-series of 60 to 70 s. The acquisition of all time-series was performed by using an excitation wavelength of 555 nm. Its intensity was set to 100% and the exposure time within a range of 200 to 300 ms. The acquisition of dual-channel fluorescence images was accomplished by combining 555 nm with 475 nm excitation light. The exposure time was set to 500 ms in both cases, whereas the intensity of the blue laser was limited to 40%. After each experiment, the cantilever was cleaned by rinsing it 1 min with sodium dodecyl sulfate (SDS) followed by several washing steps with ultrapure water. All FL-FluidFM® measurements were performed at RT and in FluoroBrite solution as experimental surrounding medium.

6.5.2 Data processing and analysis

6.5.2.1 Detachment step analysis

Prior to the data correlation of force progression and visualized de-adhesion steps, the primary data had to be converted into the form of force versus time, first, referring to the force-curve processing presented in **Chapter 6.4.4**. Afterwards, single unbinding steps of a retraction-curve were analyzed using OriginPro2020. Each force-jump that was preceded by either a ramp-like change in force or a plateau was defined as a definite detachment step and manually analyzed via a linear fit. A software-implemented tool automatically calculated the respective slope with standard deviation. To limit the fitting area, two markers were set, one at the beginning and one at the end of the step. In this way, all slopes within a detachment process could be displayed as a slope-detachment step graph.

6.5.2.2 Correlated analysis of FL-FluidFM® data

Following the force-step analysis, the data processing of recorded time-series was performed using ZEN 3.0 and ImageJ. After adjusting the fluorescent contrast, the relative time of a visualized detachment process was displayed using a software-implemented tool. Unambiguous matching of identified detachment steps and spots of cellular unbinding was achieved by using the last force-step and its corresponding time as a reference and starting point for data reconciliation. A possible temporal delay between the two data sets was compensated by considering the time difference at each correlated unbinding process. By scanning through the whole visualized detachment and the corresponding force progression, a precise matching of unbinding steps was possible.

6.6 Correlated investigation of cell-cell adhesion

6.6.1 Sample preparation

For the acquisition of adhesion forces arising from cell-cell contacts, HUVECs were seeded at a density of 10 000 to 15 000 cells cm^{-2} onto a 40 mm glass bottom dish (WillCo Wells B.V., Amsterdam, Netherlands) pre-coated with 0.1% gelatin (**Chapter 6.1.2**). After the incubation for at least one day, cellular detachment experiments were performed only with cells that were connected to adjacent cells using the FL-FluidFM® setup and its optimized optical properties. As a control, also the adhesion forces of individual HUVECs meaning cells solely contacting the surface were acquired. Thus, to ensure an increased cell singulation, the seeding density was reduced to 4000 cells cm^{-2}.

6.6.2 Correlated data acquisition

The performance of simultaneous SCFS and optical tracking of detached HUVECs was performed analogously to the already described procedure of data acquisition using FL-FluidFM® (**Chapter 6.5.1**). Also in this case, a tipless cantilever of 2 N m^{-1} nominal spring constant and 8 µm aperture was applied. However, instead of fluorescence light, only brightfield illumination was implemented. Furthermore, the working distance between cantilever and sample was reduced to a minimum to achieve the longest possible retraction range. Compared to the measurements with REF52 cells, here, the suction pressure was slightly increased to -600 to -700 mbar ensuring an appropriate sealing of the cell. Moreover, the cellular detachment of HUVECs was performed with two different retraction speeds, namely 2 and 5 µm s^{-1}. During this process, the brightfield illumination was set to 100% intensity and an exposure time of 70 ms. Another important aspect in quantifying adhesion forces of HUVECs was the adjustment of the software internal proportional-integral-derivative (PID) controller working as a feedback control loop and, thus, continuously balancing the difference between an actual and a setpoint value. In contrast to the measurements with REF52 cells where the parameters were set to 250 (P), 200 (I), and 0 (D), for the experiments with HUVECs, the proportional parameter (P) was doubled to 500 ensuring a smooth up and downward movement of cantilever and sample stage.

6.6.3 Force-curve processing and data analysis

The processing of primary data and its analysis was performed in accordance with the already described procedure in **Chapter 6.5.2**. However, for the analysis of cell-cell adhesion, also the MDFs of cells and their dependence on the retraction speed were evaluated. Therefore, the maximum forces were determined using OriginPro2020 and graphically illustrated via a box-plot.

References

(1) Angulo-Urarte, A.; van der Wal, T.; Huveneers, S. Cell-Cell Junctions as Sensors and Transducers of Mechanical Forces. *Biochimica et Biophysica Acta (BBA) - Biomembranes* **2020**, *1862* (9), 183316.

(2) Oda, H.; Takeichi, M. Structural and Functional Diversity of Cadherin at the Adherens Junction. *Journal of Cell Biology* **2011**, *193* (7), 1137-1146.

(3) Lock, J. G.; Wehrle-Haller, B.; Strömblad, S. Cell–Matrix Adhesion Complexes: Master Control Machinery of Cell Migration. *Seminars in Cancer Biology* **2008**, *18* (1), 65-76.

(4) Bartle, E. I.; Rao, T. C.; Urner, T. M.; Mattheyses, A. L. Bridging the Gap: Super-Resolution Microscopy of Epithelial Cell Junctions. *Tissue barriers* **2018**, *6* (1), e1404189-e1404189.

(5) Conway, J. R. W.; Jacquemet, G. Cell Matrix Adhesion in Cell Migration. *Essays in Biochemistry* **2019**, *63* (5), 535-551.

(6) Gumbiner, B. M. Cell Adhesion: The Molecular Basis of Tissue Architecture and Morphogenesis. *Cell* **1996**, *84* (3), 345-357.

(7) Aplin, A. E.; Howe, A. K.; Juliano, R. L. Cell Adhesion Molecules, Signal Transduction and Cell Growth. *Current Opinion in Cell Biology* **1999**, *11* (6), 737-744.

(8) Stamatovic, S. M.; Keep, R. F.; Andjelkovic, A. V. Brain Endothelial Cell-Cell Junctions: How to "Open" the blood Brain Barrier. *Current neuropharmacology* **2008**, *6* (3), 179-192.

(9) Staddon, J. M.; Rubin, L. L. Cell Adhesion, Cell Junctions and the Blood—Brain Barrier. *Current Opinion in Neurobiology* **1996**, *6* (5), 622-627.

(10) Khalili, A. A.; Ahmad, M. R. A Review of Cell Adhesion Studies for Biomedical and Biological Applications. *International Journal of Molecular Sciences* **2015**, *16* (8), 18149-18184.

(11) Clarke, D. N.; Martin, A. C. Actin-based Force Generation and Cell Adhesion in Tissue Morphogenesis. *Current Biology* **2021**, *31* (10), R667-R680.

(12) Esfahani, A. M.; Rosenbohm, J.; Reddy, K.; Jin, X.; Bouzid, T.; Riehl, B.; Kim, E.; Lim, J. Y.; Yang, R. Tissue Regeneration from Mechanical Stretching of Cell–Cell Adhesion. *Tissue Engineering Part C: Methods* **2019**, *25* (11), 631-640.

(13) Veale, D. J.; Maple, C. Cell Adhesion Molecules in Rheumatoid Arthritis. *Drugs & Aging* **1996**, *9* (2), 87-92.

(14) Smith, M. D.; Slavotinek, J.; Au, V.; Weedon, H.; Parker, A.; Coleman, M.; Roberts-Thomson, P. J.; Ahern, M. J. Successful Treatment of Rheumatoid Arthritis is Associated with a Reduction in Synovial Membrane Cytokines and Cell Adhesion Molecule Expression. *Rheumatology* **2001**, *40* (9), 965-977.

(15) Janiszewska, M.; Primi, M. C.; Izard, T. Cell adhesion in cancer: Beyond the migration of single cells. *Journal of Biological Chemistry* **2020**, *295* (8), 2495-2505.

(16) Makrilia, N.; Kollias, A.; Manolopoulos, L.; Syrigos, K. Cell Adhesion Molecules: Role and Clinical Significance in Cancer. *Cancer Investigation* **2009**, *27* (10), 1023-1037.

(17) Farahani, E.; Patra, H. K.; Jangamreddy, J. R.; Rashedi, I.; Kawalec, M.; Rao Pariti, R. K.; Batakis, P.; Wiechec, E. Cell Adhesion Molecules and Their Relation to (Cancer) Cell Stemness. *Carcinogenesis* **2014**, *35* (4), 747-759.

(18) Albelda, S. M. Role of Integrins and Other Cell Adhesion Molecules in Tumor Progression and Metastasis. *Laboratory Investigation; a journal of technical methods and pathology* **1993**, *68* (1), 4-17.

(19) Hillis, G. S.; Flapan, A. D. Cell Adhesion Molecules in Cardiovascular Disease: A Clinical Perspective. *Heart* **1998**, *79* (5), 429.

(20) Wu, T.; McGrath, K. C. Y.; Death, A. K. Cardiovascular Disease in Diabetic Nephropathy Patients: Cell Adhesion Molecules as Potential Markers? *Vascular health and risk management* **2005**, *1* (4), 309-316.

(21) Bacáková, L.; Filová, E.; Parizek, M.; Ruml, T.; Svorcik, V. Modulation of Cell Adhesion, Proliferation and Differentiation on Materials Designed for Body Implants. *Biotechnology Advances* **2011**, *29* (6), 739-767.

(22) Bacáková, L.; Filová, E.; Rypácek, F.; Svorcík, V.; Starý, V. Cell Adhesion on Artificial Materials for Tissue Engineering. *Physiological Research* **2004**, *53 Suppl 1*, S35-45.

(23) Pesáková, V.; Kubies, D.; Hulejová, H.; Himmlová, L. The Influence of Implant Surface Properties on Cell Adhesion and Proliferation. *Journal of Materials Science: Materials in Medicine* **2007**, *18* (3), 465-473.

(24) Helenius, J.; Heisenberg, C.-P.; Gaub, H. E.; Muller, D. J. Single-Cell Force Spectroscopy. *Journal of Cell Science* **2008**, *121* (11), 1785-1791.

(25) Guillaume-Gentil, O.; Potthoff, E.; Ossola, D.; Franz, C. M.; Zambelli, T.; Vorholt, J. A. Force-Controlled Manipulation of Single Cells: From AFM to FluidFM. *Trends in Biotechnology* **2014**, *32* (7), 381-388.

(26) Schubert, R.; Strohmeyer, N.; Bharadwaj, M.; Ramanathan, S. P.; Krieg, M.; Friedrichs, J.; Franz, C. M.; Muller, D. J. Assay for Characterizing the Recovery of Vertebrate Cells for Adhesion Measurements by Single-Cell Force Spectroscopy. *Febs Letters* **2014**, *588* (19), 3639-3648.

(27) Fernandes, T. F. D.; Saavedra-Villanueva, O.; Margeat, E.; Milhiet, P.-E.; Costa, L. Author Correction: Synchronous, Crosstalk-free Correlative AFM and Confocal Microscopies/Spectroscopies. *Scientific Reports* **2020**, *10* (1), 18385.

(28) Galbraith, C. G.; Galbraith, J. A. Super-Resolution Microscopy at a Glance. *Journal of Cell Science* **2011**, *124* (10), 1607-1611.

(29) Bertocchi, C.; Wang, Y.; Ravasio, A.; Hara, Y.; Wu, Y.; Sailov, T.; Baird, M. A.; Davidson, M. W.; Zaidel-Bar, R.; Toyama, Y.; et al. Nanoscale Architecture of Cadherin-based Cell Adhesions. *Nature Cell Biology* **2017**, *19* (1), 28-37.

(30) Chien, F.-C.; Dai, Y.-H.; Kuo, C. W.; Chen, P. Flexible Nanopillars to Regulate Cell Adhesion and Movement. *Nanotechnology* **2016**, *27* (47), 475101.

(31) Morton, P. E.; Parsons, M. Dissecting Cell Adhesion Architecture Using Advanced Imaging Techniques. *Cell Adhesion & Migration* **2011**, *5* (4), 351-359.

(32) Seebach, J.; Donnert, G.; Kronstein, R.; Werth, S.; Wojciak-Stothard, B.; Falzarano, D.; Mrowietz, C.; Hell, S. W.; Schnittler, H.-J. Regulation of Endothelial Barrier Function During Flow-Induced Conversion to an Arterial Phenotype. *Cardiovascular Research* **2007**, *75* (3), 598-607.

(33) Shaw, J. E.; Oreopoulos, J.; Wong, D.; Hsu, J. C. Y.; Yip, C. M. Coupling Evanescent-Wave Fluorescence Imaging and Spectroscopy with Scanning Probe Microscopy: Challenges and Insights from TIRF–AFM. *Surface and Interface Analysis* **2006**, *38* (11), 1459-1471.

(34) Gómez-Varela, A. I.; Stamov, D. R.; Miranda, A.; Alves, R.; Barata-Antunes, C.; Dambournet, D.; Drubin, D. G.; Paiva, S.; De Beule, P. A. A. Simultaneous Co-Localized Super-Resolution Fluorescence Microscopy and Atomic Force Microscopy: Combined SIM and AFM Platform for the Life Sciences. *Scientific Reports* **2020**, *10* (1), 1122.

(35) Odermatt, P. D.; Shivanandan, A.; Deschout, H.; Jankele, R.; Nievergelt, A. P.; Feletti, L.; Davidson, M. W.; Radenovic, A.; Fantner, G. E. High-Resolution Correlative Microscopy: Bridging the Gap between Single Molecule Localization Microscopy and Atomic Force Microscopy. *Nano Letters* **2015**, *15* (8), 4896-4904.

(36) Chacko, J. V.; Zanacchi, F. C.; Diaspro, A. Probing Cytoskeletal Structures by Coupling Optical Superresolution and AFM Techniques for a Correlative Approach. *Cytoskeleton (Hoboken)* **2013**, *70* (11), 729-740.

(37) Cazaux, S.; Sadoun, A.; Biarnes-Pelicot, M.; Martinez, M.; Obeid, S.; Bongrand, P.; Limozin, L.; Puech, P.-H. Synchronizing Atomic Force Microscopy Force Mode and Fluorescence Microscopy in Real Time for Immune Cell Stimulation and Activation Studies. *Ultramicroscopy* **2016**, *160*, 168-181.

(38) Friedrichs, J.; Legate, K. R.; Schubert, R.; Bharadwaj, M.; Werner, C.; Müller, D. J.; Benoit, M. A Practical Guide to Quantify Cell Adhesion Using Single-Cell Force Spectroscopy. *Methods* **2013**, *60* (2), 169-178.

(39) Potthoff, E.; Guillaume-Gentil, O.; Ossola, D.; Polesel-Maris, J.; LeibundGut-Landmann, S.; Zambelli, T.; Vorholt, J. A. Rapid and Serial Quantification of Adhesion Forces of Yeast and Mammalian Cells. *Plos One* **2012**, *7* (12), e52712.

(40) Sancho, A.; Vandersmissen, I.; Craps, S.; Luttun, A.; Groll, J. A New Strategy to Measure Intercellular Adhesion Forces in Mature Cell-Cell Contacts. *Scientific Reports* **2017**, *7*.

(41) Meister, A.; Gabi, M.; Behr, P.; Studer, P.; Voros, J.; Niedermann, P.; Bitterli, J.; Polesel-Maris, J.; Liley, M.; Heinzelmann, H.; et al. FluidFM: Combining Atomic Force Microscopy and Nanofluidics in a Universal Liquid Delivery System for Single Cell Applications and Beyond. *Nano Letters* **2009**, *9* (6), 2501-2507.

(42) Cohen, N.; Sarkar, S.; Hondroulis, E.; Sabhachandani, P.; Konry, T. Quantification of Intercellular Adhesion Forces Measured by Fluid Force Microscopy. *Talanta* **2017**, *174*, 409-413.

(43) Saha, P.; Duanis-Assaf, T.; Reches, M. Fundamentals and Applications of FluidFM Technology in Single-Cell Studies. *Advanced Materials Interfaces* **2020**, *7* (23), 2001115.

(44) Dörig, P.; Stiefel, P.; Behr, P.; Sarajlic, E.; Bijl, D.; Gabi, M.; Vörös, J.; Vorholt, J. A.; Zambelli, T. Force-Controlled Spatial Manipulation of Viable Mammalian Cells and Micro-Organisms by Means of FluidFM Technology. *Applied Physics Letters* **2010**, *97* (2), 023701.

(45) Guillaume-Gentil, O.; Zambelli, T.; Vorholt, J. A. Isolation of Single Mammalian Cells from Adherent Cultures by Fluidic Force Microscopy. *Lab on a Chip* **2014**, *14* (2), 402-414.

(46) Guillaume-Gentil, O.; Potthoff, E.; Ossola, D.; Dörig, P.; Zambelli, T.; Vorholt, J. A. Force-Controlled Fluidic Injection into Single Cell Nuclei. *Small* **2013**, *9* (11), 1904-1907.

(47) Amarouch, M. Y.; El Hilaly, J.; Mazouzi, D. AFM and FluidFM Technologies: Recent Applications in Molecular and Cellular Biology. *Scanning* **2018**, *2018*, 7801274.

(48) Zhang, H.; Huang, J.; Wang, Y.; Liu, R.; Huai, X.; Jiang, J.; Anfuso, C. Atomic Force Microscopy for Two-Dimensional Materials: A Tutorial Review. *Optics Communications* **2018**, *406*, 3-17.

(49) Johnson, D.; Hilal, N. Characterisation and Quantification of Membrane Surface Properties Using Atomic Force Microscopy: A Comprehensive Review. *Desalination* **2015**, *356*, 149-164.

(50) Li, M.; Liu, L.; Zambelli, T. FluidFM for Single-Cell Biophysics. *Nano Research* **2022**, *15* (2), 773-786.

(51) Meyer, G.; Amer, N. M. Novel Optical Approach to Atomic Force Microscopy. *Applied Physics Letters* **1988**, *53* (12), 1045-1047.

(52) Li, M.; Xi, N.; Wang, Y.; Liu, L. Advances in Atomic Force Microscopy for Single-Cell Analysis. *Nano Research* **2019**, *12* (4), 703-718.

(53) Hilal, N.; Bowen, W. R.; Alkhatib, L.; Ogunbiyi, O. A Review of Atomic Force Microscopy Applied to Cell Interactions with Membranes. *Chemical Engineering Research and Design* **2006**, *84* (4), 282-292.

(54) Kontomaris, S.-V. The Hertz Model in AFM Nanoindentation Experiments: Applications in Biological Samples and Biomaterials. *Micro and Nanosystems* **2018**, *10* (1), 11-22.

(55) Calabri, L.; Pugno, N.; Menozzi, C.; Valeri, S. AFM Nanoindentation: Tip Shape and Tip Radius of Curvature Effect on the Hardness Measurement. *Journal of Physics: Condensed Matter* **2008**, *20* (47), 474208.

(56) Stiefel, P.; Schmidt, F. I.; Dörig, P.; Behr, P.; Zambelli, T.; Vorholt, J. A.; Mercer, J. Cooperative Vaccinia Infection Demonstrated at the Single-Cell Level Using FluidFM. *Nano Letters* **2012**, *12* (8), 4219-4227.

(57) Martinez, V.; Forró, C.; Weydert, S.; Aebersold, M. J.; Dermutz, H.; Guillaume-Gentil, O.; Zambelli, T.; Vörös, J.; Demkó, L. Controlled Single-Cell Deposition and Patterning by Highly Flexible Hollow Cantilevers. *Lab on a Chip* **2016**, *16* (9), 1663-1674.

(58) Guillaume-Gentil, O.; Grindberg, R. V.; Kooger, R.; Dorwling-Carter, L.; Martinez, V.; Ossola, D.; Pilhofer, M.; Zambelli, T.; Vorholt, J. A. Tunable Single-Cell Extraction for Molecular Analyses. *Cell* **2016**, *166* (2), 506-516.

(59) Guillaume-Gentil, O.; Rey, T.; Kiefer, P.; Ibáñez, A. J.; Steinhoff, R.; Brönnimann, R.; Dorwling-Carter, L.; Zambelli, T.; Zenobi, R.; Vorholt, J. A. Single-Cell Mass Spectrometry of Metabolites Extracted from Live Cells by Fluidic Force Microscopy. *Analytical Chemistry* **2017**, *89* (9), 5017-5023.

(60) Dufrêne, Y. F.; Ando, T.; Garcia, R.; Alsteens, D.; Martinez-Martin, D.; Engel, A.; Gerber, C.; Müller, D. J. Imaging Modes of Atomic Force Microscopy for Application in Molecular and Cell Biology. *Nature Nanotechnology* **2017**, *12* (4), 295-307.

(61) Butt, H.-J.; Cappella, B.; Kappl, M. Force Measurements With the Atomic Force Microscope: Technique, Interpretation and Applications. *Surface Science Reports* **2005**, *59* (1-6), 1-152.

(62) Nguyen-Tri, P.; Ghassemi, P.; Carriere, P.; Nanda, S.; Assadi, A. A.; Nguyen, D. D. Recent Applications of Advanced Atomic Force Microscopy in Polymer Science: A Review. *Polymers* **2020**, *12* (5).

(63) Trache, A.; Meininger, G. A. Atomic Force Microscopy (AFM). *Current Protocols in Microbiology* **2008**, *8* (1), 2C.2.1-2C.2.17.

(64) Li, M.; Dang, D.; Liu, L.; Xi, N.; Wang, Y. Atomic Force Microscopy in Characterizing Cell Mechanics for Biomedical Applications: A Review. *IEEE Transactions on NanoBioscience* **2017**, *16* (6), 523-540.

(65) García, A. J.; Ducheyne, P.; Boettiger, D. Quantification of Cell Adhesion Using a Spinning Disc Device and Application to Surface-Reactive Materials. *Biomaterials* **1997**, *18* (16), 1091-1098.

(66) Kaplanski, G.; Farnarier, C.; Tissot, O.; Pierres, A.; Benoliel, A. M.; Alessi, M. C.; Kaplanski, S.; Bongrand, P. Granulocyte-Endothelium Initial Adhesion. Analysis of Transient Binding Events Mediated by E-selectin in a Laminar Shear Flow. *Biophysical Journal* **1993**, *64* (6), 1922-1933.

(67) Friedrichs, J.; Helenius, J.; Muller, D. J. Quantifying Cellular Adhesion to Extracellular Matrix Components by Single-Cell Force Spectroscopy. *Nature Protocols* **2010**, *5* (7), 1353-1361.

(68) Wysotzki, P.; Sancho, A.; Gimsa, J.; Groll, J. A Comparative Analysis of Detachment Forces and Energies in Initial and Mature Cell-Material Interaction. *Colloids and Surfaces B: Biointerfaces* **2020**, *190*, 110894.

(69) Dehullu, J.; Valotteau, C.; Herman-Bausier, P.; Garcia-Sherman, M.; Mittelviefhaus, M.; Vorholt, J. A.; Lipke, P. N.; Dufrêne, Y. F. Fluidic Force Microscopy Demonstrates That Homophilic Adhesion by Candida albicans Als Proteins Is Mediated by Amyloid Bonds between Cells. *Nano Letters* **2019**, *19* (6), 3846-3853.

(70) Potthoff, E.; Ossola, D.; Zambelli, T.; Vorholt, J. A. Bacterial Adhesion Force Quantification by Fluidic Force Microscopy. *Nanoscale* **2015**, *7* (9), 4070-4079.

(71) Potthoff, E.; Franco, D.; D'Alessandro, V.; Starck, C.; Falk, V.; Zambelli, T.; Vorholt, J. A.; Poulikakos, D.; Ferrari, A. Toward a Rational Design of Surface Textures Promoting Endothelialization. *Nano Letters* **2014**, *14* (2), 1069-1079.

(72) Sankaran, S.; Jaatinen, L.; Brinkmann, J.; Zambelli, T.; Vörös, J.; Jonkheijm, P. Cell Adhesion on Dynamic Supramolecular Surfaces Probed by Fluid Force Microscopy-Based Single-Cell Force Spectroscopy. *ACS Nano* **2017**, *11* (4), 3867-3874.

(73) Puech, P.-H.; Poole, K.; Knebel, D.; Muller, D. J. A New Technical Approach to Quantify Cell–Cell Adhesion Forces by AFM. *Ultramicroscopy* **2006**, *106* (8), 637-644.

(74) Taubenberger, A. V.; Hutmacher, D. W.; Muller, D. J. Single-Cell Force Spectroscopy, an Emerging Tool to Quantify Cell Adhesion to Biomaterials. *Tissue Engineering Part B-Reviews* **2014**, *20* (1), 40-55.

(75) Taubenberger, A.; Cisneros, D. A.; Friedrichs, J.; Puech, P.-H.; Muller, D. J.; Franz, C. M. Revealing Early Steps of Alpha2Beta1 Integrin-Mediated Adhesion to Collagen Type I by Using Single-Cell Force Spectroscopy. *Molecular Biology of the Cell* **2007**, *18* (5), 1634-1644.

(76) Bell, G. I. Models for the Specific Adhesion of Cells to Cells. *Science* **1978**, *200* (4342), 618-627.

(77) Barsegov, V.; Thirumalai, D. Dynamics of Unbinding of Cell Adhesion Molecules: Transition from Catch to Slip Bonds. *Proceedings of the National Academy of Sciences of the United States of America* **2005**, *102* (6), 1835-1839.

(78) Evans, E. A.; Calderwood, D. A. Forces and Bond Dynamics in Cell Adhesion. *Science* **2007**, *316* (5828), 1148-1153.

(79) Evans, E.; Ritchie, K. Dynamic Strength of Molecular Adhesion Bonds. *Biophysical Journal* **1997**, *72* (4), 1541-1555.

(80) Sun, M.; Graham, J. S.; Hegedüs, B.; Marga, F.; Zhang, Y.; Forgacs, G.; Grandbois, M. Multiple Membrane Tethers Probed by Atomic Force Microscopy. *Biophysical Journal* **2005**, *89* (6), 4320-4329.

(81) Franz, C. M.; Puech, P. H. Atomic Force Microscopy: A Versatile Tool for Studying Cell Morphology, Adhesion and Mechanics. *Cellular and Molecular Bioengineering* **2008**, *1* (4), 289-300.

(82) Benoit, M.; Gabriel, D.; Gerisch, G.; Gaub, H. E. Discrete Interactions in Cell Adhesion Measured by Single-Molecule Force Spectroscopy. *Nature Cell Biology* **2000**, *2* (6), 313-317.

(83) Panorchan, P.; Thompson, M. S.; Davis, K. J.; Tseng, Y.; Konstantopoulos, K.; Wirtz, D. Single-Molecule Analysis of Cadherin-Mediated Cell-Cell Adhesion. *Journal of Cell Science* **2006**, *119* (1), 66-74.

(84) Friedrichs, J.; Helenius, J.; Müller, D. J. Stimulated Single-Cell Force Spectroscopy to Quantify Cell Adhesion Receptor Crosstalk. *PROTEOMICS* **2010**, *10* (7), 1455-1462.

(85) Selhuber-Unkel, C.; Erdmann, T.; Lopez-Garcia, M.; Kessler, H.; Schwarz, U. S.; Spatz, J. P. Cell Adhesion Strength Is Controlled by Intermolecular Spacing of Adhesion Receptors. *Biophysical Journal* **2010**, *98* (4), 543-551.

(86) Ducker, W. A.; Senden, T. J.; Pashley, R. M. Direct Measurement of Colloidal Forces Using an Atomic Force Microscope. *Nature* **1991**, *353* (6341), 239-241.

(87) Gan, Y. Invited Review Article: A Review of Techniques for Attaching Micro- and Nanoparticles to a Probe's Tip for Surface Force and Near-Field Optical Measurements. *Review of Scientific Instruments* **2007**, *78* (8), 081101.

(88) Kuznetsov, V.; Papastavrou, G. Note: Mechanically and Chemically Stable Colloidal Probes from Silica Particles for Atomic Force Microscopy. *Review of Scientific Instruments* **2012**, *83* (11), 116103.

(89) Darling, E. M.; Zauscher, S.; Guilak, F. Viscoelastic Properties of Zonal Articular Chondrocytes Measured by Atomic Force Microscopy. *Osteoarthritis and Cartilage* **2006**, *14* (6), 571-579.

(90) Darling, E. M.; Topel, M.; Zauscher, S.; Vail, T. P.; Guilak, F. Viscoelastic Properties of Human Mesenchymally-derived Stem Cells and Primary Osteoblasts, Chondrocytes, and Adipocytes. *Journal of Biomechanics* **2008**, *41* (2), 454-464.

(91) Chim, Y. H.; Mason, L. M.; Rath, N.; Olson, M. F.; Tassieri, M.; Yin, H. A One-Step Procedure to Probe the Viscoelastic Properties of Cells by Atomic Force Microscopy. *Scientific Reports* **2018**, *8* (1), 14462.

(92) Schneider, A.; Francius, G.; Obeid, R.; Schwinté, P.; Hemmerlé, J.; Frisch, B.; Schaaf, P.; Voegel, J.-C.; Senger, B.; Picart, C. Polyelectrolyte Multilayers with a Tunable Young's Modulus: Influence of Film Stiffness on Cell Adhesion. *Langmuir* **2006**, *22* (3), 1193-1200.

(93) Dörig, P.; Ossola, D.; Truong, A. M.; Graf, M.; Stauffer, F.; Voros, J.; Zambelli, T. Exchangeable Colloidal AFM Probes for the Quantification of Irreversible and Long-Term Interactions. *Biophysical Journal* **2013**, *105* (2), 463-472.

(94) Lüchtefeld, I.; Bartolozzi, A.; Mejía Morales, J.; Dobre, O.; Basso, M.; Zambelli, T.; Vassalli, M. Elasticity Spectra as a Tool to Investigate Actin Cortex Mechanics. *Journal of nanobiotechnology* **2020**, *18* (1), 147-147.

(95) Efremov, Y. M.; Bagrov, D. V.; Kirpichnikov, M. P.; Shaitan, K. V. Application of the Johnson–Kendall–Roberts Model in AFM-based Mechanical Measurements on Cells and Gel. *Colloids and Surfaces B: Biointerfaces* **2015**, *134*, 131-139.

(96) Chu, Y.-S.; Dufour, S.; Thiery, J. P.; Perez, E.; Pincet, F. Johnson-Kendall-Roberts Theory Applied to Living Cells. *Physical review letters* **2005**, *94* (2), 028102.

(97) Bouchonville, N.; Meyer, M.; Gaude, C.; Gay, E.; Ratel, D.; Nicolas, A. AFM Mapping of the Elastic Properties of Brain Tissue Reveals kPa µm-1 Gradients of Rigidity. *Soft Matter* **2016**, *12* (29), 6232-6239.

(98) Guz, N.; Dokukin, M.; Kalaparthi, V.; Sokolov, I. If Cell Mechanics can be Described by Elastic Modulus: Study of Different Models and Probes Used in Indentation Experiments. *Biophysical Journal* **2014**, *107* (3), 564-575.

(99) Li, M.; Liu, L.-q.; Xi, N.; Wang, Y.-c. Nanoscale Monitoring of Drug Actions on Cell Membrane Using Atomic Force Microscopy. *Acta Pharmacologica Sinica* **2015**, *36* (7), 769-782.

(100) Dintwa, E.; Tijskens, E.; Ramon, H. On the Accuracy of the Hertz Model to Describe the Normal Contact of Soft Elastic Spheres. *Granular Matter* **2008**, *10* (3), 209-221.

(101) Abbe, E. Beiträge zur Theorie des Mikroskops und der mikroskopischen Wahrnehmung. *Archiv für Mikroskopische Anatomie* **1873**, *9* (1), 413-468.

(102) Masters, B. The Development of Fluorescence Microscopy. In *Encyclopedia of Life Science*, John Wiley & Sons, **2010**.

(103) Fish, K. N. Total Internal Reflection Fluorescence (TIRF) Microscopy. *Current Protocols in Cytometry* **2009**, *50* (1), 12.18.11-12.18.13.

(104) Klein, T.; Löschberger, A.; Proppert, S.; Wolter, S.; van de Linde, S.; Sauer, M. Live-cell dSTORM with SNAP-tag Fusion Proteins. *Nature Methods* **2011**, *8* (1), 7-9.

(105) Benke, A.; Manley, S. Live-Cell dSTORM of Cellular DNA Based on Direct DNA Labeling. *Chembiochem* **2012**, *13* (2), 298-301.

(106) Lee, S.-H.; Shin, J. Y.; Lee, A.; Bustamante, C. Counting Single Photoactivatable Fluorescent Molecules by Photoactivated Localization Microscopy (PALM). *Proceedings of the National Academy of Sciences* **2012**, *109* (43), 17436-17441.

(107) Shroff, H.; White, H.; Betzig, E. Photoactivated Localization Microscopy (PALM) of Adhesion Complexes. *Current Protocols in Cell Biology* **2013**, *58* (1), 4.21.21-24.21.28.

(108) Huang, B.; Bates, M.; Zhuang, X. Super-Resolution Fluorescence Microscopy. *Annual Review of Biochemistry* **2009**, *78* (1), 993-1016.

(109) Heilemann, M. Fluorescence Microscopy Beyond the Diffraction Limit. *Journal of Biotechnology* **2010**, *149* (4), 243-251.

(110) Behlke, M. A.; Huang, L.; Bogh, L.; Rose, S. D.; Devor, E. J. Fluorescence and Fluorescence Applications. *Integrated DNA Technologies* **2005**, 1-13.

(111) Sanderson, M. J.; Smith, I.; Parker, I.; Bootman, M. D. Fluorescence Microscopy. *Cold Spring Harbor protocols* **2014**, *2014* (10), 1042-1065.

(112) Berezin, M. Y.; Achilefu, S. Fluorescence Lifetime Measurements and Biological Imaging. *Chemical Reviews* **2010**, *110* (5), 2641-2684.

(113) Lichtman, J. W.; Conchello, J.-A. Fluorescence Microscopy. *Nature Methods* **2005**, *2* (12), 910-919.

(114) Lower, S. K.; El-Sayed, M. A. The Triplet State and Molecular Electronic Processes in Organic Molecules. *Chemical Reviews* **1966**, *66* (2), 199-241.

(115) Giepmans, B. N. G.; Adams, S. R.; Ellisman, M. H.; Tsien, R. Y. The Fluorescent Toolbox for Assessing Protein Location and Function. *Science* **2006**, *312* (5771), 217-224.

(116) Gonçalves, M. S. T. Fluorescent Labeling of Biomolecules with Organic Probes. *Chemical Reviews* **2009**, *109* (1), 190-212.

(117) Liu, J.; Cui, Z. Fluorescent Labeling of Proteins of Interest in Live Cells: Beyond Fluorescent Proteins. *Bioconjugate Chemistry* **2020**, *31* (6), 1587-1595.

(118) Toseland, C. P. Fluorescent Labeling and Modification of Proteins. *Journal of chemical biology* **2013**, *6* (3), 85-95.

(119) Kargozar, S.; Hoseini, S. J.; Milan, P. B.; Hooshmand, S.; Kim, H.-W.; Mozafari, M. Quantum Dots: A Review from Concept to Clinic. *Biotechnology Journal* **2020**, *15* (12), 2000117.

(120) Fu, C.-C.; Lee, H.-Y.; Chen, K.; Lim, T.-S.; Wu, H.-Y.; Lin, P.-K.; Wei, P.-K.; Tsao, P.-H.; Chang, H.-C.; Fann, W. Characterization and Application of Single Fluorescent Nanodiamonds as Cellular Biomarkers. *Proceedings of the National Academy of Sciences* **2007**, *104* (3), 727-732.

(121) Sahoo, H. Fluorescent Labeling Techniques in Biomolecules: A Flashback. *RSC Advances* **2012**, *2* (18), 7017-7029.

(122) Michalet, X.; Pinaud, F. F.; Bentolila, L. A.; Tsay, J. M.; Doose, S.; Li, J. J.; Sundaresan, G.; Wu, A. M.; Gambhir, S. S.; Weiss, S. Quantum Dots for Live Cells, in Vivo Imaging, and Diagnostics. *Science* **2005**, *307* (5709), 538-544.

(123) Shimomura, O.; Johnson, F. H.; Saiga, Y. Extraction, Purification and Properties of Aequorin, a Bioluminescent Protein from the Luminous Hydromedusan, Aequorea. *Journal of Cellular and Comparative Physiology* **1962**, *59* (3), 223-239.

(124) Prasher, D. C.; Eckenrode, V. K.; Ward, W. W.; Prendergast, F. G.; Cormier, M. J. Primary Structure of the Aequorea Victoria Green-Fluorescent Protein. *Gene* **1992**, *111* (2), 229-233.

(125) Specht, E. A.; Braselmann, E.; Palmer, A. E. A Critical and Comparative Review of Fluorescent Tools for Live-Cell Imaging. *Annual Review of Physiology* **2017**, *79* (1), 93-117.

(126) Suzuki, T.; Matsuzaki, T.; Hagiwara, H.; Aoki, T.; Takata, K. Recent Advances in Fluorescent Labeling Techniques for Fluorescence Microscopy. *ACTA HISTOCHEMICA ET CYTOCHEMICA* **2007**, *40* (5), 131-137.

(127) Cranfill, P. J.; Sell, B. R.; Baird, M. A.; Allen, J. R.; Lavagnino, Z.; de Gruiter, H. M.; Kremers, G.-J.; Davidson, M. W.; Ustione, A.; Piston, D. W. Quantitative Assessment of Fluorescent Proteins. *Nature Methods* **2016**, *13* (7), 557-562.

(128) Haugland, R. P.; Spence, M. T. Z.; Johnson, I. D.; Basey, A. *The Handbook : A Guide to Fluorescent Probes and Labeling Technologies*; Eugene (Or.) : Molecular probes, **2005**.

(129) Lee, S.; Xie, J.; Chen, X. Peptide-Based Probes for Targeted Molecular Imaging. *Biochemistry* **2010**, *49* (7), 1364-1376.

(130) Riedl, J.; Crevenna, A. H.; Kessenbrock, K.; Yu, J. H.; Neukirchen, D.; Bista, M.; Bradke, F.; Jenne, D.; Holak, T. A.; Werb, Z.; et al. Lifeact: A Versatile Marker to Visualize F-actin. *Nature Methods* **2008**, *5* (7), 605-607.

(131) Yuste, R. Fluorescence Microscopy Today. *Nature Methods* **2005**, *2* (12), 902-904.

(132) Alivisatos, A. P.; Gu, W.; Larabell, C. Quantum Dots as Cellular Probes. *Annual Review of Biomedical Engineering* **2005**, *7* (1), 55-76.

(133) Jaiswal, J. K.; Mattoussi, H.; Mauro, J. M.; Simon, S. M. Long-term Multiple Color Imaging of Live Cells Using Quantum Dot Bioconjugates. *Nature Biotechnology* **2003**, *21* (1), 47-51.

(134) Derfus, A. M.; Chan, W. C. W.; Bhatia, S. N. Probing the Cytotoxicity of Semiconductor Quantum Dots. *Nano Letters* **2004**, *4* (1), 11-18.

(135) Piston, D. W.; Kremers, G.-J. Fluorescent Protein FRET: The Good, the Bad and the Ugly. *Trends in Biochemical Sciences* **2007**, *32* (9), 407-414.

(136) Jares-Erijman, E. A.; Jovin, T. M. FRET Imaging. *Nature Biotechnology* **2003**, *21* (11), 1387-1395.

(137) Coling, D.; Kachar, B. Principles and Application of Fluorescence Microscopy. *Current protocols in molecular biology* **1998**, *44* (1), 14.10.11-14.10.11.

(138) Waters, J. C. Live-Cell Fluorescence Imaging. In *Methods in Cell Biology*, Vol. 81; Academic Press, **2007**; 115-140.

(139) Waters, J. C. Accuracy and Precision in Quantitative Fluorescence Microscopy. *Journal of Cell Biology* **2009**, *185* (7), 1135-1148.

(140) De Rosa, S. C. A Brilliant New Addition to the Fluorescent Probe Toolbox. *Cytometry. Part A: the Journal of the International Society for Analytical Cytology* **2012**, *81* (6), 445-446.

(141) Sacher, R. Microscope Immersion Oil. *Microscopy Today* **2000**, *8* (8), 33-35.

(142) Reihani, S. N. S.; Oddershede, L. B. Optimizing Immersion Media Refractive Index Improves Optical Trapping by Compensating Spherical Aberrations. *Optics Letters* **2007**, *32* (14), 1998-2000.

(143) Ross, S. T.; Allen, J. R.; Davidson, M. W. Chapter 2 - Practical Considerations of Objective Lenses for Application in Cell Biology. In *Methods in Cell Biology*, Waters, J. C., Wittman, T. Eds.; Vol. 123; Academic Press, **2014**; 19-34.

(144) Hell, S. W.; Wichmann, J. Breaking the Diffraction Resolution Limit by Stimulated Emission: Stimulated-Emission-Depletion Fluorescence Microscopy. *Optics Letters* **1994**, *19* (11), 780-782.

(145) Caplan, J.; Niethammer, M.; Taylor, R. M.; Czymmek, K. J. The Power of Correlative Microscopy: Multi-Modal, Multi-Scale, Multi-Dimensional. *Current Opinion in Structural Biology* **2011**, *21* (5), 686-693.

(146) Parlanti, P.; Cappello, V. Microscopes, Tools, Probes, and Protocols: A Guide in the Route of Correlative Microscopy for Biomedical Investigation. *Micron* **2022**, *152*, 103182.

(147) Jahn, K. A.; Barton, D. A.; Kobayashi, K.; Ratinac, K. R.; Overall, R. L.; Braet, F. Correlative Microscopy: Providing New Understanding in the Biomedical and Plant Sciences. *Micron* **2012**, *43* (5), 565-582.

(148) Hauser, M.; Wojcik, M.; Kim, D.; Mahmoudi, M.; Li, W.; Xu, K. Correlative Super-Resolution Microscopy: New Dimensions and New Opportunities. *Chemical Reviews* **2017**, *117* (11), 7428-7456.

(149) Mironov, A. A.; Beznoussenko, G. V. Correlative Microscopy: A Potent Tool for the Study of Rare or Unique Cellular and Tissue Events. *Journal of Microscopy* **2009**, *235* (3), 308-321.

(150) Timmermans, F. J.; Otto, C. Contributed Review: Review of Integrated Correlative Light and Electron Microscopy. *Review of Scientific Instruments* **2015**, *86* (1), 011501.

(151) Ando, T.; Bhamidimarri, S. P.; Brending, N.; Colin-York, H.; Collinson, L.; De Jonge, N.; de Pablo, P. J.; Debroye, E.; Eggeling, C.; Franck, C.; et al. The 2018 Correlative Microscopy Techniques Roadmap. *Journal of Physics D: Applied Physics* **2018**, *51* (44), 443001.

(152) Giepmans, B. N. G. Bridging Fluorescence Microscopy and Electron Microscopy. *Histochemistry and Cell Biology* **2008**, *130* (2), 211.

(153) Begemann, I.; Galic, M. Correlative Light Electron Microscopy: Connecting Synaptic Structure and Function. *Frontiers in Synaptic Neuroscience* **2016**, *8* (28).

(154) Lee, W.-C. A.; Bonin, V.; Reed, M.; Graham, B. J.; Hood, G.; Glattfelder, K.; Reid, R. C. Anatomy and Function of an Excitatory Network in the Visual Cortex. *Nature* **2016**, *532* (7599), 370-374.

(155) Briggman, K. L.; Helmstaedter, M.; Denk, W. Wiring Specificity in the Direction-Selectivity Circuit of the Retina. *Nature* **2011**, *471* (7337), 183-188.

(156) Modla, S.; Czymmek, K. J. Correlative Microscopy: A Powerful Tool for Exploring Neurological Cells and Tissues. *Micron* **2011**, *42* (8), 773-792.

(157) Fermie, J.; Liv, N.; ten Brink, C.; van Donselaar, E. G.; Müller, W. H.; Schieber, N. L.; Schwab, Y.; Gerritsen, H. C.; Klumperman, J. Single Organelle Dynamics Linked to 3D Structure by Correlative Live-Cell Imaging and 3D Electron Microscopy. *Traffic* **2018**, *19* (5), 354-369.

(158) Miranda, A.; Gómez-Varela, A. I.; Stylianou, A.; Hirvonen, L. M.; Sánchez, H.; De Beule, P. A. A. How Did Correlative Atomic Force Microscopy and Super-Resolution Microscopy Evolve in the Quest for Unravelling Enigmas in Biology? *Nanoscale* **2021**, *13* (4), 2082-2099.

(159) Smith, C. Microscopy: Two Microscopes are Better Than One. *Nature* **2012**, *492* (7428), 293-297.

(160) Zhou, L.; Cai, M.; Tong, T.; Wang, H. Progress in the Correlative Atomic Force Microscopy and Optical Microscopy. *Sensors* **2017**, *17* (4), 938-952.

(161) El-Kirat-Chatel, S.; Dufrêne, Y. F. Nanoscale Imaging of the Candida–Macrophage Interaction Using Correlated Fluorescence-Atomic Force Microscopy. *ACS Nano* **2012**, *6* (12), 10792-10799.

(162) Mathur, A. B.; Truskey, G. A.; Reichert, W. M. Atomic Force and Total Internal Reflection Fluorescence Microscopy for the Study of Force Transmission in Endothelial Cells. *Biophysical Journal* **2000**, *78* (4), 1725-1735.

(163) Roder, P.; Hille, C. Local Tissue Manipulation via a Force- and Pressure-Controlled AFM Micropipette for Analysis of Cellular Processes. *Scientific Reports* **2018**, *8* (1), 5892.

(164) Kassies, R.; van der Werf, K. O.; Lenferink, A.; Hunter, C. N.; Olsen, J. D.; Subramaniam, V.; Otto, C. Combined AFM and Confocal Fluorescence Microscope for Applications in Bio-Nanotechnology. *Journal of Microscopy* **2005**, *217* (1), 109-116.

(165) Laskowski, P. R.; Pfreundschuh, M.; Stauffer, M.; Ucurum, Z.; Fotiadis, D.; Muller, D. J. High-Resolution Imaging and Multiparametric Characterization of Native Membranes by Combining Confocal Microscopy and an Atomic Force Microscopy-Based Toolbox. *ACS Nano* **2017**, *11* (8), 8292-8301.

(166) Monserrate, A.; Casado, S.; Flors, C. Correlative Atomic Force Microscopy and Localization-Based Super-Resolution Microscopy: Revealing Labelling and Image Reconstruction Artefacts. *Chemphyschem* **2014**, *15* (4), 647-650.

(167) Bondia, P.; Casado, S.; Flors, C. Correlative Super-Resolution Fluorescence Imaging and Atomic Force Microscopy for the Characterization of Biological Samples. *Methods in Molecular Biology* **2017**, *1663*, 105-113.

(168) Miller, H.; Zhou, Z.; Shepherd, J.; Wollman, A. J. M.; Leake, M. C. Single-Molecule Techniques in Biophysics: A Review of the Progress in Methods and Applications. *Reports on Progress in Physics* **2017**, *81* (2), 024601.

(169) Bhat, S. V.; Sultana, T.; Kornig, A.; McGrath, S.; Shahina, Z.; Dahms, T. E. S. Correlative Atomic Force Microscopy Quantitative Imaging-Laser Scanning Confocal Microscopy Quantifies the Impact of Stressors on Live Cells in Real-Time. *Scientific Reports* **2018**, *8* (1), 8305-0314.

(170) Shinde, A.; Illath, K.; Gupta, P.; Shinde, P.; Lim, K.-T.; Nagai, M.; Santra, T. S. A Review of Single-Cell Adhesion Force Kinetics and Applications. *Cells* **2021**, *10* (3), 577.

(171) da Rosa Franchi Santos, L. F.; Costa, N. T.; Maes, M.; Simão, A. N. C.; Dichi, I. Influence of Treatments on Cell Adhesion Molecules in Patients with Systemic Lupus Erythematosus and Rheumatoid Arthritis: A Review. *Inflammopharmacology* **2020**, *28* (2), 363-384.

(172) Hirohashi, S.; Kanai, Y. Cell Adhesion System and Human Cancer Morphogenesis. *Cancer Science* **2003**, *94* (7), 575-581.

(173) Kobayashi, H.; Boelte, C. K.; Lin, P. C. Endothelial Cell Adhesion Molecules and Cancer Progression. *Current Medicinal Chemistry* **2007**, *14* (4), 377-386.

(174) Petruzzelli, L.; Takami, M.; Humes, H. D. Structure and Function of Cell Adhesion Molecules. *The American Journal of Medicine* **1999**, *106* (4), 467-476.

(175) Bachir, A. I.; Horwitz, A. R.; Nelson, W. J.; Bianchini, J. M. Actin-Based Adhesion Modules Mediate Cell Interactions with the Extracellular Matrix and Neighboring Cells. *Cold Spring Harbor Perspectives in Biology* **2017**, *9* (7), a023234.

(176) Ungai-Salánki, R.; Peter, B.; Gerecsei, T.; Orgovan, N.; Horvath, R.; Szabó, B. A Practical Review on the Measurement Tools for Cellular Adhesion Force. *Advances in Colloid and Interface Science* **2019**, *269*, 309-333.

(177) Burute, M.; Thery, M. Spatial Segregation Between Cell-Cell and Cell-Matrix Adhesions. *Current Opinion in Cell Biology* **2012**, *24* (5), 628-636.

(178) Ren, G.; Roberts, A. I.; Shi, Y. Adhesion Molecules: Key Players in Mesenchymal Stem Cell-Mediated Immunosuppression. *Cell Adhesion & Migration* **2011**, *5* (1), 20-22.

(179) Zamir, E.; Geiger, B. Components of Cell-Matrix Adhesions. *Journal of Cell Science* **2001**, *114* (20), 3577-3579.

(180) Barczyk, M.; Carracedo, S.; Gullberg, D. Integrins. *Cell and Tissue Research* **2009**, *339* (1), 269-280.

(181) Geiger, B.; Bershadsky, A.; Pankov, R.; Yamada, K. M. Transmembrane Crosstalk Between the Extracellular Matrix and the Cytoskeleton. *Nature Reviews Molecular Cell Biology* **2001**, *2* (11), 793-805.

(182) Harjanto, D.; Zaman, M. H. Matrix Mechanics and Receptor-Ligand Interactions in Cell Adhesion. *Organic and Biomolecular Chemistry* **2010**, *8* (2), 299-304.

(183) Harjunpää, H.; Llort Asens, M.; Guenther, C.; Fagerholm, S. C. Cell Adhesion Molecules and Their Roles and Regulation in the Immune and Tumor Microenvironment. *Frontiers in Immunology* **2019**, *10*, Review.

(184) Ley, K.; Laudanna, C.; Cybulsky, M. I.; Nourshargh, S. Getting to the Site of Inflammation: The Leukocyte Adhesion Cascade Updated. *Nature Reviews Immunology* **2007**, *7* (9), 678-689.

(185) McEver, R. P. Selectins: Initiators of Leucocyte Adhesion and Signalling at the Vascular Wall. *Cardiovascular Research* **2015**, *107* (3), 331-339.

(186) McEver, R. P.; Zhu, C. Rolling Cell Adhesion. *Annual review of cell and developmental biology* **2010**, *26*, 363-396.

(187) Rougon, G.; Hobert, O. New Insights into the Divresity and Function of Neuronal Immunoglobulin Superfamily Molecules. *Annual Review of Neuroscience* **2003**, *26* (1), 207-238.

(188) Wai Wong, C.; Dye, D. E.; Coombe, D. R. The Role of Immunoglobulin Superfamily Cell Adhesion Molecules in Cancer Metastasis. *International Journal of Cell Biology* **2012**, *2012*, 340296.

(189) Biswas, K. H.; Zaidel-Bar, R. Early Events in the Assembly of E-cadherin Adhesions. *Experimental Cell Research* **2017**, *358* (1), 14-19.

(190) Patel, S. D.; Chen, C. P.; Bahna, F.; Honig, B.; Shapiro, L. Cadherin-Mediated Cell–Cell Adhesion: Sticking Together as a Family. *Current Opinion in Structural Biology* **2003**, *13* (6), 690-698.

(191) Huntley, G. W.; Gil, O.; Bozdagi, O. The Cadherin Family of Cell Adhesion Molecules: Multiple Roles in Synaptic Plasticity. *The Neuroscientist* **2002**, *8* (3), 221-233.

(192) Saito, M.; Tucker, D. K.; Kohlhorst, D.; Niessen, C. M.; Kowalczyk, A. P. Classical and Desmosomal Cadherins at a Glance. *Journal of Cell Science* **2012**, *125* (11), 2547-2552.

(193) Pancho, A.; Aerts, T.; Mitsogiannis, M. D.; Seuntjens, E. Protocadherins at the Crossroad of Signaling Pathways. *Frontiers in Molecular Neuroscience* **2020**, *13* (117).

(194) Hartsock, A.; Nelson, W. J. Adherens and Tight Junctions: Structure, Function and Connections to the Actin Cytoskeleton. *Biochimica et biophysica acta* **2008**, *1778* (3), 660-669.

(195) Campbell, H. K.; Maiers, J. L.; DeMali, K. A. Interplay Between Tight Junctions and Adherens Junctions. *Experimental Cell Research* **2017**, *358* (1), 39-44.

(196) Brown, R. C.; Davis, T. P. Calcium Modulation of Adherens and Tight Junction Function. *Stroke* **2002**, *33* (6), 1706-1711.

(197) Hynes, R. O. Cell Adhesion: Old and New Questions. *Trends in Genetics* **1999**, *15* (12), M33-M37.

(198) Garrod, D. R.; Merritt, A. J.; Nie, Z. Desmosomal Cadherins. *Current Opinion in Cell Biology* **2002**, *14* (5), 537-545.

(199) Green, K. J.; Simpson, C. L. Desmosomes: New Perspectives on a Classic. *Journal of Investigative Dermatology* **2007**, *127* (11), 2499-2515.

(200) Holthöfer, B.; Windoffer, R.; Troyanovsky, S.; Leube, R. E. Structure and Function of Desmosomes. In *International Review of Cytology*, Vol. 264; Academic Press, **2007**; 65-163.

(201) Kowalczyk, A. P.; Green, K. J. Chapter Five - Structure, Function, and Regulation of Desmosomes. In *Progress in Molecular Biology and Translational Science*, van Roy, F. Ed.; Vol. 116; Academic Press, **2013**; 95-118.

(202) Feldman, G. J.; Mullin, J. M.; Ryan, M. P. Occludin: Structure, Function and Regulation. *Advanced Drug Delivery Reviews* **2005**, *57* (6), 883-917.

(203) Cummins, P. M. Occludin: One Protein, Many Forms. *Molecular and cellular biology* **2012**, *32* (2), 242-250.

(204) Berrier, A. L.; Yamada, K. M. Cell-Matrix Adhesion. *Journal of Cellular Physiology* **2007**, *213* (3), 565-573.

(205) Deschout, H.; Platzman, I.; Sage, D.; Feletti, L.; Spatz, J. P.; Radenovic, A. Investigating Focal Adhesion Substructures by Localization Microscopy. *Biophysical Journal* **2017**, *113* (11), 2508-2518.

(206) Burridge, K.; Guilluy, C. Focal Adhesions, Stress Fibers and Mechanical Tension. *Experimental Cell Research* **2016**, *343* (1), 14-20.

(207) Gallant, N. D.; Michael, K. E.; Garcia, A. J. Cell Adhesion Strengthening: Contributions of Adhesive Area, Integrin Binding, and Focal Adhesion Assembly. *Molecular Biology of the Cell* **2005**, *16* (9), 4329-4340.

(208) Geiger, B.; Spatz, J. P.; Bershadsky, A. D. Environmental Sensing Through Focal Adhesions. *Nature Reviews Molecular Cell Biology* **2009**, *10* (1), 21-33.

(209) Kanchanawong, P.; Shtengel, G.; Pasapera, A. M.; Ramko, E. B.; Davidson, M. W.; Hess, H. F.; Waterman, C. M. Nanoscale Architecture of Integrin-based Cell Adhesions. *Nature* **2010**, *468* (7323), 580-584.

(210) Barnett, S. F. H.; Kanchanawong, P. Visualizing the 'Backbone' of Focal Adhesions. *Emerging Topics in Life Sciences* **2018**, *2*, 677-680.

(211) Zaidel-Bar, R.; Ballestrem, C.; Kam, Z.; Geiger, B. Early Molecular Events in the Assembly of Matrix Adhesions at the Leading Edge of Migrating Cells. *Journal of Cell Science* **2003**, *116* (22), 4605-4613.

(212) Liu, J.; Wang, Y.; Goh Wah, I.; Goh, H.; Baird Michelle, A.; Ruehland, S.; Teo, S.; Bate, N.; Critchley David, R.; Davidson Michael, W.; et al. Talin Determines the Nanoscale Architecture of Focal Adhesions. *Proceedings of the National Academy of Sciences* **2015**, *112* (35), E4864-E4873.

(213) Burridge, K. Focal Adhesions: A Personal Perspective on a Half Century of Progress. *The FEBS Journal* **2017**, *284* (20), 3355-3361.

(214) Klapholz, B.; Brown, N. H. Talin – The Master of Integrin Adhesions. *Journal of Cell Science* **2017**, *130* (15), 2435-2446.

(215) Cavalcanti-Adam, E. A.; Volberg, T.; Micoulet, A.; Kessler, H.; Geiger, B.; Spatz, J. P. Cell Spreading and Focal Adhesion Dynamics are Regulated by Spacing of Integrin Ligands. *Biophysical Journal* **2007**, *92* (8), 2964-2974.

(216) Arnold, M.; Cavalcanti-Adam, E. A.; Glass, R.; Blummel, J.; Eck, W.; Kantlehner, M.; Kessler, H.; Spatz, J. P. Activation of Integrin Function by Nanopatterned Adhesive Interfaces. *Chemphyschem* **2004**, *5* (3), 383-388.

(217) Diener, A.; Nebe, B.; Luthen, F.; Becker, P.; Beck, U.; Neumann, H. G.; Rychly, J. Control of Focal Adhesion Dynamics by Material Surface Characteristics. *Biomaterials* **2005**, *26* (4), 383-392.

(218) Pelham Robert, J.; Wang, Y.-l. Cell Locomotion and Focal Adhesions are Regulated by Substrate Flexibility. *Proceedings of the National Academy of Sciences* **1997**, *94* (25), 13661-13665.

(219) Bhat, A. A.; Uppada, S.; Achkar, I. W.; Hashem, S.; Yadav, S. K.; Shanmugakonar, M.; Al-Naemi, H. A.; Haris, M.; Uddin, S. Tight Junction Proteins and Signaling Pathways in Cancer and Inflammation: A Functional Crosstalk. *Frontiers in physiology* **2019**, *9* (1942), Review.

(220) Green, K. J.; Jaiganesh, A.; Broussard, J. A. Desmosomes: Essential Contributors to an Integrated Intercellular Junction Network. In *F1000Research*, 2019; Vol. 8.

(221) Yang, R.; Broussard, J. A.; Green, K. J.; Espinosa, H. D. Techniques to Stimulate and Interrogate Cell–Cell Adhesion Mechanics. *Extreme Mechanics Letters* **2018**, *20*, 125-139.

(222) Tsukita, S.; Furuse, M.; Itoh, M. Multifunctional Strands in Tight Junctions. *Nature Reviews Molecular Cell Biology* **2001**, *2* (4), 285-293.

(223) Zihni, C.; Mills, C.; Matter, K.; Balda, M. S. Tight Junctions: From Simple Barriers to Multifunctional Molecular Gates. *Nature Reviews Molecular Cell Biology* **2016**, *17* (9), 564-580.

(224) Sawada, N.; Murata, M.; Kikuchi, K.; Osanai, M.; Tobioka, H.; Kojima, T.; Chiba, H. Tight Junctions and Human Diseases. *Medical Electron Microscopy* **2003**, *36* (3), 147-156.

(225) Förster, C. Tight Junctions and the Modulation of Barrier Function in Disease. *Histochemistry and Cell Biology* **2008**, *130* (1), 55-70.

(226) Millán, J.; Cain, R. J.; Reglero-Real, N.; Bigarella, C.; Marcos-Ramiro, B.; Fernández-Martín, L.; Correas, I.; Ridley, A. J. Adherens Junctions Connect Stress Fibres Between Adjacent Endothelial Cells. *BMC Biology* **2010**, *8* (1), 11.

(227) Leckband, D. E.; de Rooij, J. Cadherin Adhesion and Mechanotransduction. *Annual review of cell and developmental biology* **2014**, *30* (1), 291-315.

(228) Niessen, C. M. Tight Junctions/Adherens Junctions: Basic Structure and Function. *Journal of Investigative Dermatology* **2007**, *127* (11), 2525-2532.

(229) Indra, I.; Hong, S.; Troyanovsky, R.; Kormos, B.; Troyanovsky, S. The Adherens Junction: A Mosaic of Cadherin and Nectin Clusters Bundled by Actin Filaments. *The Journal of investigative dermatology* **2013**, *133* (11), 2546-2554.

(230) Ooshio, T.; Kobayashi, R.; Ikeda, W.; Miyata, M.; Fukumoto, Y.; Matsuzawa, N.; Ogita, H.; Takai, Y. Involvement of the Interaction of Afadin with ZO-1 in the Formation of Tight Junctions in Madin-Darby Canine Kidney Cells. *The Journal of biological chemistry* **2010**, *285* (7), 5003-5012.

(231) Capaldo, C. T.; Macara, I. G. Depletion of E-cadherin Disrupts Establishment but Not Maintenance of Cell Junctions in Madin-Darby Canine Kidney Epithelial Cells. *Molecular Biology of the Cell* **2007**, *18* (1), 189-200.

(232) Lewis, J. E.; Wahl, J. K., 3rd; Sass, K. M.; Jensen, P. J.; Johnson, K. R.; Wheelock, M. J. Cross-talk Between Adherens Junctions and Desmosomes Depends on Plakoglobin. *The Journal of Cell Biology* **1997**, *136* (4), 919-934.

(233) Chidgey, M. A. J.; Clarke, J. P.; Garrod, D. R. Expression of Full-Length Desmosomal Glycoproteins (Desmocollins) Is Not Sufficient to Confer Strong Adhesion on Transfected L929 Cells. *Journal of Investigative Dermatology* **1996**, *106* (4), 689-695.

(234) Nekrasova, O.; Green, K. J. Desmosome Assembly and Dynamics. *Trends in Cell Biology* **2013**, *23* (11), 537-546.

(235) El-Amraoui, A.; Petit, C. Chapter Sixteen - Cadherin Defects in Inherited Human Diseases. In *Progress in Molecular Biology and Translational Science*, van Roy, F. Ed.; Vol. 116; Academic Press, **2013**; 361-384.

(236) Meşe, G.; Richard, G.; White, T. W. Gap Junctions: Basic Structure and Function. *Journal of Investigative Dermatology* **2007**, *127* (11), 2516-2524.

(237) Goodenough, D. A.; Paul, D. L. Gap Junctions. *Cold Spring Harbor Perspectives in Biology* **2009**, *1* (1).

(238) Evans, W. H.; Martin, P. E. M. Gap Junctions: Structure and Function. *Molecular Membrane Biology* **2002**, *19* (2), 121-136.

(239) Dong, A.; Liu, S.; Li, Y. Gap Junctions in the Nervous System: Probing Functional Connections Using New Imaging Approaches. *Frontiers in Cellular Neuroscience* **2018**, *12* (320), Mini Review.

(240) Franke, W. W. Discovering the Molecular Components of Intercellular Junctions - A Historical View. *Cold Spring Harbor Perspectives in Biology* **2009**, *1* (3), a003061-a003061.

(241) Chen, X.; Gumbiner, B. M. Crosstalk Between Different Adhesion Molecules. *Current Opinion in Cell Biology* **2006**, *18* (5), 572-578.

(242) Zuidema, A.; Wang, W.; Sonnenberg, A. Crosstalk Between Cell Adhesion Complexes in Regulation of Mechanotransduction. *BioEssays* **2020**, *42* (11), 2000119.

(243) Rakshit, S.; Zhang, Y.; Manibog, K.; Shafraz, O.; Sivasankar, S. Ideal, Catch, and Slip Bonds in Cadherin Adhesion. *Proceedings of the National Academy of Sciences* **2012**, *109* (46), 18815-18820.

(244) Marshall, B. T.; Long, M.; Piper, J. W.; Yago, T.; McEver, R. P.; Zhu, C. Direct Observation of Catch Bonds Involving Cell-Adhesion Molecules. *Nature* **2003**, *423* (6936), 190-193.

(245) Rakshit, S.; Sivasankar, S. Biomechanics of Cell Adhesion: How Force Regulates the Lifetime of Adhesive Bonds at the Single Molecule Level. *Physical Chemistry Chemical Physics* **2014**, *16* (6), 2211-2223.

(246) Adhikari, S.; Moran, J.; Weddle, C.; Hinczewski, M. Unraveling the Mechanism of the Cadherin-Catenin-Actin Catch Bond. *PLOS Computational Biology* **2018**, *14* (8), e1006399.

(247) Manibog, K.; Li, H.; Rakshit, S.; Sivasankar, S. Resolving the Molecular Mechanism of Cadherin Catch Bond Formation. *Nature Communications* **2014**, *5* (1), 3941.

(248) Merkel, R.; Nassoy, P.; Leung, A.; Ritchie, K.; Evans, E. Energy Landscapes of Receptor–Ligand Bonds Explored with Dynamic Force Spectroscopy. *Nature* **1999**, *397* (6714), 50-53.

(249) Litvinov, R. I.; Barsegov, V.; Schissler, A. J.; Fisher, A. R.; Bennett, J. S.; Weisel, J. W.; Shuman, H. Dissociation of Bimolecular αIIbβ3-Fibrinogen Complex under a Constant Tensile Force. *Biophysical Journal* **2011**, *100* (1), 165-173.

(250) Jiang, G.; Giannone, G.; Critchley, D. R.; Fukumoto, E.; Sheetz, M. P. Two-Piconewton Slip Bond Between Fibronectin and the Cytoskeleton Depends on Talin. *Nature* **2003**, *424* (6946), 334-337.

(251) Kong, F.; García, A. J.; Mould, A. P.; Humphries, M. J.; Zhu, C. Demonstration of Catch Bonds Between an Integrin and its Ligand. *Journal of Cell Biology* **2009**, *185* (7), 1275-1284.

(252) Novikova, E. A.; Storm, C. Evolving Roles and Dynamics for Catch and Slip Bonds during Adhesion Cluster Maturation. *Physical Review E* **2021**, *103* (3), 032402.

(253) Sarangapani, K. K.; Yago, T.; Klopocki, A. G.; Lawrence, M. B.; Fieger, C. B.; Rosen, S. D.; McEver, R. P.; Zhu, C. Low Force Decelerates L-selectin Dissociation from P-selectin Glycoprotein Ligand-1 and Endoglycan*. *Journal of Biological Chemistry* **2004**, *279* (3), 2291-2298.

(254) Finger, E. B.; Purl, K. D.; Alon, R.; Lawrence, M. B.; von Andrian, U. H.; Springer, T. A. Adhesion Through L-selectin Requires a Threshold Hydrodynamic Shear. *Nature* **1996**, *379* (6562), 266-269.

(255) Lawrence, M. B.; Kansas, G. S.; Kunkel, E. J.; Ley, K. Threshold Levels of Fluid Shear Promote Leukocyte Adhesion Through Selectins (CD62L,P,E). *The Journal of Cell Biology* **1997**, *136* (3), 717-727.

(256) Konstantopoulos, K.; Hanley, W. D.; Wirtz, D. Receptor–Ligand Binding: 'Catch' Bonds Finally Caught. *Current Biology* **2003**, *13* (15), R611-R613.

(257) Helms, G.; Dasanna, A.; Schwarz, U.; Lanzer, M. Modeling Cytoadhesion of Plasmodium Falciparum-infected Erythrocytes and Leukocytes-common Principles and Distinctive Features. *Febs Letters* **2016**, *590*.

(258) Sivasankar, S. Tuning the Kinetics of Cadherin Adhesion. *Journal of Investigative Dermatology* **2013**, *133* (10), 2318-2323.

(259) Esfahani, A. M.; Rosenbohm, J.; Safa, B. T.; Lavrik, N. V.; Minnick, G.; Zhou, Q.; Kong, F.; Jin, X.; Kim, E.; Liu, Y.; et al. Characterization of the Strain-Rate–Dependent Mechanical Response of Single Cell–Cell Junctions. *Proceedings of the National Academy of Sciences* **2021**, *118* (7), e2019347118.

(260) Khalilgharibi, N.; Fouchard, J.; Asadipour, N.; Barrientos, R.; Duda, M.; Bonfanti, A.; Yonis, A.; Harris, A.; Mosaffa, P.; Fujita, Y.; et al. Stress Relaxation in Epithelial Monolayers is Controlled by the Actomyosin Cortex. *Nature Physics* **2019**, *15* (8), 839-847.

(261) Weigl, F.; Blum, C.; Sancho, A.; Groll, J. Correlative Analysis of Intra- Versus Extracellular Cell Detachment Events via the Alignment of Optical Imaging and Detachment Force Quantification. *Advanced Materials Technologies* **2022**, 2200195.

(262) Müller, S. J.; Weigl, F.; Bezold, C.; Bächer, C.; Albrecht, K.; Gekle, S. A Hyperelastic Model for Simulating Cells in Flow. *Biomechanics and Modeling in Mechanobiology* **2021**, *20* (2), 509-520.

(263) Nahm, D.; Weigl, F.; Schaefer, N.; Sancho, A.; Frank, A.; Groll, J.; Villmann, C.; Schmidt, H.-W.; Dalton, P. D.; Luxenhofer, R. A Versatile Biomaterial Ink Platform for the Melt Electrowriting of Chemically-Crosslinked Hydrogels. *Materials Horizons* **2020**, *7* (3), 928-933, 10.1039/C9MH01654F.

(264) Franze, K. The Mechanical Control of Nervous System Development. *Development* **2013**, *140* (15), 3069-3077.

(265) Weinberg, S. H.; Mair, D. B.; Lemmon, C. A. Mechanotransduction Dynamics at the Cell-Matrix Interface. *Biophysical Journal* **2017**, *112* (9), 1962-1974.

(266) Tan, P. S.; Teoh, S. H. Effect of Stiffness of Polycaprolactone (PCL) Membrane on Cell Proliferation. *Materials Science and Engineering: C* **2007**, *27* (2), 304-308.

(267) Luo, M.; Yang, W.; Cartwright, T. N.; Higgins, J. M. G.; Chen, J. Simultaneous Measurement of Single-Cell Mechanics and Cell-to-Materials Adhesion Using Fluidic Force Microscopy. *Langmuir* **2022**, *38* (2), 620-628.

(268) Jaatinen, L.; Young, E.; Hyttinen, J.; Vörös, J.; Zambelli, T.; Demkó, L. Quantifying the Effect of Electric Current on Cell Adhesion Studied by Single-Cell Force Spectroscopy. *Biointerphases* **2016**, *11* (1), 011004.

(269) Kade, J. C.; Dalton, P. D. Polymers for Melt Electrowriting. *Advanced Healthcare Materials* **2021**, *10* (1), 2001232.

(270) Dalton, P. D. Melt Electrowriting with Additive Manufacturing Principles. *Current Opinion in Biomedical Engineering* **2017**, *2*, 49-57.

(271) Hochleitner, G.; Fürsattel, E.; Giesa, R.; Groll, J.; Schmidt, H.-W.; Dalton, P. D. Melt Electrowriting of Thermoplastic Elastomers. *Macromolecular Rapid Communications* **2018**, *39* (10), 1800055.

(272) Mieszczanek, P.; Robinson, T. M.; Dalton, P. D.; Hutmacher, D. W. Convergence of Machine Vision and Melt Electrowriting. *Advanced Materials* **2021**, *33* (29), 2100519.

(273) Cha, C.; Kim, S. Y.; Cao, L.; Kong, H. Decoupled Control of Stiffness and Permeability with a Cell-Encapsulating Poly(ethylene glycol) Dimethacrylate Hydrogel. *Biomaterials* **2010**, *31* (18), 4864-4871.

(274) Eshraghi, S.; Das, S. Mechanical and Microstructural Properties of Polycaprolactone Scaffolds with One-Dimensional, Two-Dimensional, and Three-Dimensional Orthogonally Oriented Porous Architectures Produced by Selective Laser Sintering. *Acta biomaterialia* **2010**, *6* (7), 2467-2476.

(275) de Groot, J. H.; Spaans, C. J.; van Calck, R. V.; van Beijma, F. J.; Norrby, S.; Pennings, A. J. Hydrogels for an Accommodating Intraocular Lens. An Explorative Study. *Biomacromolecules* **2003**, *4* (3), 608-616.

(276) Kirchhof, S.; Goepferich, A. M.; Brandl, F. P. Hydrogels in Ophthalmic Applications. *European Journal of Pharmaceutics and Biopharmaceutics* **2015**, *95*, 227-238.

(277) Li, Z.; Guan, J. Hydrogels for Cardiac Tissue Engineering. *Polymers* **2011**, *3* (2), 740-761.

(278) Saludas, L.; Pascual-Gil, S.; Prósper, F.; Garbayo, E.; Blanco-Prieto, M. Hydrogel Based Approaches for Cardiac Tissue Engineering. *International Journal of Pharmaceutics* **2017**, *523* (2), 454-475.

(279) Vanaei, S.; Parizi, M. S.; Vanaei, S.; Salemizadehparizi, F.; Vanaei, H. R. An Overview on Materials and Techniques in 3D Bioprinting Toward Biomedical Application. *Engineered Regeneration* **2021**, *2*, 1-18.

(280) Gungor-Ozkerim, P. S.; Inci, I.; Zhang, Y. S.; Khademhosseini, A.; Dokmeci, M. R. Bioinks for 3D Bioprinting: An Overview. *Biomaterials Science* **2018**, *6* (5), 915-946.

(281) Groll, J.; Burdick, J. A.; Cho, D. W.; Derby, B.; Gelinsky, M.; Heilshorn, S. C.; Jüngst, T.; Malda, J.; Mironov, V. A.; Nakayama, K.; et al. A Definition of Bioinks and their Distinction from Biomaterial Inks. *Biofabrication* **2018**, *11* (1), 013001.

(282) Blaeser, A.; Duarte Campos, D. F.; Puster, U.; Richtering, W.; Stevens, M. M.; Fischer, H. Controlling Shear Stress in 3D Bioprinting is a Key Factor to Balance Printing Resolution and Stem Cell Integrity. *Advanced Healthcare Materials* **2016**, *5* (3), 326-333.

(283) Neubauer, J. W.; Hauck, N.; Männel, M. J.; Seuss, M.; Fery, A.; Thiele, J. Mechanoresponsive Hydrogel Particles as a Platform for Three-Dimensional Force Sensing. *ACS Applied Materials & Interfaces* **2019**, *11* (29), 26307-26313.

(284) Alexandrova, A. Y.; Arnold, K.; Schaub, S.; Vasiliev, J. M.; Meister, J.-J.; Bershadsky, A. D.; Verkhovsky, A. B. Comparative Dynamics of Retrograde Actin Flow and Focal Adhesions: Formation of Nascent Adhesions Triggers Transition from Fast to Slow Flow. *Plos One* **2008**, *3* (9), e3234.

(285) Ding, Y.; Xu, G. K.; Wang, G. F. On the Determination of Elastic Moduli of Cells by AFM Based Indentation. *Scientific Reports* **2017**, *7* (45575).

(286) Kuznetsova, T. G.; Starodubtseva, M. N.; Yegorenkov, N. I.; Chizhik, S. A.; Zhdanov, R. I. Atomic Force Microscopy Probing of Cell Elasticity. *Micron* **2007**, *38* (8), 824-833.

(287) Huang, W.; Anvari, B.; Torres, J. H.; Lebaron, R. G.; Athanasiou, K. A. Temporal Effects of Cell Adhesion on Mechanical Characteristics of the Single Chondrocyte. *Journal of Orthopaedic Research* **2003**, *21* (1), 88-95.

(288) Mui, K. L.; Chen, C. S.; Assoian, R. K. The Mechanical Regulation of Integrin-Cadherin Crosstalk Organizes Cells, Signaling and Forces. *Journal of Cell Science* **2016**, *129* (6), 1093-1100.

(289) Perinpanayagam, H.; Zaharias, R.; Stanford, C.; Brand, R.; Keller, J.; Schneider, G. Early Cell Adhesion Events Differ between Osteoporotic and Non-Osteoporotic Osteoblasts. *Journal of Orthopaedic Research* **2001**, *19* (6), 993-1000.

(290) Mousa, S. A. Cell Adhesion Molecules: Potential Therapeutic and Diagnostic Implications. *Molecular Biotechnology* **2008**, *38* (1), 33-40.

(291) Blankenberg, S.; Barbaux, S.; Tiret, L. Adhesion Molecules and Atherosclerosis. *Atherosclerosis* **2003**, *170* (2), 191-203.

(292) Chi, Z.; Melendez, A. J. Role of Cell Adhesion Molecules and Immune-Cell Migration in the Initiation, Onset and Development of Atherosclerosis. *Cell Adhesion & Migration* **2007**, *1* (4), 171-175.

(293) Okegawa, T.; Pong, R. C.; Li, Y.; Hsieh, J. T. The Role of Cell Adhesion Molecule in Cancer Progression and its Application in Cancer Therapy. *Acta Biochimica Polonica* **2004**, *51* (2), 445-457.

(294) Li, L.; Kang, W.; Wang, J. Mechanical Model for Catch-Bond-Mediated Cell Adhesion in Shear Flow. *International Journal of Molecular Sciences* **2020**, *21* (2).

(295) Zhu, C.; Lou, J.; McEver, R. Catch Bonds: Physical Models, Structural Bases, Biological Function and Rheological Relevance. *Biorheology* **2005**, *42*, 443-462.

(296) Christenson, W.; Yermolenko, I.; Plochberger, B.; Camacho-Alanis, F.; Ros, A.; Ugarova, T. P.; Ros, R. Combined Single Cell AFM Manipulation and TIRFM for Probing the Molecular Stability of Multilayer Fibrinogen Matrices. *Ultramicroscopy* **2014**, *136*, 211-215.

(297) Shaw, J. E.; Epand, R. F.; Epand, R. M.; Li, Z.; Bittman, R.; Yip, C. M. Correlated Fluorescence-Atomic Force Microscopy of Membrane Domains: Structure of Fluorescence Probes Determines Lipid Localization. *Biophysical Journal* **2006**, *90* (6), 2170-2178.

(298) Beicker, K.; O'Brien, E. T.; Falvo, M. R.; Superfine, R. Vertical Light Sheet Enhanced Side-View Imaging for AFM Cell Mechanics Studies. *Scientific Reports* **2018**, *8* (1), 1504.

(299) Sundar Rajan, V.; Laurent, V. M.; Verdier, C.; Duperray, A. Unraveling the Receptor-Ligand Interactions between Bladder Cancer Cells and the Endothelium Using AFM. *Biophysical Journal* **2017**, *112* (6), 1246-1257.

(300) Lherbette, M.; dos Santos, Á.; Hari-Gupta, Y.; Fili, N.; Toseland, C. P.; Schaap, I. A. T. Atomic Force Microscopy Micro-Rheology Reveals Large Structural Inhomogeneities in Single Cell-Nuclei. *Scientific Reports* **2017**, *7* (1), 8116.

(301) Miranda, A.; Martins, M.; Beule, P. A. A. D. Simultaneous Differential Spinning Disk Fluorescence Optical Sectioning Microscopy and Nanomechanical Mapping Atomic Force Microscopy. *Review of Scientific Instruments* **2015**, *86* (9), 093705.

(302) Kámán, J.; Huszánk, R.; Bonyár, A. Towards More Reliable AFM Force-Curve Evaluation: A Method for Spring Constant Selection, Adaptive Lever Sensitivity Calibration and Fitting Boundary Identification. *Micron* **2019**, *125*, 102717.

(303) Payam, A. F.; Trewby, W.; Voïtchovsky, K. Determining the Spring Constant of Arbitrarily Shaped Cantilevers in Viscous Environments. *Applied Physics Letters* **2018**, *112* (8), 083101.

(304) Nagy, A. G.; Kaman, J.; Horvath, R.; Bonyar, A. Spring Constant and Sensitivity Calibration of FluidFM Micropipette Cantilevers for Force Spectroscopy Measurements. *Scientific Reports* **2019**, *9* (1), 10287.

(305) Lulevich, V.; Honig, C.; Ducker, W. A. An Atomic Force Microscope Tip as a Light Source. *Review of Scientific Instruments* **2005**, *76* (12), 123704.

(306) Kistner, J.; Chen, X.; Weng, Y.; Strunk, H. P.; Schubert, M. B.; Werner, J. H. Photoluminescence from Silicon Nitride — No Quantum Effect. *Journal of Applied Physics* **2011**, *110* (2), 023520.

(307) Franz, C. M.; Müller, D. J. Analyzing Focal Adhesion Structure by Atomic Force Microscopy. *Journal of Cell Science* **2005**, *118* (22), 5315-5323.

(308) Kashef, J.; Franz, C. M. Quantitative Methods for Analyzing Cell–Cell Adhesion in Development. *Developmental Biology* **2015**, *401* (1), 165-174.

(309) Shen, Y.; Nakajima, M.; Kojima, S.; Homma, M.; Fukuda, T. Study of the Time Effect on the Strength of Cell–Cell Adhesion Force by a Novel Nano-Picker. *Biochemical and Biophysical Research Communications* **2011**, *409* (2), 160-165.

(310) Sumpio, B. E.; Timothy Riley, J.; Dardik, A. Cells in Focus: Endothelial Cell. *The International Journal of Biochemistry & Cell Biology* **2002**, *34* (12), 1508-1512.

(311) Dejana, E.; Corada, M.; Lampugnani, M. G. Endothelial Cell-to-Cell Junctions. *The FASEB Journal* **1995**, *9* (10), 910-918.

(312) Kocherova, I.; Bryja, A.; Mozdziak, P.; Angelova Volponi, A.; Dyszkiewicz-Konwińska, M.; Piotrowska-Kempisty, H.; Antosik, P.; Bukowska, D.; Bruska, M.; Iżycki, D.; et al. Human Umbilical Vein Endothelial Cells (HUVECs) Co-Culture with Osteogenic Cells: From Molecular Communication to Engineering Prevascularised Bone Grafts. *Journal of clinical medicine* **2019**, *8* (10), 1602.

(313) Hoelzle, M. K.; Svitkina, T. The Cytoskeletal Mechanisms of Cell–Cell Junction Formation in Endothelial Cells. *Molecular Biology of the Cell* **2011**, *23* (2), 310-323.

(314) Buckley Craig, D.; Tan, J.; Anderson Karen, L.; Hanein, D.; Volkmann, N.; Weis William, I.; Nelson, W. J.; Dunn Alexander, R. The Minimal Cadherin-Catenin Complex Binds to Actin Filaments under Force. *Science* **2014**, *346* (6209), 1254211.

(315) Charras, G.; Yap, A. S. Tensile Forces and Mechanotransduction at Cell-Cell Junctions. *Current Biology* **2018**, *28* (8), R445-r457.

(316) Panorchan, P.; George, J. P.; Wirtz, D. Probing Intercellular Interactions between Vascular Endothelial Cadherin Pairs at Single-molecule Resolution and in Living Cells. *Journal of Molecular Biology* **2006**, *358* (3), 665-674.

(317) Müller, D. J.; Helenius, J.; Alsteens, D.; Dufrêne, Y. F. Force Probing Surfaces of Living Cells to Molecular Resolution. *Nature Chemical Biology* **2009**, *5* (6), 383-390.

(318) Thomas, W. E.; Vogel, V.; Sokurenko, E. Biophysics of Catch Bonds. *Annual Review of Biophysics* **2008**, *37* (1), 399-416.

(319) dela Paz, N. G.; D'Amore, P. A. Arterial Versus Venous Endothelial Cells. *Cell and Tissue Research* **2009**, *335* (1), 5-16.

(320) Lagendijk, A. K.; Yap, A. S.; Hogan, B. M. Endothelial Cell-Cell Adhesion During Zebrafish Vascular Development. *Cell Adhesion & Migration* **2014**, *8* (2), 136-145.

(321) Shaw, S. K.; Perkins, B. N.; Lim, Y.-C.; Liu, Y.; Nusrat, A.; Schnell, F. J.; Parkos, C. A.; Luscinskas, F. W. Reduced Expression of Junctional Adhesion Molecule and Platelet/Endothelial Cell Adhesion Molecule-1 (CD31) at Human Vascular Endothelial Junctions by Cytokines Tumor Necrosis Factor-α Plus Interferon-γ Does Not Reduce Leukocyte Transmigration Under Flow. *The American Journal of Pathology* **2001**, *159* (6), 2281-2291.

(322) Vestweber, D. VE-Cadherin. *Arteriosclerosis, Thrombosis, and Vascular Biology* **2008**, *28* (2), 223-232.

(323) Ayalon, O.; Sabanai, H.; Lampugnani, M. G.; Dejana, E.; Geiger, B. Spatial and Temporal Relationships between Cadherins and PECAM-1 in Cell-Cell Junctions of Human Endothelial Cells. *The Journal of Cell Biology* **1994**, *126* (1), 247-258.

(324) Lertkiatmongkol, P.; Liao, D.; Mei, H.; Hu, Y.; Newman, P. J. Endothelial Functions of Platelet/Endothelial Cell Adhesion Molecule-1 (CD31). *Current opinion in hematology* **2016**, *23* (3), 253-259.

(325) DeLisser, H. M.; Newman, P. J.; Albelda, S. M. Molecular and Functional Aspects of PECAM-1/CD31. *Immunology Today* **1994**, *15* (10), 490-495.

(326) Piali, L.; Hammel, P.; Uherek, C.; Bachmann, F.; Gisler, R. H.; Dunon, D.; Imhof, B. A. CD31/PECAM-1 is a Ligand for Alpha-v-Beta-3 Integrin Involved in Adhesion of Leukocytes to Endothelium. *The Journal of Cell Biology* **1995**, *130* (2), 451-460.

(327) McRae, M.; LaFratta, L. M.; Nguyen, B. M.; Paris, J. J.; Hauser, K. F.; Conway, D. E. Characterization of Cell-Cell Junction Changes Associated with the Formation of a Strong Endothelial Barrier. *Tissue barriers* **2018**, *6* (1), e1405774.

(328) Benn, A.; Bredow, C.; Casanova, I.; Vukičević, S.; Knaus, P. VE-Cadherin Facilitates BMP-induced Endothelial Cell Permeability and Signaling. *Journal of Cell Science* **2016**, *129* (1), 206-218.

(329) Jiménez, N.; Krouwer, V. J. D.; Post, J. A. A New, Rapid and Reproducible Method to Obtain High Quality Endothelium in Vitro. *Cytotechnology* **2013**, *65* (1), 1-14.

(330) Bernas, M. J.; Cardoso, F. L.; Daley, S. K.; Weinand, M. E.; Campos, A. R.; Ferreira, A. J. G.; Hoying, J. B.; Witte, M. H.; Brites, D.; Persidsky, Y.; et al. Establishment of Primary Cultures of Human Brain Microvascular Endothelial Cells to Provide an in Vitro Cellular Model of the Blood-Brain Barrier. *Nature Protocols* **2010**, *5* (7), 1265-1272.

(331) Takeshita, Y.; Obermeier, B.; Cotleur, A.; Sano, Y.; Kanda, T.; Ransohoff, R. M. An in Vitro Blood-Brain Barrier Model Combining Shear Stress and Endothelial Cell/Astrocyte Co-Culture. *Journal of neuroscience methods* **2014**, *232*, 165-172.

(332) Rochfort, K. D.; Cummins, P. M. Cytokine-Mediated Dysregulation of Zonula Occludens-1 Properties in Human Brain Microvascular Endothelium. *Microvascular Research* **2015**, *100*, 48-53.

(333) O'Connor, B. B.; Grevesse, T.; Zimmerman, J. F.; Ardoña, H. A. M.; Jimenez, J. A.; Bitounis, D.; Demokritou, P.; Parker, K. K. Human Brain Microvascular Endothelial Cell Pairs Model Tissue-Level Blood-Brain Barrier Function. *Integrative biology : quantitative biosciences from nano to macro* **2020**, *12* (3), 64-79.

(334) Park, T.-E.; Mustafaoglu, N.; Herland, A.; Hasselkus, R.; Mannix, R.; FitzGerald, E. A.; Prantil-Baun, R.; Watters, A.; Henry, O.; Benz, M.; et al. Hypoxia-enhanced Blood-Brain Barrier Chip Recapitulates Human Barrier Function and Shuttling of Drugs and Antibodies. *Nature Communications* **2019**, *10* (1), 2621.

(335) Shima, A.; Nagata, S.; Takeuchi, S. Three-Dimensional Co-Culture of Blood-Brain Barrier-Composing Cells in a Culture Insert with a Collagen Vitrigel Membrane. *In Vitro Cellular & Developmental Biology - Animal* **2020**, *56* (7), 500-504.

(336) Chu, Y.-S.; Thomas, W. A.; Eder, O.; Pincet, F.; Perez, E.; Thiery, J. P.; Dufour, S. Force Measurements in E-Cadherin–Mediated Cell Doublets Reveal Rapid Adhesion Strengthened by Actin Cytoskeleton Remodeling through Rac and Cdc42. *Journal of Cell Biology* **2004**, *167* (6), 1183-1194.

(337) Mège, R.-M.; Gavard, J.; Lambert, M. Regulation of Cell–Cell Junctions by the Cytoskeleton. *Current Opinion in Cell Biology* **2006**, *18* (5), 541-548.

(338) Bershadsky, A. Magic Touch: How does Cell–Cell Adhesion Trigger Actin Assembly? *Trends in Cell Biology* **2004**, *14* (11), 589-593.

(339) Kaur, G.; Dufour, J. M. Cell Lines: Valuable Tools or Useless Artifacts. *Spermatogenesis* **2012**, *2* (1), 1-5.

(340) Yeager, T. R.; Reddel, R. R. Constructing Immortalized Human Cell Lines. *Current Opinion in Biotechnology* **1999**, *10* (5), 465-469.

(341) Katakura, Y.; Alam, S.; Shirahata, S. Chapter 5 Immortalization by Gene Transfection. In *Methods in Cell Biology*, Mather, J. P., Barnes, D. Eds.; Vol. 57; Academic Press, **1998**; 69-91.

(342) Deng, L.; Pollmeier, L.; Zhou, Q.; Bergemann, S.; Bode, C.; Hein, L.; Lother, A. Gene Expression in Immortalized Versus Primary Isolated Cardiac Endothelial Cells. *Scientific Reports* **2020**, *10* (1), 2241.

(343) Lidington, E. A.; Moyes, D. L.; McCormack, A. M.; Rose, M. L. A Comparison of Primary Endothelial Cells and Endothelial Cell Lines for Studies of Immune Interactions. *Transplant Immunology* **1999**, *7* (4), 239-246.

(344) Henry, O. Y. F.; Villenave, R.; Cronce, M. J.; Leineweber, W. D.; Benz, M. A.; Ingber, D. E. Organs-On-Chips with Integrated Electrodes for Trans-Epithelial Electrical Resistance (TEER) Measurements of Human Epithelial Barrier Function. *Lab on a Chip* **2017**, *17* (13), 2264-2271.

(345) Srinivasan, B.; Kolli, A. R.; Esch, M. B.; Abaci, H. E.; Shuler, M. L.; Hickman, J. J. TEER Measurement Techniques for In Vitro Barrier Model Systems. *Journal of Laboratory Automation* **2015**, *20* (2), 107-126.

(346) Loussert Fonta, C.; Humbel, B. M. Correlative Microscopy. *Archives of Biochemistry and Biophysics* **2015**, *581*, 98-110.

(347) Krieg, M.; Helenius, J.; Heisenberg, C. P.; Muller, D. J. A Bond for a Lifetime: Employing Membrane Nanotubes from Living Cells to Determine Receptor-Ligand Kinetics. *Angewandte Chemie International Edition in English* **2008**, *47* (50), 9775-9777.

(348) Opfer, J.; Gottschalk, K.-E. Identifying Discrete States of a Biological System Using a Novel Step Detection Algorithm. *Plos One* **2012**, *7* (11), e45896.

(349) Hein, B.; Willig, K. I.; Wurm, C. A.; Westphal, V.; Jakobs, S.; Hell, S. W. Stimulated Emission Depletion Nanoscopy of Living Cells Using SNAP-Tag Fusion Proteins. *Biophysical Journal* **2010**, *98* (1), 158-163.

(350) Hoelzel, C. A.; Zhang, X. Visualizing and Manipulating Biological Processes by Using HaloTag and SNAP-Tag Technologies. *Chembiochem* **2020**, *21* (14), 1935-1946.

(351) Bosch, P. J.; Correa, I. R., Jr.; Sonntag, M. H.; Ibach, J.; Brunsveld, L.; Kanger, J. S.; Subramaniam, V. Evaluation of Fluorophores to Label SNAP-tag Fused Proteins for Multicolor Single-Molecule Tracking Microscopy in Live Cells. *Biophysical Journal* **2014**, *107* (4), 803-814.

(352) Cole, N. B. Site-Specific Protein Labeling with SNAP-tags. *Current protocols in protein science* **2013**, *73*, 30.31.31-30.31.16.

(353) Achilli, T.-M.; Meyer, J.; Morgan, J. R. Advances in the Formation, use and Understanding of Multi-Cellular Spheroids. *Expert Opinion on Biological Therapy* **2012**, *12* (10), 1347-1360.

(354) Kim, S.-j.; Kim, E. M.; Yamamoto, M.; Park, H.; Shin, H. Engineering Multi-Cellular Spheroids for Tissue Engineering and Regenerative Medicine. *Advanced Healthcare Materials* **2020**, *9* (23), 2000608.

Appendix A

FL-FluidFM® - Standard operating procedure

A.1. Starting the FL-FluidFM® system

The correlated FL-FluidFM® device is composed of several hardware components and two separated computers controlling the fluorescence microscope and FluidFM®, respectively. A photograph of the whole system showing almost all components is illustrated in **Figure 32**.

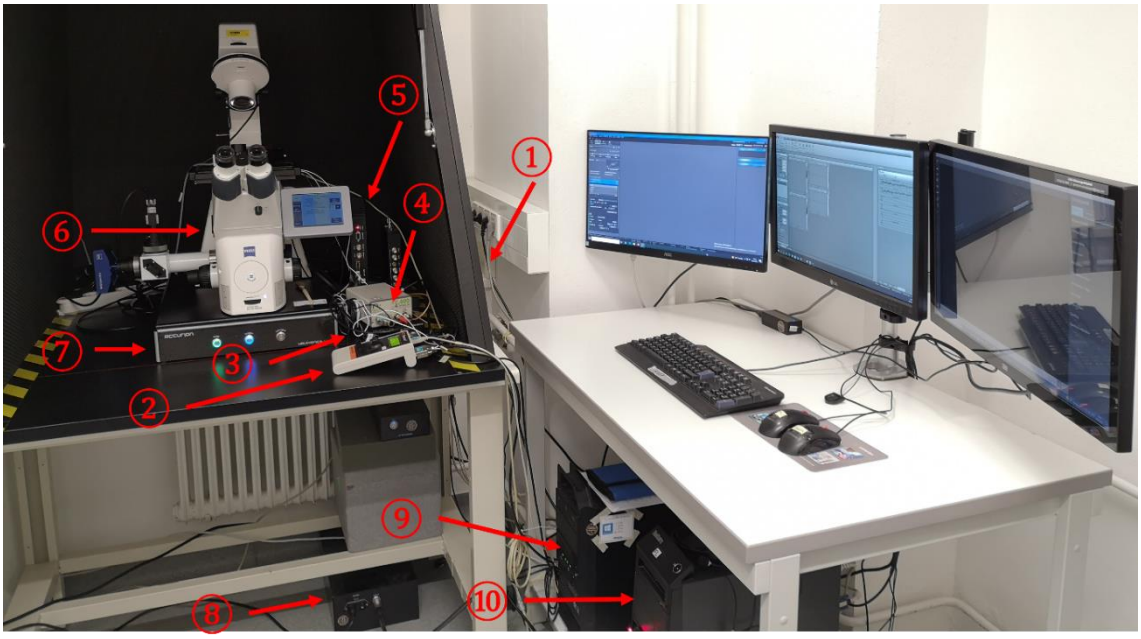

Figure 32: Photograph of the correlated FL-FluidFM® system showing the main components. On the left side, there is the microscopic setup. In the corner right next to the device box, there is a general power supply ①, which is not directly visible in this photograph. The other numbers indicate additional components. These include the Nanosurf stage controller ②, the nanoFaktur ③, the npoint LC400 ④, the C3000 controller unit ⑤, the fluorescence microscope ⑥, the Accurion isolation vibration stage ⑦, the pressure controller ⑧, and the two computers for FluidFM® ⑨ and FL ⑩. These are connected to three computer monitors. The left one corresponds to the fluorescence microscope, while the middle and the right ones are associated with the FluidFM® system.

To work with the correlated device, all components have to be switched on. First, the general power supply ① which can be found as a small white box right back in the corner next to the device box (not visible in **Figure 32**). This is followed by the Nanosurf stage controller which moves the sample stage in xy-direction ②. The speed of movement can be changed by pressing and turning the left and middle pins of the controller. By another pressing, the speed can be fixed. Afterwards, the nanoFaktur ③ is switched on, regulating the movement of the PIFOC. Subsequently, the npoint LC400 ④ and the C3000 controller unit ⑤ can be activated. The latter is composed of two black boxes, but only the left one can be turned on. This is followed by the fluorescence microscope ⑥ and the Accurion vibration isolation stage ⑦ below. Here, the left and the middle button have to be activated. The pressure controller ⑧ represents the next component and can be found as black box on the ground directly below the device table. The last

two hardware components to be switched on are the FluidFM® ⑨ and FL computers ⑩, both marked with a corresponding sign on the computer tower. The associated passwords are 'fluidfm2013' and 'gabbahey', respectively. In the end, the respective software of both systems can be started. For the fluorescence microscope, it is the ZEN 2.6 software, which is located in the upper middle of the computer screen. The 'ZEN pro' version has to be activated for data acquisition. The FluidFM® is controlled by two programs, the Nanosurf C3000 FluidFM-T, and the Cytosurge-ARYA software. The latter should be started only after the complete loading of the C3000 software. Both software programs are located on the upper right side of the computer screen.

A.2. FL software

The main panel of the ZEN 2.6 software, including an exemplary fluorescence image, is illustrated in **Figure 33a**. To define all working parameters, the sections 'Aufnahme' ① and '4-Kanal' ② have to be chosen. The latter already provides pre-defined working parameters, which are optimized for the correlated data acquisition. However, the specific setting has to be prepared prior to each experiment. By checking the 'Automatisch speichern' box ③, a new working space under 'Anwendungen' ④ occurs. Here, the storage location and the respective file name can be specified. Within the section 'Kanäle' ⑤, pre-defined illumination channels appear, including the four fluorescence channels EGFP, DsRed, DAPI, and Cy5 as well as the brightfield illumination (**Figure 33b**). A list of fluorescence dyes opens by clicking on the small "+", and further options can be chosen. However, one has to ensure that newly chosen fluorescent dyes also match the microscopic equipment such as filters or illumination wavelength. Furthermore, channels can be deleted by clicking the small trash icon. For a successful fluorescence illumination, the light intensity ① and exposure time ② have to be defined for each channel (**Figure 33b**, red arrows). These parameters occur by clicking on a fluorescence channel. With starting a new project, it is advisable to start with a low intensity and exposure time preventing direct photobleaching. Afterwards, both parameters can be adjusted to achieve a good signal quality. More precisely, the two parameters should be balanced so that no one completely dominates, and overexposure or high background signal is avoided. This can be further controlled within the section 'Anzeige' (**Figure 33a** ⑥) which appears beneath the live image after clicking the "Live" button ⑦. Here, the signal distribution of each channel is illustrated, visible as green, and orange signals. Due to the entire hardware correlation, this software provides no automated connection to the filters or objectives. Therefore, the correct hardware setting has to be manually chosen at the microscope panel (**Figure 33c**).

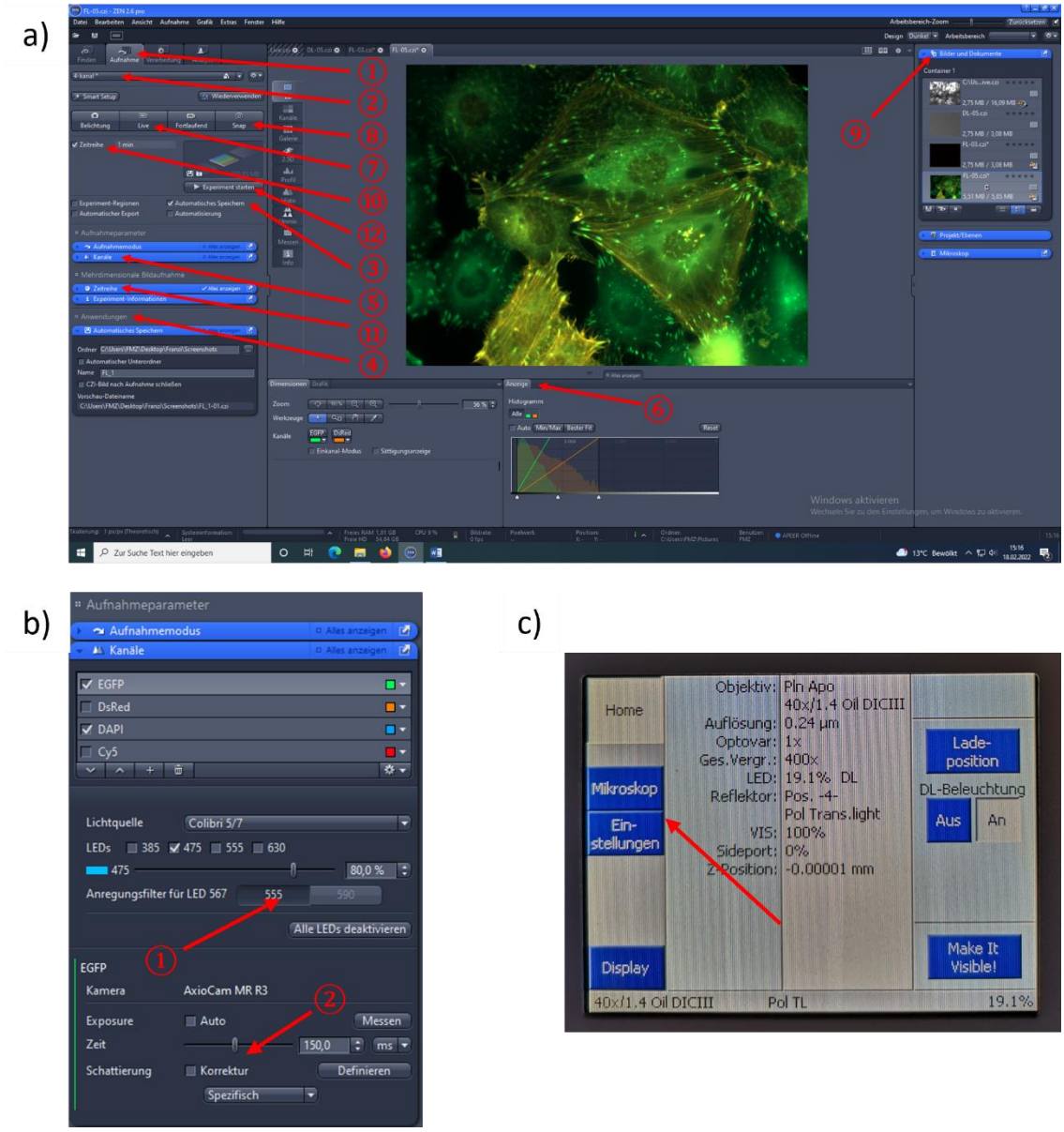

Figure 33: Settings for fluorescence imaging. (a) To achieve successful fluorescence imaging, the 'Aufnahme' ① and '4 Kanal' ② button has to be activated first. By checking the 'Automatisch speichern' box ③, a new section is opened under 'Anwendungen' ④. The section 'Kanäle' ⑤ provides specific parameters of the illumination channels, such as light intensity or exposure time. The signal quality of an image can be further controlled within the 'Anzeige' ⑥, which appears after starting the 'Live' modus ⑦. By activating the 'Snap' button ⑧, a fluorescence image is recorded and subsequently displayed in the 'Bilder und Dokumente' section ⑨. The activation of 'Zeitreihe' ⑩ induces a new field of parameters ⑪. After defining the recording time duration, the acquisition can be started via 'Experiment starten' ⑫. (b) Exemplary illustration of the 'Kanäle' settings including 'light intensity' ① and 'exposure time' ②. (c) Starting display of the microscope panel. By activating the 'Mikroskop' section, further hardware settings appear.

By clicking on 'Mikroskop', different sections of hardware settings open, including 'Objektive', 'Reflektor', 'Optovar', and 'Lichtweg'. To acquire fluorescence images, the illumination channel(s) of interest have to be checked. More precisely, the check mark is decisive and not which channel

is clicked. Afterwards, a fluorescence image is generated by activating the 'snap' button ⑧ and subsequently displayed in the 'Bilder und Dokumente' section ⑨. For the acquisition of a time series, the box of 'Zeitreihe' ⑩ has to be checked which activates another 'Aufnahmeparameter' ⑪. Here, the duration of the time series can be defined. To achieve a high frame rate, the exposure time of the illumination channel should be as low as possible. The measurement can be started by clicking the 'Experiment starten' ⑫ button.

A.3. FluidFM® software

The FluidFM® system is operated by the Nanosurf C3000 FluidFM-T and the Cytosurge-ARYA software. While the former is applied as a background control for several parameters, the ARYA software, on the other hand, provides a more user-friendly pre-defined workflow and is used for the actual performance of the FluidFM® measurements.

A.3.1. Nanosurf C3000 FluidFM-T

The home screen of the C3000 software is illustrated in **Figure 34a**. It provides a monitoring of six parameters, including 'normal deflection' ①, 'User In B' ②, 'Z-Axis Sensor' ③, 'Z-Axis Out' ④, 'User Out C' ⑤, and 'Approach Motor' ⑥. The first one shows the live cantilever deflection. The second parameter represents a measured feedback signal coming from a position sensor of the 100 µm z-stage. The two 'Z-Axis' parameters represent the movement and signal of the cantilever within a 10 µm range controlled by the FluidFM® head. Here, the 'Sensor' visualizes the actual signal from the z-axis, while the 'Out' signal represents the signal entered on the z-piezo. The 'User Out C' parameter reveals the position signal directed on the 100 µm sample stage, given as values between -50 and +50 µm. The latter parameter shows any signal connected to a running approach motor, for instance, during approach, retraction, or home position withdrawal, which represents the upper most cantilever position. This software further provides the option to independently move the sample stage via the 'Retract' and 'Advance' tools ⑦, located in the 'Approach' section. By clicking on the small arrow ⑧ in the right corner of this section, a new toolbox named 'SPM Parameters' appears allowing a more advanced parameter configuration (**Figure 34b**). Especially the 'SPM System' unit is important for a defined stage/PIFOC positioning. Under 'User Output C Idle Parameters' (marked with a red square), the exact stage position can be defined by a given value in 'Absolute Idle Position'. The 'Idle Mode' should be set to 'Set to Absolute Value' to prevent a software internal position adjustment. Furthermore, the 'Laser Control' (marked with a red square) allows switching off the FluidFM® laser.

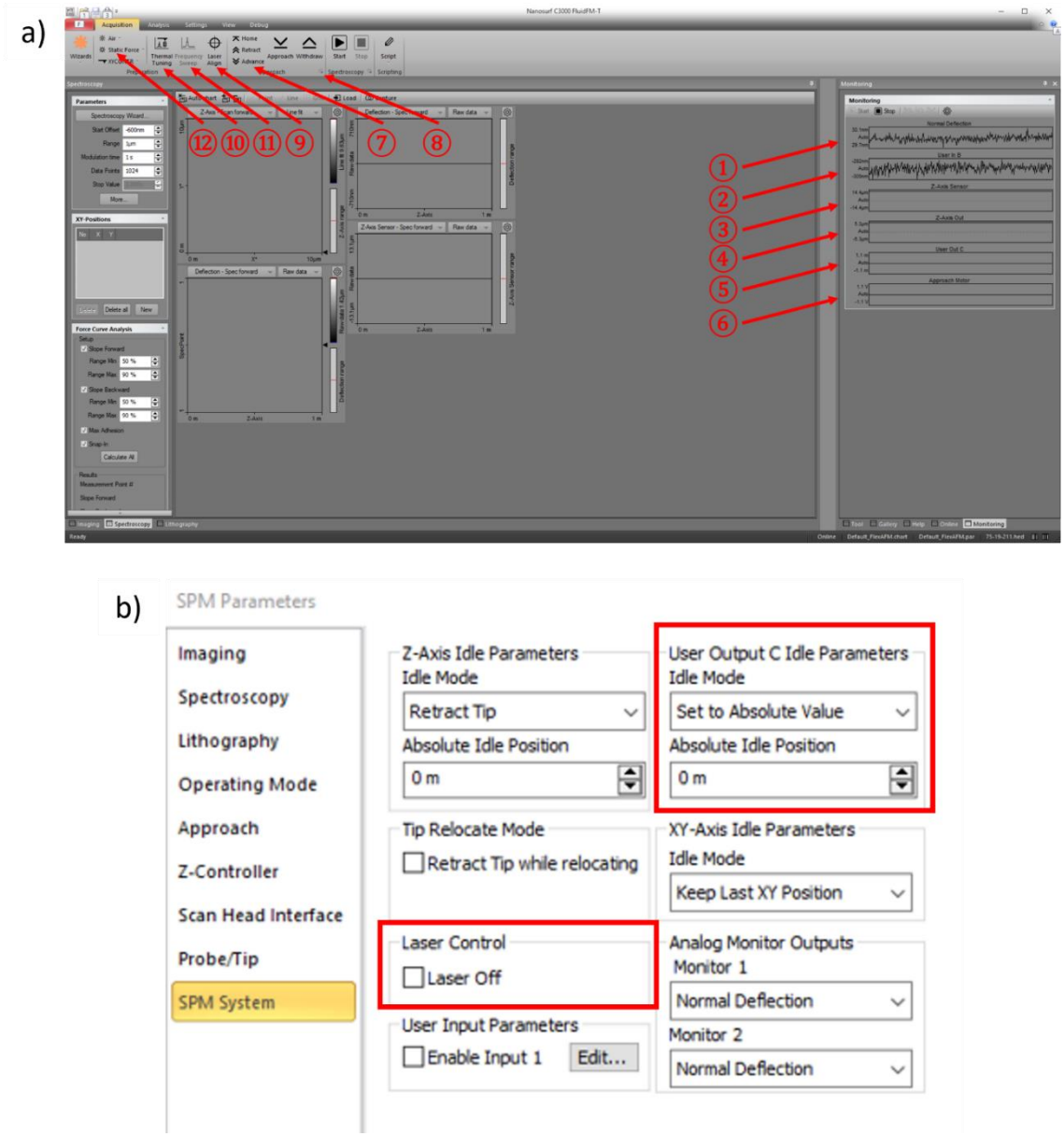

Figure 34: Exemplary screens of the Nanosurf C3000 FluidFM-T software. (a) The home screen of the software shows important tools and parameters. There is a monitoring field on its right side, visualizing different parameters such as 'normal deflection' ①, 'Z-Axis Sensor' ②, 'Z-Axis Out' ③, and 'User Out C' ④. The 'Approach' section allows the independent moving of the sample stage via the 'Advance' and 'Retract' buttons ⑤. By clicking on the small arrow ⑥, another toolbox opens named 'SPM parameters'. Next to the 'Approach' section, the 'Preparation' area provides further experimental adjustments such as 'Laser Alignment' ⑦, or two cantilever spring constant calibration methods. One can choose between 'Thermal Tuning' ⑧ or 'Frequency Sweep' ⑨. Depending on the method, the 'Static Force' or 'Dynamic Force' mode has to be activated ⑩.

The 'Preparation' section on the home screen supplies three other important tools. The first one is the 'Laser Alignment' ⑨, which can be used for checking the correct laser position on the photo detector. The other two are related to the calibration of the cantilever spring constant. One can choose between 'Thermal tuning' ⑩ and 'Frequency Sweep' ⑪. It is advisable always to do both

but starting with the 'thermal tuning', which should be performed under 'Static Force' ⑫ mode. By activating the calibration tool, a new window occurs named 'Thermal tuning' (**Figure 35**). During the calibration process, the fitting range of the peak has to be adjusted under 'Peak fit' (①, red square) until a good overlay, and a stable spring constant as well as resonance frequency is reached. The latter ones are displayed on the right side of the window (②, red square).

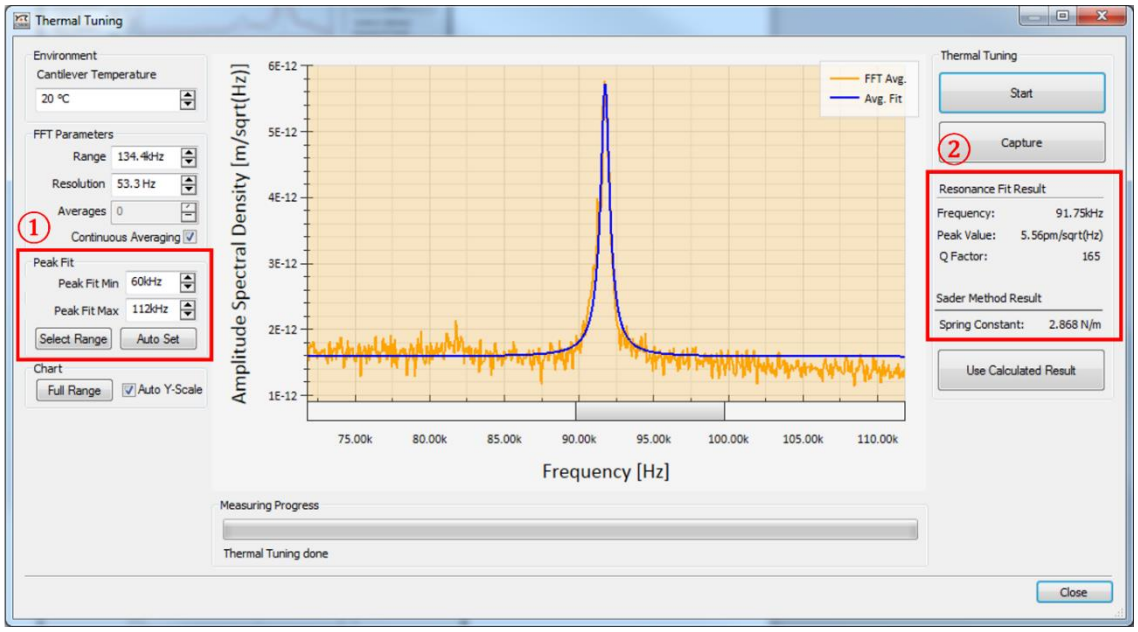

Figure 35: Exemplary window of the calibration method 'Thermal Tuning'. On the left side of the panel (①, red square), the 'Peak fit' section provides the adjustment of the fitting range. This has to be modified until a well-defined overlay between the peak of the thermal spectrum (orange) and the fit (blue) occurs. The extracted resonance frequency, quality factor and spring constant are displayed on the right side of the window (②, red square).

For the calibration via 'Frequency Sweep', the force mode has to be switched to the dynamic mode ⑫ first. As illustrated in **Figure 36**, this calibration method is separated into two steps, the 'Coarse Sweep' ① and the 'Fine Sweep' ②. The former one serves as rough tuning. For its frequency range, the resonance frequency determined under 'Thermal tuning' can be used as an orientation. The 'Step Frequency' should be set to a value between 100 and 200 Hz to avoid a long calculation time. Afterwards, the 'Fine Sweep' can be performed by entering the newly calculated resonance frequency into the 'Center Frequency' field. The 'Span Frequency' defines the surrounding fitting range, usually set to 20 to 30 kHz. The 'Step Frequency' can be reduced to a small value of about 10 Hz. The calculated resonance frequency and the spring constant are displayed on the right side of the panel (③, red square). For the decision on which extracted spring constant will be adopted, two factors have to be considered: first, which value reveals a better agreement with the nominal spring constant of the cantilever and second, which method shows the better fitting. If both calibration methods show a similar result, the one of the

'Frequency Sweep' should be preferred. Here, the cantilever is driven by a high precision shaker piezo instead of RT induced thermal motion as in the 'Thermal turning'.

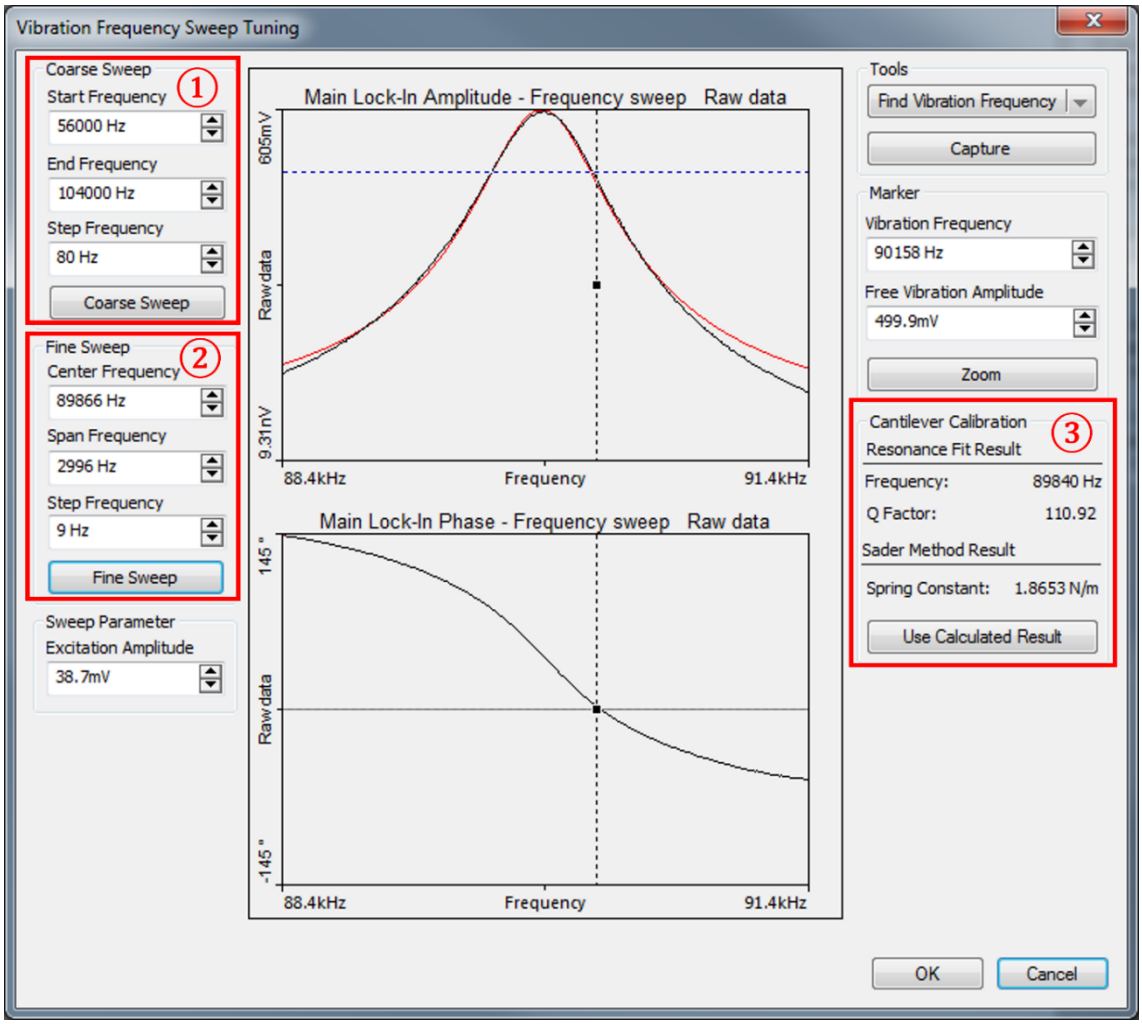

Figure 36: Toolbox of the 'Vibration Frequency Sweep Tuning'. This method is based on two steps, the 'Coarse Sweep' ①, which serves as an initial approximation, and the following defining 'Fine Sweep' ②. The first one can be limited by the 'Start' and 'End Frequency', as well as the 'Step Frequency'. The 'Fine Sweep' is narrowed down to a 'Center Frequency', which is already close to the resonance frequency. Here, only the 'Span Frequency' and the 'Step Frequency' have to be inserted. On the right side of the panel, the extracted 'Resonance Frequency' as well as the 'Spring Constant' are displayed (③, red square).

A.3.2. Cytosurge-ARYA

After starting the ARYA software, a project window appears. By clicking 'Start new experiment', a new project opens. After the software's internal configuration, the absolute coordinates of the xy-stage have to be initialized. During this process, the stage will be automatically moved to its limits in both directions and subsequently centered. This is accompanied by a high-frequency sound. Due to a high risk of breakage, no cantilever should be already implemented into the system during the initialization. The note 'The Barcode Reader could not be initialized' can be

ignored since no one is connected to the device. Afterwards, the operator software is ready-to-use (**Figure 37**). On its left side, there are several icons, such as a snapshot ①, a camera that makes a video of the whole experiment ②, or one that only records the last 30 s ③, a syringe ④, and a cantilever symbol ⑤. However, the two latter icons represent the most important ones for the FluidFM® performance. The cantilever symbol controls the cantilever movement, including surface approach ⑥ and retraction to the home/safety position ⑦. On the other hand, the syringe icon activates a panel for the pressure control. There are two operator fields on the right side of the ARYA screen, the 'Workflow' ⑧ and the 'Settings' ⑨.

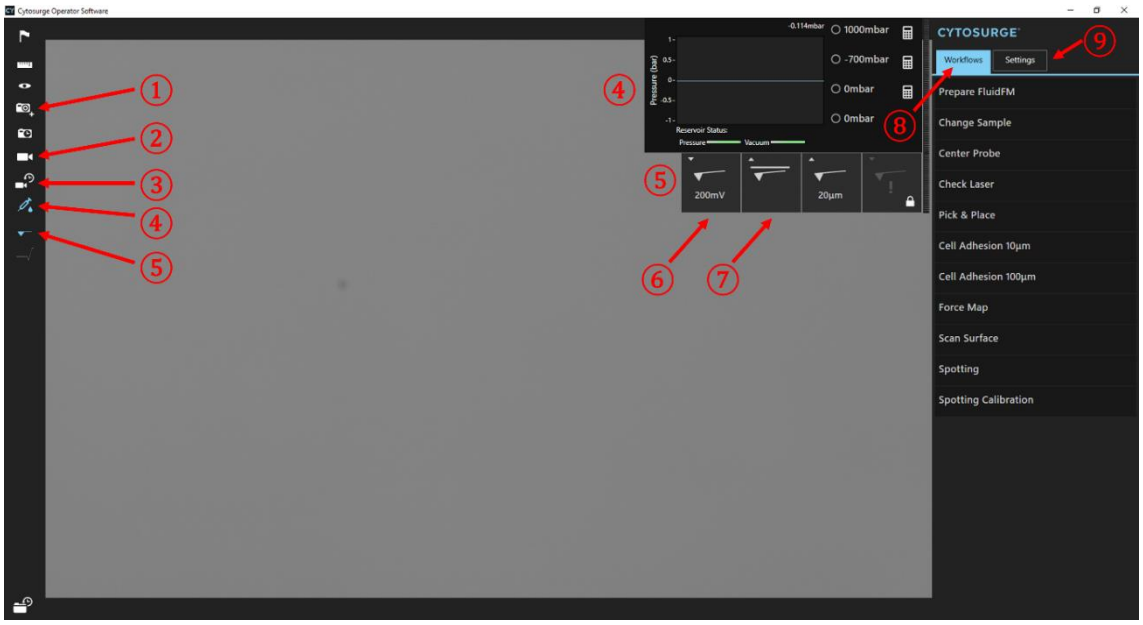

Figure 37: Exemplary starting panel of the Cytosurge ARYA software. On its left side, the software provides several tools, such as a snapshot ①, two camera tools, one for the acquisition of an entire experiment ② and one for the last 30s ③. This is followed by a syringe ④ that allows pressure control, and a cantilever icon ⑤ that includes a controlled cantilever approach ⑥ or retraction ⑦ into its home position. On the right side of the ARYA panel, there are two operator options, the 'Workflow' ⑧ and the 'Settings' ⑨ providing further toolboxes.

By activating the 'Settings' ⑨, a list of options appears. As illustrated in **Figure 38a**, the section 'AFM' provides several parameters that have to be adjusted for an appropriate FluidFM® performance. At the beginning of an experiment, the 'Approach Setpoint' is given as 200 mV in accordance with the 'Approach' operator in **Figure 37** ⑥. Only after cantilever calibration both values are automatically transformed into nanonewtons. However, this 'setpoint' can be manually modified if needed. The second parameter, 'Approach Speed', is usually set to 5 µm s^{-1} and determines the general speed of the cantilever, when approaching for the sensitivity calibration. The following three 'Gain' parameters represent a PID controller, which sometimes has to be modified for different cell types, starting with the 'P Gain'. For example, experiments with

fibroblasts, such as REF52 cells, need a 'P Gain' of 250, while HUVECs require an increased 'P Gain' of 500. The 'Active Sensitivity' is either automatically inserted after the calibration of the cantilever sensitivity or it can be manually set to a known value. The last parameter, the 'Active Spring Constant', has to be manually entered after the calibration via 'Thermal Tuning' or 'Frequency Sweep' (**Appendix A.3.1**). The second parameter, 'View', in the 'Settings' list provides the modification of the displayed camera view (**Figure 38b**). Here, only the 'Mirror Option' has to be adjusted by clicking on the right corner of this field. The option 'Left Right' activates a mirrored view of the camera image and, thus, a matching display of both fluorescence and FluidFM® cameras.

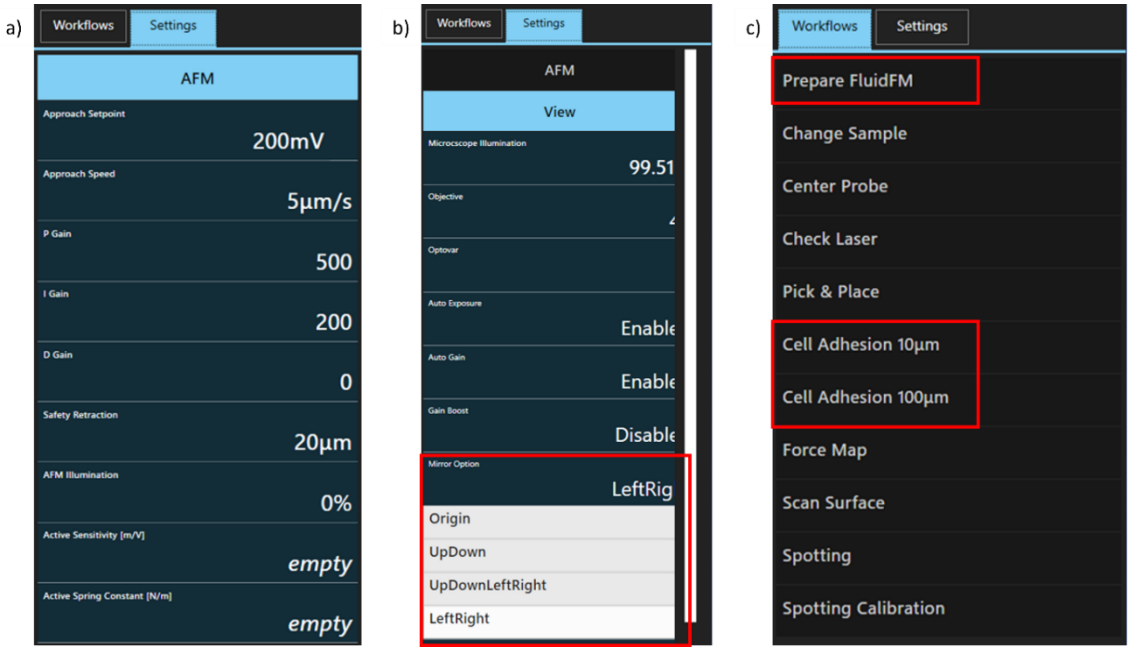

Figure 38: Exemplary images of the FluidFM® operator 'Settings'. (a) The 'AFM' toolbox provides a list of parameters that can be adjusted depending on the experiment. Here, especially the 'Active Sensitivity' and the 'Active Spring Constant' are important for a reliable and successful measurement. (b) The 'View' settings allow the mirroring of the displayed camera image by activating the 'Left Right' option in the 'Mirror Options' parameter.

The 'Workflows' operator offers a variety of toolboxes including 'Prepare FluidFM', 'Cell Adhesion 10 µm', and 'Cell Adhesion 100 µm' representing the most important ones (**Figure 38c**, red squares). The former provides a complete workflow for the correct preparation of the cantilever, which is detailed described in **Appendix A.4.3**. The second one has to be chosen for indentation or deformation experiments providing information about the elastic properties of a sample (**Appendix A.5.1**). During these measurements, the cantilever moves only in a range of 10 µm within the FluidFM® head. The 'Cell Adhesion 100 µm' workflow, on the other hand, offers a stage

retraction range of 100 µm and is therefore appropriate for long-distance experiments such as cell adhesion (**Appendix A.5.2**).

A.4. Cantilever installation

A precise and correct cantilever installation is crucial for a successful FluidFM® performance. Each cantilever is single-packed in a blister package from the Cytosurge company and provides specific parameters such as aperture size and nominal spring constant. The cantilever installation can be either performed without or with cantilever coating depending on the requirements of the experiment.

A.4.1. Cantilever preparation

To insert the cantilever into the system, there is a preparation set consisting of a magnetic FluidFM® probe holder ①, a magnetic support for the probe holder ②, a pneumatic connector tube ③, and a small screwdriver ④ (**Figure 39a**), all stored in a wooden box of the FluidFM® head. In the first step, the c-curved cyto-clip ⑤ consisting of the microchanneled cantilever ⑥, a macrochannel ⑦, and a fluidic reservoir ⑧ has to be mounted on the FluidFM® probe holder in a way that the cantilever is positioned over the small window (**Figure 39b**). It is advisable to carefully hold the cyto-clip at the outer edges of the reservoir or the c-curved arms. In case of a completely new cantilever, the fluidic reservoir has to be carefully filled with 15 to 17 µm of a solution, for instance, HEPES-2. To prevent the development of air bubbles within the reservoir, the tip of the pipette should be brought as close as possible to the macrochannel and subsequently pushed only to the first pressure point. Afterwards, the reservoir can be closed with the pneumatic connector, as illustrated in **Figure 39c**. The cantilever is then mounted on the underside of the measuring head via the magnetic linkage of the probe holder and subsequently connected to the pressure system using the pneumatic connector (**Figure 39d**). During this process, the pressure should be set to 0 mbar. To ensure a correct and straight positioning of the probe holder, a marking in the metallic frame (red arrow) that provides the direction of the cantilever serves as orientation. Afterwards, the FluidFM® head is mounted on a dry petri dish which is placed on the 100 µm z-stage and serves as robust surface during sensitivity calibration and as orientation guide. To prevent a cantilever breakage, the petri dish has to be positioned in a way that there is no contact between the cantilever and any edge. In addition, only petri dishes with a low height fitting under the FluidFM® measuring head can be used. For instance, the company WillCo Wells offers petri dishes with a height of 7 mm. Afterwards, the ‘Prepare FluidFM®’ workflow can be started

(**Appendix A.3.2**, **Figure 38c**). The corresponding step-by-step procedure is detailed explained in **Appendix A.4.3**.

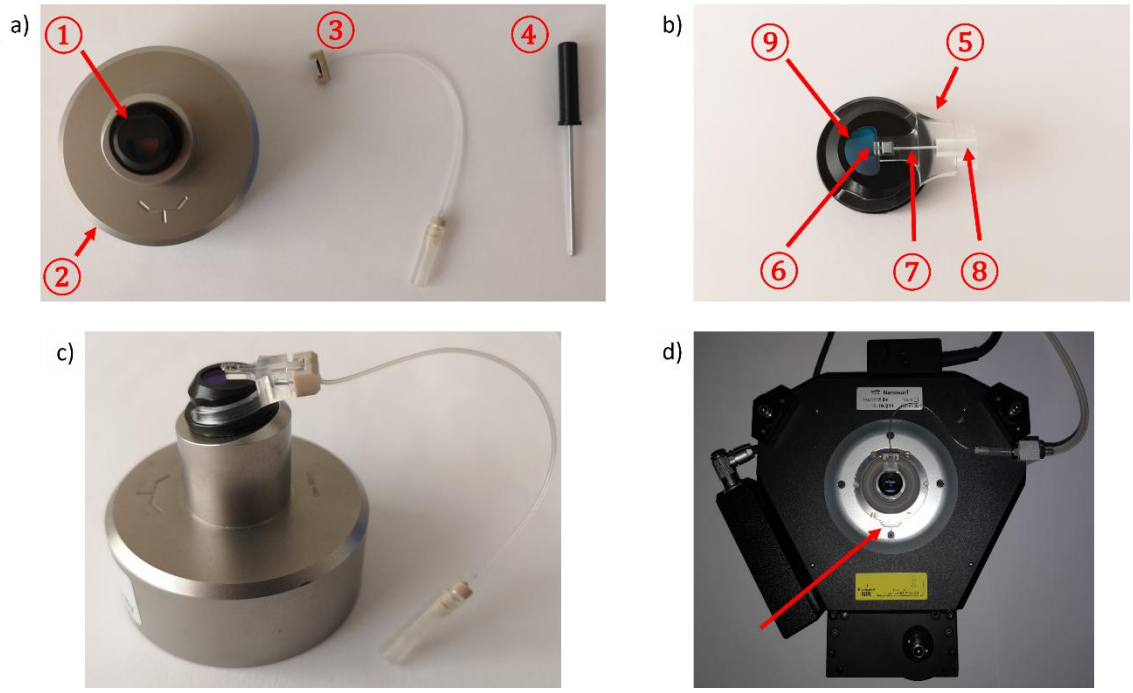

Figure 39: FluidFM® cantilever preparation. (a) The preparation setting of the cantilever consists of a magnet probe holder ①, a magnetic probe holder stage ②, a pneumatic connector ③, and a small screwdriver ④. (b) A c-curved cyto-clip ⑤, which is equipped with the microchanneled cantilever ⑥, a macrochannel ⑦ and a fluidic reservoir ⑧ is mounted on the probe holder in a way that the cantilever is oriented on the small window ⑨. (c) Sideview of the cyto-clip connected to the pneumatic connector. (d) A FluidFM® measurement head is connected to the magnetic probe holder. The cantilever is linked to the pressure system via the pneumatic connector. The marked sign in the metallic frame (red arrow) serves as orientation guide, showing the cantilever direction.

A.4.2. Non-fouling cantilever coating

Instead of directly using a new cantilever in its 'raw state', it can also be functionalized beforehand. This helps to avoid residues on the cantilever tip and to reduce subsequent washings steps to a minimum. However, the effectiveness of this anti-fouling coating depends on the applied negative pressure used for the sample aspiration and the duration of contact with the cantilever. For instance, for cells in suspension or pick-and-place experiments, this method has proven to be effective.[45] Prior to a non-fouling coating, cantilever spring constant and sensitivity have to be calibrated as described in **Appendix A.3.1** and **A.4.3**.

The cantilever coating is performed either at 80 °C or at RT. In the case of high-temperature functionalization, the whole coating process is performed in a pre-heated warming bath, as illustrated in **Figure 40a**. Therefore, a coating solution with a concentration of 0.5 mg mL^{-1} is prepared by dissolving the non-fouling PLL-*g*-PEG (PLL(20)-*g*[3.5]-PEG(2) (PEG), SuSoS AG,

Dübendorf, Switzerland) in prewarmed double distilled water (ddH_2O). Right before the coating, a fresh cantilever has to be treated with a plasma cleaner from both sides for about 1 s. Afterwards, 17 µl prewarmed PLL-*g*-PEG or HEPES-2 solution has to be loaded into the fluidic reservoir, closed with a pneumatic connector and coupled to a syringe. By slowly applying an overpressure, the filling of the macrochannel, as well as the appearance of a droplet at the cantilever, can be recognized. Using a 20 mL syringe and starting the pressure application at the 9 mL marker is advisable. After the successful cantilever filling, this pressure should be kept for about 1 min by fixing the position of the syringe via a clamp (**Figure 40b**). Subsequently, the syringe has to be removed very slowly to avoid a sudden negative pressure. To prevent evaporation of the solution within the reservoir, the cantilever stays connected to the pneumatic connector (**Figure 40a** ①) during the whole coating process. Afterwards, the cantilever has to be dipped into the pre-heated PLL-*g*-PEG solution within the probe-tube ②. Therefore, a 15 mL falcon tube (TPP centrifuge tube flat, Faust Lab Science, Klettgau, Germany) is cut at the 5.5 mL marker. The lower part of the tube is used as a probe-holder and filled with the pre-heated coating solution. Since the diameter of the tube matches exactly the width of the cyto-clip ③, the probe can be plunged into the solution without any external attachment. This probe tube, in turn, is immediately inserted into a 50 mL falcon ④, subsequently filled with pre-heated water right below the edge of the probe-tube. Additionally, a bar thermometer ⑤ is inserted to fix the position of the probe-tube and to have a control of the surrounding water temperature. Afterwards, this whole construct is transferred into the pre-heated warming bath and incubated for about 1 h. During the incubation, both the filling level of the coating solution within the probe-tube and the ambient temperature has to be checked regularly. After half of the incubation time, the coating temperature is reduced gradually by switching off the heating plate. After further 15 min, the probe-tube is taken out of the 50 mL falcon tube and incubated at RT for the rest of the time. At the end, the cantilever has to be rinsed a few times by immersion for 5 min in ddH_2O. Therefore, a petri dish has to be filled with ddH_2O and positioned onto the 100 µm z-stage. Subsequently, the cantilever is mounted on the FluidFM® head as explained in **Appendix A.4.1**. However, due to the cantilever being already wet, the window of the probe holder (**Appendix A.4.1, Figure 39b** ⑨)directly in front of the cantilever has to be filled with 40 µL ddH_2O, ensuring a wet cantilever surrounding. Afterwards, the cantilever can be inserted into the petri dish by mounting the measurement head on top. In the case of a cantilever coating at RT, the probe is only clamped into the probe-tube and kept there for the whole process of functionalization.

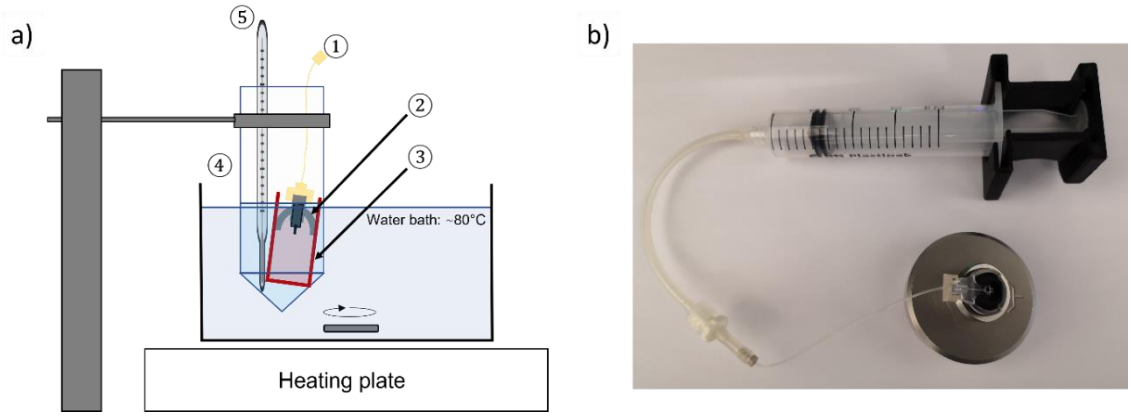

Figure 40: Schematic illustration of the non-fouling cantilever coating. (a) Schematic setup of the cantilever coating. A pneumatic connector ① covers the fluidic reservoir of the cantilever preventing the evaporation of the loaded solution. The cyto-clip ② is clamped into a probe-tube ③ filled with coating solution. This, in turn, is placed into a 50 mL falcon tube ④ which is filled with pre-heated water right below the edge of the probe-tube. To stabilize the position of the probe-tube and to control the surrounding water temperature, a bar thermometer ⑤ is additionally inserted. This whole construct is dipped into a warming bath heated via a digitally controlled heating plate. (b) Setup of a manual cantilever reservoir filling. The cantilever pneumatic connector is linked to a syringe, whose position is fixed with a black clamp, ensuring a stable overpressure.

A.4.3. ‘Prepare FluidFM®’ workflow

The ‘Prepare FluidFM®’ workflow is a user-friendly guide that helps to ensure an appropriate cantilever installation. It consists of 12 steps which are explained in detail in the following.

In the first step, ‘Name your Experiment’, an appropriate name of the experiment or sample can be entered. This is followed by the ‘Safety position’, which ensures that the cantilever is in its safety position by pressing the home button (**Appendix A.3.2**, **Figure 37** ⑦). In the third step, ‘Mount Probe’, the cantilever has to be aligned in a way that it shows a straight and centered position within the camera view. Due to its larger field of view, the position has to be checked through the eye piece of the microscope first. Therefore, the illumination has to be adjusted via the microscope panel (**Figure 41a**). If the cantilever is not visible, the focus level has to be carefully adjusted via the focus wheel on the right side of the microscope. Here, it is advisable to initially focus on the surface of the underlying petri dish as orientation. Then, the focus can be turned upwards until the cantilever and its fixation platform is visible. The position of the latter one should be as horizontal as possible. In case it is not, the cyto-clip and probe-holder position on the FluidFM® head has to be corrected. Its position can be further checked within the camera view (**Figure 41b**). Here, the edge of the fixing platform, visible as black shadow ①, should be aligned towards the upper frame of the camera viewing window ②, ensuring a straight position of the cantilever ③. Therefore, the location of the cyto-clip can be changed by a movement in

xy-direction. This is regulated via two silver screws, positioned at the left side of the xy-sample stage.

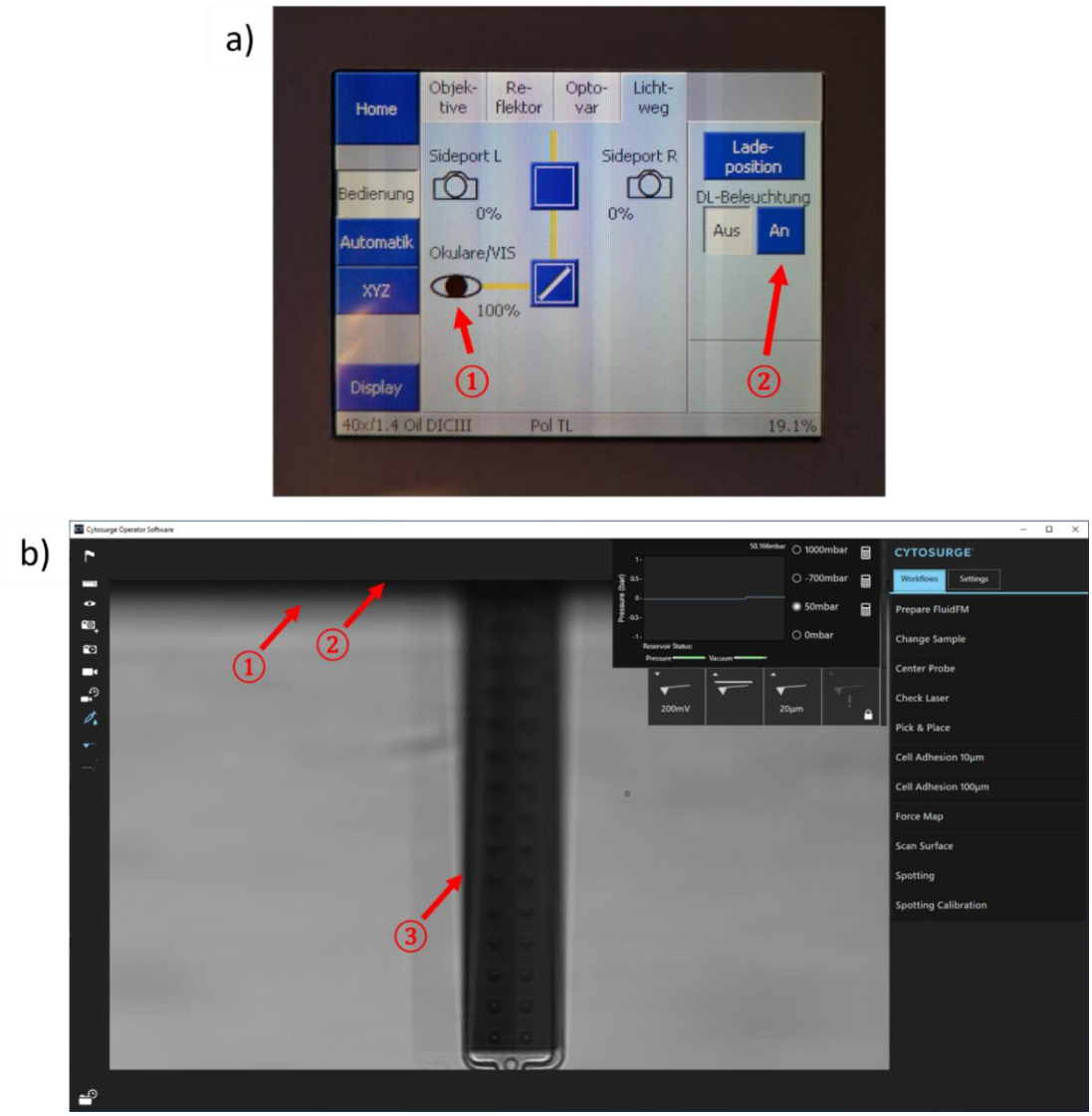

Figure 41: Illustration of a successfully mounted cantilever. (a) On the microscope panel, both the 'Okulare/VIS' ① and the brightfield illumination ② has to activated, enabling the sample visualization through the eye piece. (b) The edge of the cantilever fixing platform ①, visible as a black shadow, is well-aligned towards the upper frame of the camera viewing winding. This guarantees a horizontal orientation of the cyto-clip and, therefore, a straight position of the cantilever ③.

After the successful cantilever mounting, the probe has to be configured as 'FluidFM Micro Pipette' ('Configure Probe'), automatically inserting intrinsic parameters such as nominal spring constant or the specific cantilever dimensions. This is followed by the laser alignment in dry conditions ('Align Laser (Dry)') (**Figure 42a**). First, the signal quality has to be adjusted by positioning the laser spot on the cantilever tip. As illustrated in **Figure 42a** ①, the highest quality is usually achieved between the first and third row of pillars. The movement of the laser spot is connected to two screws which are implemented in the FluidFM® head (**Figure 42b** ①). By using

the screwdriver presented in **Appendix A.4.1** (**Figure 39a** ④), the laser spot can be directed in xy-direction. This is followed by the alignment of the photodetector which is adjusted by the screws marked with a ② in **Figure 42b**. To achieve an optimal laser signal, the laser spot, illustrated as a red dot in **Figure 42a** ③, has to be accurately centered within the coordinate system. As a supporting feature, this workflow also includes a schematic top view of the FluidFM® head, indicating the corresponding screws with 'A' for signal quality and 'B' for the photodetector (**Figure 42a** ②).

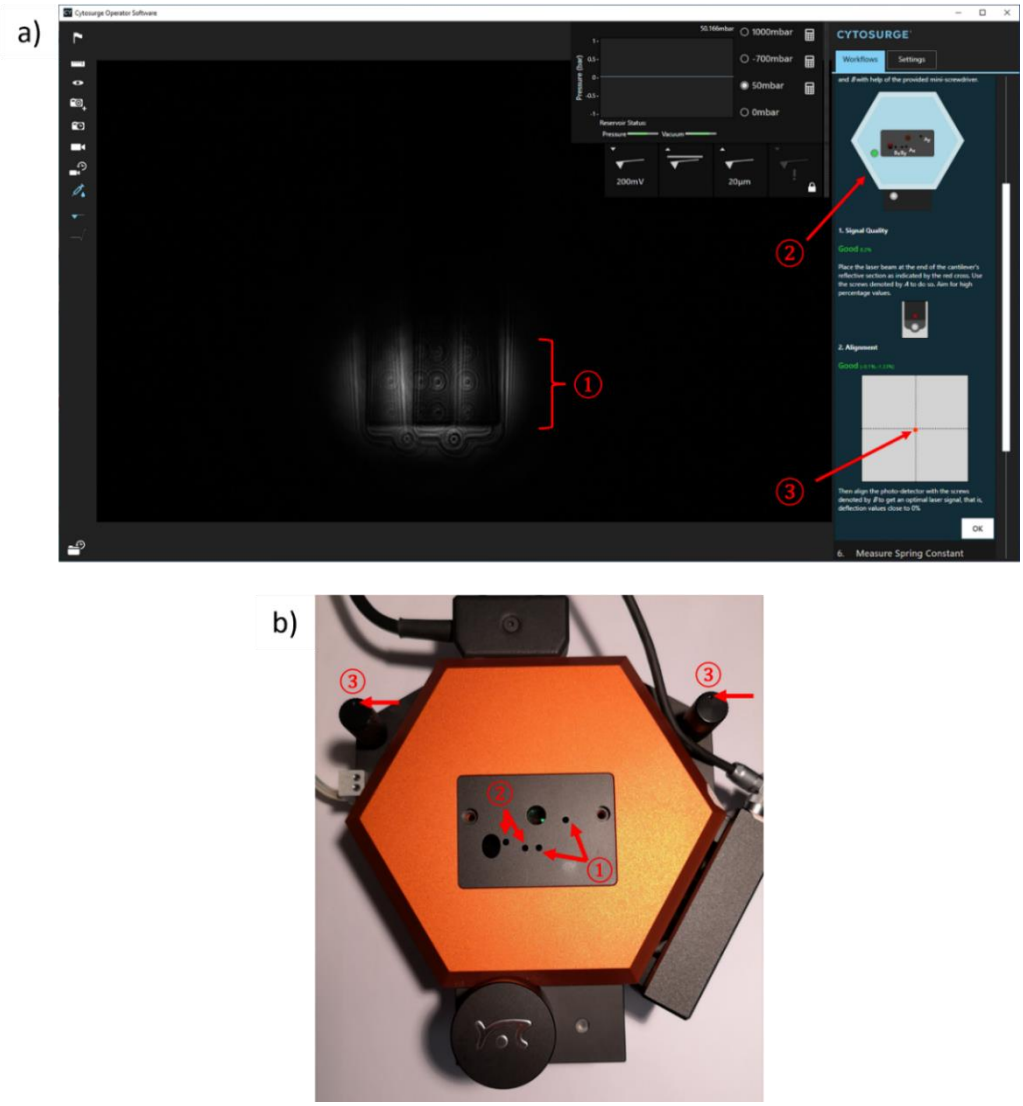

Figure 42: Laser alignment in dry conditions. (a) The laser alignment consists of two steps. First the signal quality of the laser is adjusted by positioning the laser spot within the first three pillar rows of the cantilever ①. This workflow further provides a schematic top view of the FluidFM® head, indicating the corresponding screws for the alignment ②. The second step implies the alignment of the photodetector by accurately centering the laser spot, which is shown as a red dot within the coordinate system ③. (b) Photograph of the top view of a FluidFM® measurement head showing the four screws needed for the laser alignment. The signal quality is directed via the screws marked with a ①. The alignment of the photodetector, on the other hand, is performed with the screws under ②. The two pins in the back of the measurement head ③ are responsible for the height adjustment of the FluidFM® head. Both pins are marked with a small indentation and serve as orientation guide (red arrows).

The next step, 'Measure Spring Constant', implies the calibration of the cantilever spring constant. This is performed via 'Thermal Tuning' and 'Frequency Sweep' as explained in **Appendix A.3.1**. The extracted value is subsequently entered in the 'AFM' unit of the 'Settings' (**Appendix A.3.2**, **Figure 38a**). Then, the microchanneled cantilever is loaded with the solution, which was filled in the fluidic reservoir during cantilever preparation (**Appendix A.4.1**) ('Fill Probe'). Therefore, the cantilever tip has to be clearly visible within the camera viewing window. By clicking on 'Apply pressure', a pressure of 1000 mbar is applied. Once the microchannel is completely filled, droplet formation occurs at the cantilever tip. Depending on the aperture size, this can take only a few seconds or up to a minute. To prevent the liquid from drying out and thus clogging the microchannel, the cantilever has to be always embedded in a liquid surrounding from now on. For this purpose, the small window implemented in the probe-holder has to be covered with a droplet of 40 µL ddH_2O. In addition, the underlying petri dish has to be filled with ddH_2O embedding the whole cyto-clip. Due to the surrounding water and the resulting different refraction, the laser alignment has to be re-adjusted in the next step ('Align Laser (Liquid)'). This is performed analogously to the procedure under dry conditions. Compared to the dry state, the signal quality is slightly reduced and settled between 8 and 9%. Prior to the following 'Approach', the focus is set to the upper surface of the petri dish checking the entire distance between home position and substrate. By starting the approach, the cantilever is automatically moved downwards until the surface, and an initially given setpoint of 200 mV, is reached. If the separation between cantilever and sample surface is too large, the complete FluidFM® head will be lowered via two pins at its back (**Figure 42b** ③). To ensure a horizontal position of the FluidFM® head, both pins should be moved only simultaneously and aligned in the same direction. For this purpose, they are equipped with two small indentations, which serve as an orientation guide. Afterwards, the cantilever sensitivity can be determined by an automated procedure of the software ('Measure Sensitivity'). Here, the cantilever is pressed onto the surface until the initially given setpoint of 200 mV is reached. This process should be performed five times and subsequently compared within 'Data Selection'. An exemplary composition of five curves is illustrated in **Figure 43**, showing an applicable force peak and an overall good agreement. Here, the considered data for sensitivity calculations can be defined by activating or excluding a force-curve. The cantilever sensitivity is automatically entered into the 'AFM' section of the 'Settings' by accepting the calculated value (**Appendix A.3.2**, **Figure 38a**). Moreover, the 'Approach Setpoint' is given in nanonewton from now on. During the next step, 'Center Probe', the cantilever has to be aligned until its aperture matches the crosshairs. This position serves as starting position for the following experiments conducted with 'Cell Adhesion 10 µm' or 'Cell Adhesion 100 µm'.

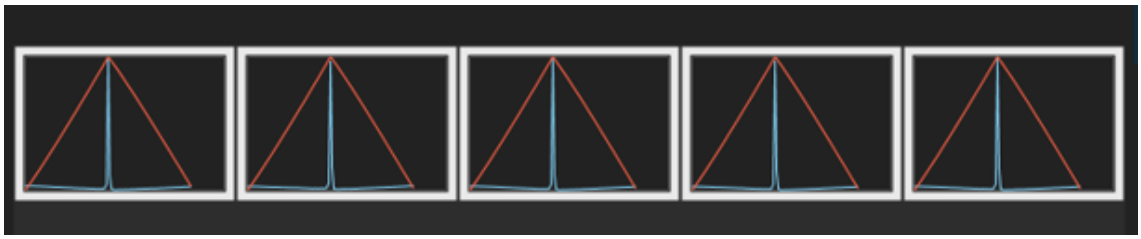

Figure 43: Exemplary data selection of five force-curves measured during the sensitivity calibration. The red course shows the up and downward movement of the cantilever. The blue peaks illustrate the force peak, appearing when a given setpoint is reached.

A.5. Data acquisition

Depending on the experiment, one can choose between two data acquisition workflows. The 'Cell Adhesion 10 µm' workflow provides a cantilever driving range of 10 µm, which is mostly used for the examination of elastic properties. On the other hand, experiments that need a long-distance retraction range, such as the cell adhesion of mature cells, are usually performed with the 'Cell Adhesion 100 µm' workflow. Here, the z-stage offers a driving range of 100 µm. The workflow of both indentation (**Appendix A.5.1**) and conventional cellular detachment (**Appendix A.5.2.1**) experiments is illustrated without a PIFOC system. This is only required in the procedure of correlated FL-FluidFM® data acquisition.

A.5.1. Cell Adhesion 10 µm

At the beginning of this workflow, sample and cantilever are brought to a defined distance of 30 µm ('Set sample distance'). This is followed by a re-alignment of the cantilever by matching the aperture with the crosshairs again ('Center probe'). Afterwards, the target sample has to be selected ('Select Target Cell'). As illustrated in **Figure 44**, this step activates a movable crosshair and a fixed square which signs the ROI. By moving the sample stage with the Nanosurf stage controller (**Appendix A.1**, **Figure 32** ②), the target sample can be positioned into the ROI and subsequently marked with the crosshair.

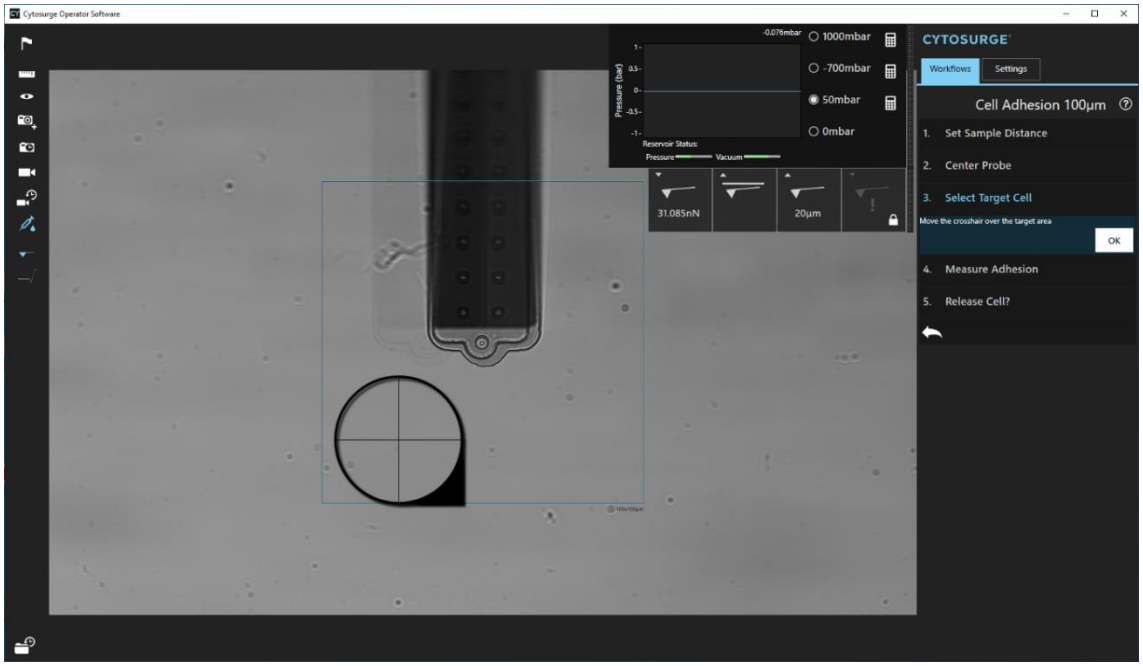

Figure 44: Illustration of the step 'Select Target Cell'. Here, a fixed square is displayed which defines the ROI in which a target sample has to be located in. The movable crosshair subsequently acts as contact point for the cantilever during attachment and has to be positioned over the target cell.

The following step, 'Measure Adhesion', provides the opportunity to define specific measurement parameters (**Figure 45**). For indentation experiments, the option 'Reuse Cell' has to be activated which blocks an automated sample attachment via negative pressure. By clicking on the displayed graph ①, a new window named 'Modulation' opens. By further clicking on the hat icon ②, a more detailed list is displayed. Here, the three sections of cantilever movement can be further specified. Since the analysis of elastic properties is based on the approach-curve, the 'Sampling Rate' of 'Towards Sample' should be increased to 1024 Hz ensuring enough data points. The 'Setpoint' corresponds to the 'Approach Setpoint' calculated after sensitivity calibration and given under 'Settings'-'AFM' (**Appendix A.3.2**, **Figure 38a**). The setpoint can be manually adjusted depending on the experimental requirements, if needed. However, it is advisable to always enter the same setpoints in both categories. The 'Speed' represents another parameter, whose value strongly depends on the experimental context. For classical indentation measurements, a slower speed of 1 µm s^{-1} is usually used. The 'Pause on Sample' section can be skipped by indicating 0 s or activated for a few seconds with a 'Sampling Rate' of 512 Hz. Also, for the last section, 'Away from Sample', a 'Sampling Rate' of 512 Hz is sufficient. The 'Distance' can be set to its maximum which is usually indicated as about 9.63 µm. The movement of 'Direction' is set to 'Backwards' and conducted with the needed 'Speed'. In general, measurements are often performed with the same speed for both the cantilever approach and retraction. After the complete parameter adjustment,

the measurement can be started. The recorded data can be displayed by activating the folder button on the left corner (**Figure 45** ③). By subsequently activating an image, different data files can be exported including 'SPIP (.asc)', 'Figure (.png)', and 'Comma Separated (.csv)'. The latter one can be opened with excel, while the former one is a special data format for the analysis software 'SPIP'. The whole data is saved at 'FluidFM User' → 'Documents' → 'Cytosurge' → 'Results'.

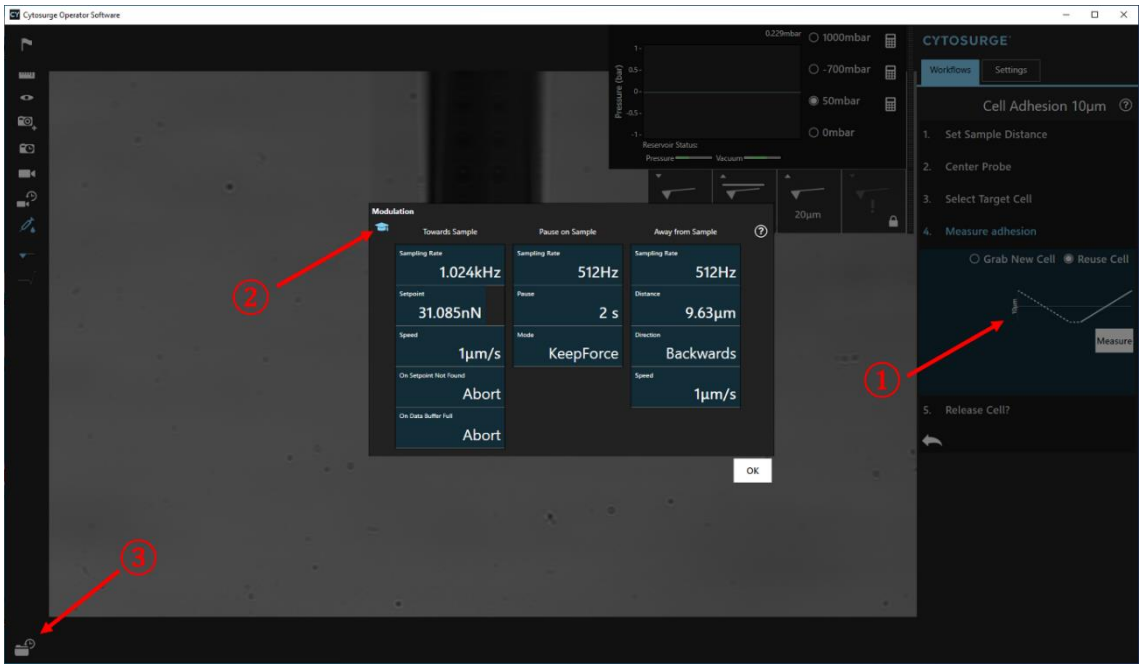

Figure 45: Exemplary view of the 'Cell Adhesion 10 µm' workflow. The 'Modulation' toolbox of 'Measure Adhesion' is activated by clicking on the graphical illustration of the cantilever movement ①. A more detailed parameter setting is displayed by clicking on the hat icon ②. Here, the three sections of 'Towards Sample', 'Pause on Sample' and 'Away from Sample' can be specified.

A.5.2. Cell Adhesion 100 µm

The 'Cell Adhesion 100 µm' workflow is used for both conventional cellular detachment as well as for the correlated one. However, the latter includes a few more extra features.

A.5.2.1. FluidFM® cell adhesion

The basic procedure of this workflow includes the same steps as the 'Cell Adhesion 10 µm' one. Only the fourth step, 'Measure Adhesion', differs in its settings. Here, the option 'Grab New Cell' has to be chosen which activates the pressure system. Depending on the cell/sample size and adhesion strength, the pressure can be set between -100 and -800 mbar. The 'Modulation' window shows the same parameter composition as described before (**Appendix A.5.1**, **Figure 45**). However, in this case, the 'Sampling Rate' of 'Towards Tip' can be set to 512 Hz. Analogously to

the ‘Cell Adhesion 10 µm’ workflow, the calculated ‘Setpoint’ and ‘Speed’ can be manually adjusted according to the experimental requirements. Normally, a speed of 5 µm s^{-1} is appropriate. To ensure a proper sealing, the ‘Pause in Contact’ is usually activated for 2 to 3 s. During this time, constant negative pressure is applied, attaching the sample to the cantilever aperture. To guarantee a stable cantilever positioning during this process, the ‘Mode’ is set to ‘Keep Force’. The last section, ‘Away from Tip’, represents the retraction-curve and, thus, plays the main role in the cellular detachment performance. To provide enough data points for the following analysis, the ‘Sampling Rate’ is increased to 1024 Hz in this case. The separation ‘Distance’ can be set to its maximum of 100 µm retraction range. Analogous to indentation experiments, the ‘Direction’ is defined as ‘Backwards’. The ‘Speed’ as last parameter depends again on the experimental interest. Subsequently, the cellular detachment can be started by clicking ‘Measure’. In case of an uncoated cantilever, the probe has to be rinsed with ddH_2O after each measurement. For this purpose, four petri dishes filled with cleaning solution are successively placed beneath the measurement head. After each cleaning round, the water has to be replaced by fresh one.

A.5.2.2. Correlated FL-FluidFM®

In principle, the correlated data acquisition is based on the same procedure as the one of conventional cellular detachment. However, the implementation of a PIFOC system entails a few special features. At the beginning of the workflow, the automated ‘Set Sample Distance’ has to be skipped and manually performed. Therefore, the cantilever is brought back into its home position (**Appendix A.3.2, Figure 37** ⑦). This is followed by a manual adjustment of the z-stage position via the ‘SPM System’, which can be found in the ‘SMP Parameters’ of the Nanosurf C3000 software (**Appendix A.3.1**, **Figure 34b**). Here, the ‘Absolute Idle Position’ has to be set to +50 µm, inducing a z-stage positioning to its upper limit. This is followed by the cantilever approach (**Appendix A.3.2**, **Figure 37** ⑥). Subsequently, the z-stage can be retracted again by entering a position between +30 and +40 µm into the ‘Absolute Idle Position’ which results in a defined sample distance of 20 to 10 µm and a remaining retraction range of 80 to 90 µm. After the appropriate positioning, the three following steps of ‘Center Probe’, ‘Select Target Cell’, and ‘Measure Adhesion’ can be performed as previously described. However, before starting the measurement, the 50:50 beam splitter has to be removed from the double camera port which directs 100% of the emission signal exclusively to the fluorescence camera (**Figure 46a,** red arrow). Afterwards, the sample illumination has to be switched from brightfield to fluorescence illumination. This includes both the manual activation of the corresponding filter, for instance, HE 90, which is suitable for several fluorescence channels, and the deactivation of the

transmission light illumination by clicking 'Aus' at 'DL-Beleuchtung' (**Figure 46b**). Then, the chosen fluorescence channel can be activated within the ZEN 2.6 software (**Appendix A.2**, **Figure 33b**). Depending on the duration of the cellular detachment, the time series is set to 60 to 70 s. It is advisable to re-check all prior set fluorescence parameters, such as intensity and exposure time, right before the measurement. The detailed handling of this software is explained in **Appendix A.2**. Afterwards, the correlated data acquisition can be started by simultaneously clicking 'Experiment starten' and 'Measure' within the corresponding software. Now the cellular detachment can be visually observed only in the ZEN software. The monitoring of the FluidFM® parameters, however, is still possible via the C3000 software.

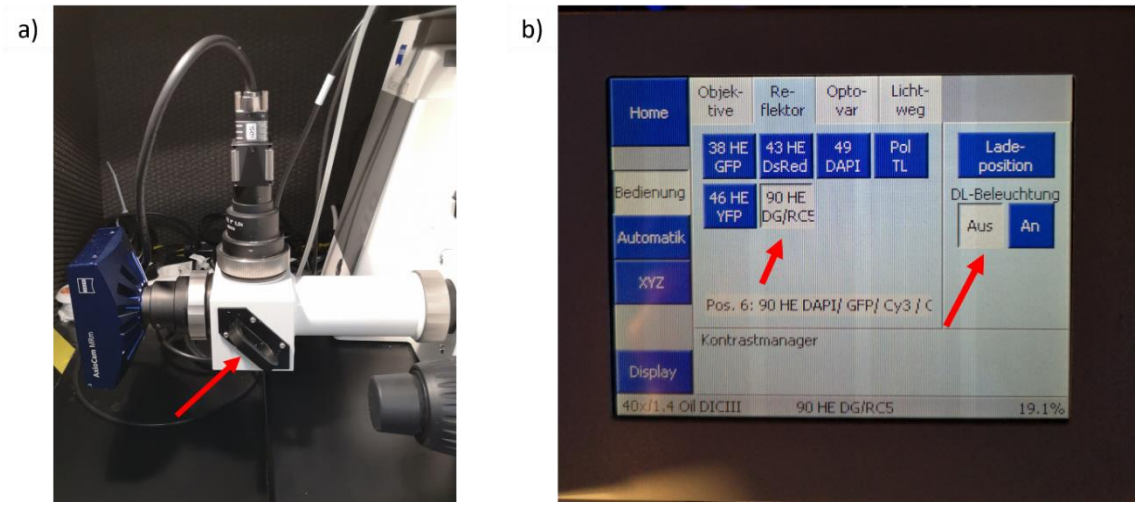

Figure 46: Hardware adjustments for correlated FL-FluidFM®. (a) The double camera port is equipped with a 50:50 beam splitter marked with a red arrow. Before correlated data acquisition, this component has to be removed from the light pathway. In this way the entire emission signal is exclusively directed to the fluorescence camera. (b) Within the microscope panel, the brightfield illumination has to be switched off by clicking the 'Aus' button at 'DL-Beleuchtung', while the fluorescence filter '90 HE' has to be activated (red arrows).

A.6. Troubleshooting and hints

Due to its high complexity, the handling of the correlated FL-FluidFM® system often entails some challenges. Nevertheless, to enable a smooth experimental workflow, this chapter provides a few tips and tricks which address the most occurring issues. If needed, there is technical support for both systems that can be contacted (**Appendix A.7**).

Storage of already installed cantilevers

If stored correctly, FluidFM® cantilevers can be used for several weeks to month. After installation, they have to be kept in a liquid surrounding. Therefore, 15 mL falcon tubes from the Faust Lab Science (TPP centrifuge tube flat, Faust Lab Science, Klettgau, Germany) have to be almost

completely filled with ddH_2O, supplemented with 1% to 2% penicillin/streptomycin (10,000 U mL^{-1}, Life Technologies, USA). Due to the inner tube diameter perfectly matching the width of the cyto-clip, they can be directly dipped into the solution without any external support. However, it has to be ensured that the cantilever reservoir is kept in air. Afterwards, the tube can be closed with its lid and stored in the fridge.

Inappropriate software start

In case of a failed software start, the easiest way to solve this problem is to do a re-start. However, sometimes a complete computer shutdown with following re-start is necessary. Also, a re-start of all hardware components might be useful.

Inappropriate laser alignment

If the laser alignment is not working, there might be different reasons. First, it has to be checked if the 'Laser off' button within the 'SPM System' parameters is checked by mistake (**Appendix A.3.1**, **Figure 34b**). Another solution to this problem could be the wrong filter setting. The laser spot is only visible by activating the filter 'Pol TL' in the microscope panel. Also, bubbles around the cantilever can disturb the clear laser spot visualization. This can be solved, for instance, by lifting and dropping the FluidFM® head a few times. However, an already applied overpressure together with an inappropriate connection between the cantilever reservoir and pneumatic connector could also induce the development of bubbles. This can usually be fixed by re-connecting these components. If none of these options helps, there is also the possibility to do a reset of the laser positioning. More precisely, the screws have to be brought back to center by first counting the rounds needed to reach the respective end and then bringing them back to the middle. Another alternative can be to check the position of the probe-holder on the measurement head. Although the magnetic linkage should serve as stabilizer, the position sometimes shows a small shift which can be quickly corrected. In case of high humidity, it sometimes happens that the small window within the probe-holder fogs up. However, this can only be checked by re-building the probe-holder-cyto-clip construct. Moisture can be removed using a lint-free tissue or by carefully applying compressed air.

Inappropriate sealing

Most of the time, an inappropriate cell-cantilever sealing is related to an insufficient negative pressure. This can be checked the easiest way by approaching any residues on the surface of a petri dish and applying an overpressure of 1000 mbar. If they are not affected by the high

pressure, then the connection between cantilever reservoir and pneumatic connector can be checked. Moreover, a bubble within the reservoir, blocking the entry to the macrochannel might be another explanation for an insufficient negative pressure. If this is the case, one can try to remove the bubble with a pipette or to remove the entire liquid and subsequently refill the reservoir. To further exclude a lacking tube, the pneumatic connector can be coupled to a syringe and completely dipped into a glass filled with water. In case of any leaks, the appearance of bubbles will be visible by manually applying an overpressure. Besides the more hardware-associated reasons, there is also a more software-related issue. Since a good sealing also depends on a well-defined contact zone between cantilever and sample, the positioning of the crosshairs should be checked. For instance, cells should always be approached at their highest point, the nucleus. Moreover, a longer 'Pause in Contact' might support a better attachment. Also, the 'Setpoint' might be an influencing factor since it determines how strong a cantilever is pressed onto a sample.

Handling of a high-numerical oil objective

The implementation of a high-numerical oil objective implies a few special features during the FluidFM® performance. Due to its direct contact with the sample surface, it only allows a small range of focus level adjustment without directly lifting the whole petri dish. Therefore, a cantilever in its home position is usually out of focus at the beginning of an experiment. However, instead of moving the objective upwards, the cantilever has to be carefully lowered by the 'Advance' button within the C3000 software until the focus level is reached. To avoid unintentional breakage of the cantilever by touching the surface too hard, it has to be ensured that the cantilever is visible within the camera viewing window. Another important aspect, which is affected by the application of an oil objective, is the procedure of cantilever washing. Usually, this entails the successive switching of several petri dishes filled with cleaning solution while the sample dish is stored in the meanwhile. However, after separating the oil objective and the sample, oil residues remain on the underside of the sample surface. To prevent the smearing of this oil, the sample dish has to be deposited so that there is no contact with the device table.

The most common error message

"Setpoint could not reached. Sample could be too far away. Please approach again." This error message often occurs directly after starting a FluidFM® measurement, when the z-stage moves towards the cantilever tip until a given setpoint is reached. A disruption within this workflow can have many different reasons. A first option could be to repeat the approach and re-start the 'Cell

Adhesion 100 µm' workflow as suggested by the error message itself. Another reason might be an inappropriate force setpoint. This can be modified via the 'Modulation' settings of the 'Measure Adhesion' step and within the 'AFM' section of 'Settings'. Apart from this, the limited motion range of the z-stage could be another explanation for the occurrence of this error message. It might happen that when the cantilever is located at the maximum height of the z-stage (+50 µm) that the approaching z-stage reaches its upper limit before the given setpoint is reached. This may be the case, especially when using the PIFOC system. Here, it is advisable to repeat and adjust the manual positioning of cantilever and z-stage in a way that the cantilever is located a bit lower, for instance, at +48 µm instead of +50 µm (**Appendix A.5.2.2**).

A.7. Technical support

FluidFM® (Nanosurf/Cytosurge):

Patrick Lang: lang@nanosurf.com

Pablo Dörig: pablo.doerig@cytosurge.com

Fluorescence Microscopy (ZEISS):

Sebastian Peters: sebastian.peters@zeiss.com

Ronald George: Ronald.george@zeiss.com (Former contact)

Acknowledgement/Danksagung

An dieser Stelle möchte ich mich herzlichst bei all denjenigen bedanken, die mich in den vergangenen vier Jahren auf verschiedenste Art und Weise begleitet haben und ohne die die Entstehung dieser Dissertation nicht möglich gewesen wäre.

Zuallererst möchte ich mich sehr herzlich bei Professor Dr. Jürgen Groll bedanken, der mir die Möglichkeit gab, meine Doktorarbeit am FMZ anzufertigen. Durch die Interdisziplinarität des Lehrstuhls konnte ich über das Spektrum meiner ursprünglich physikalischen Ausbildung hinausblicken und mich auch mit biologischen Fragestellungen auseinandersetzen. Darüber hinaus möchte ich mich dafür bedanken, dass ich die großartige und nicht selbstverständliche Gelegenheit hatte, an dem PONTEA Seminar teilzunehmen, das mir dabei geholfen hat, mich sowohl beruflich als auch persönlich weiterzuentwickeln. Außerdem möchte ich mich gerne für die Teilnahme an wissenschaftlichen Konferenzen und Summer Schools bedanken, die es mir ermöglicht haben, mich auch mit internationalen Kollegen auszutauschen.

Meinem Zweitgutachter Professor Dr. Markus Sauer möchte ich für die Betreuung und Begutachtung meiner Dissertation danken. Durch meine vorherige Masterarbeit an seinem Lehrstuhl konnte ich mein Wissen über hochauflösende Fluoreszenzmikroskopie, Zellbiologie und korrelative Mikroskopie bereits ausbauen, was für die spätere Doktorarbeit sehr hilfreich war.

Meinem Drittbetreuer Professor Dr. Franz Jakob danke ich für die Zeit, die er sich für die jährlichen GSLS Meetings genommen hat sowie die fachlichen und wertvollen Diskussionen, die in neuen Denkanstößen resultierten.

Dr. Ana Sancho möchte ich herzlichst dafür danken, dass sie mir als direkte Betreuerin und Ansprechpartnerin im Alltag stets zur Seite stand. Sie hat mich von Anfang an unter ihre Fittiche genommen, was mir den Einstieg in eine für mich komplett neue Thematik erleichtert hat. In der darauffolgenden Zeit hat sie mir mit viel Geduld und fachlicher Kompetenz die experimentelle Arbeit am FluidFM® beigebracht und mich auf die kommenden Herausforderungen vorbereitet. Danke, dass ich immer mit jeder noch so kleinen Frage zu dir kommen konnte. Auch wenn sich unsere Wege nach einem Jahr getrennt haben, war sie in den ganzen Jahren danach bei Fragen und Diskussionen immer für mich erreichbar, wofür ich ihr sehr dankbar bin. Auch in schwierigen

Zeiten hat sie mich wieder aufgebaut und unterstützt, danke dafür. Außerdem möchte ich ihr für das Korrekturlesen meiner Dissertation danken.

Mein herzlicher Dank geht auch an Harald Hümpfer und Anton Hofmann, die mich bei allen Umbaumaßnahmen, Reparaturen und technischen sowie IT-Problemen am FluidFM® unterstützt haben. Sie waren immer zur Stelle, wenn ich Spezialanfertigungen für den Aufbau und die Bedienung meines korrelativen Systems gebraucht habe.

Bei meinen Kollegen und Kolleginnen der Bio-Gruppe möchte ich mich dafür bedanken, dass ich auch als thematische Außenseiterin so herzlich aufgenommen wurde und ich bei biologischen Fragen immer auf euch zählen konnte. Insbesondere möchte ich mich bei Dr. Tatjana Schilling bedanken, dass sie mir bei Fragen zur Zellkultur mit Rat und Tat zur Seite stand und sich die Zeit genommen hat Kapitel meiner Dissertation Korrektur zu lesen. Mein herzlichster Dank geht auch an Alice Schaaf und Alevtina Rosenthal, die mich in der alltäglichen Laborarbeit unterstützt haben. Danke auch an Dr. Matthias Ryma, der sich die Zeit genommen hat Teile meiner Doktorarbeit Korrektur zu lesen. Unsere spontanen kurzen Unterhaltungen im Labor, haben mich immer zum Lachen gebracht, danke dafür. Ein weiterer Dank geht auch an Kristina Andelovic, die mir kurz vor Schluss meiner Doktorarbeit bei meinen letzten Experimenten mit Rat und Tat zur Seite stand und sogar ihre Freizeit geopfert hat, um mit mir zusammen im Labor zu stehen.

Ein besonderer Dank geht auch an Dr. Carina Blum, die während unserer gemeinsamen Zeit am FMZ nicht nur eine Büro Kollegin war, sondern auch zu einer Freundin geworden ist. Ich danke Ihr von Herzen, dass Sie immer ein offenes Ohr hatte und mich sowohl beim Schreiben meiner ersten Publikation als auch bei der Dissertation unterstützt hat. Unsere Gespräche über Gott und die Welt, werde ich vermissen.

Dr. Jörg Teßmar möchte ich für seinen unermüdlichen Einsatz zur Optimierung aller Lehrstuhl-internen EDV-Prozesse danken. Danke auch dafür, dass ich aufgrund meiner großen Datenmengen oftmals eine „Extrawurst“ bekam.

Des Weiteren möchte ich mich bei Philipp Stahlhut für seine Unterstützung am REM bedanken und die Zeit, die er sich genommen hat, um mir bei meinen Proben zu helfen. Außerdem bin ich ihm sehr dankbar für seine Hilfe bei der Etablierung einer geeigneten Softwarebedienung meines korrelativen Systems.

Außerdem möchte ich mich herzlichst bei den guten Seelen des FMZ's bedanken, Tanja Dambach und Birgit Langner-Bischof. Danke für die hervorragende Organisation und Koordination von diversen administrativen Dingen sowie das ermöglichen von (auch einmal kurzfristigen) Terminen bei Herrn Groll. Danke für euer offenes Ohr und euren unermüdlichen Einsatz für einen reibungslosen Ablauf.

Ein sehr großer Dank geht auch an die Mädels vom „Hühnerstall": Dr. Carina Blum, Jessica Brand, Dr. Annika Seifert, Johanna Lutz und Theresa Vogel. Unsere fachlichen Diskussionen, aber auch persönlichen Gespräche haben uns nicht nur zu Kolleginnen, sondern auch zu Freundinnen gemacht. Danke für die vielen schönen Momente sowohl auf der Arbeit als auch privat. Außerdem möchte ich euch herzlichst dafür danken, dass ihr bei all den Auf und Abs immer ein offenes Ohr hattet und wir uns gegenseitig unterstützt, aufgebaut und motiviert haben. Ihr habt die letzten vier Jahre zu einer unvergesslichen Zeit gemacht und ich bin unglaublich glücklich darüber, dass ich die ein oder andere auch in Zukunft noch als Kollegin an meiner Seite haben darf.

Außerdem möchte ich mich herzlichst bei Ilona Paulus, Viktoria Niklaus, Jan Weichhold, Dr. Ib Holzmeister, Dr. Florian Pinzner, Leonard Forster, Friederike Kaiser, Junwen Shan und Christoph Böhm für die vielen gemeinsamen Mittags-, oder Kaffeepausen bedanken. Danke für die allgemein schöne Arbeitsatmosphäre und eine unvergleichliche Zeit am FMZ. Bei allen nicht namentlich genannten „FMZlern" möchte ich mich an dieser Stelle für die gute Zusammenarbeit und das angenehme Arbeitsklima bedanken.

Außerdem möchte ich mich herzlichst bei meinen Eltern bedanken. Danke Mama und Papa für euren jahrelangen Rückhalt und eure mentale und finanzielle Unterstützung, die eine Dissertation letztlich für mich möglich gemacht hat. Danke auch für euer nie endendes Interesse und die zahlreichen Unterhaltungen und Gespräche über meine Arbeit, auch wenn Ihr wahrscheinlich nicht immer verstanden habt, was ich da genau tue und wovon ich rede. Ihr hattet immer ein offenes Ohr und habt mich bei so einigen Höhen und Tiefen wieder aufgebaut. Danke, dass Ihr immer hinter mit standet und stolz auf mich wart und seid.

Zu guter Letzt möchte ich mich von ganzen Herzen bei Sebastian bedanken. Danke für deine unendliche Geduld und Unterstützung in den letzten Jahren. Danke dafür, dass du mich immer wieder aufgebaut hast und auch in schwierigen Zeiten meine schlechte Laune ertragen hast. Danke, dass du immer ein offenes Ohr hattest und Verständnis dafür, wenn ich auch am

Acknowledgement/Danksagung

Wochenende mal ins Labor musste, weil die Zellen mal wieder nicht so wollten wie ich. Von Herzen danke, dass du all die Jahre immer an meiner Seite warst und immer für mich da bist. ♥

Affidavit

I hereby confirm that my thesis entitled “Correlation of FluidFM® Technology and Fluorescence Microscopy for the Visualization of Cellular Detachment Steps” is the result of my own work. I did not receive any help or support from commercial consultants. All sources and/or materials applied are listed and specified in the thesis.

Furthermore, I confirm that this thesis has not yet been submitted as part of another examination process neither in identical nor in similar form.

Place, Date

Signature

Eidesstattliche Erklärung

Hiermit erkläre ich an Eides statt, die Dissertation „Korrelation von FluidFM® Technologie und Fluoreszenzmikroskopie zur Visualisierung von zellulären Ablöseschritten“ eigenständig, d.h. insbesondere selbständig und ohne Hilfe eines kommerziellen Promotionsberaters, angefertigt und keine anderen als die von mir angegebenen Quellen und Hilfsmittel verwendet zu haben.
Ich erkläre außerdem, dass die Dissertation weder in gleicher noch in ähnlicher Form bereits in einem anderen Prüfungsverfahren vorgelegen hat.

Ort, Datum

Unterschrift

Curriculum vitae